Seismic and Gravitational Studies of Melting in the Mantle's Thermal Boundary Layers

by

Emily Mary Van Ark

B.A. Northwestern University (1999)

Submitted in partial fulfillment of the requirements for the degree of

Doctor of Philosophy

at the

MASSACHUSETTS INSTITUTE OF TECHNOLOGY

and the

WOODS HOLE OCEANOGRAPHIC INSTITUTION

June 2007

© Emily Mary Van Ark, MMVII. All rights reserved.

The author hereby grants to MIT and WHOI permission to reproduce and distribute publicly paper and electronic copies of this thesis document in whole or in part.

Author ....
MIT-WHOI Joint Program in Marine Geology and Geophysics
May 4, 2007

Certified by ....
Jian Lin
Senior Scientist, Woods Hole Oceanographic Institution
Thesis Supervisor

Certified by ....
Robert S. Detrick, Jr.
Senior Scientist, Woods Hole Oceanographic Institution
Thesis Supervisor

Certified by ....
Stéphane Rondenay
Assistant Professor, Massachusetts Institute of Technology
Thesis Supervisor

Accepted by ....
J. Gregory Hirth
Chairman, Joint Committee on Marine Geology and Geophysics

Seismic and Gravitational Studies of Melting in the Mantle's Thermal Boundary Layers

by

Emily Mary Van Ark

Submitted to the MIT-WHOI Joint Program in Marine Geology and Geophysics
on May 4, 2007, in partial fulfillment of the
requirements for the degree of
Doctor of Philosophy

Abstract

This thesis presents three studies which apply geophysical tools to the task of better understanding mantle melting phenomena at the upper and lower boundaries of the mantle. The first study uses seafloor bathymetry and small variations in the gravitational acceleration over the Hawaii-Emperor seamount chain to constrain the changes in the igneous production of the hot spot melting in the mantle which has created these structures over the past 80 My. The second study uses multichannel seismic reflection data to constrain the location and depth of axial magma chambers at the Endeavour Segment of the Juan de Fuca spreading ridge, and then correlates these magma chamber locations with features of the hydrothermal heat extraction system in the upper crust such as microseismicity caused by thermal cracking and high temperature hydrothermal vent systems observed on the seafloor. The third study uses two-dimensional global pseudospectral seismic wave propagation modeling to characterize the sensitivity of the SPdKS seismic phase to two-dimensional, finite-width ultra-low velocity zones (ULVZs) at the core-mantle boundary. Together these three studies highlight the dynamic complexities of melting in the mantle while offering new tools to understand that complexity.

Thesis Supervisor: Jian Lin
Title: Senior Scientist, Woods Hole Oceanographic Institution

Thesis Supervisor: Robert S. Detrick, Jr.
Title: Senior Scientist, Woods Hole Oceanographic Institution

Thesis Supervisor: Stéphane Rondenay
Title: Assistant Professor, Massachusetts Institute of Technology

Acknowledgments

This thesis was made possible by the support and encouragement of my advisors: Jian Lin, Robert Detrick, and Stéphane Rondenay. Vernon Cormier was patient and encouraging as I learned how to run his pseudospectral code on the MIT cluster and optomize its results for the problem I wished to study. In addition the other members of my thesis committee, Tim Grove, Dan Shim, Debbie Smith, and John Collins, provided invaluable advice and enthusiasm.

Faculty, scientists, staff, and students at both MIT and WHOI were always helpful, enthusiastic, and informative. I would especially like to thank the adminstrators and staff of the MIT-WHOI Joint Program, who made the logistics of a truly joint program manageable, especially Marsha Gomes, Julia Westwater, Stacey Brudno Drange, Valerie Caron, John Farrington, Ronni Schwartz, and Paola Rizzoli. Fellow students at both WHOI and MIT gave me great advice, cheered me up when I was stressed, encouraged me when work didn't go well, and generally made everything more fun, especially Clare Williams, Jessica Warren, Rachel Stanley, Anna Michel, Brian deMartin, Elke Hodson, Maureen Long, Jennifer Georgen, Mark Behn, Astri Kvassnes, Mike Braun, Margaret Boettcher, EInat Lev, Chang Li, Ping Ma, Chin-Wu Chen, and all the denizens of the 5th and 6th floors of the Green Building.

Chapter 2 was greatly improved thanks to comments by JGR Associate Editor Don Forsyth, Norm Sleep, and an anonymous reviewer. I am grateful to Jennifer Georgen for much assistance in the early stages of this project. Garret Ito, Mark Behn, Allegra Hosford, Seth Stein, Bob Detrick, Maria Zuber, Tim Grove, Jack Whitehead and the WHOI Marine Tectonics and Geodynamics Group gave helpful discussions and valuable suggestions.

Chapter 3 was made possible by the many contributions of the science party and crew of the *R/V Maurice Ewing*'s EW0207 leg. Pablo Canales was endlessly helpful and patient as I worked to master the seismic processing of the Endeavour data. This paper benefited greatly from suggestions by Gail Christeson and an anonymous reviewer. In addition, I would like to thank John Collins, Satish Singh, Rob Sohn, and the participants of the Ridge 2000 program's 2005 Cyprus field school for helpful conversations. There is nothing quite so motivating as to have colleagues who are eager to use your results, and the Ridge 2000 program provided that.

The support staff and users of the Alliance for Computational Earth Science (ACES) grid at MIT provided invaluable assistance in establishing the pseudospectral code base on that cluster and keeping the cluster running smoothly. Without them, Chapters 4 and 5 would not have been possible.

This thesis was funded by a National Science Foundation Graduate Research Fellowship, NSF grant OCE-0002551 to the Woods Hole Oceanographic Institution (WHOI), the WHOI Academic Programs Office, the Earth, Atmospheric, and Planetary Science Department at MIT, and by the WHOI Deep Ocean Exploration Institute.

Finally, I thank my family and friends outside of work for keeping me balanced and sane. In Cambridge, Roxane Wilber, Lisa Lassner, Ale Checka, the Lutheran Episcopal Ministry at MIT, the MIT Woman's Chorale, and Faith Church all made my life calmer, happier, and more interesting. From afar, Amy Langenhorst, Amy and Josh Berne, Sam Pan, Jennifer Rutherford, Anne and Jake Standish, Diane and Chris Wasssman, Ken Rogers, Rachel Robersson, and Lori Lamma all offered tremendous encouragement. My grandparents, aunts, uncles, cousins, in-laws, and brother supported me even when it wasn't clear what was taking so long and what I was working on anyway. My parents have always supported my choices, listened when I needed a sounding board, and welcomed me home when I needed a break. And my husband Todd Stefanik has been supportive, generous, kind, funny and wonderful in every way possible. Thanks be to God!

Contents

List of Figures

List of Tables

Chapter 1

Introduction

The interior of the Earth can be characterized as a massive heat engine, driven by radioactive heating of the mantle and cooling and crystallization of the core [*Stacey*, 1992]. This results in global mantle convection with rising mantle material carrying heat to the surface and cooled mantle material sinking back down into the depths to be reheated and continue the convection cycle. The surface expression of this cycle is plate tectonics with its associated mountain building, subduction, and volcanic activity. The effects of this cycle on the base of the mantle, the core-mantle boundary (CMB) region, are less well understood due to its inaccessibility; however, the CMB has been shown seismically to be very heterogeneous [*Jeanloz and Williams*, 1998] and is hypothesized to be a "(subducted) slab graveyard" [*van der Hilst et al.*, 1997] and the source of rising mantle plumes [*Morgan*, 1971].

Most of the mantle is solid and deforming plastically over very long time scales (millions of years) at adiabatic thermal conditions [*Turcotte and Schubert*, 2002]. However, at the top and bottom of the mantle, where it comes into contact with the relatively cold surface of the Earth and with the relatively hot outer core, conductive thermal boundary layers form. At the top of the mantle the adiabatic thermal gradient crosses the solidus, which causes rising mantle material to cool by melting as excess heat is converted into energy of fusion [*Kinzler and Grove*, 1992a, b, 1993; *Asimow et al.*, 2001]. The resulting melt then rises buoyantly to the surface, chemically interacting with mantle and crust as it percolates upward (e.g., *Kelemen et al.* [1995, 1999]). At the bottom of the mantle, the solidus, liquidus, and geotherm are all less well constrained [*Jeanloz and Williams*, 1998], however the presence of partial melt is hypothesized to account for certain ultra-low velocity anomalies [*Williams* *and Garnero*, 1996].

This thesis presents three studies which use geophysical methods to constrain aspects of melting in the mantle's thermal boundary layers. First, gravity anomalies are used to constrain crustal thickness variations related to hot spot volcanism in the central Pacific ocean. Second, multichannel seismic reflection data are used to image magma chambers at the mid-ocean spreading ridge between the Juan de Fuca plate and the Pacific plate. Third, a two-dimensional (2-D) global seismic wave propagation code is adapted to study thin patches of abnormal velocity and density on the CMB. Finally, that code is applied to understanding which aspects of 2-D ultra-low velocity zones (ULVZs) can be constrained using the SPdKS seismic phase, and those results are applied to a data set which samples the CMB under the southwest Pacific ocean. While these studies each employ very different techniques, together they build a picture of complex and interesting structure in boundary layers at the top and bottom of the mantle under the Pacific ocean.

In chapter 2, small variations in gravitational attraction over the northwest Pacific are used to calculate the maximum crustal thickness of that region. This map of crustal thickness is then used to calculate the excess crust produced by the Hawaii-Emperor hot spot volcanism. Finally, an igneous flux of the Hawaii-Emperor hotspot is calculated by integrating the excess crust in strips perpendicular to the hot spot track and correcting from along-track distance to time using relative velocities between the Hawaiian-Emperor hot spot and Pacific plate. While other studies have presented similar calculations based on bathymetry and isostasy or flexure models, this study is unique in its incorporation of gravity data to constrain the crustal underplating due to the hot spot volcanism. Our time series of Hawaii-Emperor igneous flux provides a useful basis of comparison for geochemical studies of the evolution of the Hawaii-Emperor lavas over the history of the seamount chain (e.g., *Keller et al.* [2004] and *Frey et al.* [2005]). The periods over which the igneous flux varies also provide constraints on geodynamic models of the mantle dynamics and plume-lithosphere interactions which may control the location and flux of the Hawaii-Emperor hot spot.

Chapter 3 presents a multichannel seismic survey of the Endeavour Segment of the Juan de Fuca Ridge. The magma chambers we image under the axial high of the ridge challenge previous models of heat extraction from mid-ocean ridges with intermediate spreading rates. Previous lines of evidence at the Endeavour Segment – fractured and rifted seafloor morphology, high temperature hydrothermal vents located along faults and fissures, deep (1.5–3.5 km below the seafloor) axial microseismicity, and ambiguous seismic evidence – had led to the expectation that there would not be any axial magma chambers; instead the heat driving the Endeavour hydrothermal systems would be provided by a hydrothermal cracking front propagating down into the hot, but solid, rock of the Endeavour crust. We reconcile the presence of axial magma bodies with these other lines of evidence and propose a new model for intermediate spreading center heat extraction which combines the magmatic heat source of fast spreading center heat extraction models with the fracture-controlled hydrothermal circulation paths of slow spreading center heat extraction models. In addition, the Endeavour Segment is of special interest due to its designation as a Ridge 2000 program integrated study site, and our magma chamber locations provide target areas of the seafloor in which geologists, geochemists, and biologists might fruitfully search for undiscovered active hydrothermal vent systems.

The focus shifts from volcanism at the surface of the Earth to possible partial melting at the CMB in the last two chapters. Chapter 4 introduces a 2-D "global" (cylindrical) pseudospectral wave propagation algorithm which was largely constructed by Vernon Cormier, building on a variety of seismic wave modeling approaches originally developed for small-scale seismic exploration and industrial applications. For the purposes of this thesis, three adjustments to the code were made: (1) the code was modified slightly to run well on a local parallel computer cluster at MIT, (2) variable grid spacing was implemented in order to allow much smaller vertical spacing for grid nodes around the CMB while conserving the number of grid nodes overall and retaining numerical accuracy, and (3) a consistent system for reading in velocity perturbations at the CMB was implemented. This is the first time a variable grid has been accurately implemented in a global pseudospectral modeling algorithm. The output of this code for the preliminary reference Earth model (PREM) [*Dziewonski and Anderson*, 1981] is benchmarked against the semi-analytical full wave theory method; in general there is very good agreement between the synthetic seismograms generated by the two methods.

Chapter 5 applies this pseudospectral seismic wave propagation modeling code to a variety of one-dimensional (1-D) and 2-D ULVZ models. We introduce a parameterization of ULVZ "strength" as the height of the ULVZ layer multiplied by the P-velocity perturbation of that layer. We find that no matter how strong the ULVZ, if it is narrower than 100 km it will not be detectable using changes or delays in the SPdKS waveform. Our results give four tools useful for identifying and characterizing 2-D ULVZ structures, all most useful if array data in something resembling a linear geometry is available. First, dual SPdKS pulses on a seismogram indicate exposure to at least two different CMB velocity structures. Second, a strong SKS precursor probably indicates a very strong ULVZ; the absence of such SKS precursors is most previous ULVZ studies indicates that very strong, sharp ULVZs are not very common. Third, while ULVZ models based on SPdKS travel times are highly non-unique, we present a graph of mean SPdKS delays relative to PREM which provides constraints on minimum ULVZ strength and width combinations required to produce a given travel time delay. Finally, tracing SPdKS arrivals back to the inception epicentral distance on seismic sections may offer an independent tool for identifying P-velocity perturbations at the base of the mantle.

This thesis presents a diverse body of work, covering three very different geophysical approaches applied to three distinct portions of the Earth. However, together they build up a set of constraints on the three potentially most important modes of melting in the Pacific mantle. Chapter 2 provides constraints on time variation in the mantle processes, potentially including plumes that originate at the CMB, which produce the "hot spot" volcanism of the Hawaii-Emperor seamounts. Chapter 3 fills in the intermediate spreading rate range of the models which explain magma bodies at mid-ocean ridges as a result of the interplay between hydrothermal cooling from above and adiabatic decompression melting of rising mantle from below. And the last two chapters place minimum constraints on the dimensions and seismic velocity perturbations at the bottom of the mantle which are required to produce ULVZ seismic signatures, thereby placing constraints on the geodynamic and geochemical processes, including melting, which may be the cause of these seismic velocity anomalies.

Chapter 2

Time Variation in Igneous Volume Flux of the Hawaii-Emperor Hotspot Seamount Chain

Abstract Satellite gravity, ship track bathymetry, sediment thickness, and crustal magnetic age data were combined to calculate the residual bathymetry and residual mantle Bouguer gravity anomaly (RMBA) for the northwest Pacific Ocean. The Hawaii-Emperor hotspot track appears on the RMBA map as a chain of negative anomalies, implying thickened crust or less dense mantle. The hotspot swell is clearly visible in a broad band of half width ~500 km for about 2,000 km downstream from the current hotspot location, corresponding to hotspot ages of 0–25 Ma. A much narrower expression of the hotspot is visible for the rest of the chain at hotspot ages of 25–80 Ma. Comparison of the observed RMBA with various compensation models reveals that the relatively narrow features of the Hawaii-Emperor seamounts are best explained as being supported by plate flexure while the Shatsky Rise, Hess Rise, and Mid-Pacific Mountains oceanic plateaus are best fit by Airy isostasy with a thickened crustal root. Amplitude comparisons between the RMBA predictions of various compensation models and the observed RMBA for the Hawaiian swell are ambiguous. However, based on the shape of the predicted anomalies we favor a model of flexure in response to a buried load at 120 km depth. We further calculate igneous (i.e., crustal) volume

---

Previously published as Van Ark, E., and J. Lin, (2004), Time variation in igneous volume flux of the Hawaii-Emperor hot spot seamont chain, *J. Geophys. Res., 109*, B11401, doi:10.1029/2003JB002949. Reprinted here with permission.

flux along the axis of the Hawaii-Emperor hotspot by integrating cross sectional areas of gravity-derived excess crustal thickness and seafloor elevation, respectively, with respect to the normal oceanic crust. The highest values of the calculated igneous volume flux along the Hawaiian and Emperor ridges (∼8 m^3/s) occur at present and about 20 Ma. The flux was reduced to only 50% of this maximum (∼4 m^3/s) at 10 Ma. The calculated igneous volume flux is systematically smaller (maximum values of ∼4 m^3/s) along the Emperor ridge. Overall the Hawaiian and Emperor ridges appear to have experienced quasi-periodic variations in fluxes on time scales of 6–30 Ma. Furthermore during the low flux periods at 25–48, 57, and 75 Ma, the height and size of individual hotspot seamounts appear to be noticeably less than those of the high flux periods. We hypothesize that the variations in the fluxes of the Hawaiian ridge might be controlled by the thickness of the overlying lithosphere at the time of hotspot emplacement, while the variations along the Emperor ridge may be influenced by the dynamics of the slow absolute motion of the hotspot at the time.

2.1 Introduction

Hotspot plumes have often been imagined and modeled as stationary conduits of hot, enriched material from the deep mantle to the surface of the Earth [*Wilson*, 1963; *Morgan*, 1971; *Sleep*, 1990; *Schilling*, 1991; *Ribe and Christensen*, 1994; *Ito and Lin*, 1995b; *Phipps Morgan et al.*, 1995; *Hoffman*, 1997; *Ribe and Christensen*, 1999]. This view is almost certainly too simplistic, but attempts at more complex models were limited by the scarcity of constraints on time variation in plume dynamics. Recent observations provide some of the constraints necessary for the development of time-varying models of hotspot behavior. One line of evidence uses new paleolatitudes found for several Emperor seamounts to calculate a southward drift rate of 30 – 50 mm/y from 45 – 80 Ma for the Hawaii-Emperor hotspot [*Tarduno and Cottrell*, 1997; *Party*, 2002a; *Cottrell and Tarduno*, 2003; *Tarduno et al.*, 2003]. New models of mantle convection incorporating stratified mantle viscosities and rigid plates show the natural evolution of dynamic plume systems alternating between periods of motion and periods of relative stability [*King et al.*, 2002; *Lowman et al.*, 2003]. This study attempts to quantify variations in the Hawaiian plume igneous (crustal) production over time.

A number of approaches have been proposed to estimate fluxes of hotspot material. These have generally fallen into three categories: estimates of the buoyancy or mass flux of the hotspots underlying mantle plume, estimates of the volume flux of the underlying mantle plume, and estimates of the igneous volume flux produced by hotspot melting. Buoyancy flux estimates generally assume isostatic compensation of the hotspot swell, the broad topographic anomaly associated with a hotspot. The rate at which the swell is generated can then be used to estimate the buoyancy or mass flux of the underlying mantle plume [*Davies*, 1988, 1992; *Sleep*, 1990]. Volume fluxes of hotspot mantle plumes have been estimated using fluid dynamics models [*Sleep*, 1990; *Ribe and Christensen*, 1994] and geochemical signatures of plume interactions with mid-ocean ridges [*Schilling*, 1991].

Volcanic or igneous fluxes of the Hawaii-Emperor hotspot have been estimated by several authors using bathymetry data alone. *Bargar and Jackson* [1974] were the first to calculate the volume of individual volcanic shields along the Hawaii-Emperor chain, resulting in values ranging from 42.5 x 103 km^3 for Mauna Loa to 0.3 x 103 km^3 for a shield on one of the northernmost Emperor seamounts. *White* [1993] assumed Airy isostasy supporting observed bathymetry to estimate the total melt production of the Hawaii-Emperor chain over time, arriving at values of 0.03–0.16 km^3/y (or 0.95–5.08 m^3/s). Most recently, *Vidal and Bonneville* [2004] used bathymetry with Airy isostasy and flexure assumptions to calculate magma production rates for Hawaii in a continuous manner. Our method is similar to that of *Vidal and Bonneville* [2004] in that it produces a continuous along-axis volcanic flux measurement. However, in addition to using bathymetry data, we also use gravity anomalies to constrain crustal thickness.

This paper uses satellite gravity anomalies and shipboard data to show that the igneous crustal production of the Hawaii-Emperor hotspot has changed over the history of the hotspot on time scales of 6-30 My, with the igneous volume flux varying between 0-10 m^3/s. We have chosen to study the Hawaii-Emperor hotspot because it has the longest and clearest hotspot track on Earth, and therefore offers the longest time record of possible hotspot flux variations. Unlike many other hotspots, the Hawaii-Emperor track is not complicated by complex interactions with mid-ocean ridges. We also compare the observed residual gravity anomaly with different models of isostatic compensation to investigate the specific geodynamic mechanisms supporting the topography of the relatively narrow Hawaiian-Emperor seamounts, the broad Hawaiian swell, and the Mid-Pacific Mountains, Hess Rise, and Shatsky Rise oceanic plateaus.

2.2 Data

Our study utilizes four global data sets: satellite free air gravity [*Sandwell and Smith*, 1995, 1997], oceanic sediment thickness [*Divins*, 2001], shiptrack bathymetry [*Smith and Sandwell*, 1994, 1997], and oceanic crustal age [*Muller et al.*, 1997]. From each of these data sets we select a study region of 150°E to 215°E and 10°N to 55°N in the northern Pacific Ocean (Figure 2-1).

The satellite marine free air gravity map of *Sandwell and Smith* [1995, 1997] (Figure 2-2a) is available as a 1 minute by 1 minute data base that was derived from satellite altimetry taken on the Geosat and ERS1 missions. The Hawaii-Emperor seamount chain is a prominent feature on this map due to the point-like, uncompensated loading of the seamounts on the plate. In contrast, longer wavelength areas of crustal thickening are isostatically compensated by deformation of the elastic plate and/or crustal underplating and are therefore not prominent on the free air gravity map. Because this is a marine gravity data set, we lack coverage for the Hawaiian islands. We have therefore masked out the Hawaiian islands on all our calculation results presented as maps. This lack of Hawaiian island coverage results in an underestimation of the igneous volume flux at the current hotspot position, but does not limit our ability to quantify the long-period variation of the Hawaiian hotspot flux over time.

Global shiptrack bathymetry has been compiled by the National Geophysical Data Center (NGDC) and is available on CD. The same information has been incorporated into the *Smith and Sandwell* [1994, 1997] predicted topography map along with data from various other archives. The shiptrack coverage of the Hawaii-Emperor seamount chain and its surrounding region is adequate for our purposes (Figure 2-2b). Prominent tectonic features in our study region include the Hawaii-Emperor seamount chain, the Mid-Pacific Mountains (MPM), Shatsky Rise, and Hess Rise (Figure 2-1). Ocean Drilling Program results dated the sediments on the MPM to be at least 123 132 Ma old [*Arnaud-Vanneau and Sliter*, 1995; *Jenkyns*, 1995; *Jenkyns et al.*, 1995; *Pringle and Duncan*, 1995] and paleomagnetic studies of basalts from the MPM [*Tarduno and Sager*, 1995] support the interpretation of its formation over the region of thinned, weak lithosphere and low viscosity asthenosphere

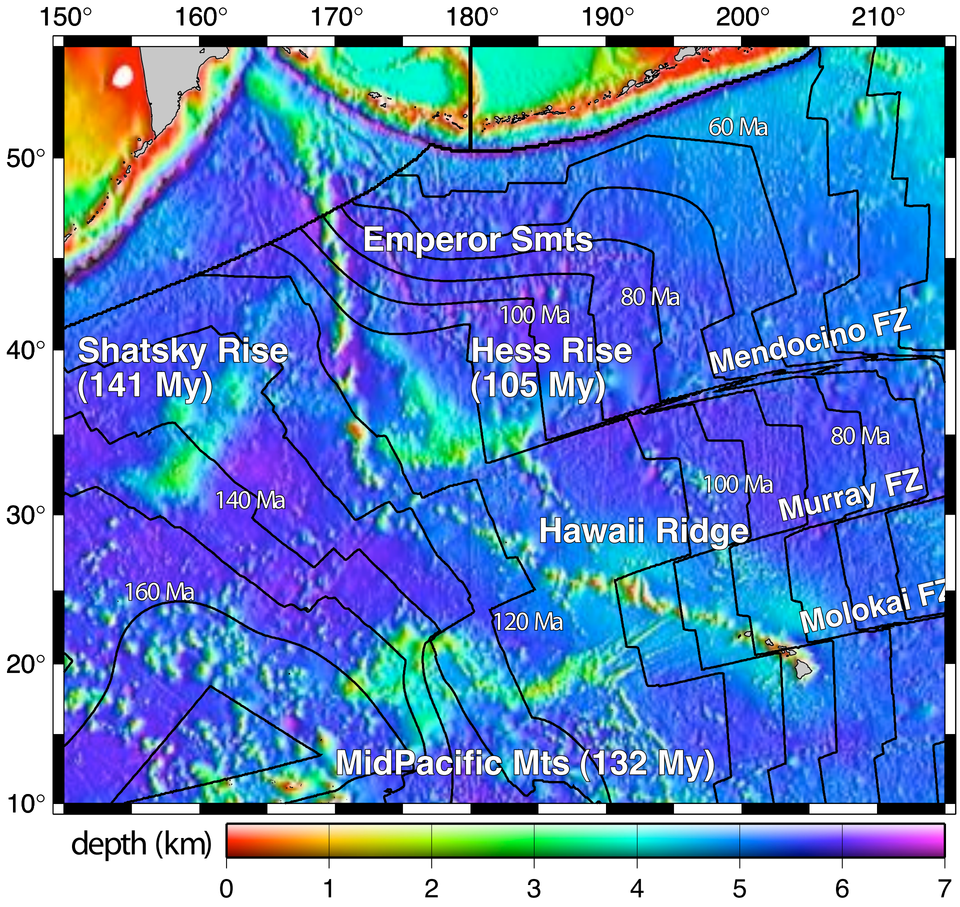

Figure 2-1: Interpolated shiptrack bathymetry shows the Hawaii-Emperor seamount chain, Hess and Shatsky Rises, and the Mid-Pacific Mountains. Also marked are the crustal age contours based on digital magnetic data of *Muller et al.* [1997] and the location of the Mendocino, Murray, and Molokai Fracture Zones.

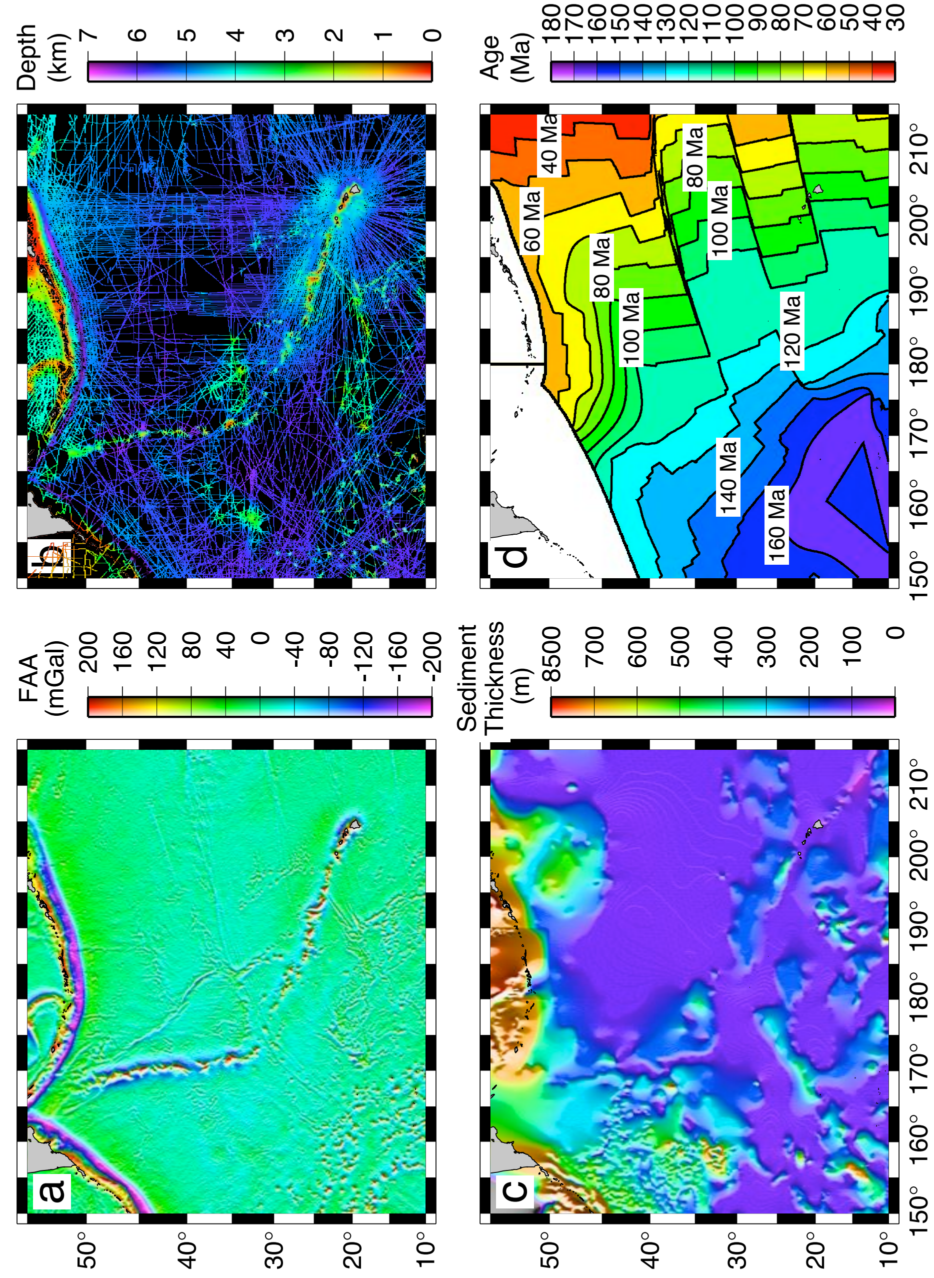

Figure 2-2: Data used to calculate the northwest Pacific gravity anomalies. a) Free air gravity anomaly from satellite altimetry [*Sandwell and Smith*, 1997]. The Hawaii-Emperor seamount chain is clearly visible with positive anomalies of up to 200 mGal, due to the lack of compensation of these short-wavelength features. The broad Hawaiian swell is marginally visible. Other major bathymetric features of the region such as the Hess and Shatsky Rises and the Mid-Pacific Mountains do not appear as prominent features on the free air anomaly map, indicating probable shallow isostatic compensation. b) Shiptrack bathymetry coverage from National Geophysical Data Center and *Smith and Sandwell* [1994, 1997]. c) Marine sediment thickness map for the northwest Pacific [*Divins*, 2001]. d) Oceanic crustal age based on the digital magnetic data of *Muller et al.* [1997].

bathymetrically expressed as the Pacific Superswell [*McNutt and Judge*, 1990]. The formation of Hess Rise, to the northeast of the bend in the Hawaii-Emperor chain, has been dated at 98-110 Ma [*Pringle and Dalrymple*, 1993] and is thought to have formed on or very near the Pacific-Farallon spreading center [*Vallier et al.*, 1981; *Kroenke and Nemoto*, 1982; *Mammerickx and Sharman*, 1988]. Shatsky Rise, to the west of the bend in the hotspot track, has been dated at 138-145 Ma [*Sager and Han*, 1993; *Party*, 2002b] and magnetic lineations around the rise indicate that it formed along the trace of the Pacific-Farallon-Izanagi triple junction [*Larson and Chase*, 1972; *Hilde et al.*, 1976; *Sager et al.*, 1988; *Nakanishi et al.*, 1989]. The bend in the hotspot track has been dated between 40 and 53 Ma [*Sharp and Clague*, 2002] and its origin is interpreted to be related to the cessation of southward motion of the Hawaii-Emperor hotspot that has been measured for the Emperor segment of the seamount chain [*Tarduno and Cottrell*, 1997; *Party*, 2002a; *Cottrell and Tarduno*, 2003; *Tarduno et al.*, 2003].

The oceanic sediment thicknesses map of *Divins* [2001] was compiled from three primary sources: previously published isopach maps [*Divins and Rabinowitz*, 1991; *Hayes and LaBrecque*, 1991; *Divins and Eakins*, in preparation], DSDP and ODP ocean drilling results, and seismic reflection and refraction data archived by the National Geophysical Data Center (NGDC) and the Intergovernmental Oceanographic Commission (IOC) Geological/Geophysical Atlas of the Pacific (GAPA) project. The possible influence of strongly reflective chert and volcanic layers above the acoustic basement lead to seismic estimates of sediment thickness that represent a minimum value. The average background thickness over most of the northwest Pacific is 100 m, although much greater values are reached near the continental margins (Figure 2-2c).

The *Muller et al.* [1997] digital age grid of the ocean floor (Figure 2-2d) has a grid spacing of 6 min. It was created from a compiled global magnetic data base and models of global plate reconstruction. Ten million-year age contours overlain on the northwest Pacific bathymetry map (Figure 2-1) reveals that the Hawaii seamounts were emplaced on crust that was, on average, 70-80 My old at the time of active volcanism. We also note that the Hawaii-Emperor chain crosses, from northwest to southeast, the Mendocino, Murray, and Molokai Fracture Zones (Figure 2-1).

2.3 Analysis and Results

2.3.1 Residual Bathymetry

We calculate residual bathymetry by correcting observed shiptrack bathymetry for the effect of plate cooling. This calculation is done in three steps. First the three-dimensional thermal structure of the Pacific lithosphere is calculated at each grid point from 0 to 100 km depth using the digital age grid and a simple plate cooling model [*Turcotte and Schubert*, 2002] with thermal diffusivity $\kappa = 10^{-6}\mathrm{m}^2/\mathrm{s}$. We used temperature boundary values of $\mathrm{T}_0 = 0°\mathrm{C}$ at the surface of the plate and $\mathrm{T}_1 = 1350°\mathrm{C}$ at a plate thickness of $\mathrm{z}_{\mathrm{L0}} = 100$ km, which are parameters chosen as intermediate values between the plate models of *Parsons and Sclater* [1977] and *Stein and Stein* [1992].

The thermal structure is next translated into a density anomaly structure using a simple thermal expansion equation, $\Delta\rho = (T_0 - T)\alpha\rho_0$, where $\mathrm{T_o}$ and ρ_o represent reference temperature and density, respectively, and α is the coefficient of thermal expansion. We used $\rho_0 = 3{,}300$ kg m^{-3} and $\alpha = 3.4{*}10^{-5}$ K^{-1} with the reference temperature T_0 set equal to the value in the middle of our study region. We are therefore calculating an anomaly relative to center of our map, so that areas with temperatures higher than the center of our map will have a negative density anomaly while areas with temperatures lower than the center of our map will have a positive density anomaly.

Finally, the density anomalies of the thermal model are translated into expected topography, h, based on a simple isostatic model:

$$h(x,y) = \frac{1}{(\rho_m - \rho_w)} \int_0^{z_{\mathrm{L0}}} \Delta\rho dz, \tag{2.1}$$

where ρ_m and ρ_w are the average densities of the mantle and the ocean water, respectively. Since the thermal density anomaly $\Delta\rho$ may be positive or negative relative to the value at the center of our map, the resulting expected topography may be positive or negative relative to that reference value. The calculated thermal topography (Figure 2-3b) is subtracted from the actual bathymetry (Figure 2-3a) to produce the residual bathymetry (Figure 2-3c). This correction deepens the youngest lithosphere (~30 Ma) relative to the mean bathymetry, reducing the range between the shallowest and deepest bathymetry by ~1 km in the resultant residual bathymetry (Figure 2-3).

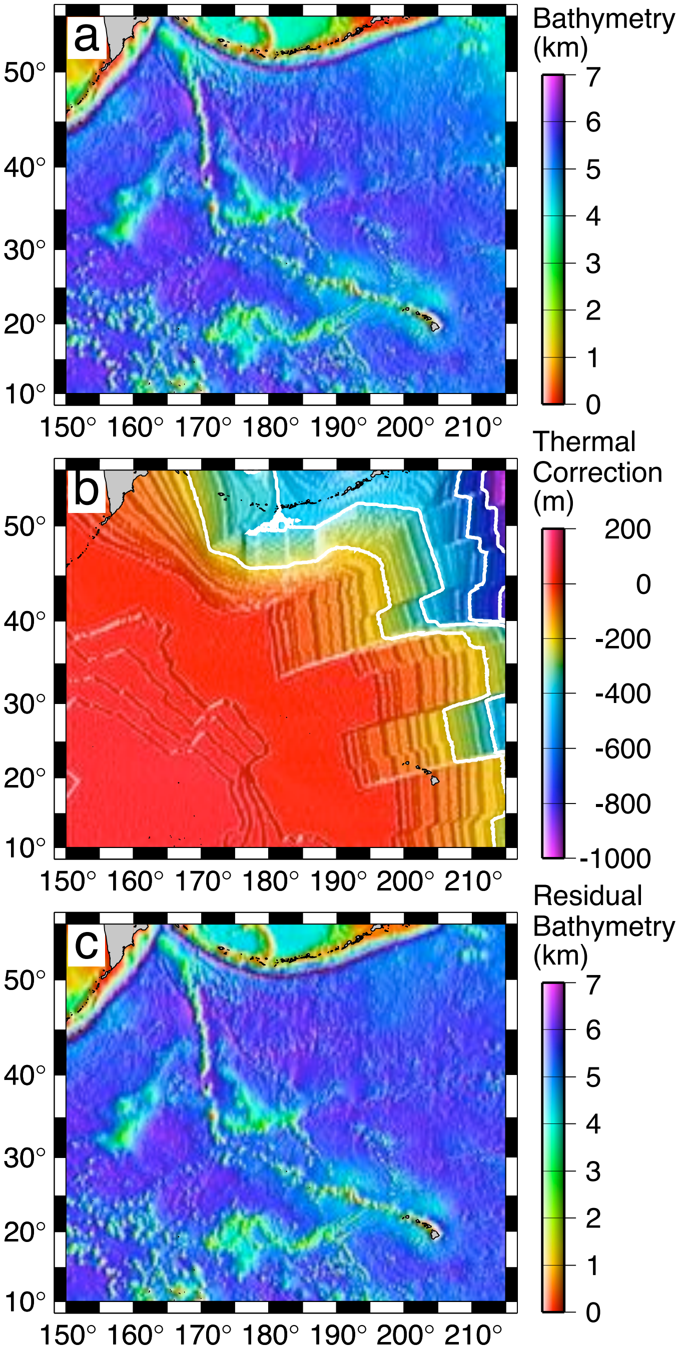

Figure 2-3: Residual bathymetry calculation. (a) Shiptrack bathymetry. (b) Thermal bathymetric correction calculated from the plate cooling model as discussed in the text. (c) Residual bathymetry calculated by subtracting thermal bathymetric correction in panel b from the shiptrack bathymetry in panel a.

2.3.2 Gravity Anomalies

Gravity anomalies are used to investigate sub-seafloor density variations. The Bouguer anomaly (BA) is found by subtracting the attraction of sediment cover and seafloor topography from the free air anomaly, while the mantle Bouguer anomaly (MBA) subtracts the additional attraction of the crust-mantle interface assuming an average 6-km-thick uniform crust. The residual mantle Bouguer anomaly (RMBA), similar to the residual bathymetry discussed above, further subtracts out the gravitational influence of plate cooling using the same three-dimensional thermal model as in the residual bathymetry calculations. The resultant RMBA should reflect variations in crustal density and thickness, or variations in mantle density, or both. We calculate MBA and RMBA using an upward continuation algorithm developed by *Parker* [1972] and implemented by *Kuo and Forsyth* [1988].

The effect of the Hawaii-Emperor hotspot on the northwest Pacific lithosphere is clearly visible as a broad region of negative RMBA anomalies coinciding with the seamounts and swell of the hotspot chain (Figure 2-4). The magnitude of Hawaii-Emperor hotspot RMBA anomalies reaches -200 mGal, larger than any other hotspot except Iceland (up to -300 mGal) [*Ito et al.*, 1996]. The swell anomaly is $\sim$1,000 km wide and extends upstream for $\sim$2,000 km. The Hess and Shatsky Rises as well as the Mid-Pacific Mountains are also prominent features on the RMBA map (Figure 2-4), in comparison to their smaller signal on the free air gravity anomaly map.

2.3.3 Admittance

Admittance functions predict the gravity anomaly associated with a given surface topography for specified assumptions about how the topographic load is supported [*Watts*, 2001]. Admittance functions were earlier applied to understanding the relationship between free air gravity anomalies and elevations of the Hawaii-Emperor seamounts by *Watts* [1978]. Following the approach of *Ito and Lin* [1995a], we investigate admittance functions for the northwest Pacific to better understand the sources of our calculated mantle Bouguer gravity anomalies. A generic gravitational admittance function $Z(k)$ is defined as:

$$\Delta g(\mathbf{k}) = Z(k)H(\mathbf{k}) \tag{2.2}$$

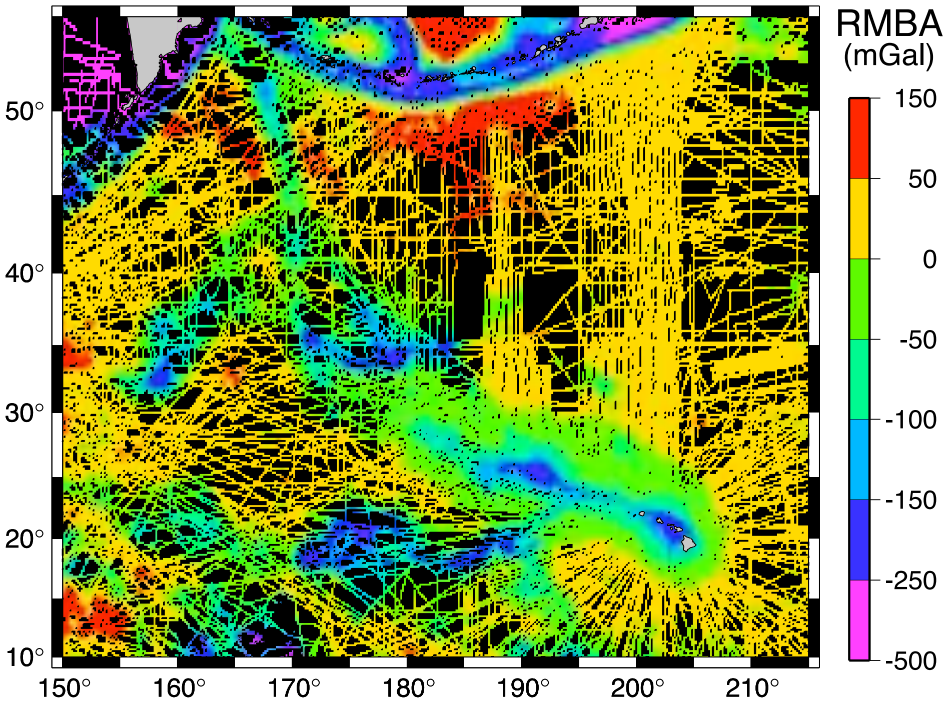

Figure 2-4: Residual mantle Bouguer anomaly for the northwest Pacific region. Prominent negative anomalies are seen for the Hawaii-Emperor seamount chain, the Hawaiian hotspot swell, the Hess and Shatsky Rises, and the Mid-Pacific Mountains (see location of these features in Figure 2-1).

where $\mathbf{k}$ is the two-dimensional wavenumber, $k = |\mathbf{k}| = 2\pi/\lambda$, $\Delta g(\mathbf{k})$ is the Fourier transform of the gravity anomaly and $H(\mathbf{k})$ is the Fourier transform of the topography of an interface such as the seafloor or Moho. We test admittance functions for Airy isostasy, surface load plate flexure with a range of elastic plate thicknesses, and buried load plate flexure with a range of load depths. Each of these functions is applied to the northwest Pacific residual bathymetry to calculate a corresponding map of predicted RMBA. These predicted RMBA maps are then compared with the observed RMBA to assess which mechanisms of isostatic compensation can best explain each of the major bathymetric features in the northwest Pacific. This comparison is quantified by calculating the root mean square (r.m.s.) of the misfit between the admittance-predicted RMBA and the observed RMBA over the areas of interest outlined in Figure 2-5. The results of the comparison are presented in Figure 2-6 and parameters used in admittance functions are given in Table 2.1.

Airy Isostasy

Airy isostasy is a model in which the lateral variations in surface topography are assumed to be supported by subsurface variations in the thickness of the crust. The free air gravity anomaly for Airy isostasy would therefore have contributions from the seafloor and crust-mantle interfaces. When calculating the mantle Bouguer anomaly and RMBA, we have subtracted the gravitational effects of the seafloor interface and an assumed reference crust that follows the bathymetry. The RMBA admittance function for Airy compensation of residual bathymetry is therefore given by:

$$Z(k)_{Airy} = -2\pi G \left[(\rho_m - \rho_c) \exp\left(-k z_{RM}\right) + (\rho_c - \rho_w) \exp\left(-k z_{CR}\right) \right] \tag{2.3}$$

where ρ_w, ρ_c, and ρ_m are the densities of the seawater, crust, and mantle respectively, z_{RM} is the reference Moho depth below sealevel, and z_{CR} is the assumed mean depth of the crustal root below sealevel [*Ito and Lin*, 1995a]. The first term of this expression subtracts the attraction of the reference crust and the second term reflects the attraction of the crustal root assumed to support the overlying topography.

We use 11 km for z_{RM} since the mean ocean depth in the Pacific is ~5 km and our reference Moho is 6 km below the seafloor. We use 17 km for z_{CR} as this seems consistent with the seismic result available for the Hawaiian islands [*Ten Brink and Brocher*, 1987].

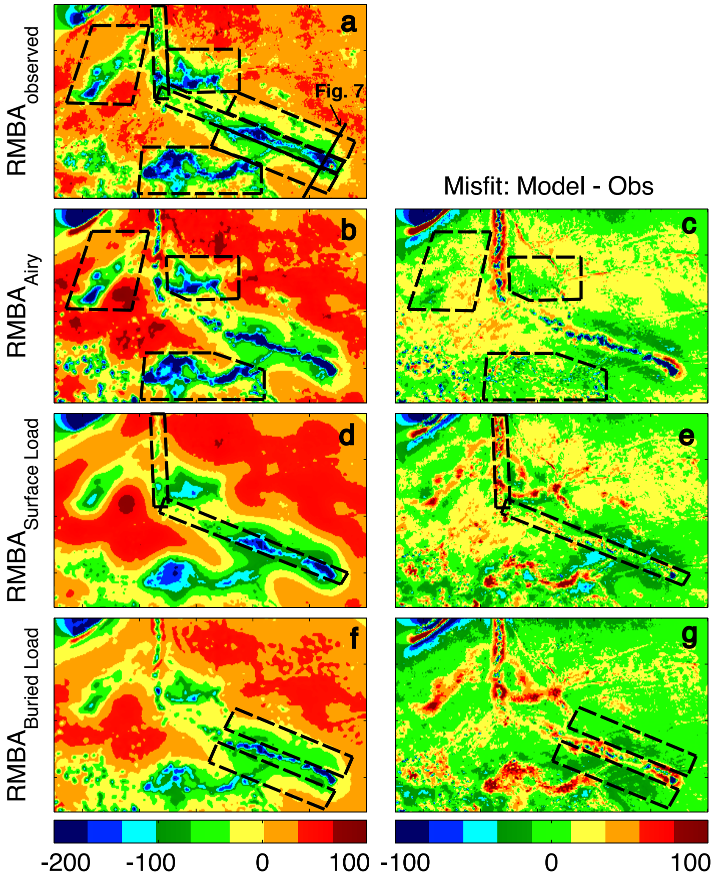

Figure 2-5: Admittance model comparisons. (a) The "observed RMBA" calculated from shiptrack bathymetry and satellite free air gravity anomalies. The areas used to calculate the r.m.s. misfit between the admittance predictions and the observed gravity anomalies are outlined with dashed boxes. The line across the Hawaiian seamounts and swell is the profile used for Figure 7. All values are in mGal. (b) RMBA predicted by Airy isostatic compensation of bathymetry. (c) Misfit between the RMBA modeled with Airy isostasy and the observed RMBA. The areas contained in the dashed boxes (the Mid-Pacific Mountains, Shatsky Rise, and Hess Rise) are well modeled by Airy isostasy and have a small misfit. (d) RMBA predicted from elastic plate flexure with a plate under the observed bathymetric load with an effective elastic thickness of 60 km. (e) Misfit between the surface loading flexure model of RMBA and the observed RMBA. In general the flexure equation best predicts the gravity anomalies in the dashed boxes containing the Hawaii and Emperor seamounts. (f) RMBA predicted from a buried load plate flexure admittance function with an elastic plate thickness of 40 km and a load depth of 120 km. (g) Misfit between the buried load model of RMBA and the observed RMBA. The buried load models best predicts the shape of the gravitational anomaly due to the Hawaiian swell contained within the dashed boxes.

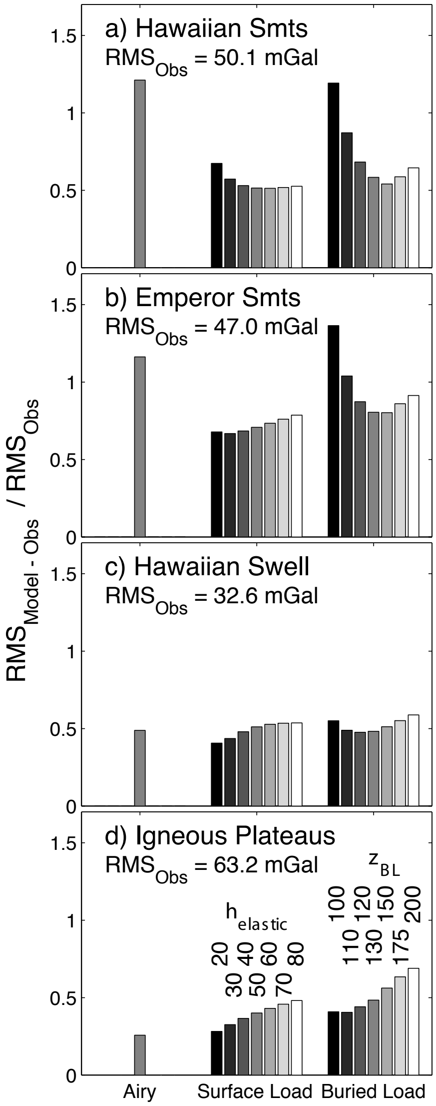

Figure 2-6: Comparison of misfit between admittance models with varying model parameters and the observed RMBA for selected bathymetric features of the northwest Pacific: (a) the Hawaiian ridge seamounts; (b) the Emperor seamounts; (c) the Hawaiian swell; and (d) the large igneous plateaus of the region (Hess and Shatsky Rises and the Mid-Pacific Mountains). The r.m.s. values of the model minus the observed RMBA misfit for each region has been normalized by the r.m.s. of the observed RMBA in that region. The regions chosen for evaluation of the r.m.s. misfit are shown as dashed boxes in Figure 5. The bars for the elastic plate flexure model represent different values of elastic plate thickness (from left to right: 20, 30, 40, 50, 60, 70, and 80 km). The bars for the buried load model represent different values of load depth (from left to right: 100, 110, 120, 130, 150, 175, and 200 km).

Table 2.1: Parameters used in admittance calculations and associated functions. Surface and Buried indicate use in the equations associated the surface load plate flexure and buried load plate flexure, respectively. All depths are given relative to the sea surface.

Variable	**Symbol**	**Value**	**Function(s)**
Ocean water density	ρ_w	1,030 $\mathrm{kg/m^3}$	Airy, Surface, Buried
Crustal density	ρ_c	2,800 $\mathrm{kg/m^3}$	Airy, Surface
Mantle density	ρ_m	3,300 $\mathrm{kg/m^3}$	Airy, Surface, Buried
Reference Moho depth	$\mathrm{z_{RM}}$	11 km	Airy, Surface
Crustal root depth	$\mathrm{z_{CR}}$	17 km	Airy, Surface
Depth of buried load	$\mathrm{z_L}$	100, 110, 120, 130, 150, 175, and 200 km	Buried
Thickness of elastic plate	$\mathrm{h_e}$	20, 30, 40, 50, 60, 70, and 80 km	Surface, Buried
Young's modulus	E	$7\mathrm{x}10^7$ Pa	Surface, Buried
Poisson's ratio	ν	0.25	Surface, Buried
Gravitational constant	G	$6.67\mathrm{x}10^{-11}\ \mathrm{m^3/(kgs^2)}$	Airy, Surface, Buried
Gravity acceleration	g	9.8 $\mathrm{m/s^2}$	Surface, Buried

The results from applying $Z(k)_{Airy}$ to the residual bathymetry (Figure 2-5b,c) show a good match to the observed RMBA for the Hess and Shatsky Rises and the Mid-Pacific Mountains. However, Airy isostasy does less well predicting the RMBA signature of the Hawaiian swell and greatly overpredicts the negative RMBA associated with short wavelength signals such as the Hawaii-Emperor seamount chain (Figure 2-6).

Plate Flexure with Surface Loading

Elastic plate flexure models predict bending of a plate under applied loads. In this section we examine flexure models associated with topography loads applied on the surface of the elastic plate. This results in crustal deflection similar to the Airy model, but the deflection is dependent on the wavelength of the load and is distributed over a broader region. The RMBA admittance function for flexure with surface loading is therefore given by:

$$Z(k)_{SurfaceLoad} = -2\pi G\left[(\rho_m - \rho_c)\exp(-kz_{RM}) + (\rho_c - \rho_w)\exp(-kz_{CR})\,\phi'_e(k)\right] \tag{2.4}$$

which is very similar in form to $Z(k)_{Airy}$ except that the crustal root term now has an additional multiplication factor $\phi'_e(k)$ which is defined as:

$$\phi'_e(k) = \left[\frac{Dk^4}{(\rho_m - \rho_c)\,g} + 1\right]^{-1} \tag{2.5}$$

where g is the acceleration of gravity, $D = Eh_e^3/12(1-\nu^2)$ is the flexural rigidity of the plate, E is Young's modulus, h_e is the elastic thickness of the plate, and ν is Poisson's ratio [*Watts*, 2001]. Previous studies of flexure of the lithosphere under the Emperor and Hawaiian seamounts have suggested values for h_e between 10.5 and 40 km, depending on the location of the study along the seamount chain and the method used [*Walcott*, 1970; *Watts and Cochran*, 1974; *Watts*, 1978; *Kunze*, 1980; *Watts et al.*, 1985; *Calmant*, 1987]. We apply $Z(k)_{SurfaceLoad}$ to the residual bathymetry using the parameters of Table 2.1, including a range of elastic plate thicknesses: 20, 30, 40, 50, 60, 70 and 80 km.

Comparison of the observed RMBA with the RMBA predicted from $Z(k)_{SurfaceLoad}$ (Figures 2-5d,e) reveals that the flexure equation with surface loading does better in predicting the gravity anomalies from the relatively narrow Hawaiian and Emperor seamounts than other forms of compensation, although plate flexure with buried loading at a depth of

150 km (presented in the next section) also has a relatively low r.m.s. misfit for the Hawaiian seamounts (Figure 2-6). For the surface loading flexure models, the Hawaiian seamounts are better fit with thicker elastic thicknesses, 60 km, while the Emperor seamounts are better fit with thinner elastic thicknesses, 30 km (Figure 2-6). In contrast, the flexure model with surface loading does not do as well as the Airy model in predicting the gravity signature of the Hess, Shatsky, and Mid-Pacific igneous plateaus. The surface loading flexure model produces a relatively small r.m.s. misfit for the Hawaiian swell (Figure 2-6).

Plate Flexure with Buried Loading

The final option we consider for supporting seafloor topography is a buried load exerting forces on an interface below the crust. This is essentially plate flexure with the load exerted by a buried density anomaly at the bottom of the elastic plate. In such a case, the surface topography $H(k)$ is a function of the interface between the underlying load and the normal mantle, $W(k)$:

$$H(k) = -W(k)\frac{(\rho_m - \rho_L)}{(\rho_m - \rho_w)}\phi_e''(k) \tag{2.6}$$

where ρ_L is the density of the load, $\phi_e''(k)$ is defined as:

$$\phi_e''(k) = \left[\frac{Dk^4}{(\rho_m - \rho_w)\,g} + 1\right]^{-1} \tag{2.7}$$

and D has the same definition as in the flexure model [*Watts*, 2001]. After we rearrange Equation 5 so that $W(k)$ is in terms of $H(k)$, we find that the admittance equation for a buried load is:

$$Z(k)_{BuriedLoad} = -2\pi G\,(\rho_m - \rho_w)\,\frac{\exp(-kz_L)}{\phi_e''(k)} \tag{2.8}$$

where z_L is the depth of the buried load supporting the topography. There is only one term in equation 2.8 because the lack of crustal thickening in this model enables the mantle Bouguer corrections to eliminate all the crustal interfaces. The presence of the flexural rigidity, D, in equation 2.7 results in the inclusion of the elastic plate thickness, h_e, in this set of admittance models as well as the flexure models above. Rather than run every buried load model with a range of h_e values, we use a value of 40 km which is intermediate between the two values which best fit the Hawaiian and Emperor seamounts in our calculations and is consistent with previous estimates of h_e for the Hawaii-Emperor system (catalogued in

Watts and Zhong [2000]).

Previous studies of subsurface support of the Hawaiian swell have found loading or compensation depths of 100-200 km [*Watts*, 1976], 70-120 km [*Crough*, 1978], 40 km [*Sandwell*, 1982], and 70 km [*McNutt and Shure*, 1986]. We apply $Z(k)_{BuriedLoad}$ to the residual bathymetry for z_L = 100, 110, 120, 130, 150, 175, and 200 km. Comparing the observed RMBA with the RMBA predicted from $Z(k)_{BuriedLoad}$ (Figure 2-5f,g) reveals that while the buried load flexure model does a poor job of predicting the gravity anomaly for the seamounts and the igneous plateaus, it does noticeably better at predicting the gravitational signal for the Hawaiian swell with the best fit model obtained for a load depth of z_L = 120 km (Figure 2-6). As noted above, the surface load flexure admittance model also produces relatively small r.m.s. values for the Hawaiian swell region. However, the buried load more closely models the spatial shape of the anomaly for the swell (Figure 2-5 and 2-7).

Admittance Comparison

By focusing in on key portions of our study area (Figures 2-5 and 2-6) we can compare in detail the results of the above three models of topography support. While it is simplistic to assume that any one mechanism completely accounts for the support of complicated tectonic features such as the Hawaiian ridge and swell system, attempting to separate out the fractional contribution of each mechanism to every major feature is a problem of complexity beyond the scope of this paper. However, by geographically separating out individual regions, we can attempt to constrain the dominant mechanism for those regions of interest. Separating out the Hawaiian and Emperor seamount chains from the Hawaiian swell and igneous plateaus has the additional benefit of providing a sort of ad hoc wavelength separation.

The smallest r.m.s. misfit between the observed RMBA and the RMBA predicted by our admittance models for the Hawaiian swell is given by flexure due to surface loading with an elastic plate thickness of 20 km. However, comparison of the results for the swell in Figures 2-5 and 2-6 reveals that the shape of the swell is better eliminated from the misfit by the buried load flexure model with a load depth of 120 km. Thus, while the results of the modeling are inconclusive, we prefer the interpretation that the swell is supported by a buried load at 120 km depth, which is consistent with the common attribution of the swell to low-density (either hot or chemically depleted) hotspot material trapped beneath the

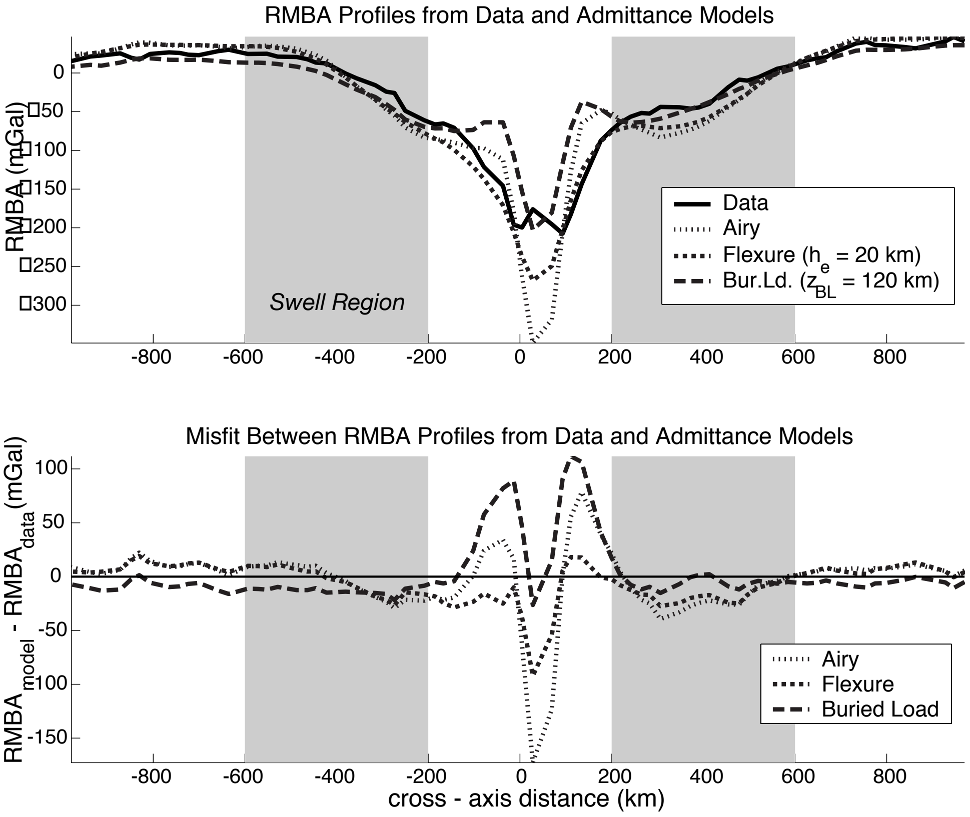

Figure 2-7: (a) Profiles of the observed RMBA calculated from the free air gravity anomaly and the modeled RMBA calculated from topography using admittance functions for Airy isostasy, flexure of a thin elastic plate of thickness 20 km, and flexure of an elastic plate of thickness 40 km in response to a buried load at 120 km depth. (b) Misfit between the modeled RMBA amplitudes and the observed amplitudes for each of the admittance models along the same profile. The profile used is shown in Figure 2-5a, and the shadowed regions on the profiles show the region used to calculate the Hawaiian swell misfit. It can be seen that while the amplitudes of the misfits for Airy and flexure admittance are comparable to that of the buried load, the buried load has a much flatter misfit function. This indicates that the buried load at 120 km better models the shape of the Hawaiian swell and in turn makes this our preferred model for the support of the Hawaiian swell.

lithosphere at a depth found in previous studies to be between 40 and 200 km [*Watts*, 1976; *Crough*, 1978; *Sandwell*, 1982; *McNutt and Shure*, 1986; *Phipps Morgan et al.*, 1995]. Our interpretation is also compatible with the recent discovery of 100-110 km thick lithosphere under the island of Hawaii with lithospheric thinning to 50-60 km upstream under the island of Kauai by *Li et al.* [2004] using S-wave receiver functions. Likewise, the low-velocity P-wave seismic anomaly observed in the shallow mantle under the Hawaiian swell region by *Montelli et al.* [2004] is consistent with a buoyancy anomaly supporting the swell. Finally, multichannel seismic data collected by *Ten Brink and Brocher* [1988] shows normal crustal thickness values of 6-7 km in areas of the Hawaiian swell north and south of Oahu, further supporting the interpretation of deep mantle support for the swell topographic anomaly rather than the shallow crustal support which would be implied by plate flexure with surface loading.

In contrast, the RMBA of the Hawaiian and Emperor seamounts are best modeled in our results by surface load flexure with 60 and 30 km elastic plate thicknesses, respectively. Although the r.m.s. misfit for the 150 km deep buried load flexure model is almost as small as the best surface load flexure models for the Hawaiian seamounts, a close examination of Figure 2-5e and Figure 2-5g reveals that the surface loading flexure model does a better job of modeling the shape of the flexural moat associated with the seamounts. The success of the surface loaded flexural admittance model is perhaps to be expected as such short-wavelength features are commonly understood to be supported by plate strength. Previous studies have found greater elastic thicknesses for the Hawaiian islands and the Hawaiian ridge than for the Emperor Seamounts [*Walcott*, 1970; *Watts and Cochran*, 1974; *Watts*, 1978; *Kunze*, 1980; *Watts et al.*, 1985; *Calmant*, 1987; *Watts and Zhong*, 2000]. *Watts and Zhong* [2000] suggest that the apparent elastic thickness of a plate increases with the thermal age of the plate at the time of loading and decreases with time after loading due to the viscoelastic behavior of the plate. Both of these factors could explain the smaller elastic plate thickness estimates for the Emperor seamounts, which were emplaced much earlier and on younger lithosphere [*Mammerickx and Sharman*, 1988; *Keller et al.*, 2000]. While our estimate agrees with that trend, the magnitude of our values is greater than most of those studies. This may be in some measure due to the fact that we are using a two-dimensional admittance function and averaging over the entire Hawaiian and Emperor seamount chains, while previous studies have looked at discrete cross-axis profiles along the chains. Additionally, it is important to note that the swell does not cease to exist under the seamounts and therefore the gravitational anomaly we measure probably has contributions from both surface loading of the seamounts and the buried load that supports the swell.

Lastly, the Mid-Pacific Mountains, Hess Rise, and Shatsky Rise are best modeled by Airy isostasy. Figure 2-5c shows that Hess and Shatsky are extremely well modeled at all wavelengths, while the larger-wavelengths of the Mid-Pacific Mountains are well modeled but the small wavelength features remain uncompensated. This is consistent with an interpretation of the Mid-Pacific Mountains, Hess Rise, and Shatsky Rise as old igneous plateaus that were emplaced on young, weak lithosphere at spreading centers (Hess and Shatsky Rises) or over low viscosity mantle (Mid-Pacific Mountains) that has relaxed to the point where the load floats in isostatic equilibrium. The Mid-Pacific Mountains, Hess Rise, and Shatsky Rise are dated as old as 123–132 Ma [*Arnaud-Vanneau and Sliter*, 1995; *Jenkyns*, 1995; *Jenkyns et al.*, 1995; *Pringle and Duncan*, 1995], 98–100 Ma [*Pringle and Dalrymple*, 1993], and 138–145 Ma [*Sager and Han*, 1993; *Party*, 2002b], respectively. Recent two-layer viscoelastic models of the lithosphere show that for cases where the viscosity ratio between the upper and lower layers is on the order of $10^{24}/10^{21}$, 10–100 Ma after a load is applied to the lithosphere the system relaxes to a state resembling Airy isostasy [*Watts and Zhong*, 2000]. While there was likely a buried buoyant load related to the vast quantities of volcanism produced in the formation of these features, thermally buoyant support is likely to have cooled to ambient density in the 100 Ma or more since the formation of these features. Additionally, plate motion is likely to have carried these loads away from the asthenospheric material that was under them at the time of formation. Admittance and coherence studies of another Pacific large igneous province, the Ontong Java Plateau similarly show that for long wavelength features either Airy isostasy or a very thin elastic plate is required to support the topography, while for shorter wavelengths more complicated loading histories with both surface and subsurface loads are required to match observations [*Ito and Taira*, 2000].

2.3.4 Crustal Thickness

The admittance calculations in the previous section have shown that shallow crustal compensation, either through Airy isostasy or plate flexure due to surface loading, accounts for most of the RMBA signal we observe in the northwest Pacific region. The only apparent exception is the Hawaiian swell, which could be alternatively explained as resulting from deep buried loads in the mantle. We therefore estimate crustal thickness variations by converting the RMBA map into a Moho topography map through downward continuation of the gravity anomaly signal to an appropriate depth. It should be emphasized that while we have used various compensation models to evaluate the probable source of observed RMBA gravity anomalies, no specific compensation model goes into the crustal thickness calculation. We simply estimate the amount of excess crust necessary to account for the total observed gravity anomalies. This therefore represents an end-member maximum crustal thickness variation: contributions to the observed RMBA from mantle density variations or buried loads would reduce the fraction of the gravity signal which comes from crustal thickening and make our calculated Moho topography too deep.

The equation for the downward continued Moho topography $M(k)$ in terms of the observed gravity anomaly $B(k)$ is

$$M(k) = -\frac{\exp\left(kz_{CR}\right)}{2\pi G\left(\rho_m - \rho_c\right)} B(k)C(k) \tag{2.9}$$

where z_{CR} is the mean crustal root depth below sealevel, as in equation 2.3, and $C(k)$ is a low-pass cosine filter applied to prevent the amplification of short-wavelength noise in the RMBA. All wavelengths larger than λ_{long} are completely preserved in the calculation, all wavelengths smaller than λ_{short} are completely filtered out, and wavelengths between the two are tapered smoothly. In order to choose the best value for the two parameters, we tested many λ_{short} values with a constant offset between λ_{short} and λ_{long} of 20 km. We then tested a variety of offsets for two likely λ_{short} values, 35 km and 75 km (Figure 2-8). The best values were taken to be the combination of parameters that minimized both the r.m.s. relief on the Moho and the r.m.s. misfit between the observed gravity anomaly and that predicted by upward continuation, i.e., working backwards, from the Moho topography [*Blackman and Forsyth*, 1991]. We choose λ_{long} to be 135 km and λ_{short} to be 35 km, which is consistent with the coherence of satellite gravity signals when compared to shipboard gravity [*Neumann et al.*, 1993]. The resulting Moho topography is converted to a crustal thickness map by subtracting the seafloor bathymetry from the calculated Moho depth (Figure 2-9). For consistency, we filter the seafloor bathymetry with the same cosine filter that was applied to the Moho topography calculation. The resultant crustal thickness map shows an

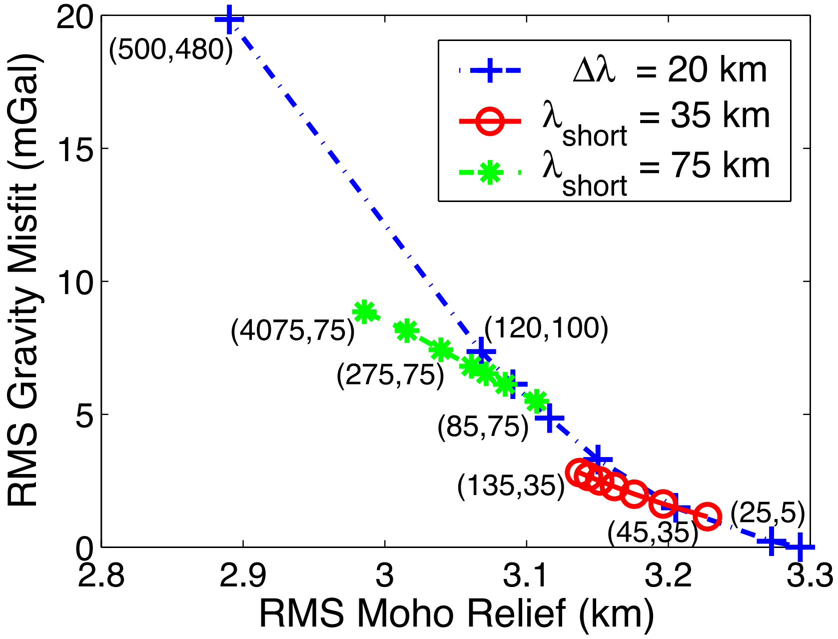

Figure 2-8: Finding the best filtering wavelengths for the calculation of Moho topography by downward continuation of the RMBA gravity signal. The filter should minimize amplification of short wavelength noise while introducing minimal misfit between the original observed RMBA and that predicted from upward continuation of the resulting Moho topography. These two goals are measured by the r.m.s. Moho relief axis and the r.m.s. gravity misfit axis, respectively. Each point represents a downward continuation run with a different combination of (λ_{long},λ_{short}) cutoff wavelengths, and select points are labeled with the values used for that run. The dash-dot line shows runs with a constant offset of 25 km between the small and large wavelengths, the dash line shows runs with a short wavelength cutoff of 75 km and various long wavelength cutoffs, and the solid line shows runs with a short wavelength cutoff of 35 km and various long wavelength cutoffs. We choose a best-fitting combination of (135 km, 35 km), which is consistent with the spatial precision found for marine and satellite gravity anomalies in other studies [*Blackman and Forsyth*, 1991; *Neumann et al.*, 1993].

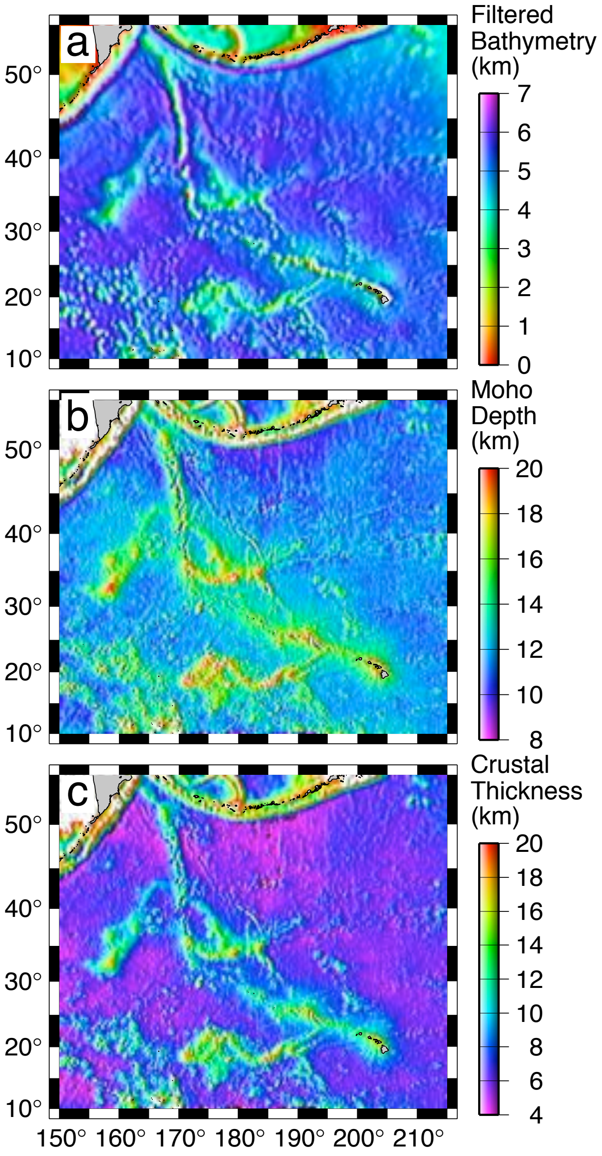

Figure 2-9: Calculation of crustal thickness. (a) Shiptrack bathymetry filtered with a cosine taper between $\lambda_{\mathrm{long}} = 135$ km and $\lambda_{\mathrm{short}} = 35$ km. (b) The Moho depth below sealevel, calculated from downward continuation of the observed RMBA after applying a cosine taper similar to that applied to the bathymetry in panel a. The values shown in (b) are based on the assumption that all the observed RMBA signal is due to excess crustal thickness. (c) The calculated crustal thickness, which is obtained by subtracting the seafloor bathymetry in panel (a) from the calculated Moho depth in panel (b). The crustal thickness map shows an average thickness of 6 km with 2-4 km of excess crustal thickness along the Hawaiian swell and up to 12 km of excess crustal thickness along the Hawaii-Emperor Seamount chain and under Hess Rise. These results are consistent with the limited seismic reflection and refraction data available around Hawaii *Ten Brink and Brocher* [1987].

average thickness of 6 km with 2–4 km of excess crustal thickness along the Hawaiian swell and up to 12 km of excess crustal thickness along the Hawaii-Emperor seamount chain and under Hess Rise. Comparing an interpreted seismic profile across the Hawaiian island of Oahu [*Ten Brink and Brocher*, 1987] with our crustal thickness estimation (Figure 2-10) shows that within 200 km of the island our gravity-derived crust-mantle boundary depth is roughly consistent with the seismically determined Moho. Beyond 200 km distance from Oahu, the Hawaiian swell RMBA leads us to overpredict the crustal thickness compared to the interpreted seismic profile. Note that if part of the observed RMBA over the Hawaiian swell is due to deep buried loads in the mantle as discussed previously, the discrepancy between the remaining RMBA signals and the seismic data would be less. However it is also worth noting that all of the seismic data used to produce the *Ten Brink and Brocher* [1987] Oahu crustal structure profile is confined to a distance of 200 km or less from the Oahu island, so they lack constraints on crustal structure under the full width of the Hawaiian swell.

It would be useful to compare our calculated crustal thickness maps for the Mid-Pacific Mountains and Hess and Shatsky Rises with seismic crustal thicknesses. Unfortunately, few seismic surveys or measurements appear to have been made for the Mid-Pacific Mountains. The seismic data that exists for Hess Rise [*Kogan et al.*, 1982; *Kroenke and Nemoto*, 1982; *Vallier et al.*, 1983] is restricted to multichannel reflection profiles of sediment and basement structures that fails to image a Moho reflector, although *Kogan et al.* [1982] do note that the crustal thickness must be at least twice as thick as normal ocean crust. Although modern seismic work on Shatsky Rise appears to be limited to reflection survey for ODP Leg 198 [*Klaus and Sager*, 2002], two older seismic refraction studies exist. *Den et al.* [1969] found that the depth to the mantle was at least 22 km under the crest of the Shatsky Rise and *Gettrust et al.* [1980] concluded that if a Moho discontinuity exists in their data, its depth is greater than 26 km. The greatest crustal thickness we calculated for Shatsky Rise is 19 km, a result which is comparable to although slightly smaller than those two observations.

2.3.5 Igneous Volume Flux

Using our crustal thickness map for the northwest Pacific, we can calculate the along-axis profiles of excess crust and the corresponding hotspot igneous volume flux generated by the interaction of the Hawaiian hotspot with the Pacific lithosphere. First we subtract the 6

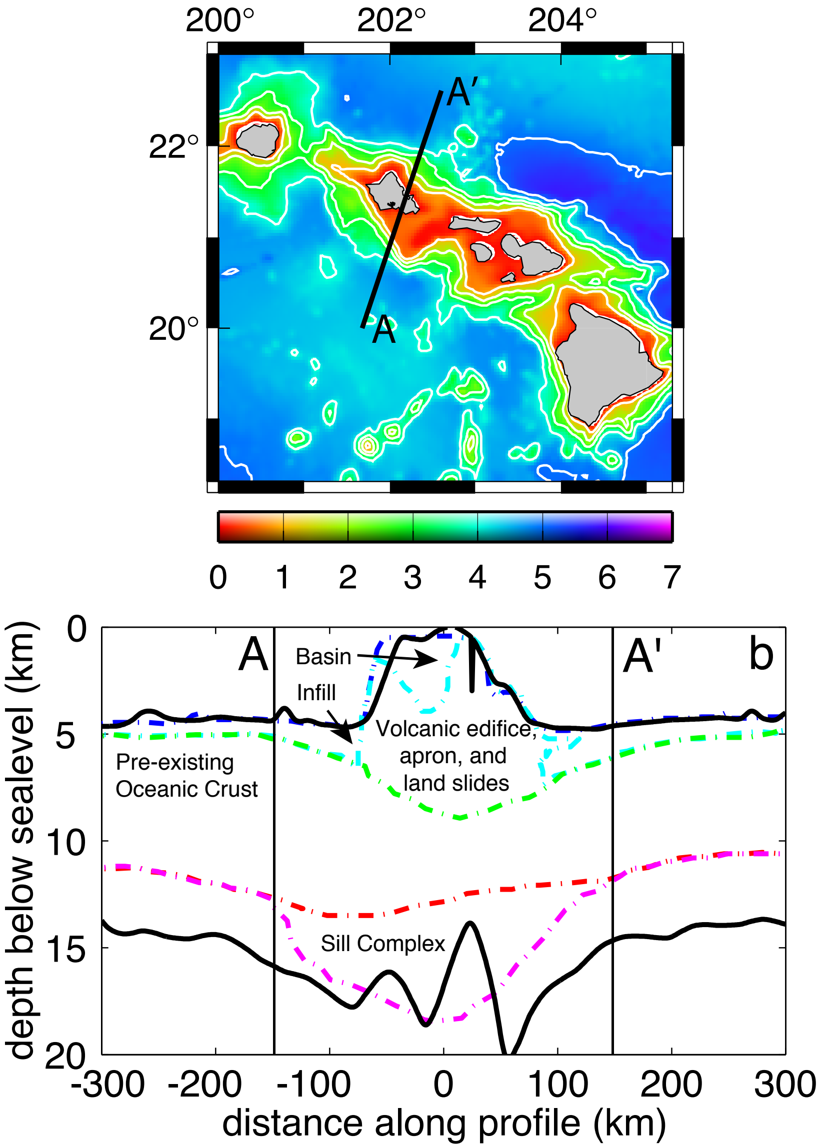

Figure 2-10: Crustal cross section across the island of Oahu. (a) Shiptrack bathymetry contoured every 1000 m with the A-A' profile used by ten Brink and Brocher [1987]. (b) Digitized interfaces from the crustal structure of the island of Oahu inferred from reflection and refraction marine seismic profiles collected around the island [*Ten Brink and Brocher*, 1987] (dash-dot lines) are compared with the shiptrack bathymetry and our gravity-derived crust-mantle interface (solid lines). Our calculated Moho (lower solid line) compares well with the seismic crustal thickness (lowest dash-dot line) near the seamount. At distances greater than 200 km from Oahu, the gravitational signal of the Hawaiian swell leads us to overpredict crustal thickness relative to the seismic interpretation. However, it is worth noting that the seismic interpretation is based on data that is confined between A and A' and is therefore not well constrained under the swell.

km reference crust from the crustal thickness map (Figure 2-9c) to find the excess crustal thickness E(x,y) (Figure 2-11a). Next we rotate the coordinates from latitude and longitude to x' and y', where y' follows the axis of the Hawaii-Emperor seamount chain (Figure 2-11b). Finally we integrate:

$$\mathrm{Flux}(\mathrm{y}') = \mathrm{v}\int_{-\mathrm{hw}}^{+\mathrm{hw}} \mathrm{E}(\mathrm{x}',\mathrm{y}')\mathrm{dx}' \qquad (2.10)$$

where v is the relative speed between the hotspot and the plate and converts a volume per unit distance along-axis to a volume per unit time. Flux is therefore an along-axis crustal volume flux (Figure 2-11c), which we use as a proxy for igneous production flux over time.

In order to capture all of the Hawaii-Emperor seamounts we use a half width, hw, of 200 km. This choice deliberately fails to capture the whole width of the Hawaiian swell because the broad swell could be supported by deep buried loads rather than thickened crust. Using a half width of 200 km limits the swell contamination to ∼10% of the crustal thickness used to calculate the flux (Figure 2-10). If we take a wider half width of 600 km, the whole swell would be captured, resulting in slightly higher flux values in the younger parts of the Hawaiian chain, while retaining a similar shape to the flux curve. However, choosing such a greater half width would lead to some contamination in the Emperor-Hawaii flux calculations due to the unintended inclusion of the Hess Rise and Shatsky Rise signals near the bend between the Emperor and Hawaiian ridges.

For the Hawaiian ridge we use a constant plate velocity, v, of 8.3 cm/y [*Gordon and Jurdy*, 1986], while for the Emperor seamounts we use a rate of hotspot motion relative to the plate suggested by recent paleomagnetic results. *Tarduno et al.* [2003] produced two estimates of hotspot motion southward during the formation of the Emperor seamounts: 43.1±22.6 mm/y and 57.7±19.2 mm/y. We use the larger value as it seems to result in a good correlation between the peaks in the Emperor seamounts section of Figure 2-11c and the ages of the Koko (49 Ma), Nintoku (56 Ma), and Detroit (75-81 Ma) seamounts summarized in *Tarduno et al.* [2003].

Results of the igneous volume flux calculations show that the hotspot has had a volcanic production rate of near 8 m^3/s (0.25 km^3/y) in recent times (Figure 2-11c), although this is probably an underestimation due to the lack of proper gravity data coverage for the Hawaiian islands. The volcanic flux was only 4 m^3/s from 8-18 Ma, however it was slightly greater than 8 m^3/s at 20 Ma. For the Emperor ridge, the calculated flux reached two very

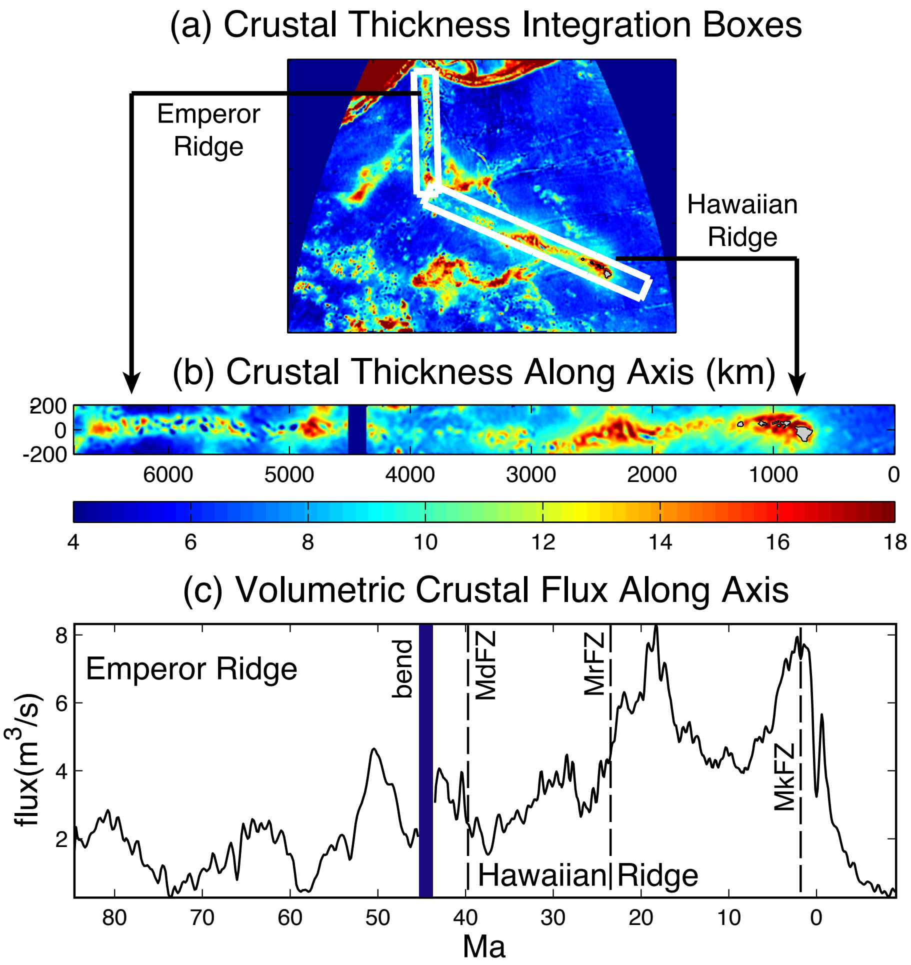

Figure 2-11: Igneous volume flux calculation. (a) Calculated map of crustal thickness. The cut-out stripes of the Emperor ridge and Hawaiian ridge are shown by white boxes. (b) Crustal thickness stripes cut from panel a and rotated. Data within these stripes are then integrated to find the igneous (crustal) volumetric flux shown in panel c. The half width of the stripe chosen for the crustal volume flux integration calculations is 200 km, and the along-axis distance is converted to an along-axis age of the Hawaiian chain by assuming a constant plate velocity of 8.3 cm/y [*Gordon and Jurdy*, 1986] and along-axis age of the Emperor chain using the hotspot-plate relative speed of 5.77 cm/y proposed by *Tarduno et al.* [2003]. The thick blue line shows the location of the bend in the hotspot chain and the dashed lines show the approximate location of the major Pacific fracture zones (FZ) as inferred from Figure 2-1, where MkFZ = Molokai FZ, MrFZ = Murray FZ, and MdFZ = Mendocino FZ.

low flux periods near 55 Ma and 65 Ma (Figure 2-11c). Furthermore, we note that during the low flux periods at 25-48, 57, and 75 Ma, the height and size of individual hotspot seamounts also appear to be noticeably less than those of the high flux periods.

The two previous studies which calculated igneous or volcanic fluxes over the time span of the Hawaii-Emperor chain share certain gross features with our results. *White* [1993] and *Vidal and Bonneville* [2004] both have high magmatic production rates during the Hawaiian chain from 0 to ∼25 Ma with a low point within that time span at ∼10 Ma, a large decrease in flux around the bend in the chain, and much lower magmatic fluxes during the Emperor chain. The 0 Ma magnitude of the flux is much greater for *Vidal and Bonneville* [2004] than in our study. One of the effects that may contribute to such a discrepancy is underestimation due to the lack of gravity data coverage on the Hawaiian islands in our calculations. The magnitude of the next peak in the igneous volume flux down the chain from the present is similar between our result and *Vidal and Bonneville* [2004] and double that found by *White* [1993]. However that peak is offset in time between our result (∼19 Ma) and *Vidal and Bonneville* [2004] (∼15 Ma). It is unclear how *Vidal and Bonneville* [2004] converted distance to time along the Hawaiian ridge, which makes it difficult to account for this difference. The largest difference between our igneous volume flux and that of the prior studies is found in the Emperor chain, where both prior studies found similar low flux values (1–2 m^3/s) which remained fairly constant over the length of the chain. In contrast, we have distinct variations in flux between 4 and 0 m^3/s in the Emperor chain on a time scale of 10–20 Ma. This is perhaps due to the finer 10 km along-axis distance steps used in our calculation, as opposed to the 1° along-axis windowing used by *Vidal and Bonneville* [2004].

2.3.6 Igneous Volume Flux Periods

In order to better quantify the flux variations we observed, the power spectral density of the crustal volume flux, or igneous volume flux (Figure 2-11c) was calculated using a fast Fourier transform convolved with a Hanning filter. The spectra were then smoothed using a moving window that averaged every ten adjacent frequency bins, reducing the variance of the spectra at the expense of reduced resolution.

The spectral energy in both the unsmoothed and smoothed power density spectrums of the igneous volume flux (Figure 2-12) is largest in a range of periods between 6.2 and 30.8

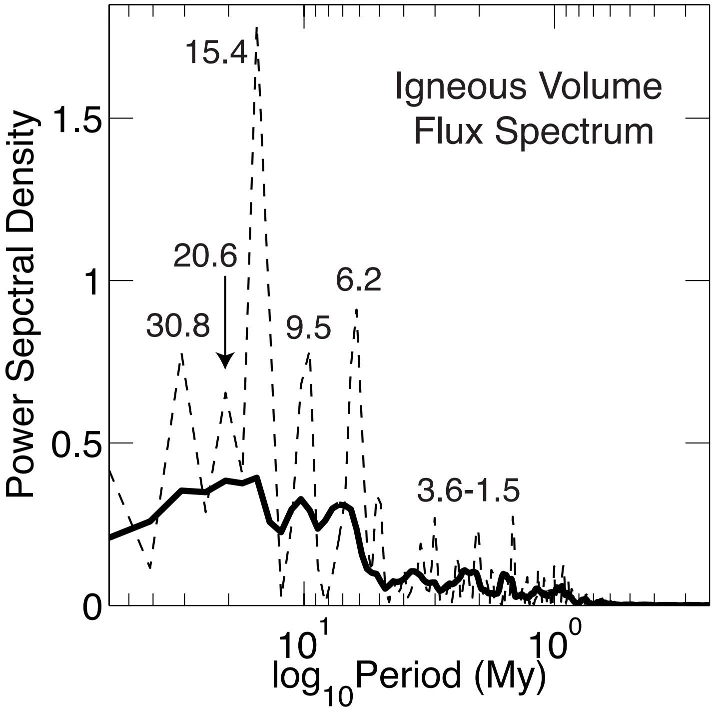

Figure 2-12: Power spectral density of the igneous volume flux time series shown in Figure 2-11. The spectra were calculated using a Fourier transform with a Hanning filter. The raw power spectral densities (dashed line) and the ten-bin windowed average of the raw spectrum (thick solid line) are shown.

My. This reflects the somewhat irregular spacing of the peaks and troughs of the igneous volume flux in Figure 2-11c, which varies between 8.3 and 17.4 Ma with an average of 12.8 My and a standard deviation of 3.1 My. The 15.4 My period on the unsmoothed spectrum thus seems to be an average value corresponding to the 8–17 My spacing of peaks and troughs in the flux results. The 30.8 My peak seems to be an average value of the distance between the 20 Ma, 50 Ma, and 80 Ma peaks in Figure 2-11c. Short wavelength signals have largely been filtered out by the $\lambda_{\text{short}} = 135$ km value used in the crustal thickness calculation, equivalent to ~1.6 My.

2.4 Discussion

2.4.1 Admittance and Flux Implications

The results from the admittance functions for Airy isostasy, plate flexure with surface loading, and plate flexure with buried loading indicate that the relatively narrow Hawaiian hotspot seamounts are probably supported by plate flexure in response to surface loading. While admittance modeling results for the broader Hawaiian hotspot swell are ambiguous, the greater success of the buried load flexure in modeling the shape of the Hawaiian swell leads to our preference of the hypothesis that the swell is likely supported by a buried buoyant load at approximately 120 km depth. The support of the seamounts by plate flexure is not surprising since the theory of elastic plates predicts that short wavelength features should be supported by the plate strength.

Our preferred hypothesis of a buried load supporting the Hawaiian hotspot swell contrasts with the other Pacific long-wavelength bathymetric features, the Hess, Shatsky, and Mid-Pacific igneous plateaus, which seem to be supported by Airy isostasy with a low density crustal root. There are a few probable explanations for a buried load supporting the swell: a depleted, low-density region caused by the melt extraction from the mantle to supply the Hawaiian hotspot volcanism [*Jordan*, 1979; *Robinson*, 1988; *Phipps Morgan et al.*, 1995] or a warm, low-density region of thermally buoyant material supplied by a plume from deep in the mantle and trapped under the oceanic lithosphere [*Crough*, 1978, 1983; *Detrick and Crough*, 1978; *Davies*, 1988; *Sleep*, 1990], or a combination of both. While we cannot definitively select one of these models, we can speculate that if a buoyant depleted mantle is supporting the swell, the volume of that depleted melting source could be correlated with the amount of excess crustal material which has been erupted as seamounts and underplated the crust. Thus the igneous volume flux might provide some measure of the volume of a depleted, buoyant mantle melting source located under the hotspot track.

2.4.2 Potential Causes of Flux Variations

We have shown that the igneous volume flux of the Hawaii-Emperor hotspot has varied widely on time scales of 6–30 My with amplitude variations between 0 and 8 m^3/s (Figure 2-11c). With the igneous volume flux we have measured the end-member crustal production of the hotspot. Are the variations we observe in such hotspot crustal production controlled by variations in the mantle plume supplying the hotspot, the nature of the lithosphere with which the hotspot is interacting, or both?

Phipps Morgan et al. [1995] have hypothesized that the variations in Hawaiian volcanic production are due to changes in the overlying lithosphere as the various Pacific fracture zones crossed the stationary mantle source. This hypothesis argues that under the younger, warmer, and thus thinner lithosphere between the Molokai and Murray FZs, hotspot material would ascend higher and melt more than under the older, cooler, and thicker lithosphere between the Murray and Mendocino FZs (Figure 2-1). While this is a plausible explanation for the Hawaiian ridge portion of the hotspot track, it fails to account for the flux variations we have observed in the Emperor seamount chain, which lacks dramatic fracture zone crossings. This model is also unable to explain the observed reduction in the fluxes at $\sim$10 Ma on the Hawaiian chain, which lies within the warmer lithosphere bounded by the Molokai and Murray FZs (Figure 2-11). However, we note that this low flux region is geographically close to where the Mid-Pacific Mountains feature (123–132 Ma old) connected to the Hawaiian ridge, although the detailed style of potential interaction between the two volcanic features is not clear at present.

To explain the variations in the Emperor seamount crustal volume fluxes, we turn our attention to recent paleomagnetic studies [*Tarduno and Cottrell*, 1997; *Party*, 2002a; *Cottrell and Tarduno*, 2003], which have suggested that the Hawaii-Emperor hotspot was moving south at rates of 30–50 mm/y during the formation of the Emperor seamounts. It seems possible that the dynamics of the moving hotspot plume conduit during this time period could affect the hotspot flux being supplied under the lithosphere. The detailed kinematics of interactions between a moving plume conduit and the surrounding mantle convection have been investigated by *Steinberger and O'Connell* [1998] and *Steinberger* [2000]. The further expansion of such studies to include flux variations in the plume conduits should be an interesting area for further research.

V-shaped ridges propagating along the Mid-Atlantic Ridge south of the Iceland hotspot were successfully modeled by *Ito* [2001] as the result of hotspot flux variation due to a periodic oscillation in the radius of the hotspot mantle plume conduit. *Ito* [2001] hypothesized that such an oscillation could be caused by the surfacing of solitary waves in the Iceland mantle plume. Solitary waves are stable traveling perturbations in the width of a buoyant, viscous fluid conduit due to perturbations in the flux of the fluid entering the conduit [*Scott et al.*, 1986; *Olson and Christensen*, 1986; *Whitehead*, 1987]. *Sleep* [1992] suggested a possible source of those perturbations in the flux of the fluid entering the conduit due to the dynamics of the evolving boundary layer at the bottom of the mantle. The presence of similar V-shaped anomalies south of the Azores hotspot [*Escartin et al.*, 2001] suggests that such a mechanism may be applicable for other hotspots as well. Because of their close proximity to the mid-ocean spreading center, the variations in the Azores and Iceland hotspot flux is expressed as changes in crustal thickness along the Mid-Atlantic Ridge [*Escartin et al.*, 2001]. Similarly, it is possible that solitary wave-like variations in the Hawaiian-Emperor hotspot flux might result in crustal thickness variations as reflected in our results (Figures 2-11 and 2-12).

One possible way to distinguish between the proposed lithospheric versus plume conduit sources of flux variation would be to examine the geochemistry of the volcanic rocks along the Hawaii-Emperor seamount chain for signals of melting depth variation. *Regelous et al.* [2003] compare MgO/FeO ratios, La/Yb and Lu/Hf ratios, and trace element compositions between Detroit and Meiji tholeiites and other Hawaiian-Emperor tholeiites and conclude that those values vary with the age of the underlying oceanic lithosphere at the time of seamount formation. Likewise, *Keller et al.* [2000] see a correlation between ^{87}Sr/^{86}Sr ratios and seamount-crust age difference. However, *Keller et al.* [2004] did not find simple correlations between ^{3}He/^{4}He isotope ratios and the igneous volume flux calculated in our study. And *Frey et al.* [2005] inject a discussion of a geochemically depleted component in the Hawaiian-hotspot source material that may complicate the above interpretations.

2.5 Conclusions

(1) We have calculated the residual bathymetry and residual mantle Bouguer anomalies (RMBA) of the northwest Pacific region. The interaction of the Hawaii-Emperor hotspot with the Pacific lithosphere has left a large negative RMBA anomaly, suggesting thickened crust, low density mantle, or both. The width and magnitude of the RMBA anomaly along the hotspot track vary widely, with the 1,000 km-wide hotspot swell visible for a few thousand kilometers downstream from the hotspot's present location.

(2) Applying admittance functions for Airy isostasy, elastic plate flexure with surface loading, and elastic plate flexure with buried buoyant loading to the residual bathymetry allows us to discriminate between sources of the observed RMBA. Incorporating our results with previous seismic and flexure studies of the Hawaiian chain, we conclude that the Hawaii and Emperor seamounts are best explained as being supported by surface loading of elastic plates with thicknesses of 60 and 30 km, respectively, and the Hess Rise, Shatsky Rise, and the Mid-Pacific Mountains igneous plateaus are best modeled by Airy isostasy. Our r.m.s. misfit results are more ambiguous for the Hawaiian swell. However, the shape of the Hawaiian swell is best modeled by the flexure due to a buried load at approximately 120 km depth.

(3) Since all bathymetric features except possibly the Hawaiian swell seem to be supported by thickened crust, either through Airy isostasy or through plate bending, we downward continue our calculated residual Bouguer anomaly to find the crustal thickness model that best predicts the observed gravity anomaly while filtering out short-wavelength signals. Integrating the crustal anomaly within a narrow stripe of 200 km half width centered on the hotspot track yields an estimated present-day Hawaiian igneous volume flux of 8 m^3/s, while the flux was only 4 m^3/s during 8–18 Ma and greater than 8 m^3/s at 20 Ma. From 25 to 48 Ma, the igneous volume flux was in a low period with amplitudes as small as 1 m^3/s. The overall calculated igneous volume flux of the Emperor ridge is substantially smaller than that of the Hawaiian ridge with minimums occurring near 57 and 75 Ma. Furthermore, we note that during the low flux periods at 25–48, 57, and 75 Ma, the height and size of individual hotspot seamounts also appear to be noticeably less than those of high flux periods.

(4) We hypothesize that the quasi-periodic variations in the hotspot flux along the

Hawaiian ridge may be due to changes in the lithospheric age, temperature, and thickness as the hotspot crossed Pacific fracture zones, as well as potential pulsation of the plume source. We also hypothesize that the quasi-periodic variations in the hotspot flux along the Emperor seamount chain may be due to fluctuations in the plume conduit due to its motion through the mantle. Further combined geochemical and geophysical analyses are required to distinguish between these mechanisms. Since the presence and size of the hotspot swell correlates with hotspot crustal flux variations, we suggest that the likely source of the buried buoyant load supporting the Hawaiian swell is melt-depleted, low density residual mantle.

Chapter 3

Seismic Structure of the Endeavour Segment, Juan de Fuca Ridge: Correlations with Seismicity and Hydrothermal Activity

Abstract Multichannel seismic reflection data collected in July 2002 at the Endeavour Segment, Juan de Fuca Ridge show a mid-crustal reflector underlying all of the known high-temperature hydrothermal vent fields in this area. Based on the character and geometry of this reflection, its similarity to events at other spreading centers, and its polarity, we identify this as a reflection from one or more crustal magma bodies rather than from a hydrothermal cracking front interface. The Endeavour magma chamber reflector is found under the central, topographically shallow section of the segment at two-way travel time (twtt) values of 0.9–1.4 s (∼2.1–3.3 km) below the seafloor. It extends approximately 24 km along axis and is shallowest beneath the center of the segment and deepens toward the segment ends. On cross-axis lines the axial magma chamber (AMC) reflector is only 0.4–1.2 km wide and appears to dip 8–36° to the east. While a magma chamber underlies all known Endeavour high temperature hydrothermal vent fields, AMC depth is not a

---

Previously published as Van Ark, E. M., R. S. Detrick, J. P. Canales, S. M. Carbotte, A. J. Harding, G. M. Kent, M. R. Nedimovic, W. S. D. Wilcock, J. B. Diebold, and J. M. Babcock (2007), Seismic structure of the Endeavour Segment, Juan de Fuca Ridge: Correlations with seismicity and hydrothermal activity, *J. Geophys. Res., 112*, B02401, doi:10.1029/2005JB004210. Reprinted here with permission.

dominant factor in determining vent fluid properties. The stacked and migrated seismic lines also show a strong layer 2a event at twtt values of 0.30±0.09 s (380±120 m) below the seafloor on the along-axis line and 0.38±0.09 s (500±110 m) on the cross-axis lines. A weak Moho reflection is observed in a few locations at twtt values of 1.9–2.4 s below the seafloor. By projecting hypocenters of well-located microseismicity in this region onto the seismic sections, we find that most axial earthquakes are concentrated just above the magma chamber and distributed diffusely within this zone, indicating thermal-related cracking. The presence of a partially molten crustal magma chamber argues against prior hypotheses that hydrothermal heat extraction at this intermediate spreading ridge is primarily driven by propagation of a cracking front down into a frozen magma chamber, and indicates that magmatic heat plays a significant role in the hydrothermal system. Morphological and hydrothermal differences between the intermediate spreading Endeavour and fast-spreading ridges are attributable to the greater depth of the Endeavour AMC and the corresponding possibility of axial faulting.

3.1 Introduction

Morphological and hydrothermal differences between fast-spreading and slow-spreading mid-ocean ridge systems have led to the hypothesis that these systems have fundamentally different mechanisms of heat extraction and hydrothermal circulation [*Wilcock and Delaney*, 1996; *Lister*, 1974, 1980a, b, 1982; *Fornari and Embley*, 1995]. The permeability structure of the crust and subsequent hydrothermal venting at fast spreading ridges is thought to be controlled by diking events from a steady-state axial magma chamber (Figure 3-1a). This results in small, relatively short-lived hydrothermal vents whose heat flux increases following magmatic eruptions, as observed at the fast-spreading East Pacific Rise (EPR) [*Haymon et al.*, 1991, 1993; *Baker et al.*, 2002]. In contrast, control of the permeability structure of crust at slow spreading ridges has been attributed to extension-driven faulting and downward propagation of a cracking front into the lower crust where either no magma chamber is present or small, deep, pockets of melt occur (Figure 3-1b). This can lead to long-lived hydrothermal systems and massive sulfide deposits whose activity does not seem to be consistently correlated with recent volcanism, exemplified by the TAG hydrothermal system on the slow-spreading Mid-Atlantic Ridge (MAR) [*Wilcock and Delaney*, 1996; *White et al.*, 1998].

The Juan de Fuca Ridge (5.6–5.7 cm/yr full spreading rate [*Wilson*, 1993; *DeMets et al.*, 1994]) is often taken as the type example of intermediate spreading rate mid-ocean ridges (4-9 cm/yr full spreading rate). Previous studies of the morphology and hydrothermal vent structures of the Juan de Fuca Ridge (Figure 3-2) led to the hypothesis that the Endeavour Segment was an example of the slow-spreading ridge style of heat extraction, controlled by the downward propagation of a cracking front into a frozen magma chamber [*Wilcock and Delaney*, 1996; *Kelley et al.*, 2002]. The Endeavour Segment has a ∼150 m deep axial valley with numerous faults and fissures and there is no evidence of recent eruptions (although preliminary U-series dating of recently-collected lavas indicates ages of several thousand years [James Gill, personal communication]). This suggested that Endeavour is currently in an extension-dominated tectonic regime rather than a magmatic regime [*Delaney et al.*, 1992; *Kappel and Ryan*, 1986; *Tivey and Delaney*, 1986]. The large size, regular spacing, and location of known Endeavour high-temperature vent fields along visible faults and fissures in the axial valley floor suggested a long-term pattern of stable sub-surface hydrothermal circulation consistent with a cracking-front model of heat extraction [*Tivey and Delaney*, 1986; *Delaney et al.*, 1992; *Robigou et al.*, 1993; *Butterfield et al.*, 1994; *Lilley et al.*, 1995; *Wilcock and Delaney*, 1996; *Delaney et al.*, 1997; *Yoerger et al.*, 2000; *Kelley et al.*, 2001, 2002, 2003]. In addition, the large heat fluxes recorded at the Endeavour hydrothermal vent fields were thought to be high enough to freeze a magma chamber with a thin conductive lid [*Lister*, 1974, 1980a, b, 1982; *Wilcock and Delaney*, 1996].

Evidence from petrology and seismology was also interpreted as supporting the cracking front model at Endeavour. Lavas collected from the Endeavour axial valley have enriched E-MORB and T-MORB signatures and a high degree of heterogeneity over short length scales which suggests a low degree of melting in a clinopyroxene-rich source [*Karsten et al.*, 1990; *Sours-Page et al.*, 1999]. Levels of seismicity on the Endeavour Segment [*Wilcock et al.*, 2002] were much higher than observed at the EPR [*Sohn et al.*, 1998, 1999] in similar ocean bottom seismometer experiments conducted in 1995. At the EPR axial seismicity is confined to the uppermost 1 km of crust [*Sohn et al.*, 1998, 1999] while at Endeavour seismicity in the axial region occurs in a depth range of 1.5–3.5 km [*Wilcock et al.*, 2002]. The predominant focal mechanism for both EPR and Endeavour micro-earthquakes implies a thermal cracking source, however the EPR hypocenters are located at least 300 m above the axial magma

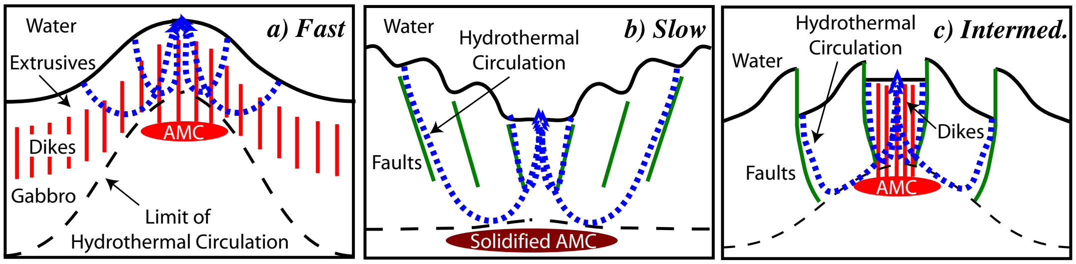

Figure 3-1: Cartoons illustrating proposed hydrothermal circulation regimes for fast, slow, and intermediate spreading centers. Thick dotted lines show proposed paths of hydrothermal circulation through the crust. a) Fast spreading ridges may have hydrothermal circulation controlled by the heat and porosity provided by an axial magma chamber (AMC) with frequent diking and eruptive events. Hydrothermal vents are relatively short-lived and major faults are absent in the axial region [*Wilcock and Delaney*, 1996]. b) Slow spreading ridges, in contrast, may have circulation controlled by faulting and heat mining through propagation of a cracking front into a frozen magma chamber. Hydrothermal systems can be long-lived and are often localized along major faults [*Wilcock and Delaney*, 1996]. c) Intermediate spreading ridges appear to include elements of both faster spreading ridges (a mid-crustal magma body) and slower spreading ridges (long-lived, fault-controlled hydrothermal systems). Faulting along the margins of the neovolcanic zone may be controlled by episodic dike intrusion as opposed to lithospheric extension as at slow spreading ridges [*Carbotte et al.*, 2006].

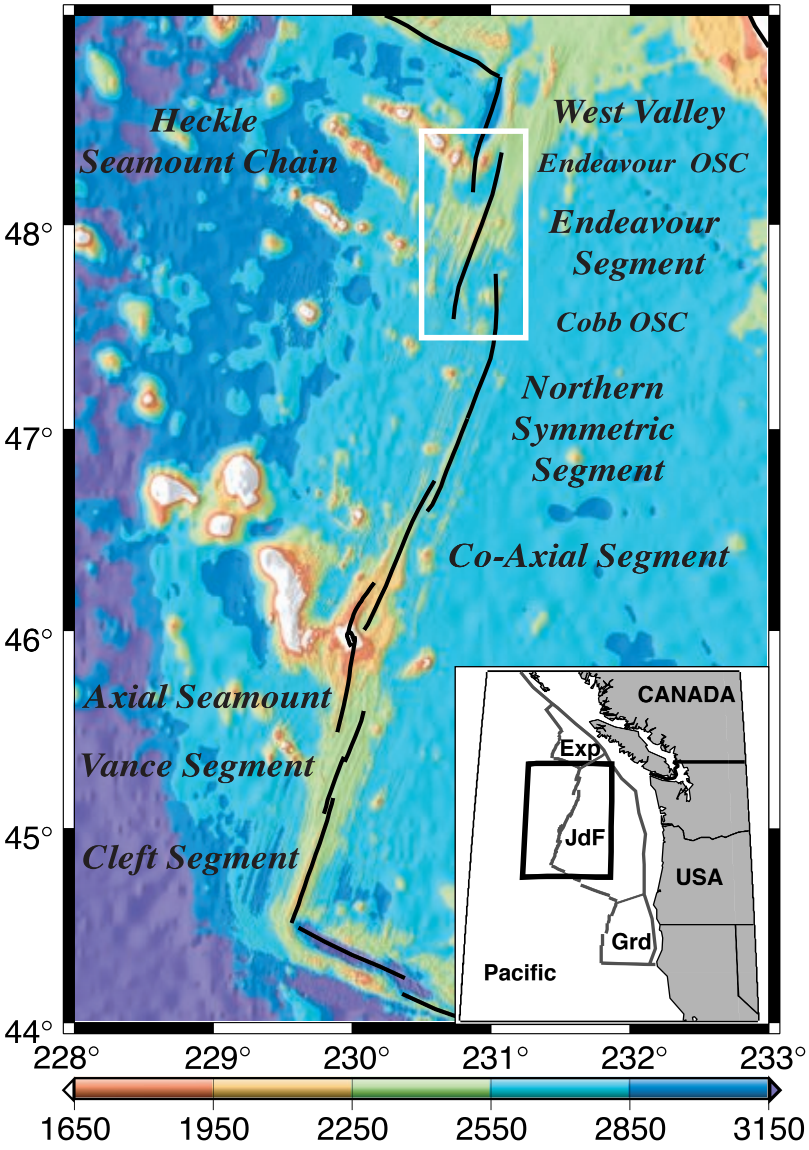

Figure 3-2: Bathymetry of the Juan de Fuca Ridge (in meters) showing the location of the Endeavour segment (white box outlines location of Figure 3-3) and the plate boundary (black line). The Endeavour Segment is bounded to the north by the Endeavour overlapping spreading center (OSC) and to the south by the Cobb OSC. Inset: tectonic setting of the Juan de Fuca Ridge, where JdF = Juan de Fuca Plate, Exp = Explorer Plate, Grd = Gorda Plate, and Pacific = Pacific Plate (black box outlines location of main map).

chamber (AMC) reflection imaged by *Kent et al.* [1993a] while the Endeavour hypocenters were thought to extend to depths greater than the apparent depth of the one possible AMC reflection imaged prior to this work [*Rohr et al.*, 1988]. Finally, the SEISRIDG-85 seismic refraction survey [*Cudrak et al.*, 1987; *Cudrak*, 1988; *White and Clowes*, 1990; *Cudrak and Clowes*, 1993] failed to find major low velocity anomalies under the Endeavour axial high, as would be expected for an active magmatic system.

Here we present data from a July 2002 multichannel seismic reflection survey of the Juan de Fuca Ridge on the *R/V Maurice Ewing* [*Carbotte et al.*, 2006] which shows that all of the major Endeavour Segment hydrothermal vent fields are underlain by a crustal magma chamber at a depth of ∼2.1–3.3 km below the seafloor. Earthquake hypocenters in the axial region occur just above this magma body. We therefore conclude that the heat extraction mechanism at intermediate-spreading systems such as the Endeavour Segment requires a model distinct from that of both fast and slow-spreading ridges. One proposed intermediate heat extraction model (Figure 3-1c) features a magmatic heat source with hydrothermal circulation pathways determined by dike-controlled faulting along the margins of the neovolcanic zone [*Carbotte et al.*, 2006]. The magmatic-hydrothermal system at intermediate spreading ridges thus appears to include elements of both faster spreading ridges (a mid-crustal magma body) and slower spreading ridges (long-lived, fault-controlled hydrothermal systems).

3.2 Overview of the Endeavour Segment

3.2.1 Morphology and Geology

The Juan de Fuca Ridge (Figure 3-2) is the spreading boundary between the Pacific and Juan de Fuca plates. The ∼90-km long Endeavour Segment is located between the Endeavour and Cobb overlapping spreading centers on the northern Juan de Fuca Ridge. The central portion of the Endeavour Segment out to crustal ages of ∼500,000 years (Figure 3-3) is dominated by a series of ridge-parallel (orientation N20E) abyssal hills spaced ∼6 km (∼200,000 years) apart with intervening extensional basins. This ridge-basin pattern is superimposed on a broader (30–40 km-wide) cross-axis swell of young oceanic crust [*Kappel and Ryan*, 1986; *Holmes and Johnson*, 1993]. The abyssal hills are asymmetric with outer constructional volcanic surfaces and inner steep faulted faces [*Kappel and Ryan*, 1986; *Tivey* *and Johnson*, 1987; *Holmes and Johnson*, 1993; *Delaney et al.*, 1997], a shape repeated in the current axial high (Figure 3-4). Sediment thicknesses on terrain younger than 0.8 Ma vary between a few meters and several tens of meters [*Holmes and Johnson*, 1993].

The 25 km-long, 4 km-wide, and 300 m-high central axial volcanic ridge is rifted with a 0.8–1.4 km-wide axial graben (Figures 3-4 and 3-5). This axial graben deepens from north to south with 55–85 m relief at the latitude of the Salty Dawg vent field and 140–160 m relief at the latitude of the Mothra vent field (Figure 3-4) and is bounded by steep, inward-facing normal fault surfaces [*Karsten et al.*, 1986; *Tivey and Delaney*, 1986]. SeaMARC I sonar imagery of the shoulders of the ridge crest suggested overlapping asymmetrical bulbous lava flows dripping down the outer sides of the ridge and identified intense faulting and fissuring confined to the axial graben [*Kappel and Ryan*, 1986]. Alvin submersible and DSL120 deep-towed side scan sonar observations confirmed that the youngest volcanic units in the axial valley are truncated by recent faulting [*Tivey and Delaney*, 1986; *Delaney et al.*, 1992; *Bhat et al.*, 1997].

These morphological details, combined with observations from other segments of the Juan de Fuca Ridge, were interpreted by *Kappel and Ryan* [1986] as supporting a model of episodic, volcanic construction with stages of ridge growth, summit trough collapse, and amagmatic axial extension and faulting, followed by renewed axial ridge growth. However, *Karsten et al.* [1986] noted that the shallowest portion of the Endeavour Ridge coincides with a broad plateau which marks the intersection of the Heckle Seamount chain with the ridge axis (Figure 3-2), suggesting long-term enhanced magma supply to that portion of the spreading axis. They also suggested that the north and south valleys located at either end of the Endeavour Ridge could be caused by diminished magma supply as magma flows along-axis from a central magma chamber under the shallowest portion of the ridge, in combination with the cooling effects due to thermal contrasts at the overlapping spreading centers at either end of the Endeavour Segment. More recently, *Carbotte et al.* [2006] have suggested that the periodic changes in seafloor relief moving away from the axis of the various Juan de Fuca Ridge segments could be attributed to variations in faulting controlled by magmatic, dike injection processes rather than the alternating tectonic-magmatic phases proposed by *Kappel and Ryan* [1986].

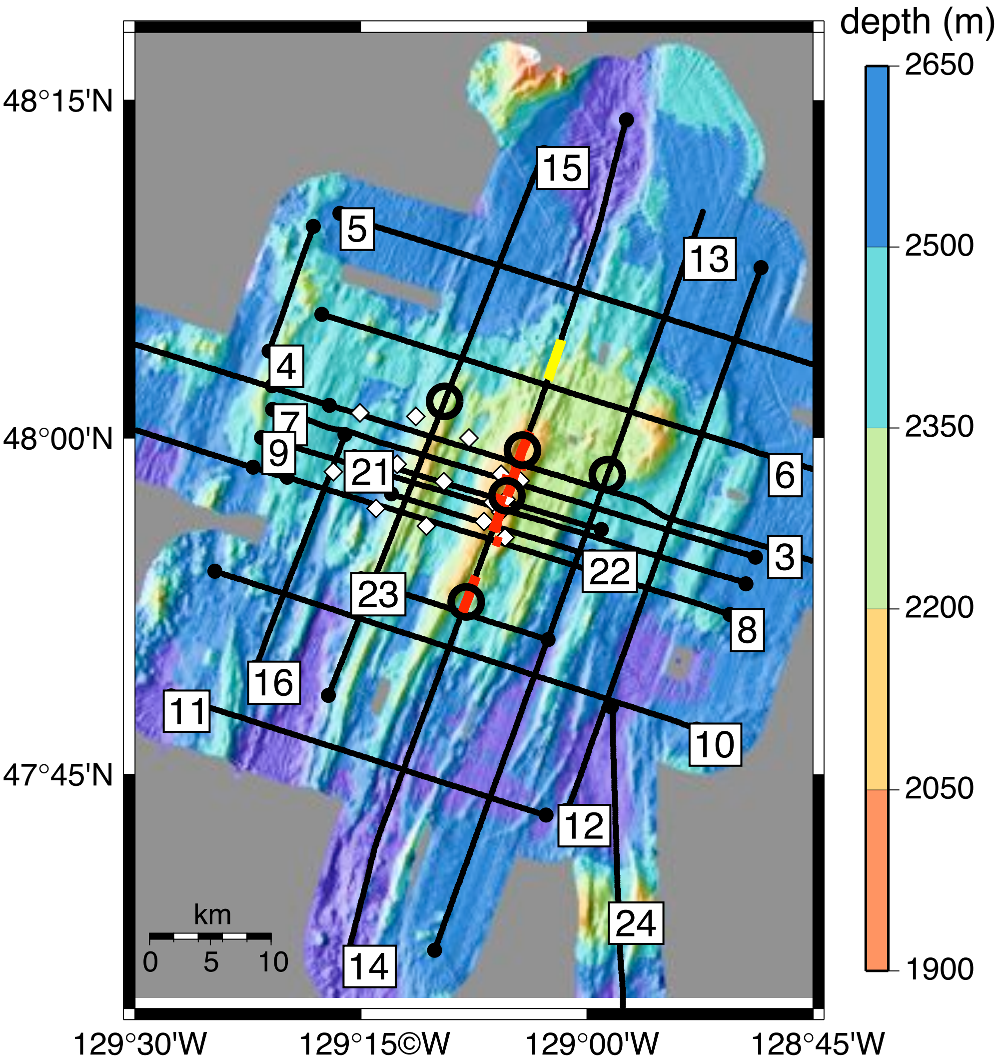

Figure 3-3: Bathymetry of the Endeavour Segment collected during the EW0207 seismic survey. Tracks of the seismic lines collected are labeled and shown using solid black lines. Red and yellow areas on Line 14 show axial magma chamber locations picked from the Line 14 stack – red are more certain picks, yellow are less certain. Black circles indicate locations of supergathers used to produce Figure 3-11 and 3-12. White diamonds show the locations of the ocean bottom seismometers used by *Wilcock et al.* [2002]. The location of the multichannel seismic reflection line shot by *Rohr et al.* [1988], as reported by *White and Clowes* [1990], is nearly coincident with our Line 3.

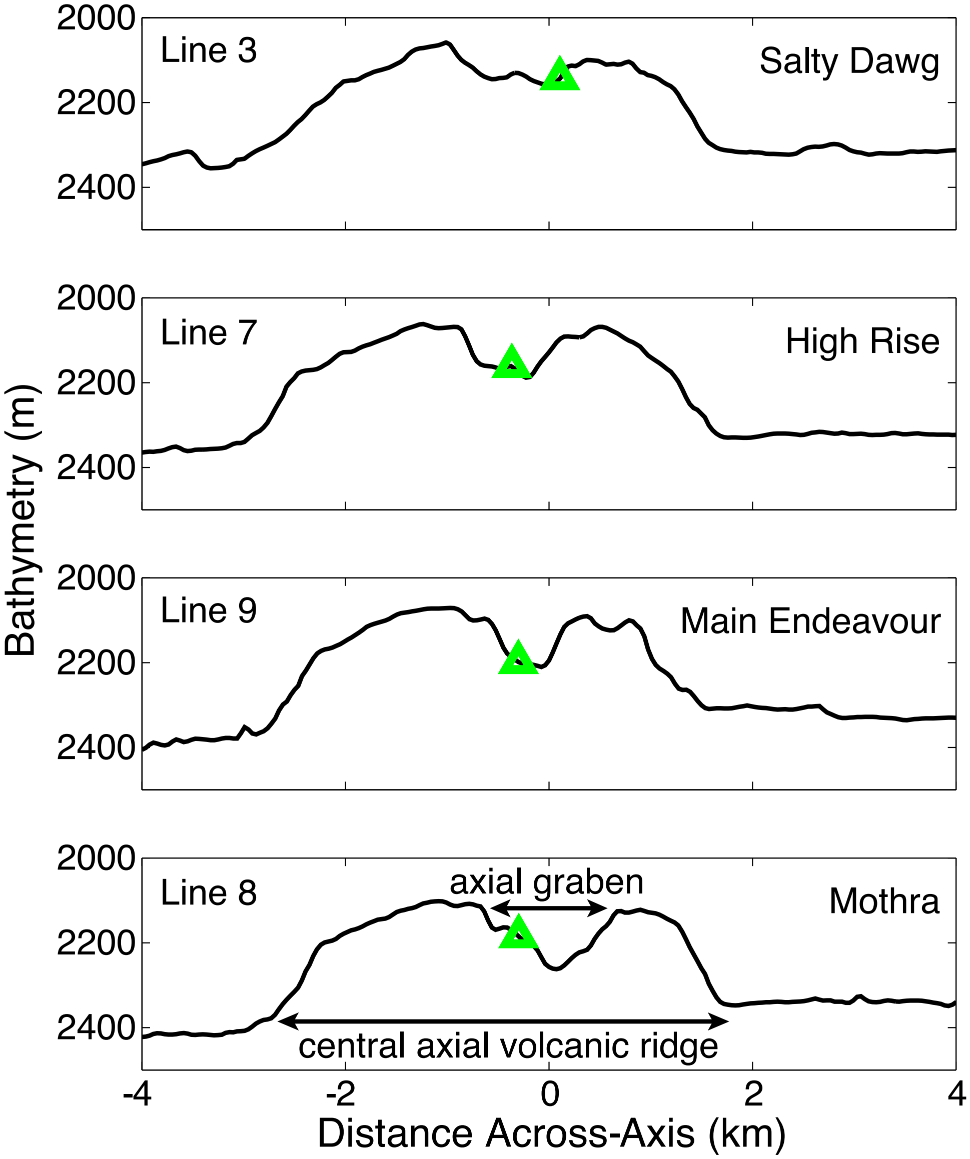

Figure 3-4: Bathymetry profiles across the Endeavour axial high at four vent field locations. Profiles follow the tracks of the labeled seismic lines and are centered at their intersection with the along-axis seismic line. Triangles show location of indicated vent fields.

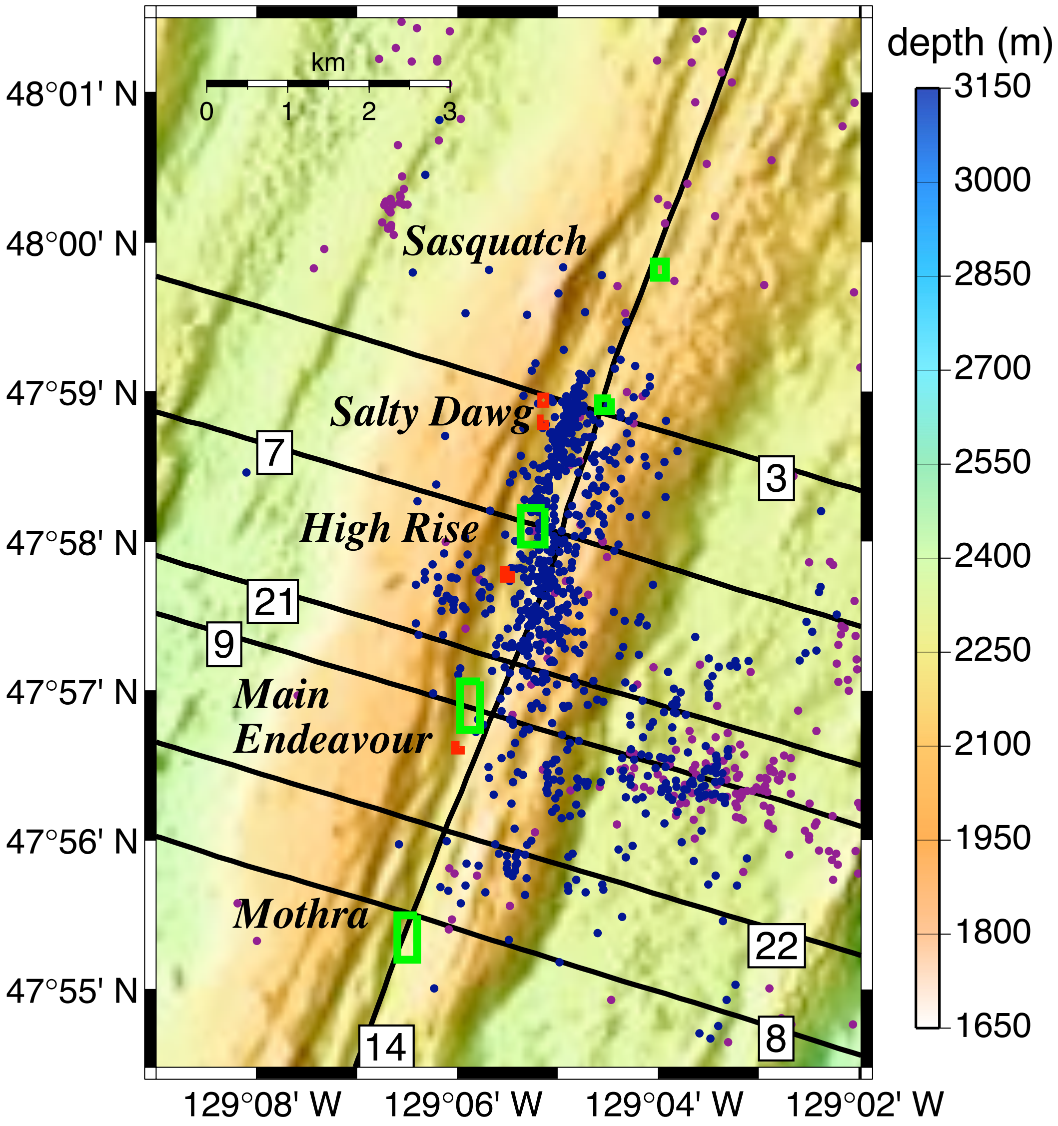

Figure 3-5: Bathymetry of the Endeavour Segment axial high. Green boxes show the location of the five known large, high temperature hydrothermal vent fields. Red boxes show the location of diffuse, low temperature vent fields: Cirque, Dune, Clambed, and Quebec, from north to south. (Vent locations from personal communication with Deb Glickson.) Blue circles show microseismicity hypocenters located in latitude, longitude, and depth, while purple circles show hypocenters located only in latitude and longitude [*Wilcock et al.*, 2002].

3.2.2 Hydrothermal Activity

Hydrothermal vent fields on the Endeavour Ridge have been identified through seafloor mapping, water column thermal and chemical anomalies, dredging, and submersible observations and sampling [*Tivey and Delaney*, 1986; *Kadko et al.*, 1990; *Delaney et al.*, 1992; *Thomson et al.*, 1992; *Robigou et al.*, 1993; *Lilley et al.*, 1995; *Bhat et al.*, 1997; *Kelley et al.*, 2001]. Currently five large, high temperature (300-400°C) vent fields have been identified [*Kelley et al.*, 2002], from north to south: Sasquatch [*Kelley et al.*, 2003], Salty Dawg [*Lilley et al.*, 1995], High Rise [*Robigou et al.*, 1993], Main Endeavour [*Tivey and Delaney*, 1986; *Delaney et al.*, 1992] and Mothra [*Kelley et al.*, 2001] (Figure 3-5). These high temperature vent fields are on the order of 400–500 m long and are spaced approximately every 2–3 km along axis. All appear to be localized along major faults. Each vent field contains many tall (>20 m-high) sulfide structures on top of which many smaller black smoker chimneys are found [*Tivey and Delaney*, 1986; *Delaney et al.*, 1992; *Robigou et al.*, 1993; *Kelley et al.*, 2001, 2002]. Diverse biological communities containing tube worms, sulfide worms, palm worms, galatheid crabs, and a variety of snails and limpets are sustained by lower temperature fluids venting through porous chimney walls and sulfide-structure flanges found on the vents [*Sarrazin et al.*, 1997; *Kelley et al.*, 2002].

Areas of diffuse, lower-temperature flow are present along-axis between these high-temperature vent fields (Figure 3-5), suggesting nested subsurface circulation cells [*Alt*, 1995; *Delaney et al.*, 1997; *Kelley et al.*, 2002]. Magnetic anomalies give further evidence for the isolation of deep, high temperature circulation from shallower low-temperature circulation. High resolution magnetic field data collected over the Endeavour axial valley reveal circular magnetization-anomaly lows associated with known active and extinct hydrothermal vent complexes [*Tivey and Johnson*, 2002]. These circular anomalies were interpreted by *Tivey and Johnson* [2002] as the result of pipe-like zones of upward hydrothermal fluid flow under each vent system, each isolated through at least the magnetic layer (the top $\sim$500 m of the crust) due to "armoring" by silica deposition [*Cann and Strens*, 1989; *Hannington et al.*, 1995; *Tivey et al.*, 1999].

Off-axis heat flow measurements 3–24 km perpendicular to the Endeavour Ridge [*Johnson et al.*, 1993] imply that crust younger than 1 Ma continues to cool primarily by circulation of hydrothermal fluid in topographically controlled pathways associated with deep crustal faults.

3.2.3 Microseismicity

Ocean bottom seismometer (OBS) deployments on the Endeavour Ridge have detected abundant small-magnitude "microearthquakes" which seem to be associated with activity underneath the hydrothermal vent fields [*McClain et al.*, 1993; *Wilcock et al.*, 2002, 2004]. Earthquakes beneath the ridge axis are concentrated in a band of intense seismicity at 1.5–3.5 km depth with fault mechanisms showing subhorizontal tension axes oriented in all directions except parallel to the ridge, indicating a stress field influenced by both ridge spreading and hydrothermal cracking [*Wilcock et al.*, 2002]. Figure 3-5 shows the microseismicity observed in 55-day OBS deployment in 1995 [*Wilcock et al.*, 2002]. More recent observations show a sharp drop in microseismic activity to the north of the High Rise vent field, which seems to correlate with a reduced vigor of hydrothermal venting [*Wilcock et al.*, 2004].

Endeavour axial microearthquakes often occur in swarms, probably signaling either tectonic crustal-cracking events or magmatic diking events [*McClain et al.*, 1993; *Wilcock et al.*, 2002]. Correlations between microseismicity and black smoker visual activity, black smoker fluid temperature variations, and diffuse flow flux variations were first recorded by *Delaney et al.* [1990]. More recently *Johnson et al.* [2000] reported on a June 8, 1999 earthquake swarm which was interpreted to be of tectonic origin and observed to correlate with vent temperature and inferred fluid flux increases. However, *Lilley et al.* [2003] presented evidence that chemical signatures in the vent fluids instead suggested a volcanic origin of the same microseismic swarm and *Bohnenstiehl et al.* [2004] interpreted hydroacoustic records of seismic swarms at Endeavour from March 1999 through January 2000 in terms of dike propagation.

3.2.4 Seismic Structure

The only previous multichannel seismic reflection study of the Endeavour Ridge consisted of a single-cross axis line near the Main Endeavour vent field [*Rohr et al.*, 1988]. This profile revealed a narrow (∼1 km wide) mid-crustal axial reflector at a two-way travel time (twtt) of ∼1.0 s, which was estimated to be 2.5 km below the seafloor. Since the low signal-to-noise of these data prevented determination of the polarity of the reflection and available refraction data [*Cudrak et al.*, 1987] did not indicate major velocity anomalies under the axis, *Rohr et al.* [1988] interpreted this reflector as an increase in seismic velocity related to a vertical thermal gradient caused by a hydrothermal circulation boundary.

Seismic refraction data collected on the SEISRIDG-85 survey of the Endeavour segment [*Cudrak et al.*, 1987; *Cudrak*, 1988; *White and Clowes*, 1990; *Cudrak and Clowes*, 1993] also failed to find evidence for an axial magma chamber. Two-dimensional travel time tomography [*White and Clowes*, 1990] on a cross-axis line coincident with the reflection line of *Rohr et al.* [1988] was interpreted with a three layer upper crustal model with an abrupt velocity increase from 2.5 to 4.8 km/s 250-600 m below the sea floor attributed to a metamorphic front in pillow basalts. A shallow low velocity anomaly with magnitude $<\sim$0.45 km/s beneath the ridge was attributed to a zone of hydrothermal circulation. No evidence was found for a crustal magma chamber at 1.5–3.5 km depth below seafloor, however the sensitivity of the experiment required a zone of partial melt of at least 1 km width and 1 km thickness to produce a detectable delay in travel time arrivals for rays passing through or around the body. Two-dimensional velocity models of the crust [*Cudrak and Clowes*, 1993] revealed significant lateral variations in thickness and velocity of crustal layers 2a, 2b, and 2c which appeared to be random rather than distributed symmetrically about the ridge. These variations were attributed to variations in fracturing, hydrothermal circulation, and magmatic and/or deformational processes. Again no evidence for a large crustal magma body was found, but a small (0.1–0.2 km/s) velocity decrease along axis in seismic layer 3 was interpreted as a possible indicator of elevated temperature.

3.3 Data Acquisition and Processing

In a 30 day multichannel seismic (MCS) reflection survey of the Juan de Fuca Ridge on the *R/V Maurice Ewing* in July 2002 [*Carbotte et al.*, 2002; *Detrick et al.*, 2002a], nine days were spent surveying the Endeavour segment (Figure 3-3). A total of 23 MCS lines were collected parallel and perpendicular to the ridge axis; each line was between 16.4 and 73.3 km long. The track lines were chosen so that 30–40 km-long cross-axis lines would be spaced 3–10 km apart and ridge-parallel lines would follow isochrons at 0.25 Ma (Lines 15 and 13) and 0.5 Ma (Lines 16 and 12) on both ridge flanks. Isochron lines were located along abyssal hills where possible to minimize side-scattering from nearby shallow topography. Line 14 runs along the axis of the Endeavour Segment while Lines 3, 7, 8, and 9 were positioned to cross the four vent fields known at the time of the cruise: Salty Dawg, High Rise, Mothra, and Main Endeavour, respectively.

The MCS data for this study were collected using the *R/V Maurice Ewing*'s 6-km-long, 480 channel Syntron digital streamer with hydrophone group spacing of 12.5 m, maintained at a depth of ∼7.5 m. The seismic source was a 3005 cu. in. airgun array, also towed at a nominal depth of 7.5 m, which fired every 37.5 m. For each shot, data were recorded for 10.24 seconds. A 4 ms sampling interval was used for lines focused on studying the ridge axis and a 2 ms sampling interval was used on the long, sediment-covered ridge-flank lines which are presented elsewhere [*Nedimovic et al.*, 2005].

Table 3.1 summarizes the processing sequence applied to the MCS data. Dip-moveout migration and dip filtering were performed on all cross-axis lines to eliminate side-scattered energy from seafloor topography [*Kent et al.*, 1996]. The axis-parallel lines were associated with smoother topography and less scattering, which made pre-stack dip filtering unnecessary for these lines. Although dip filtering was not applied to the along-axis lines, our interpretation is limited to events that are consistent between the cross and along-axis lines, so we are confident that those events are not out-of-plane noise. A post-stack finite difference time migration was applied to all cross-axis lines using the 1-D crustal velocity function compiled by *Wilcock et al.* [2002] from earlier Endeavour reflection and refraction seismic experiments [*Rohr et al.*, 1988; *Cudrak and Clowes*, 1993] hung from the seafloor. We processed all of the Endeavour segment lines, but present only the most relevant subset in this paper.

3.4 Results

3.4.1 Along-Axis Seismic Structure

Layer 2a

The stacked along-axis Line 14 (Figure 3-6) shows a strong continuous event throughout the line at a two-way travel times (twtt) of 140–500 ms below the seafloor. We interpret this event as marking the base of seismic layer 2a, which probably corresponds to the transition from volcanic extrusives above to predominantly dikes below (layer 2b) [*Harding et al.*, 1993]. The on-axis layer 2a is thin (140–270 ms twtt) beneath the northern part of

Table 3.1: Data processing sequence and parameters.

Processing Step	**Parameters**
Geometry:	
CMP gather	80-fold, 6.25 m CMP interval
Trace editing:	
Hand-edit bad channels	
Automatic spike detection	0.5 s windows, 1.25-2.75 s twtt on each trace
DMO-based suppression of scattered energy:	
NMO	1500 m/s (water velocity)
Bottom mute below first multiple	
DMO f-k dip filter	apparent dips > 2 ms/trace
Remove NMO	1500 m/s
Stacking:	
Band-pass filter	5–30 Hz, 12 db/oct.
Velocity analysis	every 100 CMP
NMO Mute	stretch and surgical
Stack	
Time migration:	
Band-pass filter	5-30 Hz, 12 db/oct.
Top mute above seafloor	
Finite-difference algorithm[a]	maximum dip 5 ms/trace, layer thickness 50 ms
Display:	
Band-pass filter	5-30 Hz, 12 db/oct.
Top mute above seafloor	
Bottom mute below first multiple	
AGC for Stack plots	200 ms window
Exponential gain for Migrated plots	24 db amplitude increase from 0–0.5 s below the seafloor

[a] Algorithm of *Lowenthal et al.* [1976].

the Endeavour Ridge and then thickens systematically up to almost 500 ms twtt south of the mid-segment axial high (Figure 3-7a). The 2a event can be traced all the way to the northern end of Line 14, but disappears to the south of the mid-segment axial high. The southern disappearance of the layer 2a event may be related to the overlap between the Endeavour Segment and the Northern Symmetric Segment at the Cobb Offset (Figure 3-2).

AMC

The Line 14 section (Figure 3-6) also shows a clear mid-crustal reflection under the shallowest section of the spreading segment at two-way travel times of 0.9–1.4 s below the seafloor. This reflector is interpreted as the top of an axial magma chamber reflection based on its polarity (presented below) and its similarity in geometry and reflection character to AMC reflections imaged and studied extensively along both the northern [*Kent et al.*, 1993a, b; *Collier and Singh*, 1997, 1998; *Carbotte et al.*, 2000] and southern [*Kent et al.*, 1994; *Hooft et al.*, 1997] East Pacific Rise, along the Galapagos Spreading Center [*Detrick et al.*, 2002b; *Blacic et al.*, 2004], at the Valu Fa Ridge, Lau Spreading Center [*Collier and Sinha*, 1992; *Jacobs et al.*, 2003], and along the Southeast Indian Ridge [*Baran et al.*, 2005].

The AMC reflector appears segmented into four or five sections, from south to north between CMPs 5500–6100 at two-way travel times (twtts) of 4.7–4.4 s, between CMPs 6600–6950 at twtts of 4.2–4.1 s, between CMPs 6900–7100 at twtts of 4.2–4.1 s, between CMPs 7100–8300 at a travel time of 3.9–4.0 s, and a weak but possible AMC event between CMPs 8900–9500 at traveltimes of 4.1–4.3 s. The apparent overlap of the second and third events is likely an artifact of diffraction effects around the CMP 6900-7100 event. CMP gathers of data in the CMP 8900–9500 range show some sub-seafloor reflections, but they are often overwhelmed by scattered energy from the seafloor and our identification of the northernmost event as an AMC reflection is therefore tentative. This gives the axial magma chamber a total possible along-axis extent of 16–24 km, depending on whether the weak, northernmost event is included. The reflections seem more characteristic of a segmented series of magma lenses than a continuous magma body, however this could be an artifact of streamer feathering [*Nedimovic et al.*, 2003], seafloor topography, or the inherent problems of imaging a narrow 3-D body with a single profile. The apparent length scale of the segmentation is consistent with that observed at other well-studied ridges [*Collier and*

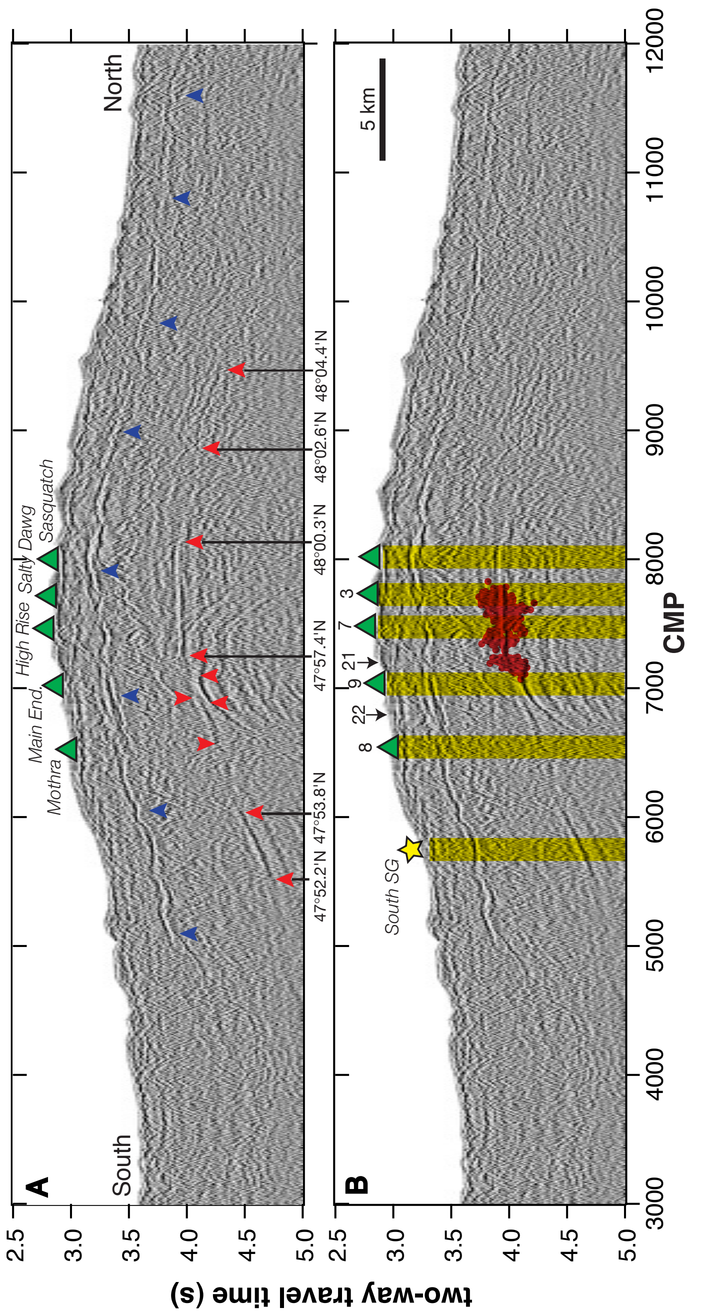

Figure 3-6: Both (A) and (B) show the same stack of along–axis Line 14. Green triangles show locations of the five large hydrothermal vent fields. (A) Blue arrows indicate the seismic layer 2a event and red arrows indicate the segments of the axial magma chamber reflection. Latitude labels show the extent of the southernmost, northernmost, and shallowest AMC segments. B) Red circles show relatively relocated microseismicity hypocenters within 0.5 km of the line [*Wilcock et al.*, 2002]. Numbers label points where Line 14 intersects cross-axis lines. Yellow star shows the location of the southern supergather. Yellow highlights indicate regions of the subsurface underlying known high-temperature hydrothermal vent fields and the southern supergather.

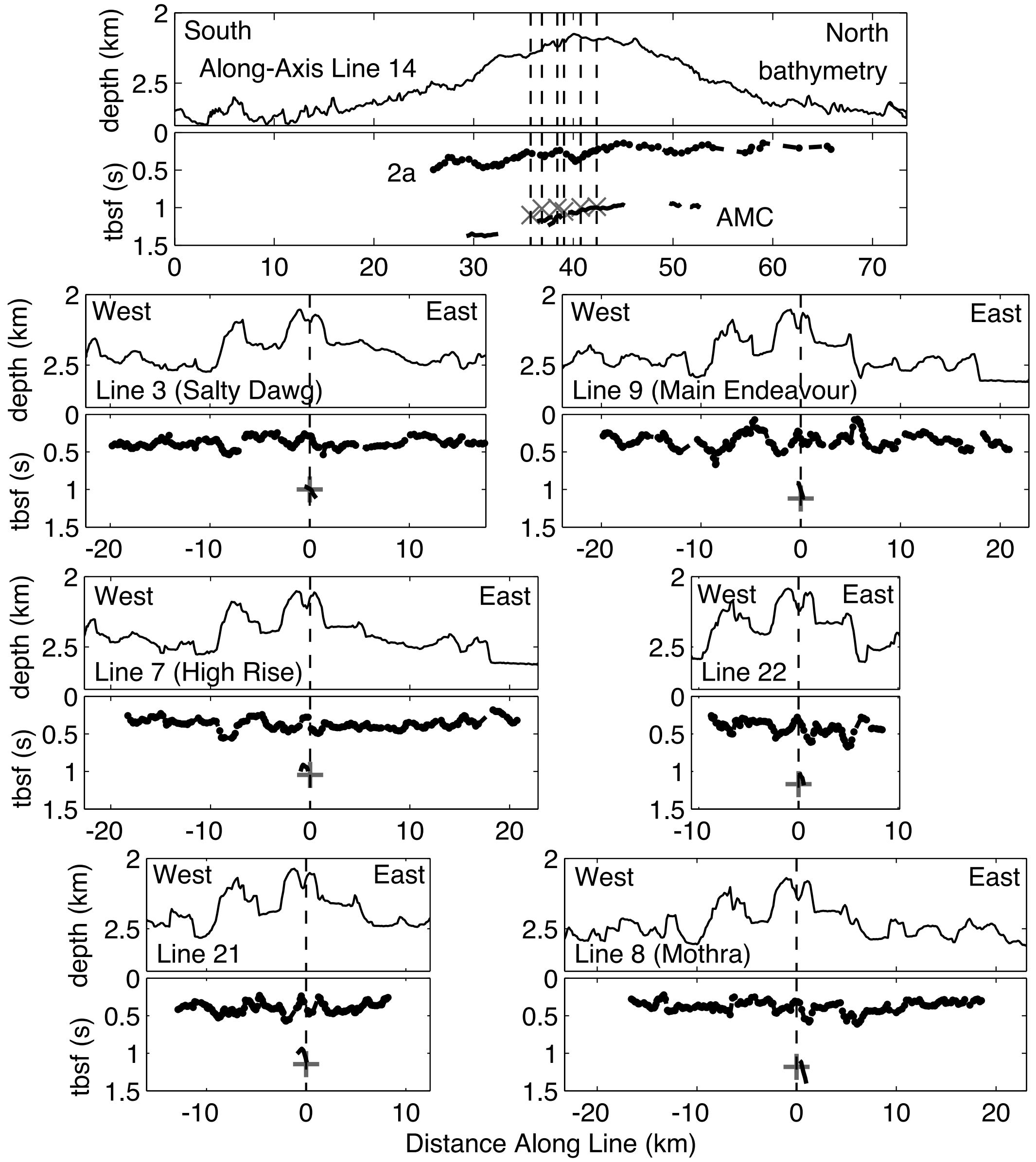

Figure 3-7: Bathymetry (upper panel) and two-way traveltimes below the seafloor (tbsf) for 2a (upper black dots) and AMC picks (lower black dots) from stacked Line 14 and migrated cross-axis seismic sections (Figures 3-6 and 3-10). Vertical dashed lines show the intersections of along and cross-axis lines. Gray "x" marks on along-axis Line 14 show the tbsf of AMC picks on cross-axis lines where they intersect with Line 14 (from left to right: Lines 8, 22, 9, 21, 7, and 3). Gray crosses show the tbsf of the AMC from Line 14 where it intersects each cross axis line.

Sinha, 1992; *Kent et al.*, 1993a; *Hooft et al.*, 1997; *Carbotte et al.*, 2000; *Blacic et al.*, 2004; *Baran et al.*, 2005].

The thickest axial layer 2a occurs above the deepest part of the AMC (Figures 3-6 and 3-7). This is consistent with the predicted positive correlation between AMC depth and 2a thickness due to the ability of a magma lens under higher pressure to push more magma to the surface [*Buck et al.*, 1997]. Such a correlation has also been observed at other ridges (e.g. *Blacic et al.* [2004]).

3.4.2 Cross-Axis Seismic Structure

Figure 3-8 shows the full length of a single cross-axis stacked section (Line 3), displaying the off-axis layer 2a variability and an example of weakly-imaged Moho. Figure 3-9 shows the central portion of all the stacked sections which sample the Endeavour axial magma chamber (Lines 3, 7, 21, 9, 22, and 8, from north to south) and Figure 3-10 shows the migrated versions of those same stacked sections. We present both the stacked and migrated sections because the AMC reflector is better imaged on the stacks while the layer 2a event is better imaged on the migrated sections. The migration process collapses diffractions from the edges of the magma chamber reflection but also introduces artifacts which make it more difficult to pick the sub-horizontal AMC reflections. Seismic layer 2a events and AMC reflections are picked from the along and cross-axis lines and displayed along with bathymetry in Figure 3-7.

Layer 2a

A strong, continuous seismic layer 2a event can be seen on the stacked (Figures 3-8 and 3-9) and migrated (Figure 3-10) seismic sections. Figure 3-7 shows that the mean layer 2a thickness perpendicular to the Endeavour Ridge is relatively constant with mean values for each line between 350 and 420 ms two-way travel time below the seafloor (tbsf) and standard deviations for each line ranging between 70 and 100 ms. These results are consistent with results of the seismic refraction study on the Endeavour Segment reported by *Cudrak and Clowes* [1993]. Visual inspection of Figure 3-7 shows some level of correlation between bathymetry and 2a thickness with thicker 2a sometimes occurring under the shallower bathymetry associated with the axis-parallel volcanic ridges. This is most clearly evident on Lines 3, 7, and 9 where thicker 2a seems to occur under the volcanic ridge ∼7–9

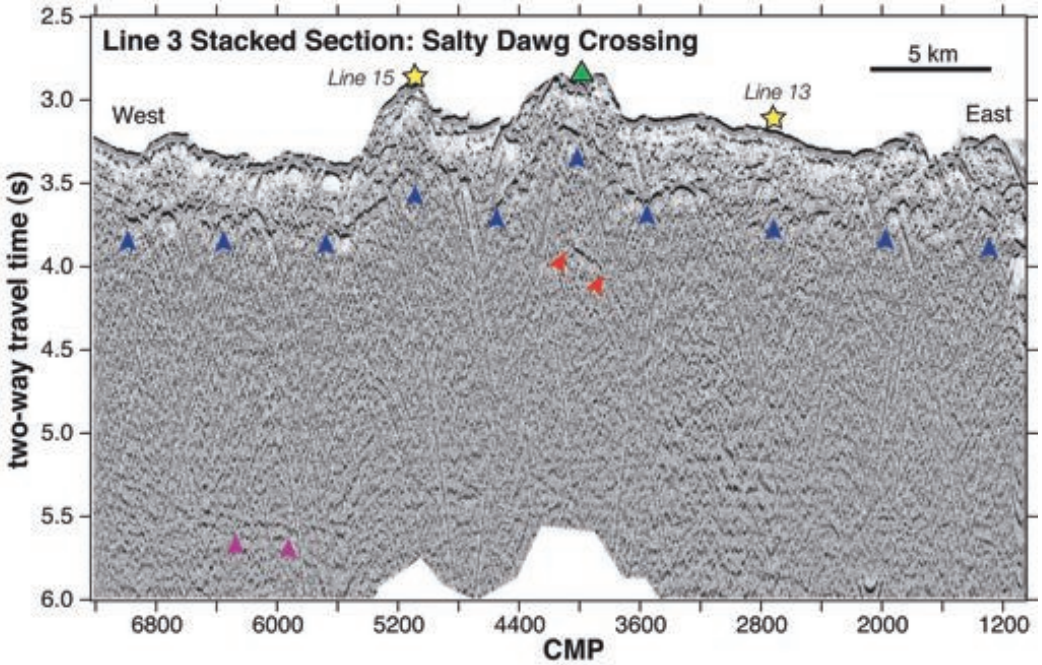

Figure 3-8: Stack of cross-axis Line 3. Triangle shows the location of the Salty Dawg hydrothermal vent field. Stars shows where axis–parallel Lines 13 and 15 cross Line 3; the Line 15 and Line 13 supergathers are located to the northeast of these intersections (see Figure 3-3). Blue arrows indicate the seismic layer 2a event, red arrows at ∼4.0 s twtt indicate the AMC reflection, and magenta arrows at ∼5.7 s twtt indicate a probable Moho reflection.

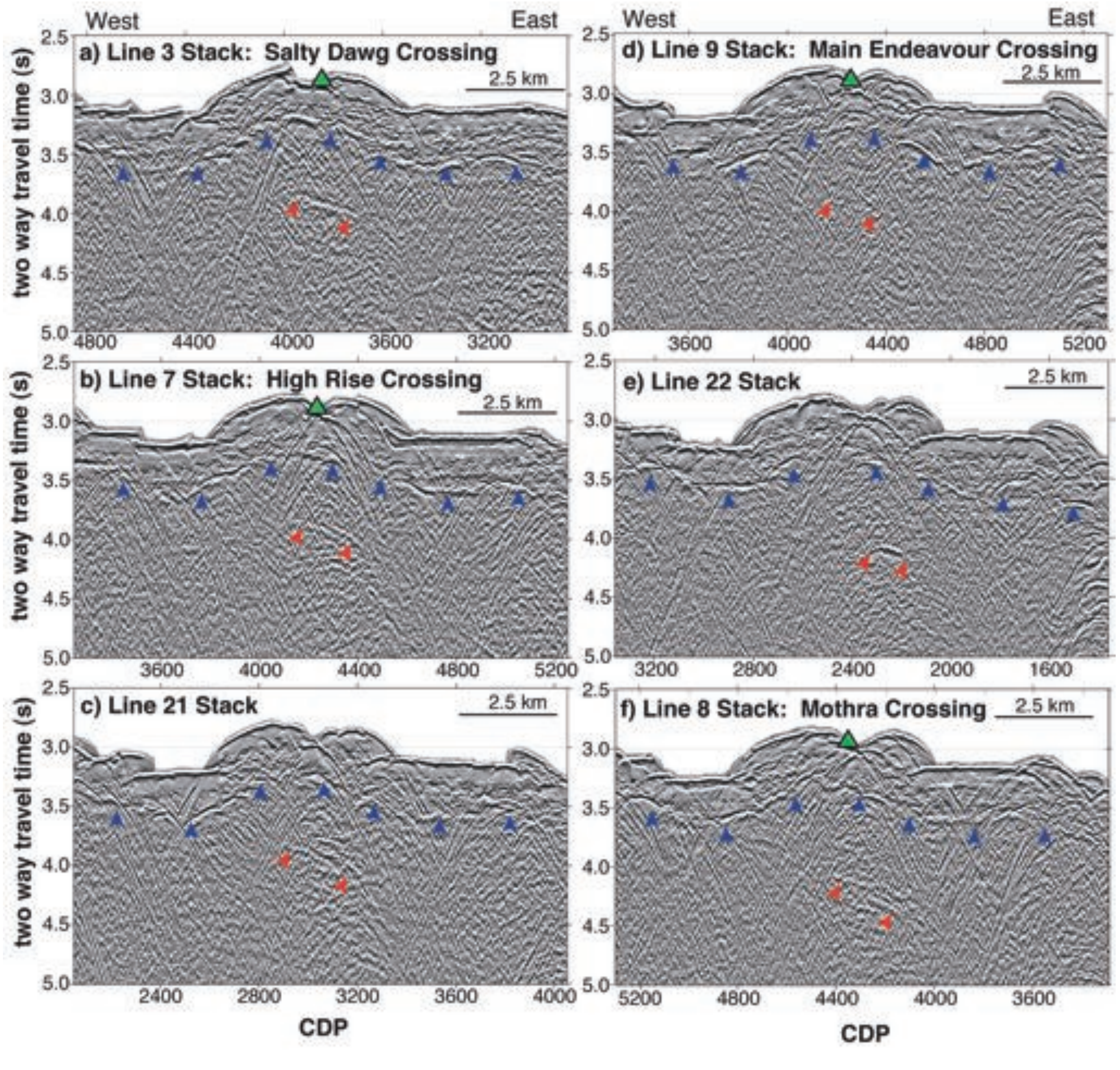

Figure 3-9: Stacks of cross–axis Lines 3, 7, 21, 9, 22, and 8 (in order from north to south). Triangles shows location of the hydrothermal vent fields. Blue arrows indicate the seismic layer 2a event and red arrows indicate the AMC reflection.

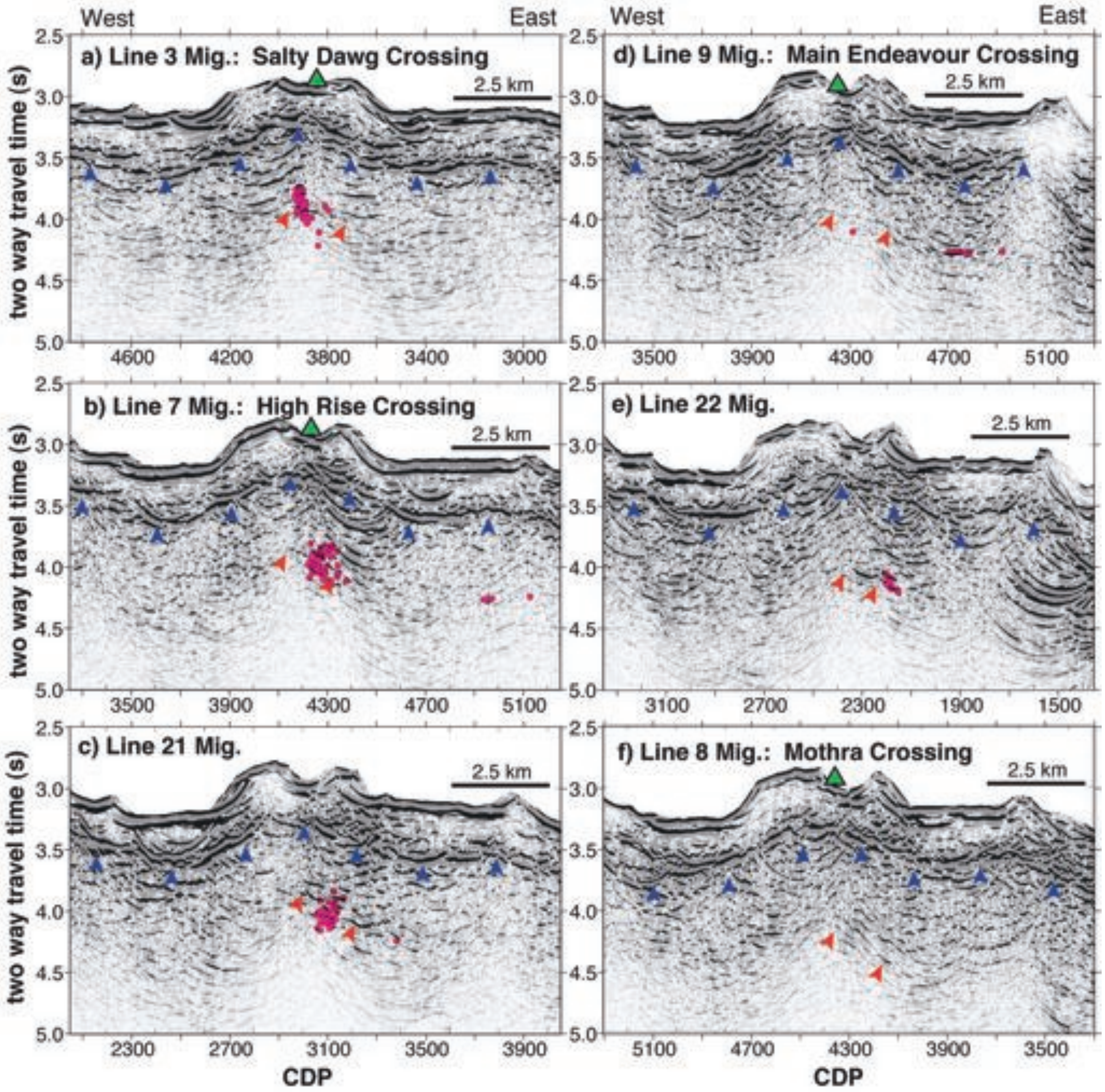

Figure 3-10: Migrations of cross–axis Lines 3, 7, 21, 9, 22, and 8 (in order from north to south). Triangles shows location of the hydrothermal vent fields. Blue arrows indicate the seismic layer 2a event and red arrows indicate the AMC reflection. Red circles show relatively relocated microseismicity hypocenters within 0.5 km of each line [*Wilcock et al.*, 2002].

km to the west of the axis.

AMC

The stacked and migrated cross-axis lines in Figures 3-8, 3-9, and 3-10 show mid-crustal AMC reflections at two-way travel times consistent with those of the AMC on the along-axis Line 14 (Figure 3-6). The cross-axis AMC reflections are narrow (0.5 – 1.2 km wide) and they tend to dip from shallower depths under the ridge axis to greater depths under the eastern flank of the ridge axis. Moving from north to south, the AMC events for Lines 3, 7, 21, and 9 all appear at a range of two-way travel times between 0.9 and 1.1 s below the seafloor, while the AMC events are progressively deeper for Line 22 (1.0–1.2 s tbsf) and Line 8 (1.1–1.4 tbsf). This implies that magma chamber depths below the Salty Dawg, High Rise, and Main Endeavour vent fields are similar while the magma chamber beneath the Mothra vent field is significantly deeper, which is consistent with the AMC imaged on along-axis Line 14 (Figure 3-6).

The AMC event has the highest amplitudes on Line 3, which crosses the Salty Dawg vent field, and Line 22, which crosses the axis between the Main Endeavour and Mothra vent fields. The event is weaker on the other lines. It is probable that large lateral velocity changes due to rough seafloor topography for the cross-axis lines result in complex ray paths that cannot be modeled using the simple two-way travel time reflection equation that was developed for at most gently dipping stratigraphy and smooth continuous interfaces. This would lead to poor and variable signal alignment (from CMP to CMP) before stack and variable signal strength (from CMP to CMP and from one line to another) of the AMC reflection on stacked sections. Furthermore, we show that the AMC is dipping east on all cross axis lines, which may have a significant impact on the strength of the AMC reflection. Pre-stack migrations or three-dimensional seismic studies may be required to better image the amplitude variability between the different cross-axis lines.

Moho

A Moho reflection is weakly visible in a few locations on the cross-axis Lines 3, 7, 8, and 9. One specific example is highlighted in Figure 3-8. In general, the Moho event appears at 2.0–2.3 s twtt beneath the seafloor on the Endeavour cross-axis lines. This is consistent with the weak, very discontinuous, low-frequency Moho reflection event observed at 2.1–2.3

s twtt at the Cleft Segment of the Juan de Fuca Ridge by *Canales et al.* [2005] and the Moho events observed by *Nedimovic et al.* [2005] for long cross-axis lines which sample the Juan de Fuca Ridge flanks.

3.4.3 Velocity Analysis

To determine the Endeavour Segment upper crustal velocity structure we modeled the travel times of the main seismic arrivals observed in the data. One dimensional upper crustal velocities were forward-modeled [*Zelt and Smith*, 1992] at three on-axis locations along Line 14 and two off-axis locations (Figure 3-3). Two of the three on-axis locations were chosen to coincide with the Salty Dawg and Main Endeavour vent sites. The third was chosen at a location over the southern segment of the AMC in order to investigate possible differences between the main axial-high magma body and the deeper reflector to the south. The two off-axis locations were modeled using data from the axis-parallel Lines 13 and 15 in order to minimize data complexity due to topographic effects. Both off-axis velocity analysis locations are positions close to the Line 3 profile (Figure 3-8), one of the highest quality cross-axis profiles.

To improve signal-to-noise ratios and allow easier identification of the main seismic arrivals, 5-fold constant-offset stacks (supergathers) were created at each location. For each supergather, the two-way travel time of key arrivals were handpicked on all traces where they were visible (an example is shown in Figure 3-11). These events included the seafloor reflection, the retrograde refraction from the velocity transition at the base of layer 2a, and the refracted wave in seismic layer 2b on all supergathers. In addition, on the along-axis supergathers an intermediate event within layer 2a (labeled “P1P”) and the reflection from the top of the mid-crustal axial magma chamber reflector were identified and picked. The resulting velocity functions are shown in Figure 3-12.

Layer 2a thicknesses in our velocity models are systematically greater (~200 m) than the thickness observed in the seismic reflection sections at the location of the velocity models, probably due to difficulty in picking the first arrival on the supergather sections. The layer 2a velocities of our off-axis velocity models (2.50–2.83 km/s) are comparable to those of the Cudrak and Clowes model (2.56–2.76 km/s). Uppermost layer 2a velocities of our on-axis models are significantly slower (1.80 km/s on Main Endeavour and the Deep AMC supergathers, 2.06 km/s under Salty Dawg) than the off-axis 2a velocities. However, the

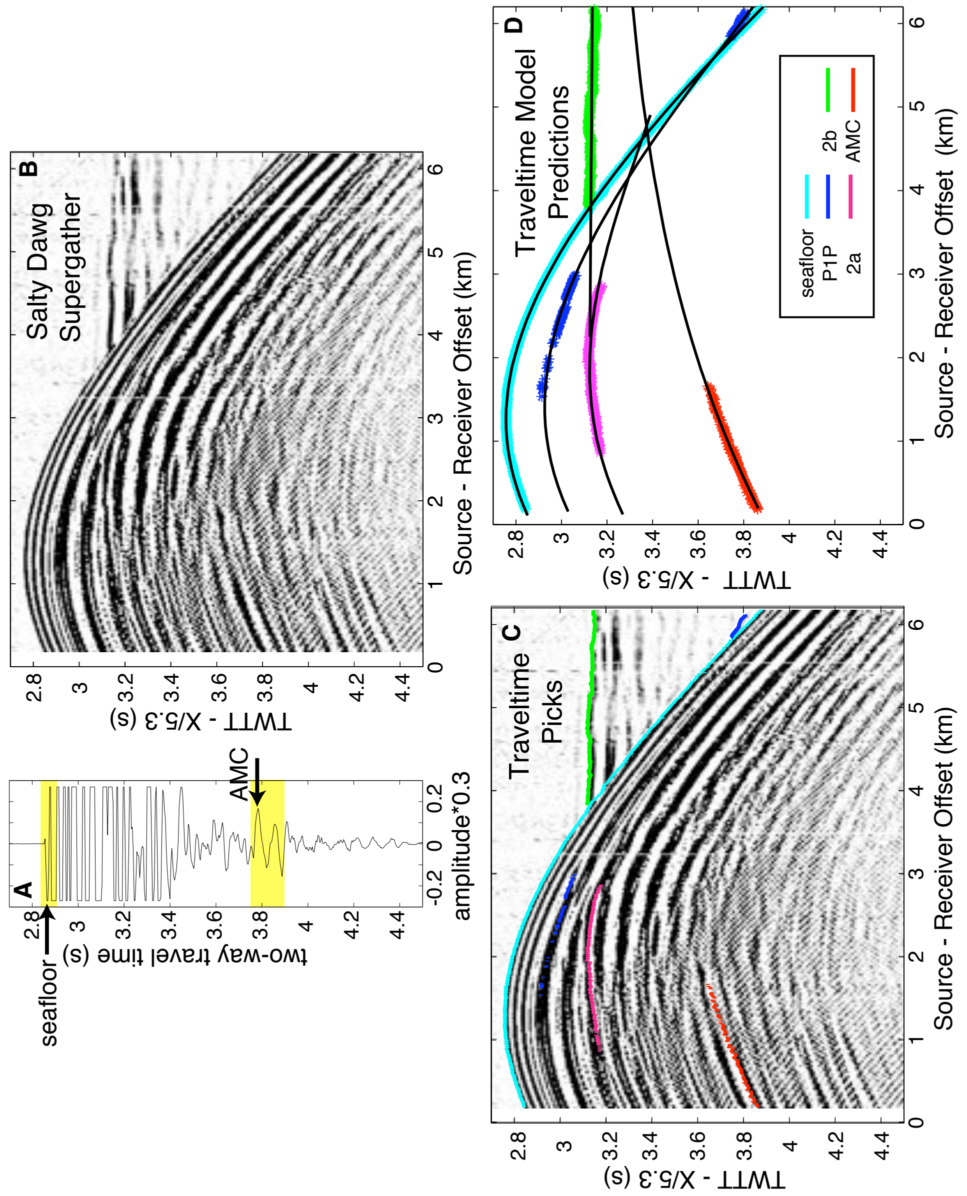

Figure 3-11: Salty Dawg supergather modeling and AMC polarity. A) Trace created by stacking 0–1.5 km offset traces from the supergather shown in (B) with normal moveout correction and without any filtering. Yellow boxes highlight the negative polarity of seafloor reflection and the opposite, positive polarity of the AMC reflection. The onset of the AMC event is indicated by the increase in amplitude and change in the frequency content of the signal. B) Supergather of along-axis Line 14 data with 30 CMPs located above the Salty Dawg vent field. C) Same supergather overlain with the picks used to forward model the velocity structure of the upper crust at this location (same color code for events as in part D). D) Supergather picks from (C) with ±10 ms errors and travel times predicted from the one-dimensional Salty Dawg supergather velocity profile (black lines).

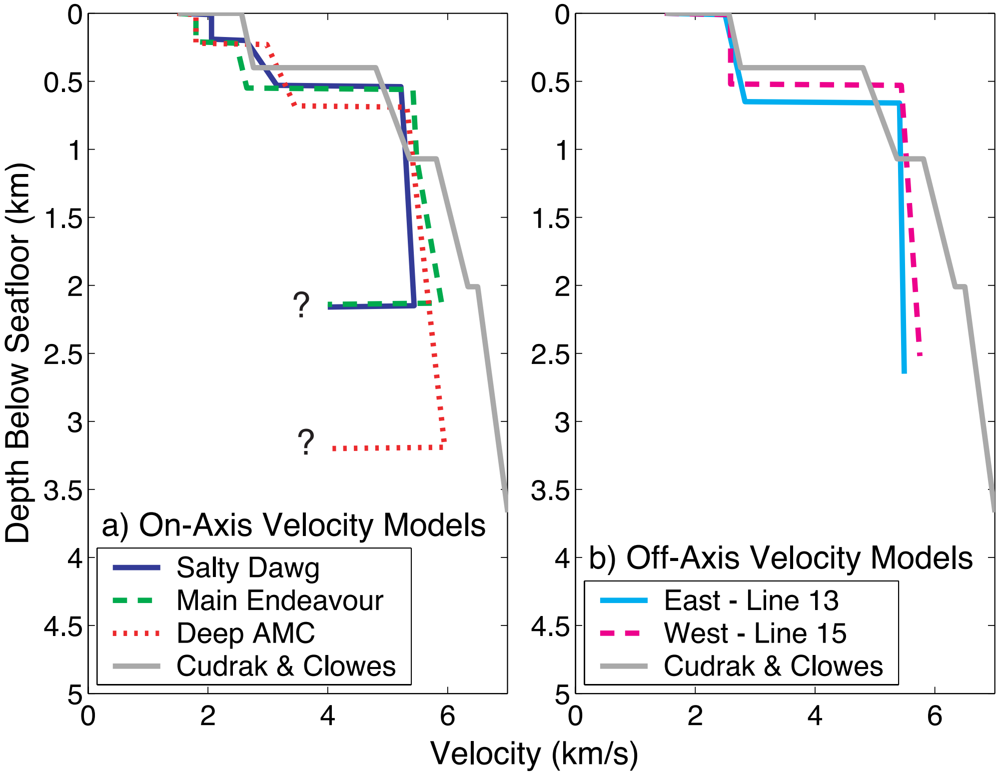

Figure 3-12: One-dimensional Endeavour velocity structures. a) Blue, green, and red lines show velocity profiles derived from forward travel time modeling of on-axis supergathers above two vent fields (Salty Dawg and Main Endeavour) and the southern, deep portion of the AMC. Velocities are only constrained by the supergather to the top of the AMC-associated negative velocity jump. Gray line shows the *Cudrak and Clowes* [1993] average one-dimensional Endeavour velocity structure for comparison. b) Cyan and magenta lines show velocities from forward modeling of off-axis Lines 13 and 15 supergathers. The gray line again shows the *Cudrak and Clowes* [1993] velocity model for comparison.

on-axis velocities at the bottom of layer 2a are somewhat faster (2.47–3.45 km/s) than those off-axis.

The Salty Dawg, Main Endeavour, and Southern AMC supergather velocity functions have total seismic layer 2a thicknesses of 530, 550, and 680 meters, respectively. The Line 13 and Line 15 supergathers have total layer 2a thicknesses of 650 and 520 meters, respectively. The depth to the axial magma chamber is 2.1, 2.1, and 3.2 km below the seafloor on the Salty Dawg, Main Endeavour, and Deep AMC supergathers respectively. The thickness of the axial magma bodies and the velocity structure below the AMC in Figure 3-12a are unconstrained by the travel time modeling, since we have no reflectors beneath the AMC to give us further information about the velocity structure at depth.

3.4.4 Variation of Layer 2a Thickness

Two-way travel times for layer 2a observed on the reflection profiles were converted into depth using our velocity functions (Figure 3-12). Figure 3-13 shows that the thickness of crustal layer 2a varies between 180 and 630 m on the along-axis Line 14. The mean ± standard deviation 2a thickness on all the cross-axis lines is 500±110 m, and results for each line are presented in Table 3.2. Our results indicate that layer 2a thickness is highly variable without a clear pattern of off-axis thickening (Figure 3-14). This is unlike the Cleft and Vance segments of the southern Juan de Fuca Ridge [*Canales et al.*, 2005], the inflated portions of the Galapagos ridge [*Blacic et al.*, 2004], and the East Pacific Rise [*Harding et al.*, 1993] where the 2a thickness is seen to increase significantly off-axis.

The range of layer 2a thicknesses measured on the Endeavour Segment lines presented here is 90–880 meters. We report layer 2a thicknesses throughout this paper as mean ± standard deviations because the extremes of this range are more likely representative of either the effects of faulting or imaging issues associated with steep bathymetry and the wide angle nature of the 2a event than actual volcanic production of the ridge. This can be seen by examining Figure 3-13, especially the profile of Line 9, where the extremes of 2a thickness are seen to occur underneath the faults bounding the off-axis volcanic ridges. While the means and standard deviations are more useful for trying to understand systematic variations between seismic lines, it is important to note that faulting is probably one of the factors which contributes to the large variability observed in Endeavour layer 2a thickness.

In addition to the faulting contribution to layer 2a variability, the axis-parallel bathymet-

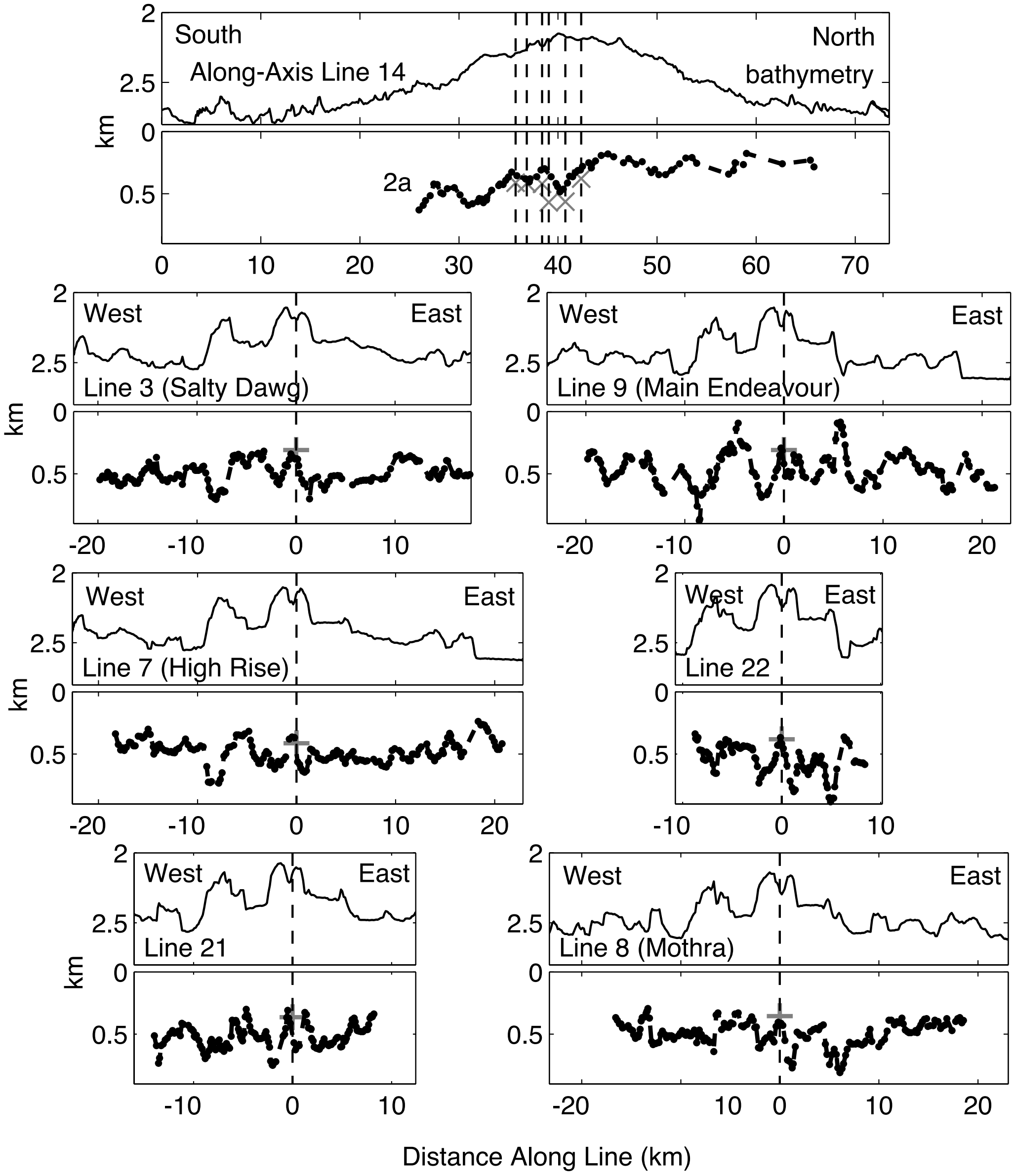

Figure 3-13: Bathymetry (black line, top panels) and 2a depths below the seafloor (black dots, bottom panels) from stacked Line 14 and migrated cross-axis sections (Figures 3-6 and 3-10). Vertical dashed lines show the intersections of along and cross-axis lines. Gray "x" marks on along-axis Line 14 show the depth below the seafloor of layer 2a picks on cross-axis lines where they intersect with Line 14 (from left to right: Lines 8, 22, 9, 21, 7, and 3). Gray crosses show the depth below the seafloor of the AMC from Line 14 where it intersects each cross axis line. Picks were converted from two-way travel time (twtt) to depth using the on and off-axis average forward-modeled supergather velocity functions Figure 3-12 as described in the text.

Table 3.2: Summary of 2a, AMC, and Moho observations in two-way travel time below the seafloor (tbsf) and depth below the seafloor. Two-way travel time is converted to depth using layer 2a (2.54 km/s on-axis and 2.63 km/s off-axis) and layer 2b (5.53 km/s) interval velocities derived from the supergather velocity functions (Figure 3-12). Layer 2a observations for each line are given as mean ± standard deviation, while AMC and Moho observations are given with the range of observations.

	Layer 2a Thickness		**Axial Magma Chamber**			**Moho**
	tbsf (s)	depth (m)	tbsf (s)	depth (km)	width (km)	tbsf (s)
Line 14 (Along-Axis)	0.30±0.09	380±120	0.9–1.4	2.2–3.3	16–24	
Line 3 (Salty Dawg)	0.39±0.08	510±100	1.0–1.1	2.2–2.4	1.2	2.0–2.2
Line 7 (High Rise)	0.37±0.07	480±90	0.9–1.0	2.1–2.3	0.8	2.1–2.4
Line 21	0.40±0.07	520±100	0.9–1.1	2.2–2.5	1.0	
Line 9 (Main Endeavour)	0.35±0.11	460±140	0.9–1.1	2.1–2.5	0.8	1.9–2.3
Line 22	0.42±0.09	550±120	1.0–1.2	2.3–2.6	0.4	
Line 8 (Mothra)	0.38±0.07	490±100	1.1–1.4	2.5–3.1	0.7	2.0–2.3

ric highs often appear to be associated with a thicker layer 2a (Figures 3-13 and 3-14). This correlation between bathymetric highs and thicker layer 2a is consistent with the banded Endeavour upper crustal velocities observed by *Barclay and Wilcock* [2004] which show a correlation between slower velocities and bathymetric highs. The regions of thicker layer 2a and bathymetric highs could correspond to the intermittent periods of magma supply predicted by the model of *Kappel and Ryan* [1986]. Alternatively, these regions could correspond to the axial volcanic rift (AVR) building phase of the *Carbotte et al.* [2006] model, which assumes more steady-state magma supply and predicts periodic topography through the interaction between dike-induced stress pertubations and tectonic extensional stresses.

3.4.5 AMC Depth

The depth profile of the magma chamber reflection was found by picking the AMC event on Line 14 stacked and the cross axis stacked and migrated lines and converting the two-way travel times into depth using the average layer 2b interval velocity from the three on-axis supergather velocity models (5.55 km/s), in combination with the depth of the layer 2a picks above each AMC pick. The map-view locations of these AMC picks are plotted on Figure 3-3. The depth of the AMC varies between 2.2 and 3.3 km below the seafloor on the along-axis line while the AMC depths on the cross axis lines vary between 2.1 and 3.1 km below the seafloor (details in Table 3.2).

A 200–600 meter range of AMC depths is observed on each cross-axis line due to the dipping nature of the AMC reflector. Using the depth range and the width of each cross-axis AMC event, dips between 8 and 36° are calculated. The dips increase from the northern lines to the southern ones, which reflects the narrower AMC event on (southern) Lines 22 and 8 and the greater depth range of the AMC picks from Line 8 (Table 3.2). The 36° dip calculated for Line 8 is surprisingly high, however it reflects picks from one of the weaker migrated AMC events (Figure 3-10) and therefore may be exaggerated due to the difficulty in picking that event. The 22° dip calculated for Line 22 represents a much more robust event (Figure 3-10), however its relative narrowness results in a much higher dip for AMC depth ranges similar to those observed on the northern lines.

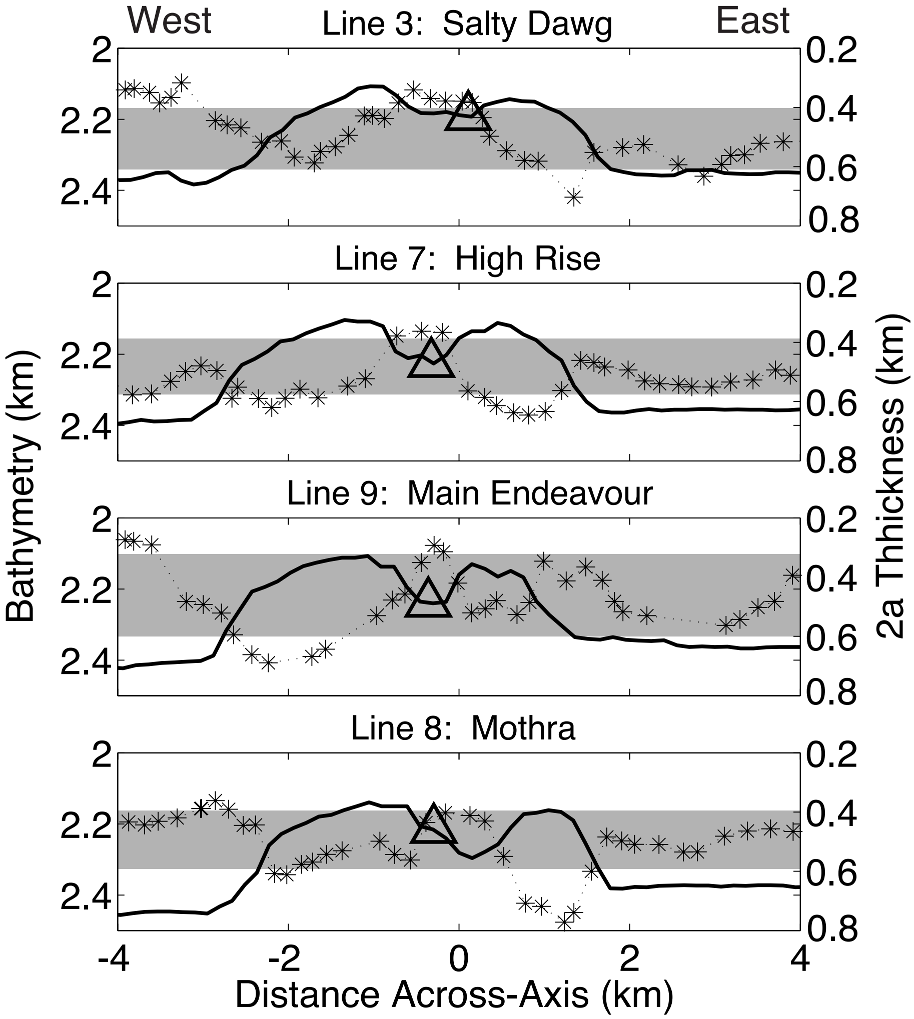

Figure 3-14: Bathymetry (black line) and 2a depths below the seafloor (black stars) from four stacked and migrated cross-axis lines, zoomed in on the central axial high. Black triangles show the location of Endeavour high temperature vent fields (personal communication, Deborah Glickson). Gray boxes show the region of mean ± standard deviation layer 2a thickness for each line.

3.4.6 Polarity of AMC Event

The polarity of a near-vertical reflection is a diagnostic difference between a cracking front and a magma chamber interface. For a cracking front associated with the downward propagation of a hydrothermally active, thermally fractured regime into a hot but solidified region, an increase in seismic velocities is expected and a reflection from such an interface would be expected to have the same polarity as the first arrival reflection from the seafloor. For an interface of solid rock over a pure melt or partially molten magma chamber, the resultant decrease in seismic velocities results in a polarity reversal for near-vertical reflections.

In order to test the polarity of the Endeavour AMC event, we took traces from the Salty Dawg supergather (Figure 3-11b) with source-receiver offsets of 0–1.5 km, applied an appropriate normal moveout correction, and summed the traces without applying any filtering at any stage. The result is shown in Figure 3-11a, where the seafloor reflection and the AMC reflection are highlighted and have opposite polarity, indicating that the AMC reflection is from a negative impedance contrast. The inversion of polarity between these two reflections reinforces our conclusion that the reflector we have identified as an axial magma chamber is not, as previously proposed, a cracking front boundary.

We attempted an amplitude-offset analysis in the intercept time - slowness (τ-p) domain to quantify the crystal versus melt content of the Endeavour AMC at the location of our three along-axis supergathers (e.g. *Collier and Singh* [1997]). Unfortunately, the AMC reflection at offsets greater than 2 km is highly disrupted by side echos from the axial graben walls (Figure 3-11b), making it difficult to differentiate between the amplitude-offset behavior expected for pure molten and partially crystalline magma chamber models.

3.5 Discussion

3.5.1 Reconciling the Endeavour AMC with Previous Seismic Studies

Previous seismic studies of the Endeavour Segment failed to definitively locate an axial magma chamber, however the multichannel reflection profile collected by *Rohr et al.* [1988] does show the same mid-crustal axial reflection at the same two-way travel time that we image. It was not interpreted as an AMC reflection due to the uncertainty in the polarity of the AMC and the lack of a velocity anomaly in the available seismic refraction data.

Previous seismic refraction data [*Cudrak et al.*, 1987; *Cudrak*, 1988; *White and Clowes*, 1990; *Cudrak and Clowes*, 1993] were only sensitive to zones of partial melt (1.5 - 2.0 km/s velocity reduction relative to surrounding 6.0-6.5 km/s P-wave velocity) with cross-axis dimensions greater than 1 km wide and 1 km thick. This resolution would not be sensitive to a thin melt lens such as the AMC reported here (assuming the thickness of the Endeavour AMC is similar to that of the EPR melt lens [*Collier and Singh*, 1998; *Kent et al.*, 1993a]). However, the transition from layer 2c to layer 3 (commonly identified as the transition from sheeted dikes to gabbros formed by crystallization of the magma chamber) occurs at 2.01 km below the seafloor in the *Cudrak and Clowes* [1993] average one-dimensional model, which is roughly coincident with the AMC depths we find in this study.

This leaves the question of why previous refraction studies did not detect a low-velocity region, indicative of high temperatures and partial melt, in the lower crust as described for other magmatic spreading centers (e.g. *Canales et al.* [2000] and *Dunn et al.* [2001]). The resolution tests for the Endeavour tomography of *White and Clowes* [1990] show significant smearing and poor resolution for features more than 1 km below the seafloor (see *White and Clowes* [1990] Figure 14). The forward modeling of *Cudrak and Clowes* [1993] did show a decrease by 0.1-0.2 km/s in seismic layer 3 velocities for seismic waves passing under the axial ridge and attributed this to elevated temperatures but not the presence of partial melt. A new tomographic study of the Endeavour ridge would be useful in distinguishing whether the apparent absence of an EPR-like low-velocity zone under the Endeavour AMC in these prior studies is real or an artifact of data limitations.

3.5.2 Seismicity and the Axial Magma Chamber

Hypocenters of well-located microseismicity from a 55–day deployment of 15 ocean bottom seismometers (OBSs) on the central Endeavour Ridge [*Wilcock et al.*, 2002] are projected onto our stacked and migrated sections if they are within 0.5 km of our lines (Figures 3-6 and 3-10). The positions of the OBSs used to locate the seismicity are shown in Figure 3-3. We use the events which have been relatively relocated, meaning that closely spaced earthquakes with similar waveforms were cross-correlated to generate self-consistent travel time picks whose relative errors are much smaller than the absolute errors of individual picks. This results in small relative location errors between events within a swarm (on the order of 100 m) while absolute hypocenter location errors remain on the order of 0.5 km.

Most axial earthquakes are concentrated in a depth range of 1.5–2.7 km. These depths

are translated to a two-way travel time range of 0.7–1.1 s below the seafloor with the velocity function that was used in locating the hypocenters. The seismicity is mostly clustered above the AMC reflector. The appearance of seismicity occurring within the (presumably non-brittle) regime of the magma chamber is an artifact of location uncertainties and the projection of 3D event locations onto 2D lines, which ignores the topography of the dipping magma chamber observed in all cross-axis lines (Figure 3-10). A 3D graphic of the seismic lines and the seismicity is available at the Ridge 2000 Data Portal:
http://www.marine-geo.org/link/entry.php?id=JdF:Endeavour_VanArk.

In general the seismicity is distributed diffusely within the observed depth range, however the cross-axis line which underlies the Salty Dawg vent field also shows seismicity localized along a steeply dipping fault-like plane. The diffuse axial seismicity localized above the AMC reflector may indicate cracking activity in a conductive lid above the melt lens. This would be consistent with the observation that focal mechanisms for axial earthquakes had sub-horizontal tension axes oriented in all directions except parallel to the ridge, interpreted as indicating a stress field influenced equally by ridge spreading and hydrothermal cooling [*Wilcock et al.*, 2002].

The axial seismicity seems to be confined to the region above the shallowest portion of the magma chamber (Figures 3-6 and 3-10), with much activity beneath the Salty Dawg and High Rise vent fields, a little below the Main Endeavour vent field, and no events beneath the northernmost (Sasquatch) and southernmost (Mothra) vent fields. This may, however, be a sampling bias induced by the seismometer array geometry, variable instrument coupling to the seafloor within the array, and short two month time-span of the OBS study. Preliminary results of the new Keck Observatory on the Endeavour Ridge [*Wilcock et al.*, 2004] show a similar cluster of hypocenters, but the cluster seems to have moved south slightly with more activity under the Main Endeavour and Mothra vent fields and less under the Salty Dawg vent field.

For two similar experiments in 1995, Endeavour segment microearthquakes were both more numerous and deeper than those observed at the East Pacific Rise, yet the earthquake activity at the two ridges seemed to have similar source mechanisms. In a three month OBS deployment at 9°50'N on the EPR, *Sohn et al.* [1998, 1999] detected 283 local microearthquakes which were found to have seismic moments of 10^7–10^9 N-m (moment magnitude M $\approx$ -1– 0). At the Endeavour segment, 1750 microearthquakes with moments of 10^9–4x10^{13} N-m (moment magnitude M $\approx$ 0–3) were located by *Wilcock et al.* [2002] with data from a shorter, 55-day OBS deployment. The EPR hypocenters were located above the 1.5 km deep AMC reflection imaged at that location, clustered between 0.7 and 1.1 km depth. The focal mechanisms and the correlation of earthquake swarms with changes in the chemistry of vents above them suggest that the EPR microseismic events arise from thermal stresses at the base of the hydrothermal system in the shallow crust [*Sohn et al.*, 1998, 1999]. The Endeavour Segment microseismicity is also clustered above the observed magma chamber and also has focal mechanisms suggestive of a thermal cracking mechanism. However, due to the greater depth of the Endeavour AMC, the axial earthquakes are correspondingly deeper [*Wilcock et al.*, 2002]. Preliminary results from more recent OBS experiments at the EPR [*Weekly et al.*, 2005] and Endeavour [*Wilcock et al.*, 2004] indicate that seismicity rates vary greatly over time and are likely related to temporal changes in stress and thermal conditions above the magma lens.

3.5.3 Hydrothermal Activity and the Axial Magma Chamber

Our results show that all five large, high-temperature Endeavour hydrothermal vent fields are underlain by an axial magma chamber (Figures 3-6 and 3-10). We therefore looked for correlations between the geometry and properties of the AMC and the location and activity of the vents. The focusing of Endeavour seismicity and hydrothermal vents above the shallowest part of the AMC (Figure 3-6), combined with the cracking focal mechanisms of the microseismic events might reflect a “chimney effect” with upflow of hydrothermal fluid channeled predominantly above the shallowest areas of the magma chamber heat source. However, a hydrographic survey of the Endeavour ridge [*Veirs et al.*, 1999] found possible hydrothermal sources south of Mothra as far as 47°54’N. More exploratory studies looking for high-temperature hydrothermal outflow and their vent sources above the deeper, southern portion of the AMC (CMPs 6600–6950 on Figure 3-6, latitudes 47°52.2’ – 47°53.8’ N) would help to determine whether the apparent focusing of hydrothermal flow above the shallowest portion of the AMC is real or merely a sampling artifact.

There is no simple relationship between Endeavour magma chamber depth and vent temperatures and chlorinities (Tables 3.3) [*Butterfield et al.*, 1994; *Delaney et al.*, 1997; *Kelley et al.*, 2002]. The AMC is approximately the same depth range ($\sim$2.1–2.4 km on each cross-axis line) beneath all the Endeavour hydrothermal vent fields except Mothra

Table 3.3: Endeavour vent field temperature (°C) and chemistry (chlorinity, carbon dioxide concentration, and methane concentration in mmol/kg) organized from south to north and compared to average seawater values [*Delaney et al.*, 1997; *Kelley et al.*, 2002] and the depth of the axial magma chamber (AMC) under each vent field in kilometers.

	Seawater	**Mothra**	**Main Endeav.**	**High Rise**	**Salty Dawg**
T	2	304	330–400	315–343	297–329
Cl	540	680	40–505	420–587	710
CO_2	2.3	6	11–26	15–19	18
CH_4	0	1.5	1.5–3.4	2.8–3.4	3.3–3.6
AMC		2.5–3.1	2.1–2.5	2.1–2.3	2.2–2.4

(2.5–3.1 km), and the range of published temperatures and chlorinity values within each well-sampled vent field is as large as the differences between the fields. There might be a correlation between lower CO_2 values at Mothra and the deeper AMC below that location (Table 3.3). More observations would be useful to constrain this possible relationship. There is no clear correlation between published methane concentrations at the various vent fields and AMC depth. While many more chemical components of vent fluids have been studied within specific vent fields, especially the Main Endeavour vent field [*Lilley et al.*, 2003], cross-field observations on the large spatial scale necessary for comparison with Endeavour AMC depths have not been published.

In general, our preliminary comparison suggests that AMC depth is not a dominant factor in determining vent fluid properties. In particular, temperature and chlorinity are probably controlled instead by phase separation, subsurface mixing of hydrothermal fluids and seawater, and other complexities of the circulation path through the crust [*Butterfield et al.*, 1994; *Delaney et al.*, 1997; *Bach and Humphris*, 1999; *Kelley et al.*, 2002]. A recent study has tied the 1999 earthquake swarms to magmatic volatile signatures in Main Endeavour vent fluids [*Lilley et al.*, 2003], which indicates that magmatic diking and eruption activity may influence vent fluid properties even if the depth of the magma chamber does not (see also *Butterfield and Mossoth* [1994], *Butterfield et al.* [1997], and *Von Damm* [2000]).

3.5.4 Ridge System Comparisons

Table 3.4 presents a comparison of on and off-axis layer 2a thickness and axial magma chamber depth and width for the fast-spreading East Pacific Rise (EPR) [*Kent et al.*, 1993b, 1994;

Hooft et al., 1997; *Carbotte et al.*, 2000] and four intermediate spreading systems: the Juan de Fuca Ridge (our Endeavour segment results and *Canales et al.* [2005]), the Southeast Indian Ridge (SEIR) [*Baran et al.*, 2005], the Galapagos Spreading Center (GSC) [*Detrick et al.*, 2002b; *Blacic et al.*, 2004], and the Lau Back-Arc Spreading Centers [*Jacobs et al.*, 2003].

The Endeavour axial layer 2a thickness is greater in magnitude and variability than that of the EPR and the Vance and Cleft segments of the Juan de Fuca Ridge, however, it is similar to that of the GSC, the portions of the SEIR with a rifted axial high, and the Central Lau Spreading Center (CLSC). The Endeavour axial layer 2a is thinner than that found on the portions off the SEIR with a shallow axial valley and the Eastern Lau Spreading Center and Valu Fa Ridge (ELSC/VFR). While off-axis 2a thickening is observed for most of the ridge systems presented in Table 3.4, the Endeavour layer 2a cross-axis variability shows no such clear pattern, the western portion of the GSC has limited off-axis 2a thickening, and the rifted axial high and shallow axial valley portions of the SEIR [*Baran et al.*, 2005] are not observed to have significant off-axis layer 2a thickness increases.

Why does layer 2a thicken off-axis on some ridge systems and not on others? Several authors have suggested that the difference is due to the interplay between magma supply and ridge topography [*Mutter et al.*, 1995; *Carbotte et al.*, 1998; *Blacic et al.*, 2004; *Canales et al.*, 2005]. The ridge topography is controlled by a combination of tectonic extension, flexure, and volcanic construction. In turn, the slope of the axial high and the depth of the axial summit graben promote or hinder the flow of volcanic eruptions off-axis which leads to layer 2a thickening. Large variability in off-axis 2a thickness is found on the parts of the GSC which have a narrow (<0.8 km) AMC [*Blacic et al.*, 2004], perhaps reflecting lower magma supply. This is similar to the variability observed on all the cross-axis Endeavour lines, independent of AMC width.

The range of AMC widths observed at many different places on the mid-ocean ridge system (Table 3.4) seems to be a relatively constant ∼0.5–1.5 km, with values as low as 0.25 and as high as 4.15 on the EPR [*Kent et al.*, 1993b, 1994; *Hooft et al.*, 1997; *Carbotte et al.*, 2000]. Our Endeavour AMC width observations of 0.5–1.2 km fall within this range. The lack of correlation between spreading rate and AMC width stands in contrast to AMC depth observations, which do seem to inversely correlate with spreading rate [*Purdy et al.*, 1992]. The southern portion of the EPR (full spreading rate >15 cm/yr) has the shallowest

Table 3.4: Comparison of on and off-axis 2a thickness, AMC depth, and AMC width for various spreading ridges including the Endeavour (this study), Cleft, and Vance segments of the Juan de Fuca Ridge [*Canales et al.*, 2005], the Galapagos Spreading Center (GSC) [*Blacic et al.*, 2004], the Southeast Indian Ridge (SEIR) [*Baran et al.*, 2005], the Lau Back-Arc spreading system [*Jacobs et al.*, 2003], and the East Pacific Rise (EPR) [*Kent et al.*, 1993b, 1994; *Hooft et al.*, 1997; *Carbotte et al.*, 2000]. The full spreading rate for each ridge system is also given [*Wilson*, 1993; *DeMets et al.*, 1994; *Blacic et al.*, 2004; *Baran et al.*, 2005]. Dashes indicate that the appropriate measurement was not available for that system.

	Layer 2a Thickness		**Axial Magma Chamber**	
	on-axis (km)	off-axis (km)	depth (km)	width (km)
Galapagos Spreading Center: 4.5–5.6 cm/yr				
E. GSC[a]	0.24–0.42	0.40–0.70 on-axis	~1.0–2.5	0.5–1.5
W. GSC[b]	0.36–0.60	0.35–0.65	2.5–4.5	0.7–2.4
Juan de Fuca Ridge: 5.6–5.7 cm/yr				
Endeavour	**0.38±0.12**	**0.50±0.11**	**2.1–3.3**	**0.4–1.2**
Vance	0.30–0.35	0.5–0.6	2.4–2.7	0.6–1.7
Cleft	0.25–0.30	0.5–0.6	2.0–2.3	0.6–1.7
Southeast Indian Ridge[c]: 7.2–7.6 cm/yr				
Axial high	~0.31	thicker	~1.5	—
Rifted axial high	~0.46	same	~2.1	—
Shallow axial valley	~0.45, 0.80	same	No AMC	—
Lau Back-Arc Basin: 4.0–9.0 cm/yr				
CLSC (faster) [d]	0.38	—	1.49	—
N. ELSC [d]	0.51	—	No AMC	—
C. ELSC [d]	0.62–0.74	—	2.18–2.34	—
VFR (slower) [d]	0.66–1.00	—	2.35–2.82	—
East Pacific Rise:				
15°30'–17°N [e]	0.16–0.31	0.34–0.53	1.4–1.7	0.25–1.7
9°17'–9°53N	0.18–0.38	0.44–0.56	1.42–1.56	0.25–4.15
14°–14°30'S [e]	0.19–0.28	0.51–0.57	0.94–1.25	0.375–1.05
17°4'–20°10'S	0.20–0.33	0.35–0.62	0.76–1.55	0.375–1.54

[a] Hot spot influenced portion of the GSC – east of 92.5° W

[b] Non-hot spot influenced portion of the GSC – west of 92.5° W

[c] Results for SEIR are categorized by surface morphology of the ridge [*Baran et al.*, 2005].

[d] CLSC = Central Lau Spreading Center; axial high morphology. N. ELSC = Northern Eastern Lau Spreading Center; rifted axis. C. ELSC = Central Eastern Lau Spreading Center; rounded axial high. VFR = Value Fa Ridge; blade-like morphology due to high viscosity lavas resulting from a subduction component in the magma.

[e] The 15°30'–17°N section of the EPR has spreading rate of 8.5 cm/yr and the 14°–14°30'S of the EPR has a spreading rate >15 cm/yr.

AMC depths [*Hooft et al.*, 1997] while the non-hotspot influenced western portion of the GSC (full spreading rate 4.5–5.6 cm/yr) has the deepest AMC observed to date [*Blacic et al.*, 2004]. The Endeavour AMC is significantly deeper than the fast spreading AMC depths, but comparable to depths found along other intermediate spreading ridges with similar ridge morphologies.

A combination of spreading rate and ridge morphology seems to be a better predictor of subsurface similarities between ridges than spreading rate values alone. The Juan de Fuca Ridge has similar spreading rates to the Galapagos Spreading Center and the Southeast Indian Ridge, however, those ridge systems are both heavily influenced by nearby mantle temperature anomalies. The eastern portion of the GSC is strongly influenced by the Galapagos hot spot [*Detrick et al.*, 2002b; *Blacic et al.*, 2004], while the SEIR has strong changes in ridge morphology and subsurface crustal structure correlated with distance from the Australian Antarctic Discordance area of cold mantle [*Baran et al.*, 2005]. The Endeavour segment crustal structure is similar to portions of those ridges, but only where the ridge morphology indicates a similar thermal state in the crust and upper mantle.

3.5.5 Intermediate Spreading Ridge Heat Extraction

The existence of a magma chamber beneath the Endeavour Ridge indicates that heat is supplied at this intermediate spreading ridge by the same magmatic source as at fast-spreading ridges such as the East Pacific Rise. There is no need to invoke a cracking front propagating down into and mining heat from an area of hot but unmolten rock in the lower crust [*Wilcock and Delaney*, 1996]. The observed differences between small, short-lived, magmatically controlled hydrothermal systems on the EPR and larger, longer-lived, fault-controlled hydrothermal systems on the Endeavour Segment still require explanation, however. We propose a hybrid model of heat extraction for intermediate spreading ridges which combines the magmatic heat source of the fast spreading ridge and the fault-controlled hydrothermal circulation of the slow spreading ridge model (Figure 3-1). However, the source of the faulting remains a subject of debate.

In general, the observed Endeavour magma chamber depths are consistent with model predictions from numerical studies relating half-spreading rate to depth to the top of a steady-state magma lens through the thermal balance between heat supply from magmatic crustal injection and cooling due to hydrothermal circulation [*Phipps Morgan and Chen*, 1993; *Chen and Lin*, 2004]. These models depend on the supposition that magma rises within the oceanic crust due to buoyancy forces or viscous pressures until it reaches a freezing horizon where it ponds into a quasi steady state magma lens. The axial morphology and faulting above the magma lens are a function of the thermal structure, which determines the thickness of the axial lithosphere and therefore the yield strength of the axial lithosphere as it is pulled apart. According to this model, the Endeavour axial summit graben and the faults which bound it and provide permeability pathways for the hydrothermal circulation are the result of tectonic extensional stresses interacting with a cooler upper crust due to a deeper magma chamber.

Another model for the evolving axial topography on the Juan de Fuca Ridge emphasizes the contribution of dike intrusion to subsidence and fault slip at the seafloor due to feedback between the rheology of the crust above a magma sill and dike intrusion [*Carbotte et al.*, 2006]. Within the framework of this model, the faulting related permeability pathways which sustain Endeavour's massive, high temperature hydrothermal vent fields are a result of the interaction between the regional tectonic extension and stress perturbations due to dike intrusions from the axial magma chamber. The tensional regime of this model could lead to the higher microseismicity levels on Endeavour discussed in section 3.5.2. That small scale fracturing is needed to keep the upgoing hydrothermal pathways open in the face of ongoing quartz precipitation in the upwelling portion of the hydrothermal system [*Wilcock and Delaney*, 1996].

A final paradox is presented by the *Wilcock and Delaney* [1996] estimate that the heat flux from the Main Endeavour vent field is between 5 and 50 times the steady-state heat flux necessary to solidify and cool a 6 km thick crust. They calculate that mining this amount of heat from a 2 km wide AMC would require a conductive boundary only ~ 1 m thick, which they interpret to be implausibly thin. One possible resolution is that the heat flux has been overestimated, or that the portion of the ridge which is cooled by the subsurface circulation cell supplying each vent field has been underestimated. Another possible solution is that the cracking front model proposed by *Wilcock and Delaney* [1996] is locally correct on the margins of the imaged magma chambers, perhaps resulting in the apparent segmentation of the Endeavour AMC (although that could also be an artifact of streamer feathering, topographic effects on the data, or attempting to image a narrow three-dimensional body with a one-dimensional line). Possible issues with the flux estimate may be resolved by further heat flux measurements and modeling, while the possible segmentation of the Endeavour AMC would be fully revealed with a three-dimensional multichannel seismic reflection survey.

3.6 Conclusions

Multichannel seismic reflection data gathered on the Endeavor segment of the Juan de Fuca Ridge during July 2002 reveal the presence of a crustal magma body underlying all five known hydrothermal vent fields of the Endeavour segment. The magma body is relatively deep (2.1–3.3 km) and narrow (0.4–1.2 km wide), and appears to be segmented into multiple crustal magma lenses adding up to a total along-axis distance of 16–24 km.

The polarity of the reflection from the top of the AMC combined with similarities to well-studied AMC events at other ridges confirms that the reflection is due to a decrease in seismic velocities at the top of a magma chamber rather than a hydrothermal cracking front. Microseismicity within 0.5 km of the axis is mostly confined to a region above the shallowest portions of the AMC. We interpret the thermal cracking focal mechanisms of the microseismic events as hydrothermal circulation penetrating into a conductive lid above a magma lens which is continually replenished with new magma from below. Cross axis lines show the magma chamber to be dipping from the west to the east, with the vent fields located over shallower portions of the AMC.

The AMC is approximately the same depth (dipping from $\sim$2.1 to 2.4 km) beneath all the Endeavour hydrothermal vent fields except Mothra (2.5–3.1 km), and the range of temperatures and chemistry values within each well-sampled vent field tends to be larger than the differences between the fields. Our results suggest that AMC depth is not a dominant factor in determining vent fluid properties, which are probably controlled instead by phase separation, subsurface mixing of hydrothermal fluids and seawater, and other complexities of the circulation path through the crust.

Hydrothermal systems at the intermediate spreading Endeavour Segment, like those at fast spreading ridges, appear to be driven by heat extraction from a crustal magma body. Morphological, hydrothermal, and seismic differences between the intermediate-spreading Endeavour and the fast-spreading EPR are attributable either to the greater depth of the Endeavour AMC and the correspondingly cooler, more brittle shallow crust overlying the magma chamber or to faulting controlled by dike intrusions from the axial magma chamber.

Chapter 4

Two-Dimensional Pseudospectral Modeling of Global Seismic Wave Propagation

Abstract Seismic wave propagation in two-dimensional global (cylindrical) Earth models is simulated using a pseudospectral algorithm. The pseudospectral method is distinguished by its use of Fourier transforms to estimate the spatial derivatives in the elastic equations and the equations of motion. First order velocity-stress equations are solved on a staggered grid in order to increase stability and to accommodate the half-grid step Fourier shift required to maintain real first-order spectral derivatives. Attenuation is optionally included through the use of stress and strain dependent memory function. Boundary conditions are implemented using cancellation of periodic and anti-periodic wrap-around wavefields. Variable radial grid spacing is implemented to allow fine sampling of a chosen area of the model space (in this case, the core-mantle boundary) while maintaining reasonable computational times. Synthetic seismograms produced by this method for a 1-D PREM Earth model are benchmarked against synthetics produced by the semi-analytic full wave theory method, which in turn have been benchmarked against the reflectivity method.

4.1 Introduction

The object of seismic forward modeling is to predict the signal which would be recorded by receivers at a given location due to a seismic wave propagating through a given assumed structure of the subsurface. The ability to make these predictions is key to interpreting the seismic data we collect and absolutely necessary for any attempt to invert such data for earth structure.

All seismic forward modeling is based on solutions of an appropriate form of the governing wave equation, which can be anything from a simple one dimensional acoustic wave equation to a full three dimensional elastic wave equation incorporating anisotropy and attenuation. The current approaches to solving this problem can be divided into three main groups: analytical methods, geometrical optics, and direct methods [*Kosloff and Kessler*, 1990; *Cormier*, in press].

Analytical methods use closed form solutions of the governing wave equation and are therefore limited to simple earth structures. They are very accurate and are therefore often used to test other approaches. For multilayer structures, analytical solutions often include integrals with singularities (i.e. the reflectivity method [*Fuchs*, 1968; *Fuchs and Müller*, 1971; *Müller*, 1985]) — these call for numerical caution and are only "semi-analytical".

Geometrical optics, also known as ray tracing, uses a high frequency approximation to treat the seismic wave as a simple ray. It is generally fast and effective for calculating travel-time information, but does not always give correct amplitudes or explain non-geometrical optical phenomena (e.g. tunneling). It can become complicated in situations with complex structures involving many multiples and converted phases.

Direct methods include finite difference, finite element, the Fourier or pseudospectral method, and the spectral element method. They use direct solution of the equations of motion after approximating the region of propagation by a numerical grid. Usually there are no restrictions on material variability or structural complexity. These methods are very accurate in principle if a fine enough grid is used. However, they can be computationally expensive and/or have a high frequency limit on resolution. They easily produce snapshots of the wavefield propagating through the medium, which can be useful for interpretation.

Within the direct modeling methods, the approaches can be differentiated based on whether they use a simple grid of nodes to solve the "strong" (differential) form of the wave equation (finite difference and pseudospectral) or they use more complex and flexible multi-node elements to solve the “weak” (integral) form of the wave equation (finite element and spectral element). They can also be differentiated based on their approach to calculating the spatial derivative. The finite difference and finite element methods approximate the spatial derivative using local functions of the displacement at neighboring nodes. The pseudospectral [*Fornberg*, 1988, 1996] and spectral element methods [*Komatitsch et al.*, 2002; *Komatitsch and Tromp*, 2002a, b] approximate the spatial derivative globally by approximating the displacement as a series of weighted orthogonal basis functions (such as, but not limited to, a Fourier series). They then use the derivative of the basis functions to calculate the derivative of the spatial function. All direct methods use a finite difference approach to approximating the time derivative of the displacement in the wave equation.

This paper will present details of a pseudospectral method for simulating seismic wave propagation through a 2-D cylindrical Earth first developed by *Cormier* [2000]. The pseudospectral method is advantageous because it has greatly reduced numerical dispersion in comparison to finite difference or finite element methods, and it is computationally less expensive than the spectral element method. The Fourier transform incorporated into the pseudospectral calculations restricts the method to relatively simple grid geometries, which may make it less useful for solving global three-dimensional wave propagation in the future than the spectral element method. However, the pseudospectral method can be very accurate and useful for solving two-dimensional global problems. Here we focus on the portion of our synthetic seismograms which include the SKS phase and its associated SPdKS phase (Figure 4-1) which we use elsewhere to examine core-mantle boundary structure.

4.2 Seismic Wave Propagation Equations

To study global seismic problems with 2-D velocity model variability, we use a 2-D polar coordinate system with coordinates (r, θ) where all fields are implicitly invariant in the direction perpendicular to the polar plane. All variables used in this section are defined in Table 4.1. The equations of momentum conservation ($\rho \ddot{u}_i = \sigma_{ij,j} + f_i$) in polar coordinates become [*Furumura et al.*, 1998; *Aki and Richards*, 2002]:

$$\rho \frac{\partial^2 u_r}{\partial t^2} = \frac{1}{r}\frac{\partial}{\partial r}\left(r\sigma_{rr}\right) + \frac{1}{r}\frac{\partial \sigma_{r\theta}}{\partial \theta} - \frac{\sigma_{\theta\theta}}{r} + f_r \qquad (4.1)$$

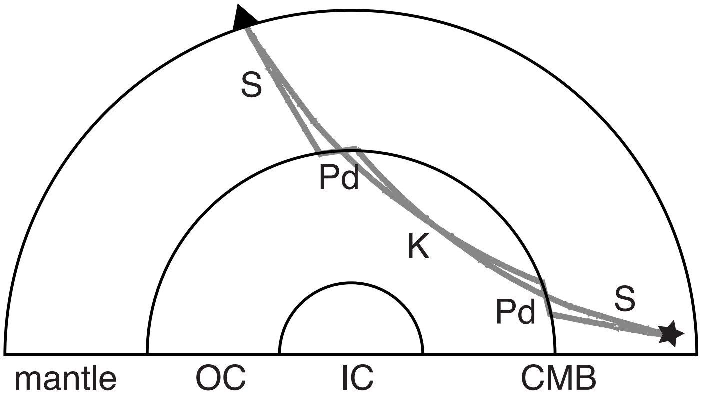

Figure 4-1: Illustration of the SPdKS / SKPdS ray-paths with sub-segments labeled. SPdKS is an SKS that intersects the source-side CMB at the ScP critical angle and propagates along the mantle-side of the CMB as a diffracted P-wave (Pdiff). SKPdS is the same phenomena on the receiver-side CMB. Star shows earthquake source and triangle shows receiver location. IC = inner core, OC = outer core, and CMB = core-mantle boundary.

Table 4.1: Pseudospectral method notation

Coordinates:	
r	radial coordinate of polar geometry
θ	angular component of polar geometry
dt	time step increment
Material Properties:	
ρ	density
λ, μ	elastic Lamé parameters
π	viscoelastic parameter $\approx \lambda + 2\mu$
μ'	viscoelastic parameter $\approx \mu$
τ_ϵ^P, τ_ϵ^S	P, SV strain relaxation times
τ_θ	P and SV stress relaxation time
Fields:	
u_r,u_θ	radial and angular components of displacement
v_r, v_θ	radial and angular components of velocity
f_r,f_θ	body forces
σ_{rr},$\sigma_{r\theta}$,$\sigma_{\theta\theta}$	components of stress tensor
r_{rr},$r_{r\theta}$,$r_{\theta\theta}$	memory functions
Numerical Indices:	
ix	grid index in θ direction
iy	grid index in r direction
it	time step index

$$\rho \frac{\partial^2 u_\theta}{\partial t^2} = \frac{1}{r^2}\frac{\partial}{\partial r}\left(r^2 \sigma_{r\theta}\right) + \frac{1}{r}\frac{\partial \sigma_{\theta\theta}}{\partial \theta} + f_\theta \tag{4.2}$$

where the variables are defined in Table 4.1. Likewise the constitutive equations in polar coordinates for an isotropic medium ($\sigma_{ij} = \lambda\delta_{ij}\epsilon_{kk} + 2\mu\epsilon_{ij}$, where σ is stress and ϵ is strain) become:

$$\sigma_{rr} = (\lambda + 2\mu)\frac{\partial u_r}{\partial r} + \frac{\lambda}{r}\frac{\partial u_\theta}{\partial \theta} + \frac{\lambda}{r}u_r \tag{4.3}$$

$$\sigma_{\theta\theta} = \lambda\frac{\partial u_r}{\partial r} + \left(\frac{\lambda + 2\mu}{r}\right)\frac{\partial u_\theta}{\partial \theta} + \left(\frac{\lambda + 2\mu}{r}\right)u_r \tag{4.4}$$

$$\sigma_{r\theta} = \frac{\mu}{r}\frac{\partial u_r}{\partial \theta} + \mu\frac{\partial u_\theta}{\partial r} - \frac{\mu}{r}u_\theta. \tag{4.5}$$

The system of equations (4.1–4.5) are transformed into the first order velocity-stress system by changing the time derivative of the displacement to velocity ($\partial u/\partial t = v$) in equations (4.1–4.2) and by taking the time derivative of equations (4.3–4.5) [*Virieux*, 1984, 1986]:

$$\frac{\partial v_r}{\partial t} = \frac{1}{\rho}\left[\frac{1}{r}\frac{\partial}{\partial r}\left(r\sigma_{rr}\right) + \frac{1}{r}\frac{\partial \sigma_{r\theta}}{\partial \theta} - \frac{\sigma_{\theta\theta}}{r} + f_r\right] \tag{4.6}$$

$$\frac{\partial v_\theta}{\partial t} = \frac{1}{\rho}\left[\frac{1}{r^2}\frac{\partial}{\partial r}\left(r^2\sigma_{r\theta}\right) + \frac{1}{r}\frac{\partial \sigma_{\theta\theta}}{\partial \theta} + f_\theta\right] \tag{4.7}$$

$$\frac{\partial \sigma_{rr}}{\partial t} = \left(\lambda + 2\mu\right)\frac{\partial v_r}{\partial r} + \frac{\lambda}{r}\frac{\partial v_\theta}{\partial \theta} + \frac{\lambda}{r}v_r \tag{4.8}$$

$$\frac{\partial \sigma_{\theta\theta}}{\partial t} = \lambda\frac{\partial v_r}{\partial r} + \left(\frac{\lambda + 2\mu}{r}\right)\frac{\partial v_\theta}{\partial \theta} + \left(\frac{\lambda + 2\mu}{r}\right)v_r \tag{4.9}$$

$$\frac{\partial \sigma_{r\theta}}{\partial t} = \frac{\mu}{r}\frac{\partial v_r}{\partial \theta} + \mu\frac{\partial v_\theta}{\partial r} - \frac{\mu}{r}v_\theta. \tag{4.10}$$

An approximation of viscoelastic attenuation is included using memory functions, as developed by *Robertsson et al.* [1994]. Memory functions, r_{ij}, are coupled to the stress and strain at a particular location and evolve over time, dissipating seismic wave energy. This coupling is accomplished through the use of strain relaxation times for the P and SV waves (τ_ϵ^P and τ_ϵ^S, respectively) and one stress relaxation time τ_θ for both P and SV waves, all of which are related to the P and S-wave quality factors input for each layer of the velocity model. In addition, viscoelastic relaxation moduli μ' and π replace the elastic Lamé constants μ and $\lambda + 2\mu$, respectively.

When the memory functions and their related viscoelastic parameters are incorporated into equations 4.6–4.10 the total system of seismic wave propagation equations becomes:

$$\frac{\partial v_r}{\partial t} = \frac{1}{\rho}\left[\frac{1}{r}\frac{\partial}{\partial r}\left(r\sigma_{rr}\right) + \frac{1}{r}\frac{\partial \sigma_{r\theta}}{\partial \theta} - \frac{\sigma_{\theta\theta}}{r} + f_r\right] \tag{4.11}$$

$$\frac{\partial v_\theta}{\partial t} = \frac{1}{\rho}\left[\frac{1}{r^2}\frac{\partial}{\partial r}\left(r^2\sigma_{r\theta}\right) + \frac{1}{r}\frac{\partial \sigma_{\theta\theta}}{\partial \theta} + f_\theta\right] \tag{4.12}$$

$$\begin{aligned}\frac{\partial r_{rr}}{\partial t} = \frac{1}{\tau_\sigma}\Bigg[&r_{rr} + \pi\left(\frac{\tau_\epsilon^P}{\tau_\sigma} - 1\right)\left(\frac{\partial v_r}{\partial r} + \frac{1}{r}\frac{\partial v_\theta}{\partial \theta} + \frac{v_r}{r}\right)\\ &-2\mu'\left(\frac{\tau_\epsilon^S}{\tau_\sigma} - 1\right)\left(\frac{1}{r}\frac{\partial v_\theta}{\partial \theta} + \frac{v_r}{r}\right)\Bigg]\end{aligned} \tag{4.13}$$

$$\begin{aligned}\frac{\partial r_{\theta\theta}}{\partial t} = \frac{1}{\tau_\sigma}\Bigg[&r_{\theta\theta} + \pi\left(\frac{\tau_\epsilon^P}{\tau_\sigma} - 1\right)\left(\frac{\partial v_r}{\partial r} + \frac{1}{r}\frac{\partial v_\theta}{\partial \theta} + \frac{v_r}{r}\right)\\ &-2\mu'\left(\frac{\tau_\epsilon^S}{\tau_\sigma} - 1\right)\left(\frac{\partial v_r}{\partial r}\right)\Bigg]\end{aligned} \tag{4.14}$$

$$\frac{\partial r_{r\theta}}{\partial t} = \frac{1}{\tau_\sigma}\left[r_{r\theta} + \mu'\left(\frac{\tau_\epsilon^S}{\tau_\sigma} - 1\right)\left(\frac{\partial v_\theta}{\partial r} + \frac{1}{r}\frac{\partial v_r}{\partial \theta} - \frac{v_\theta}{r}\right)\right] \tag{4.15}$$

$$\frac{\partial \sigma_{rr}}{\partial t} = \pi\frac{\tau_\epsilon^P}{\tau_\sigma}\left(\frac{\partial v_r}{\partial r} + \frac{1}{r}\frac{\partial v_\theta}{\partial \theta} + \frac{v_r}{r}\right) - 2\mu'\frac{\tau_\epsilon^S}{\tau_\sigma}\left(\frac{1}{r}\frac{\partial v_\theta}{\partial \theta} + \frac{v_r}{r}\right) + r_{rr} \tag{4.16}$$

$$\frac{\partial \sigma_{\theta\theta}}{\partial t} = \pi \frac{\tau_\epsilon^P}{\tau_\sigma}\left(\frac{\partial v_r}{\partial r} + \frac{1}{r}\frac{\partial v_\theta}{\partial \theta} + \frac{v_r}{r}\right) - 2\mu' \frac{\tau_\epsilon^S}{\tau_\sigma}\frac{\partial v_r}{\partial r} + r_{\theta\theta} \tag{4.17}$$

$$\frac{\partial \sigma_{r\theta}}{\partial t} = \mu' \frac{\tau_\epsilon^S}{\tau_\sigma}\left(\frac{1}{r}\frac{\partial v_r}{\partial \theta} + \frac{\partial v_\theta}{\partial r} - \frac{v_\theta}{r}\right) + r_{r\theta}. \tag{4.18}$$

This system of equations can now be numerically stepped forward in time through calculation of the spatial derivatives of the stress and velocity fields. However, in order to preserve the highest frequencies possible in the waveforms presented here, the attenuation is usually turned off in our simulations.

4.3 Pseudospectral Implementation

The spatial derivatives of the velocity and stress fields are numerically calculated using Fourier transforms. (This is what distinguishes a "pseudospectral" method from finite difference methods, although it has been shown that the pseudospectral approach is the high-accuracy limit of the finite difference method [*Fornberg*, 1996].) For any field f(x) sampled at intervals Δx with Fourier transform F(k), the spatial derivative can be evaluated as

$$\frac{\partial f(x)}{\partial x} = \sum_{k=0}^{K_N} ikF(k)e^{ikx} \tag{4.19}$$

where $K_N = \pi/\Delta x$ is the Nyquist wavenumber. However, for a real function f(x), the value of the Fourier transform at the Nyquist wavenumber, F(K_N), is also real, which means that $iK_N F(K_N)$ is imaginary, and the numerical evaluation of equation (4.19) will result in a complex derivative of a real function. In order to calculate a purely real spatial derivative, we apply the Fourier shift theorem and evaluate the derivative halfway between the sampled points, such that the derivative operator ik is replaced by the staggered spectral differential operator $ik\, e^{ik\Delta x/2}$ [*Witte*, 1989; *Witte and Richards*, 1990]. The value of the staggered derivative operator at the Nyquist wavenumber is then purely real: $iK_N\, e^{iK_N \Delta x/2} = -\pi/2$. The spatial derivative becomes:

$$\frac{\partial f(x + \frac{\Delta x}{2})}{\partial x} = \sum_{k=0}^{K_N} ike^{ik\Delta x/2}F(k)e^{ikx}. \tag{4.20}$$

The numerical solution of equations (4.11–4.18) using Fourier spatial derivatives (equation 4.20) is thus naturally driven towards a staggered grid approach: the velocity components are evaluated at locations half a step away from the sampling locations of the stress components (Figure 4-2), as each depends on the derivatives of the others [*Virieux*, 1984, 1986; *Witte*, 1989; *Witte and Richards*, 1990]. Thus the Fourier staggered derivative of the stress components are calculated from the stress field at time $it - \frac{1}{2}$:

$$\frac{\partial \sigma_{\theta\theta}}{\partial \theta}\left(ix, iy, it - \frac{1}{2}\right) = \frac{\partial \sigma_{\theta\theta}\left(ix + \frac{1}{2}, iy, it - \frac{1}{2}\right)}{\partial \theta} \tag{4.21}$$

$$\frac{\partial \sigma_{rr}}{\partial r}\left(ix + \frac{1}{2}, iy + \frac{1}{2}, it - \frac{1}{2}\right) = \frac{\partial \sigma_{rr}\left(ix + \frac{1}{2}, iy, it - \frac{1}{2}\right)}{\partial r} \tag{4.22}$$

$$\frac{\partial \sigma_{\theta r}}{\partial r}\left(ix, iy, it - \frac{1}{2}\right) = \frac{\partial \sigma_{\theta r}\left(ix, iy + \frac{1}{2}, it - \frac{1}{2}\right)}{\partial r} \tag{4.23}$$

$$\frac{\partial \sigma_{\theta r}}{\partial \theta}\left(ix + \frac{1}{2}, iy + \frac{1}{2}, it - \frac{1}{2}\right) = \frac{\partial \sigma_{\theta r}\left(ix, iy + \frac{1}{2}, it - \frac{1}{2}\right)}{\partial \theta} \tag{4.24}$$

These spatial derivatives of the stress field are used to step the velocity components forward in time. Here we show only the functional dependence, but the full equations are equivalent to equations 4.11 and 4.12:

$$\begin{aligned} v_r\left(ix + \frac{1}{2}, iy + \frac{1}{2}, it\right) = f\Bigg[& v_r\left(ix + \frac{1}{2}, iy + \frac{1}{2}, it - 1\right), \\ & \frac{\partial \sigma_{rr}}{\partial r}\left(ix + \frac{1}{2}, iy + \frac{1}{2}, it - \frac{1}{2}\right), \\ & \frac{\partial \sigma_{\theta r}}{\partial \theta}\left(ix + \frac{1}{2}, iy + \frac{1}{2}, it - \frac{1}{2}\right), \\ & \sigma_{rr}\left(ix + \frac{1}{2}, iy, it - \frac{1}{2}\right)\Bigg] \end{aligned} \tag{4.25}$$

$$\begin{aligned} v_\theta\left(ix, iy, it\right) = f\Bigg[& v_\theta\left(ix, iy, it - 1\right), \frac{\partial \sigma_{\theta\theta}}{\partial \theta}\left(ix, iy, it - \frac{1}{2}\right), \\ & \frac{\partial \sigma_{\theta r}}{\partial r}\left(ix, iy, it - \frac{1}{2}\right), \sigma_{\theta r}\left(ix, iy + \frac{1}{2}, it - \frac{1}{2}\right)\Bigg]. \end{aligned} \tag{4.26}$$

The spatial derivatives of the velocity components at time *it* are then calculated:

$$\frac{\partial v_r}{\partial r}\left(ix + \frac{1}{2}, iy, it\right) = \frac{\partial v_r\left(ix + \frac{1}{2}, iy + \frac{1}{2}, it\right)}{\partial r} \tag{4.27}$$

$$\frac{\partial v_r}{\partial \theta}\left(ix, iy + \frac{1}{2}, it\right) = \frac{\partial v_r\left(ix + \frac{1}{2}, iy + \frac{1}{2}, it\right)}{\partial \theta} \tag{4.28}$$

$$\frac{\partial v_\theta}{\partial \theta}\left(ix + \frac{1}{2}, iy, it\right) = \frac{\partial v_\theta\left(ix, iy, it\right)}{\partial \theta} \tag{4.29}$$

$$\frac{\partial v_\theta}{\partial r}\left(ix, iy+\frac{1}{2}, it\right) = \frac{\partial v_\theta\left(ix, iy, it\right)}{\partial r} \tag{4.30}$$

and used to step the stress tensor components forward in time. Again we show the functional dependence while the full equations are equivalent to equations 4.16–4.18:

$$\begin{aligned}
\sigma_{rr}\left(ix+\frac{1}{2}, iy, it+\frac{1}{2}\right) &= f\left[\sigma_{rr}\left(ix+\frac{1}{2}, iy, it-\frac{1}{2}\right), \frac{\partial v_\theta}{\partial \theta}\left(ix+\frac{1}{2}, iy, it\right),\right.\\
&\quad \left.\frac{\partial v_r}{\partial r}\left(ix+\frac{1}{2}, iy, it\right), v_r\left(ix+\frac{1}{2}, iy+\frac{1}{2}, it\right)\right] \qquad (4.31)\\
\sigma_{\theta\theta}\left(ix+\frac{1}{2}, iy, it+\frac{1}{2}\right) &= f\left[\sigma_{\theta\theta}\left(ix+\frac{1}{2}, iy, it-\frac{1}{2}\right), \frac{\partial v_\theta}{\partial \theta}\left(ix+\frac{1}{2}, iy, it\right),\right.\\
&\quad \left.\frac{\partial v_r}{\partial r}\left(ix+\frac{1}{2}, iy, it\right), v_r\left(ix+\frac{1}{2}, iy+\frac{1}{2}, it\right)\right] \qquad (4.32)\\
\sigma_{\theta r}\left(ix, iy+\frac{1}{2}, it+\frac{1}{2}\right) &= f\left[\sigma_{\theta r}\left(ix, iy+\frac{1}{2}, it-\frac{1}{2}\right), \frac{\partial v_\theta}{\partial r}\left(ix, iy+\frac{1}{2}, it\right),\right.\\
&\quad \left.\frac{\partial v_r}{\partial \theta}\left(ix, iy+\frac{1}{2}, it\right), v_\theta\left(ix, iy, it\right)\right]. \qquad (4.33)
\end{aligned}$$

The numerical solution scheme presented here uses a simple first order finite difference algorithm in time. By careful examination of the spatial indices in equations 4.21–4.33 (represented graphically in Figure 4-2) the spatial derivatives of velocities and stresses are seen to align perfectly with the velocity and stress components with which they are coupled in the seismic wave propagation equations. However, the cylindrical geometry introduces a dependence on a non-differentiated velocity or stress quantity in each equation, and these non-differentiated quantities do not align perfectly. This is a potential source of inaccuracy in the calculations, although it does not appear to introduce significant errors.

The computational implementation of this scheme takes advantage of some number, N, of parallel processors. The grid is split into N horizontal slices. (For this particular code, N must be a power of 2 to ensure equal loading of all the processors.) At each time step the spatial derivatives in the horizontal (θ) direction can be calculated using only grid nodes which are on the local processor. However, calculation of the vertical (r) spatial derivatives requires a matrix transform so that vertical slices of the nodes are temporarily collected onto one local processor. Then another matrix transform is required to restore the grid back to the original configuration. This requires extensive communication between all the processors, and is implemented using the message passing interface (MPI) parallel instruction set [*Gropp et al.*, 1998, 1999].

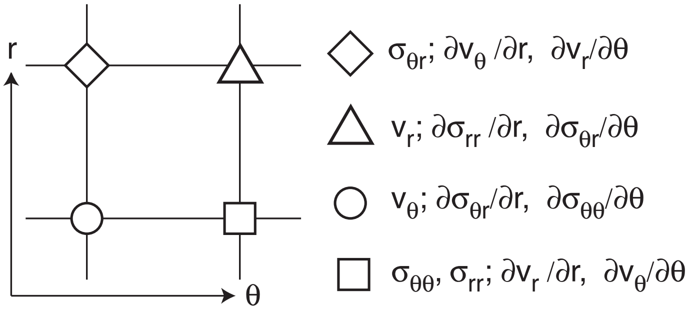

Figure 4-2: Staggered grid configuration in pseudospectral code. Each model node consists of four sub-nodes at which velocity and stress components and their derivatives are evaluated as labeled.

4.4 Boundary Conditions

The half-cylinder grid configuration for our calculations assumes that θ goes from 0 to 180° and the model radius goes from ∼950 km to ∼7000 km. The inner radial boundary in set so that the model extends down into the inner core, but does not reach the center of the Earth. This allows us to model all mantle and outer core seismic phases of interest. The outer radial boundary is set to extend several hundred kilometers beyond the surface of the Earth so that the free surface boundary condition is implicitly applied by setting the Lamé parameters to 0 in the "atmosphere" layer while maintaining a non-zero density for computational stability.

The calculation of velocity and stress spatial derivatives by Fourier transforms imposes implicit periodic boundary conditions on the grid. Any wave energy that exits one edge of the half-cylinder model space therefore wraps around and emerges immediately on the opposite edge of the model space. While such transmission in the radial direction is prevented due to the "atmosphere" layer at the top of the model, another strategy is needed to eliminate the wrap-around transmission between the two lateral edges of the half-cylinder model.

We run each wave propagation simulation twice [*Furumura and Takenaka*, 1995], using Fourier differentiation algorithms which are identical except for a single line of code. The first, "periodic", differentiation performs the Fourier transform on each row or column of length N, repeated once as follows:

$$\tilde{f}_{periodic}(n\Delta x) = \begin{cases} f(n\Delta x), & (1 \le n \le N); \\ f[(n-N)\Delta x], & (N+1 \le n \le 2N). \end{cases} \tag{4.34}$$

The second, "anti-periodic", differentiation performs the Fourier transform on each row or column of length N, repeated with the opposite sign once as follows:

$$\tilde{f}_{aperiodic}(n\Delta x) = \begin{cases} f(n\Delta x), & (1 \le n \le N); \\ -f[(n-N)\Delta x], & (N+1 \le n \le 2N). \end{cases} \tag{4.35}$$

The first half of the values (n = 1...N) from the extended signals are returned from the Fourier differentiation. The wrap-around wavefield from the anti-periodic extensions (equation 4.35) has opposite polarity to that of the wrap-around wavefield from the periodic extension (equation 4.34). When the two signals are averaged, the wrap-around portion therefore cancels out exactly (Figure 4-3). This method is elegant in its simplicity, although computationally expensive in that every seismic wave propagation calculation is done twice.

4.5 Variable Radial Grid Spacing

A basic grid configuration for the Earth model described above using 1024 evenly-spaced nodes in the radial direction and 2048 evenly-spaced nodes in the θ direction results in a radial node separation of 6 km and a lateral node spacing which varies linearly from 10.8 km at the top of the model to 9.5 km at the surface of the Earth to 5.2 km at the CMB to 1.4 km at the bottom of the model. While this grid spacing would be sufficient for many modeling problems (e.g., D" heterogeneity explored by *Cormier* [2000]), our goal is to explore relatively thin features at the base of the mantle with thicknesses between 40 km and 5 km. A radial grid spacing smaller than 6 km is therefore desirable near the CMB, however decreasing the radial grid spacing everywhere (for example, by doubling the number of radial grid nodes) is both unnecessary and computationally expensive.

Instead we adapt the approach developed by *Fornberg* [1988] for introducing variable grid spacing into the pseudospectral method (further developed by *Tessmer et al.* [1992] and *Nielsen et al.* [1994] for Cartesian coordinates and applied in a less accurate way to global seismic propagation in cylindrical coordinates by *Furumura et al.* [1998]). Since the pseudospectral derivative calculation depends on evenly sampled signals for the Fourier transform, the derivative of a variable f with respect to a smoothly varying grid coordinate r can be calculated using the chain rule after first calculating the derivative of f with respect to a constantly spaced grid coordinate y:

$$\frac{\partial f}{\partial r} = \frac{\partial y}{\partial r}\frac{\partial f}{\partial y}. \tag{4.36}$$

Furumura et al. [1998] approximated $\partial y/\partial r$ as $\Delta y/\Delta r$, using the simple ratio of the grid spacings at a given point. We tested this approximation against a direct analytical derivative of a gaussian function and found it to be insufficiently accurate. However, when $\partial y/\partial r$ is approximated with a cubic spline interpolation, the results are highly accurate. As a result, we adopt the grid spacing shown in Figure 4-4, where the $\Delta\theta$ spacing remains constant in

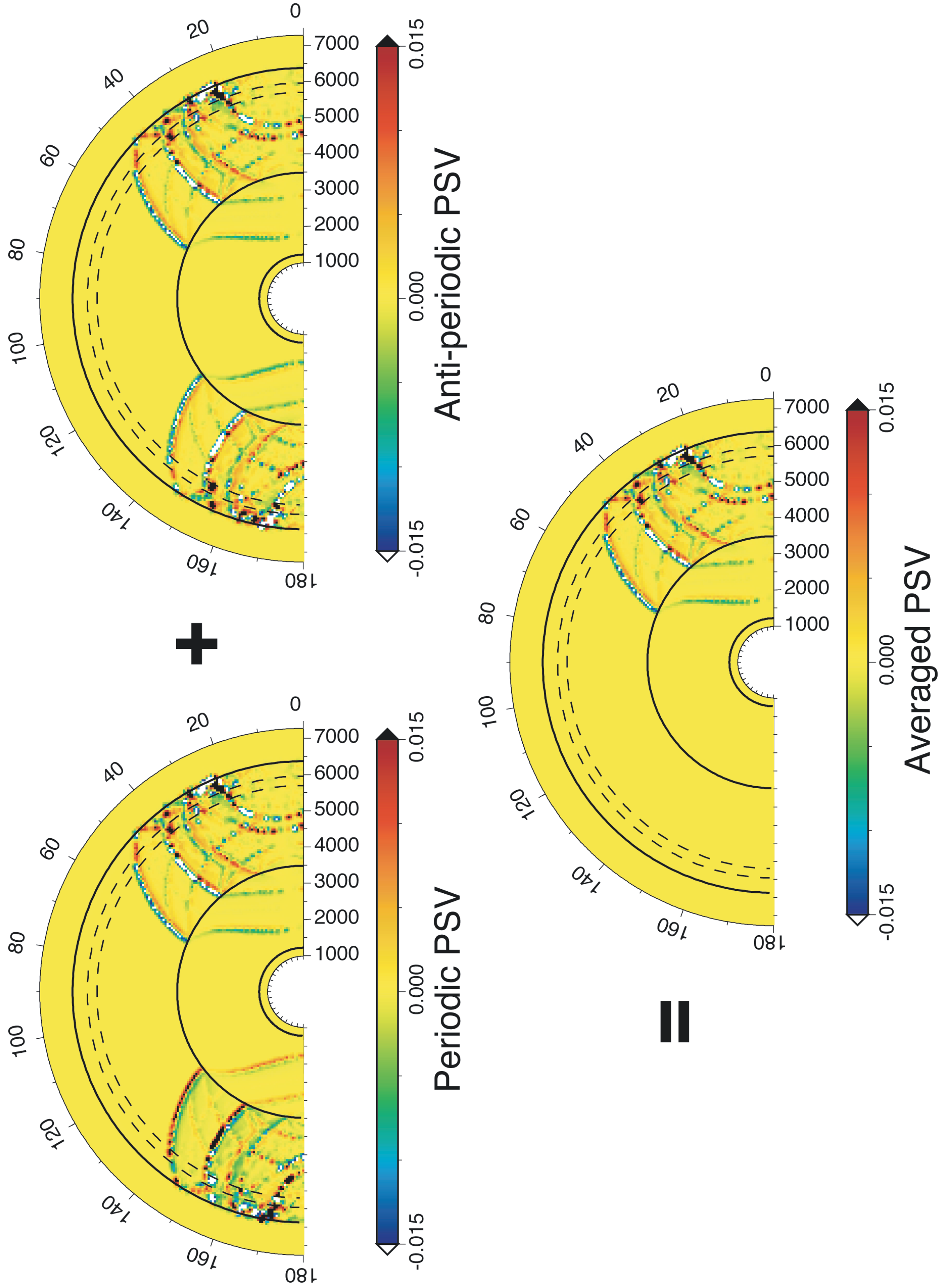

Figure 4-3: Averaging the periodic and anti-periodic wavefields results in cancellation of wrap-around energy and preservation of the desired signal.

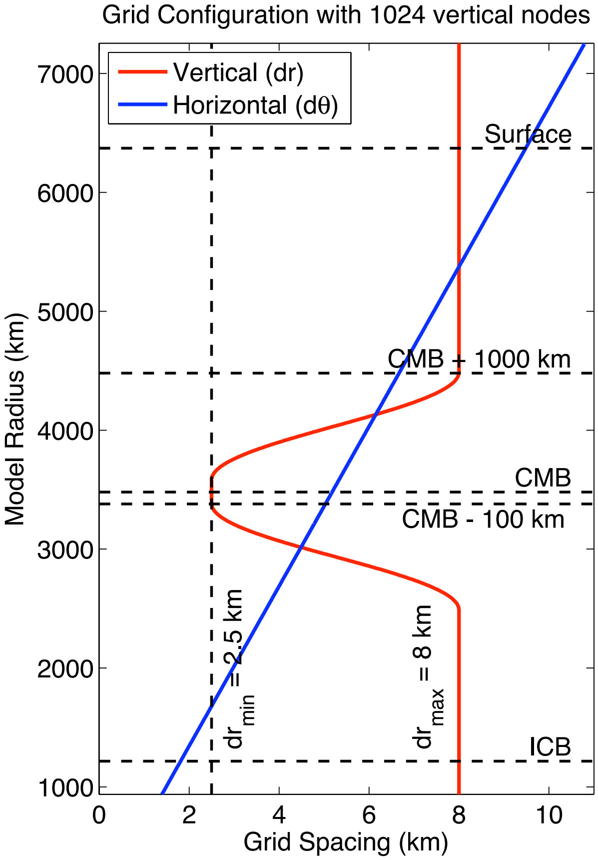

Figure 4-4: Radial (Δr) and lateral ($\Delta\theta$) grid node spacing as a function of model radius. Minimum radial grid spacing of 2.5 km is maintained for 100 km above and below the CMB, and then gradually increased with a cosine shape to 8 km for the rest of the grid. Lateral grid spacing is constant in angular measurement and therefore varies linearly in kilometers as a function of radius. $\Delta\theta$ at the CMB is 5.2 km. ICB = inner core boundary.

angular measurement and linearly varying in kilometers and the Δr spacing decreases to 2.5 km around the CMB and smoothly increases to 8 km in the other regions of the grid. The spline approximation of $\partial y/\partial r$ is read into the code with the velocity model and does not introduce significant direct numerical costs.

While this method preserves the number of grid nodes used, it is still computationally more expensive than the evenly-spaced grid due to the finer spatial sampling of the area of the model with the fastest seismic velocities. In order to maintain computational stability, the time step used throughout the model run was halved, increasing by a factor of two the model run time required to produce a given timespan of modeled wave propagation and the corresponding length of synthetic seismograms.

4.6 Source Implementation

This pseudospectral code has input parameters that define a source location in distance from the surface of the Earth and distance from the side of the model. It also has parameters that define the width of a spatial gaussian around that source location, which in the models presented here is set to zero so that a point pulse is input on a single node. Finally, the input parameters chose one of several source-time functions and define appropriate parameters for that function; we use a gaussian in time with a standard deviation of 0.6 seconds whose peak is reached eight standard deviations in time (4.8 seconds) after the start of the model run. This offset in time is corrected for in post-processing, with 2 standard deviations from the peak set as the t=0 onset time.

If a node is located within the source area during the time in which the source is activated, the appropriate source-time value is added to either the v_θ or v_r component of that grid node. The choice of component has a strong effect on which seismic phases are more strongly excited. For the purposes of studying the SPdKS phase which samples the ULVZs on the core-mantle boundary, a v_θ pulse is more appropriate, channeling energy into the downgoing mantle shear SKS wave and directing energy away from the upper mantle multiples which tend to arrive at similar times to the SPdKS phase.

Post-processing of the synthetic seismograms produced by this code applies a line-source to point-source correction to partially account for the differences between the 2-D geometry of the model space and the 3-D nature of the real Earth.

4.7 Benchmarking

Synthetic seismograms produced by our pseudospectral wave propagation code are converted from velocity to displacement and are compared with those produced by the full wave theory [*Aki and Richards*, 2002; *Cormier and Richards*, 1988] for the same Earth and source models. Full wave theory core phases have in turn been successfully compared to the reflectivity method [*Fuchs*, 1968; *Fuchs and Müller*, 1971] by *Choy et al.* [1980]. In addition, pseudospectral S, ScS, and SKS waveforms generated by our code base were comparable to those generated by a modified 2-D WKBJ semi-analytical method in *Ni et al.* [2003].

Figure 4-5 shows our pseudospectral synthetic seismograms in gray and full wave theory synthetics in black, with ray theory predicted SKS travel times shown in blue and pseudospectral SPdKS picks in red. There are two distinct differences between the pseudospectral and the full wave theory results. First, the full wave theory SKS amplitude decays faster with distance, as is expected for 3D spherical wavefront spreading compared to the 2-D cylindrical wavefronts of the pseudospectral model. Second, the pseudospectral method shows significant contamination from upper mantle multiples such as sPPP, pPPP, and PPP which naturally emerge from our wave propagation calculations and decay slowly with distance due to 2-D geometry. These phases are not strongly observed in real data due to the large degree of heterogeneity and attenuation in the uppermost mantle of the real Earth, and are likewise often unobserved in 1-D modeling methods due to exclusion of upgoing rays and free-surface reflections. Their presence makes our analysis of SPdKS slightly more “noisy”, but does not preclude useful results.

The SPdKS arrivals are very similar between the two methods. The measurements we extract from our pseudospectral synthetic seismograms are the SKS and SPdKS travel times and observations of SKS and SPdKS waveform changes. These measurements are consistent between the pseudospectral and full wave theory synthetics, which creates confidence in our results.

4.8 Conclusions

The global 2-D pseudospectral method presented here has both advantages and disadvantages. The amplitude decay of all phases due to geometric spreading will never be correctly predicted for a 3-D, quasi-spherical Earth by this 2-D, cylindrical algorithm. Making an accurate spreading correction for all phases over all epicentral distances would be very complicated, so this code will probably never produce reliable absolute amplitudes in its synthetic seismograms. However, over short ranges of epicentral distances for a specific phase of interest, the difference in geometric spreading is small enough that it should not impede relative comparisons between two related phases, such as SKS and SPdKS.

This 2-D global pseudospectral code produces much stronger upper mantle multiple seismic phases (e.g. pPPP, sPPP, and PPPP) than are observed in the real Earth or the synthetics produced by many other modeling algorithms. This is partially because

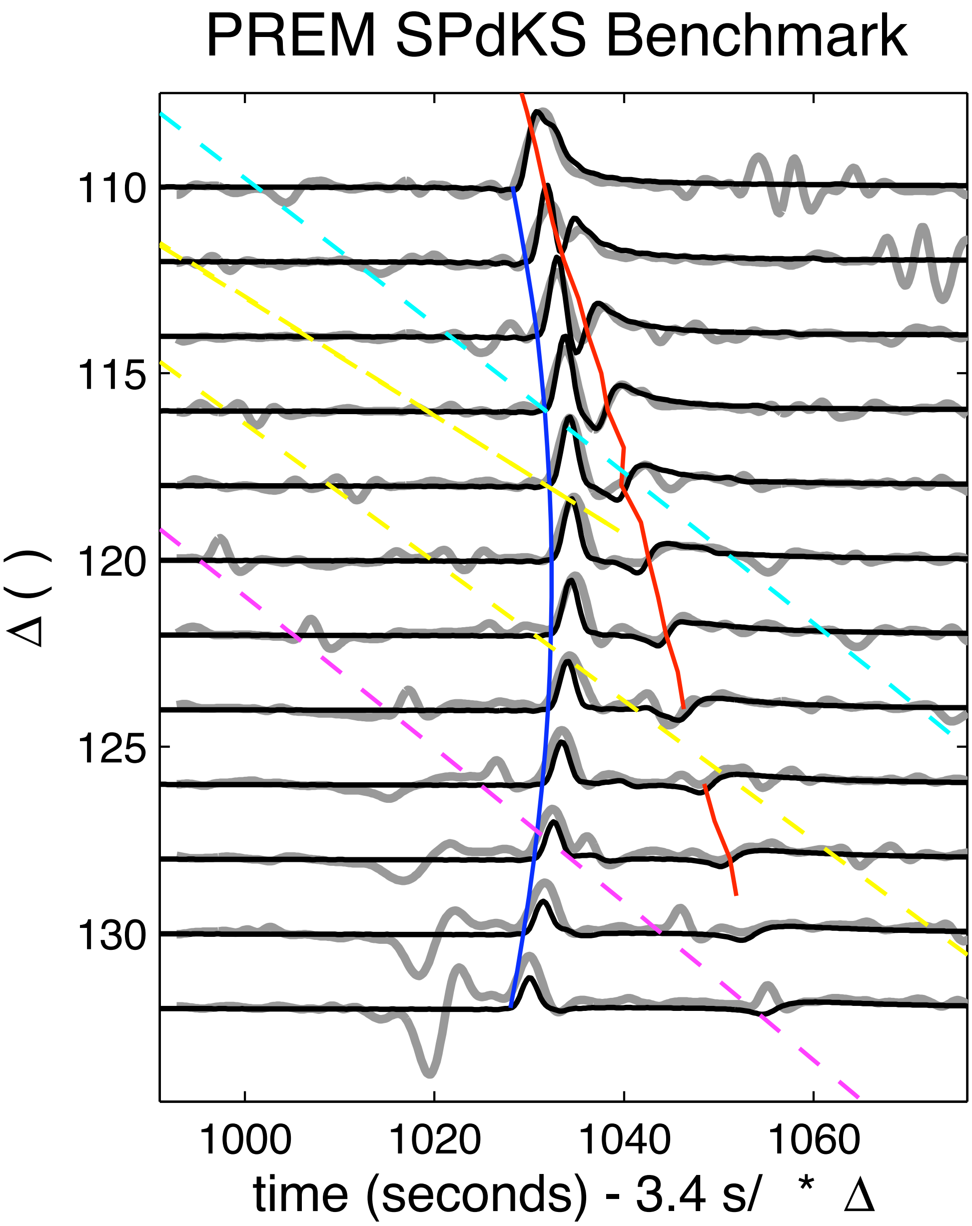

Figure 4-5: Pseudospectral synthetic seismograms (gray lines) and full wave theory synthetic seismograms (black lines) for PREM [*Dziewonski and Anderson*, 1981] and identical source functions. Blue line shows SKS travel time predictions from the TauP Toolkit *Crotwell et al.* [1999], red line shows SPdKS picks from pseudospectral traces, and cyan, yellow, and magenta dashed lines show sPPP, PPPP, and pPPPP TauP travel time predictions.

the Earth models we use with this code tend to be simple, 1-D PREM [*Dziewonski and Anderson*, 1981] everywhere except the region of interest (in our case, the core-mantle boundary). The lack of real-world heterogeneity and attenuation in the upper mantle, lithosphere, and crust of these models prevents the natural dissipation of these upper-mantle reverberations. This is probably exacerbated by the slower amplitude decay associated with our 2-D, cylindrical geometric spreading of the wavefronts. Finally, this algorithm allows unrestricted interaction of the full wave field with the free-surface, while many other algorithms exclude upgoing waves from the source and free-surface reflections.

Computationally the pseudospectral method excels at simulating seismic wave propagation with very low numerical dispersion for relatively coarse grid spacing. However, the computational cost of running the code is fairly high due to the multiple fourier transforms of the wavefield at every time step, and using periodic and anti-periodic cancellation of the wrap-around wavefield doubles it. The current variable grid implementation of this code with periodic boundary conditions runs at our local Linux cluster on 16 two-processor nodes for around twelve hours in order to calculate 1638 seconds of P-SV wave propagation (the SH code runs on 8 two-processor nodes for a slightly shorter time to calculate the same time span of wave propagation). This must then be doubled in order to run the version of the code with the anti-periodic boundary conditions, so that the wrap-around wavefield may be averaged out.

Despite these costs and compromises, the global pseudospectral algorithm presented here provides a useful and reliable way to forward model seismic wave propagation through complex 2-D Earth structures. Those complex 2-D structures are inaccessible to popular 1-D modeling approaches, and the results are produced with lower computational costs and higher frequencies than are currently available from the 3-D spectral element method. While this algorithm is not the final word in forward modeling global seismic wave propagation through complex Earth structure, it is a useful intermediate step between the easily calculated 1-D methods of the past and the very computationally intensive 3-D methods of the future.

Chapter 5

SKS and SPdKS Sensitivity to Two-dimensional Ultra-low Velocity Zones

Abstract Seismic wave propagation through two-dimensional core-mantle boundary (CMB) ultralow velocity zones (ULVZs) is modeled using a global pseudospectral algorithm. Synthetic seismograms are constructed for several types of ULVZ models, focusing on SKS and the related SPdKS / SKPdS phase which results from the intersection of the SKS wave with the CMB at the ScP critical incidence angle. One-dimensional (1-D) models with sharp and gradational upper boundaries and one-sided two-dimensional (2-D) models with different quasi-1-D CMB structures on the source and receiver sides of the CMB are run to provide a baseline for comparison of other 2-D models. Finite width 2-D ULVZ models are used to test the sensitivity of the SPdKS travel time and waveform to different portions of the P-diffracted portion of the wavepath and to explore the minimum width necessary for a ULVZ to produce observable changes in SPdKS. We find that ULVZs narrower than 100 km will not produce observable changes or delays in the SPdKS waveform. Our results give four tools useful for identifying and characterizing 2-D ULVZ structures, all most useful if array data in something resembling a 2-D geometry is available. First, dual SPdKS pulses on a seismogram indicate exposure to at least two different CMB velocity structures. If the two SPdKS pulses are similar in amplitude, they may indicate different quasi-1-D velocity structures on the source and receiver-side CMB. If the first pulse is PREM-like and signif-

icantly smaller than the second ULVZ-like SPdKS, it may indicate Pdiff inception outside of and propagation into a ULVZ. Second, a strong SKS precursor probably indicates a very "strong" (thick and/or large velocity-perturbations) ULVZ. If the precursor is similar in amplitude to the SKS pulse, it indicates similarly strong ULVZ structure on both source and receiver-side CMB regions, and if the precursor is smaller than the SKS pulse, it may indicate a ULVZ on only the source or receiver side of the CMB. The absence of SKS precursors in most previous ULVZ studies indicates that very strong, sharp ULVZs are not very common. Third, while ULVZ models based on SPdKS travel times are highly non-unique, we present a graph of mean SPdKS delays relative to PREM which provides constraints on minimum ULVZ strength and width combinations required to produce a given travel time delay. Finally, tracing SPdKS arrivals back to the inception epicentral distance on seismic sections may offer an independent tool for identifying P-velocity perturbations at the base of the mantle. Combining all of this with other CMB-sensitive phases (especially ScS, PcP, and ScP precursors and postcursors) may provide the best constraints on fine-scale CMB structure.

5.1 Introduction

The boundary between Earth's liquid, mostly-iron outer core and its solid silicate mantle spans contrasts in density, chemical composition, and viscosity as great as those found at the surface of the Earth between the solid crust and the fluid ocean and atmosphere [*Jeanloz and Williams*, 1998]. At the Earth's surface, we observe that the contrast in physical, chemical, and thermal states leads to many interesting dynamic processes, from plate tectonics and its associated mountain building and subduction to weathering and erosion. These processes in turn lead to interesting structure and heterogeneity at spatial scales ranging from the continent-ocean dichotomy to basin and range features to erosion-created fractal drainage basin structures. This complexity of the Earth's surface leads to speculation on what analogous complexity may exist at the Earth's core-mantle boundary (CMB).

Large-scale (hundreds to thousands of kilometers) structures probably related to mantle downwelling (subduction) and upwelling (the Pacific and African "super-plumes") have been observed at the bottom of the mantle using seismic tomography [*van der Hilst et al.*, 1998;

Grand, 2002; *Trampert and van der Hilst*, 2005] and have been inferred from geodynamic models of mantle convection [*Tackley*, 1998; *Tackley et al.*, 2005; *van Thienen et al.*, 2005]. Very small-scale (micrometers to millimeters) compositional variation near the CMB may be probed by mineral physics using high-pressure, laser-heated diamond cells [*Knittle*, 1998; *Murakami et al.*, 2004; *Shim*, 2005] or theoretical calculations [*Wentzcovitch et al.*, 1995; *Bukowinski and Akber-Knutson*, 2005]. The intermediate spatial scales are studied using a variety of seismic tools. Together, these approaches hint at complex structures at the CMB [*Garnero*, 2004].

Here we focus on ultra-low velocity zones (ULVZs): thin regions of mantle just above some portions of the CMB which are characterized by large P and S-wave velocity reductions. There are several proposed explanations for low velocities in ULVZs. Probably the most often-quoted hypothesis is the presence of partial melt [*Williams and Garnero*, 1996; *Revenaugh and Meyer*, 1997; *Helmberger et al.*, 1998; *Vidale and Hedlin*, 1998; *Williams et al.*, 1998; *Zerr et al.*, 1998; *Berryman*, 2000; *Wen*, 2000; *Ross et al.*, 2004]. However, variations in chemical composition on the mantle side of the CMB [*Manga and Jeanloz*, 1996; *Stutzmann et al.*, 2000], "sediments" of finite rigidity collecting on the top of the outer core [*Buffett et al.*, 2000; *Rost and Revenaugh*, 2001], and a gradient in the mantle-core transition (rather than the traditional sharp CMB) [*Garnero and Jeanloz*, 2000a, b] have also been proposed, singly and in combination. Most recently, *Mao et al.* [2006] proposed that iron enrichment in the newly discovered post-perovskite phase [*Murakami et al.*, 2004] might account for ULVZs.

There are several seismic phases which are very sensitive to CMB structure and have been used to test many areas of the CMB for the presence of ULVZs (well summarized by *Thorne and Garnero* [2004]). They include precursors and postcursors in stacks of short period and broad band ScP [*Vidale and Benz*, 1992; *Garnero and Vidale*, 1999; *Castle and van der Hilst*, 2000; *Reasoner and Revenaugh*, 2000; *Persh et al.*, 2001; *Rost and Revenaugh*, 2001, 2003], ScS [*Avants et al.*, 2006], and PcP [*Mori and Helmberger*, 1995; *Kohler et al.*, 1997; *Revenaugh and Meyer*, 1997; *Havens and Revenaugh*, 2001; *Persh et al.*, 2001; *Ross et al.*, 2004]; scattered precursors to PKP [*Vidale and Hedlin*, 1998; *Wen and Helmberger*, 1998a; *Thomas et al.*, 1999; *Wen*, 2000; *Ni and Helmberger*, 2001; *Niu and Wen*, 2001], and SKS [*Stutzmann et al.*, 2000]; and travel time and waveform anomalies in PKPdf and PKPbc [*Helmberger et al.*, 2000], PKPab-PKPdf [*Ni and Helmberger*, 2001], and various combinations of ScS-S, SKS-S, PcP-P, SHdiff, Pdiff, and SKS [*Wen*, 2001; *Simmons and Grand*, 2002; *Ni and Helmberger*, 2003].

This project focuses on SPdKS / SKPdS (Figure 4-1), a phase which is derived from an SKS wave that intersects the CMB at the ray parameter for which there is a complex pole in the mantle S to core K transmission coefficient; this results in a diffracted P-wave (Pdiff, or Pd) traveling along the mantle side of the CMB on either the source (SPdKS) or receiver (SKPdS) side of the path [*Choy*, 1977]. (Henceforth we refer to both the source-side SPdKS and the receiver-side SKPdS as "SPdKS".) Because the mantle paths of SKS and SPdKS are nearly identical, comparison of these two phases allows isolation of travel time and waveform effects of CMB structure. Short and long-period SPdKS have been used to search for and characterize ULVZs on the CMB under the Pacific Ocean, North America, Iceland, Africa, the Atlantic Ocean, and the Indian Ocean [*Garnero et al.*, 1993; *Garnero and Helmberger*, 1995, 1996; *Helmberger et al.*, 1996; *Garnero and Helmberger*, 1998; *Helmberger et al.*, 1998; *Wen and Helmberger*, 1998b; *Helmberger et al.*, 2000; *Rondenay and Fischer*, 2003; *Thorne and Garnero*, 2004].

Most previous studies applied 1-D modeling approaches to characterizing the ULVZ layer. However, there are limitations to the constraints SPdKS alone can provide on ULVZ structure. The non-uniqueness of 1-D ULVZ models and the trade-offs between the layer thickness, velocity perturbations, and density perturbations in controlling SPdKS delay time and amplitude have been well documented [*Garnero and Helmberger*, 1998; *Garnero et al.*, 1998; *Garnero and Jeanloz*, 2000a]. Additionally, the best-fitting 1-D ULVZ structures for earthquake-station pairs with very similar SPdKS CMB paths are often quite different; later we present an example where two SPdKS paths are separated by less than 50 km and yet one is best modeled by PREM and the other by fairly strong velocity perturbations from PREM [*Thorne and Garnero*, 2004]. The complexity of these results indicates that the assumptions underlying the use of 1-D modeling are not always valid.

Two previous studies modeled the seismic effects of 2-D ULVZ structures. *Helmberger et al.* [1996] modeled SPdKS waveforms due to 2-D CMB structure with the Cagniard-de Hoop method by combining different 1-D source and receiver-side CMB structures, in the form of different source and receiver-side transmission and reflection coefficients. *Wen and Helmberger* [1998b] combined generalized ray theory solutions, finite-difference calculations, WKB, and Kirchhoff theory to model wave propagation through a variety of dome and box-shaped 2-D ULVZ structures on the CMB. We introduce a new approach to modeling seismic wave propagation through 2-D ULVZ models, the pseudospectral method [*Fornberg*, 1988, 1996], which combines the flexibility of arbitrarily complex velocity structures with the simplicity of a single numerical approach.

While the 2-D global pseudospectral method offers the opportunity to investigate many interesting questions, in this paper we focus on three main points of inquiry. First, does the presence of different quasi-1-D structures on the source and receiver side of the SPdKS path produce useful "fingerprints" in the observed waveforms? Second, which part of the Pdiff section of the SPdKS propagation path has the most influence on the SPdKS travel time and waveform – the inception point, the point at which it exits into the core, or the middle of the path? Finally, how wide must a 2-D finite-width ULVZ be in order to produce measurable SPdKS delays relative to PREM?

5.2 Pseudospectral Wave Propagation Modeling

Global seismic wave propagation through 1-D and 2-D ULVZs is modeled using a cylindrical pseudospectral algorithm (see Chapter 4). The pseudospectral method is distinguished by its use of Fourier transforms to estimate the spatial derivatives in the elastic equations and the equations of motion as the wavefield is stepped forward through time. It can be thought of as the high accuracy limit of the finite difference method, and is advantageous because this approach results in very low numerical dispersion [*Fornberg*, 1988; *Kosloff and Kessler*, 1990; *Fornberg*, 1996; *Furumura et al.*, 1998; *Cormier*, 2000].

A gaussian source-time function with a standard deviation of 0.6 seconds is added to the horizontal component of the velocity at the source node, 500 km below the surface of the Earth. Synthetic seismograms are produced by reading out the velocity wavefields at given surface nodes every 0.2 s. A line-source to point-source correction is applied to the output seismograms for better comparison between the 2-D geometry of the pseudospectral model space and the 3-D geometry of the Earth. The output seismograms are also converted from velocity to displacement.

We use the SPdKS-SKS delay time as the main parameter for characterizing ULVZ structure. While differences in SKS and SPdKS waveform shape and amplitude are also of interest, they are more difficult to quantify and are complicated in our synthetic seismograms by the presence of upper mantle multiple phases (sPPP, pPPP, PPPP, etc.) which interfere with the SKS and SPdKS arrivals in the epicentral distance range of interest. The epicentral distance at which SPdKS first appears in the synthetic seismograms and the absolute moveout of the SPdKS phase are also useful for characterizing ULVZ velocities, but these parameters are less readily observable on seismograms from single stations or arrays which are not aligned along the event-station great-circle path. In addition, referencing the SPdKS travel times to the SKS travel times removes most influence of the mantle and core portions of the wave propagation path and allows us to focus on the influence of the CMB portion of the SPdKS path.

In order to more quantitatively compare the SPdKS arrivals resulting from different velocity models, we used the following processing steps. First, the SKS arrivals were automatically picked, starting with the SKS predicted travel time from the TauP toolkit [*Crotwell et al.*, 1999] and finding the appropriate zero crossing near that prediction. Second, SKS was eliminated from the section using principal component analysis (PCA) [*Rondenay and Fischer*, 2003], and on some sections PCA was also used to eliminate some of the upper mantle multiple phases which cross SKS and SPdKS in the epicentral range of interest. However, sometimes the PCA introduced more waveform anomalies than it usefully eliminated and we therefore restricted its use. Finally, SPdKS arrival times were hand picked on all sections.

5.3 Pdiff Inception Point Location

In order to create 2-D ULVZ velocity models to explore the properties of SPdKS, we need to understand where the Pdiff inception is expected to occur on the CMB. As *Choy* [1977] described and *Garnero et al.* [1993] and *Helmberger et al.* [1996] elaborated upon, there is a particular ray parameter, p_{incep}, for which a complex pole exists in the mantle S to core K transmission coefficients and S-wave energy incident on the CMB is converted to a diffracted P-wave traveling along the mantle-side of the core-mantle boundary. We use the TauP Toolkit [*Crotwell et al.*, 1999] to calculate where that critical point of Pdiff inception occurs along the SPd(iff)KS and SKPd(iff)S paths for a suite of one-dimensional ULVZ and PREM velocity models.

The inception slowness for a given velocity model is calculated with the simple formula

$p_{incep} = R_{CMB}/V_P$ where V_P is the P-wave velocity on the mantle side of the CMB. This parameter has values ranging from 253.7 s/rad (4.43 s/°) for PREM to 281.9 s/rad (4.92 s/°) for a 10% P-wave velocity reduction at the base of the mantle. The slowness associated with SKS arriving at a range of epicentral distances (90° to 131°, at 1° increments) was calculated using the taup_time module. The output of these calculations was interpolated to find the inception epicentral distance, Δ_{incep}, for which the SKS arrival had slowness p_{incep}. The inception epicentral distance was then used with taup_pierce to find the point at which an SKS ray of inception slowness pierces the CMB on the source and receiver sides of the SKS path. We call these piercing points the Pdiff inception points.

Table 5.1 shows the results of these calculations for multiple ULVZ models and the PREM standard earth model. ULVZ models are designated as follows:
ULVZ_{a}km_{1D/grad}_{b}P_{c}S where {a} gives the thickness of the 1-D ULVZ layer, {1D/grad} denotes whether the layer has constant or gradational P and S velocity perturbations within that layer, and {b} and {c} give the percent P and S-wave low velocity perturbations, respectively. Velocity models with "1D" in the name have the same P and S-velocity perturbations relative to PREM from the top of the ULVZ layer to the CMB. Gradient models are as described in section 5.4.1.

Two factors control the inception epicentral distance and the position of the inception point along the SKS ray path in this calculation. The mantle-side P-wave velocity at the CMB controls the inception slowness directly. Then the integrated effect of the height of the velocity anomaly and magnitude of the S-velocity perturbations controls the amount of deflection the mantle S-wave experiences in the ULVZ and therefore the location at which the ray path for a given inception slowness pierces the CMB, and the epicentral distance at which that ray reaches a receiver on the surface. When the inception distance (Δ_{incep}) is plotted against the P-velocity perturbation for all models in Table 5.1, it becomes clear that the control of the P-velocity on the inception slowness is the dominant factor influencing the epicentral distance at which SPdKS should be first observed (Figure 5-1).

These results imply that if it were possible to trace back the SPdKS branch and determine the inception epicentral distance using array data covering a useful range of epicentral distances (95 - 130 degrees), this would give an independent constraint on the P-velocity perturbation at the base of the mantle, since Δ_{incep} and the Pdiff inception point are both much more sensitive to changes in the inception slowness than to changes in the thickness

Table 5.1: Inception Point Calculation Results. Variations in inception slowness, p_{incep}, are controlled by the P-velocity at the base of the mantle, while variations in the inception epicentral distance, Δ_{incep}, and the source and receiver-side Pdiff inception points on the SPdKS path are controlled by p_{incep} and the ray-path deflection of the mantle S wave due to the ULVZ.

Model	**p_{incep}**		**Δ_{incep} (°)**	**inception point (°)**	
	(s/rad)	**(s/°)**		**source-side**	**receiver-side**
ULVZ_40km_1D_10P_30S	281.91	4.9202	99.497	14.39	84.07
ULVZ_20km_1D_10P_30S	281.91	4.9202	99.642	14.48	84.12
ULVZ_10km_1D_10P_30S	281.91	4.9202	99.854	14.50	84.32
ULVZ_5km_1D_10P_30S	281.91	4.9202	99.890	14.53	84.33
ULVZ_40km_fullgrad_10P_30S	281.91	4.9202	99.645	14.48	84.13
ULVZ_40km_halfgrad_10P_30S	281.91	4.9202	99.633	14.42	84.18
PREM_variabledy_v11	253.72	4.4282	106.06	12.77	82.36
ULVZ_40km_1D_2.5P_7.5S	260.22	4.5418	104.57	13.13	90.49
ULVZ_40km_1D_2.5P_2.5S	260.22	4.5418	104.64	13.16	90.53
ULVZ_40km_1D_5P_15S	267.07	4.6613	102.87	13.55	88.33
ULVZ_40km_1D_5P_5S	267.07	4.6613	103.01	13.60	88.42
ULVZ_40km_1D_7.5P_22.5S	274.29	4.7873	101.29	13.91	86.38
ULVZ_40km_1D_7.5P_7.5S	274.29	4.7873	101.42	14.00	86.41
ULVZ_5km_1D_2.5P_7.5S	260.22	4.5418	104.65	13.17	90.53
ULVZ_5km_1D_2.5P_2.5S	260.22	4.5418	104.66	13.17	90.54
ULVZ_5km_1D_5P_15S	267.07	4.6613	103.01	13.63	88.39
ULVZ_5km_1D_5P_5S	267.07	4.6613	102.99	13.65	88.36
ULVZ_5km_1D_7.5P_22.5S	274.29	4.7873	101.52	14.02	86.50
ULVZ_5km_1D_7.5P_7.5S	274.29	4.7873	101.55	14.03	86.51

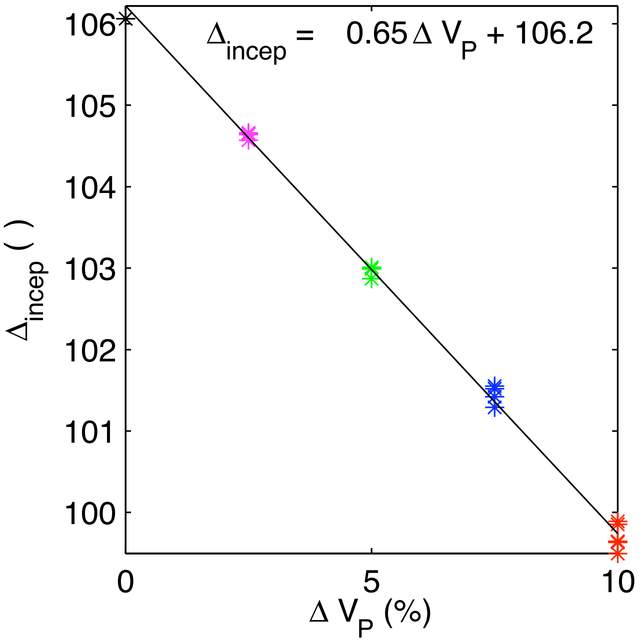

Figure 5-1: SPdKS Pdiff inception epicentral distance, Δ_{incep}, plotted against P-velocity perturbation for all the models presented in Table 5.1.

and S-velocity structure of the ULVZ. However, this scenario may be less applicable to real, finite-frequency waves for which the single inception point of ray theory becomes a frequency dependent shift in the value of the S to K transmission coefficient over a more dispersed set of wavenumbers [*Choy*, 1977], even for relatively simple 1-D ULVZ models.

5.4 Ultra-low Velocity Zone Models

5.4.1 Velocity Models

All velocity, density, and attenuation Earth models (henceforth referred to as simply "velocity models") presented in this paper are based on the one-dimensional isotropic Preliminary Earth Reference Model (PREM) [*Dziewonski and Anderson*, 1981]. However, the crust and ocean layers of PREM are replaced by mantle parameters for the following combination of reasons. The low velocity crust and ocean layers occur in the portion of the grid space with the greatest lateral grid spacing and therefore would limit the frequency content of the whole model. In addition the 1-D approximations of PREM are probably least valid for the crust and ocean layers, which are highly variable in the real Earth. And finally, for the SKS and SPdKS seismic phases modeled here, the paths through the crust and mantle are nearly identical and any differences in Earth structure along those paths cancel out when we consider the difference between those two phases. The substitution of mantle for crust and ocean therefore increases the frequency content of our results with no negative effects on our ability to study the sensitivity of these seismic waves to CMB structure.

"Ultralow Velocity Zones" (ULVZs) are created by multiplying the 1-D PREM P and S-wave velocities by a 2-D matrix of perturbation factors in the region of interest just above the CMB. We ran the pseudospectral seismic wave propagation code on four sets of ULVZ models, with a total of sixty-three different models. All used P:S velocity perturbation ratios of 1:3 as suggested by *Williams and Garnero* [1996] for core-mantle boundary velocity reductions related to the presence of partial melt. *Williams and Garnero* [1996] arrived at this ratio by modeling elastic properties of two-phase aggregates of mantle silicate and melt at CMB conditions and finding the range of silicate melt volume fractions which could cause a 10% P-velocity decrease (<5 to 30% melt fraction, depending on aspect ratio of the fluid geometry in the solid-liquid aggregate). They then found that this range of melt fractions would cause a ∼30% S-velocity decrease, roughly independent of melt geometry.

One-dimensional models

Nine one-dimensional models were run. The first is PREM, which is used as a baseline for comparing the synthetic seismograms produced by all other models. The other eight (Figure 5-2a) contain ULVZs of varying heights (40 km, 20 km, 10 km, and 5 km), varying velocity perturbations (10% P-velocity and 30% S-velocity decreases or 5% P-velocity and 15% S-velocity decreases), and in two cases, varying vertical gradients in velocity perturbation at the top of the model. These 1-D models gave us a basis for comparison with other 1-D modeling results and with our 2-D ULVZ models.

If ULVZs are the result of partial melting or some other interaction between the geotherm and the chemical composition of the lower mantle rocks, a gradational "fuziness" of the ULVZ upper boundary might be expected. In contrast, if ULVZs are related to a phase change over a fairly small pressure (and therefore, depth) range, similar to the upper mantle discontinuities, a much sharper ULVZ upper boundary might be expected. We test whether SKS and SPdKS waveforms would be sensitive to the difference between "sharp" and "fuzzy" ULVZ upper boundaries using two models with vertical gradients in ULVZ velocity perturbations. The "full gradient" model has a linear increase in the velocity perturbations from 0 at 40 km above the CMB to 10% P and 30% S perturbations at the CMB. The "half gradient" model has a similar linear increase in velocity perturbations from 0 at 40 km above the CMB to the full 10% P and 30% S velocity perturbations 20 km above the CMB, and then constant 10% P and 30% S velocity perturbations down to the CMB.

One-sided ULVZ models

The second class of velocity models (Figure 5-2b and c) feature a simple ULVZ with constant velocity perturbations on either the source or the receiver side of the core mantle boundary region. The CMB region on the other side of the SKS ray path has PREM velocities. Each ULVZ has 10% P and 30% S-velocity perturbations and is 40 km, 20 km, 10 km, or 5 km thick. A smooth cosine horizontal gradient transitions between the ULVZ velocity perturbations and the PREM velocity model halfway between the source and the receivers (at an epicentral distance of 54°) with a half-width of 10° (600 km). These represent the simplest possible 2-D ULVZ models and also form a useful comparison set for narrower "finite-width" 2-D models.

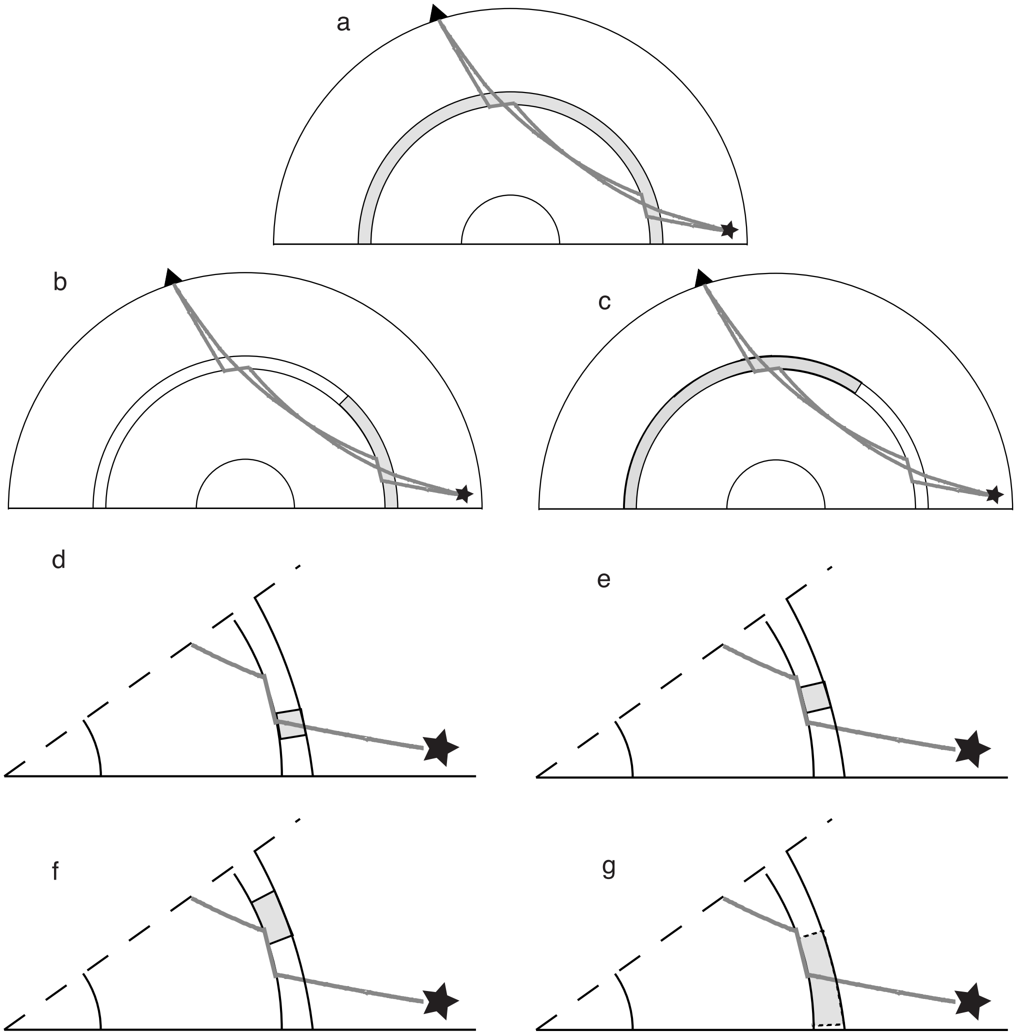

Figure 5-2: Illustrations of various ultra-low velocity zone model configurations. Dark gray line shows SPdKS ray path on the source side of the CMB. Light shaded patch shows approximate ULVZ geometry, with exaggerated vertical dimensions. (a) 1-D ULVZ models. (b) Source-sided ULVZ models. (c) Receiver-side ULVZ models. Finite-width ULVZ models centered on (d) the Pdiff inception point, (e) the middle portion of the P diffracted path, or (f) the Pdiff exit point into the core; and (g) Finite width ULVZ models centered on the Pdiff inception point with varying widths.

Pdiff path sensitivity models

The third class of ULVZs is designed to test the sensitivity of the SPdKS phase to the different portions of the P-diffracted section of the ray path along the CMB. There are three subsets of these models, each of which is constructed with thicknesses of either 20 km or 40 km and P-velocity perturbations of either 5% or 10%, with corresponding S-velocity perturbations of 15% or 30%. All models have a 0.5° ($\sim$ 30 km) wide smooth cosine lateral transition between ULVZ velocities and PREM velocities and sharp upper boundaries.

The "inception point" ULVZ models (Figure 5-2d) have a finite width which begins 2.5° ($\sim$150 km) before the predicted source-side Pdiff inception point for the relevant ULVZ velocity model (thereby also including the PREM inception point) and extend to 1.5° ($\sim$90 km) beyond the ULVZ inception point (Table 5.1). "Core exit" ULVZ models (Figure 5-2f) are placed to begin 1.5° before the core entry point for SPdKS arriving at an epicentral distance of 110° and to end 1.5° after the core entry point for SPdKS arriving at an epicentral distance of 120°, giving them a total width of 13° ($\sim$780 km). "Middle" ULVZ models (Figure 5-2e) are placed to begin 2° beyond the Pdiff inception point for a 1-D version of the ULVZ in question and to end 2° before the Pdiff core entry point for an SPdKS arriving at an 110° epicentral distance, which results in a width of 6° ($\sim$360 km).

Inception point sensitivity models

The fourth class of velocity models is designed to explore how wide a simple, finite width ULVZ centered on the Pdiff inception point must be to produce detectable effects on the SPdKS arrival times and waveforms (Figure 5-2g). The parameter space explored includes ULVZ heights of 5 km, 10 km, 20 km, or 40 km above the CMB, all with 10% P and 30% S-velocity reductions. The lateral extent of the ULVZ has a value of 10 km, 20 km, 30 km, 60 km, 120 km, 240 km, 480 km, 960 km, or 1920 km (0.16°, 0.33°, 0.5°, 1°, 2°, 4°, 8°, 16°, or 32° at the CMB) centered on the Pdiff inception point. Each model has sharp upper boundaries and sharp lateral edges.

5.5 Results

5.5.1 1-D Modeling Results

Synthetic seismograms produced by running the pseudospectral seismic wave propagation code through the PREM and 1-D ultra-low velocity zone models described in section 5.4.1 are presented in Figure 5-3 plots a, c, g, and i. The SKS and SPdKS arrival times from pseudospectral PREM synthetics (Figure 5-3k) are plotted on these seismic sections for comparison.

A primary observation from Figure 5-3a is that very thick, strong ULVZs (in this case, 40 km-thick with 10% P and 30% S-velocity reductions) have strong effects on the SKS waveform as well as the SPdKS arrival time. In this case, the SKS peak is split into two peaks of quasi-equal amplitude, one of which arrives at the PREM SKS travel time and one of which arrives 5–6 s later. This travel time separation is well modeled by an S to P conversion at the top of the ULVZ using the full wave theory [*Cormier and Richards*, 1988]. The second of the "SKS" peaks is therefore the true SKS and the first peak is a phase we will call S_{ULVZ}pKS (following the convention of *Ward* [1978]), where *ULVZ* may be replaced with the depth of the top of the ULVZ.

As the strength of the ULVZ decreases with either thinner ULVZs or smaller velocity reductions (Figure 5-3c,g, and i) the travel time separation between S_{ULVZ}pKS and SKS narrows and the SKS pulse returns to a very PREM-like shape and arrival time. *Stutzmann et al.* [2000] predicted S_{ULVZ}pKS–SKS travel time separations of 3.6 s, 2.3 s, and 1.3 s for 10% P and 30% S-velocity perturbations in layers of 30 km, 20 km, and 10 km thickness, which agrees well with the modeling here. They used the lack of observed SKS precursors in a data set with SPdKS paths sampling the southwest Pacific CMB to place upper limits on the possible ULVZ strength in that region.

Figure 5-4a shows the SPdKS travel times for each 1-D model relative to the SKS travel time for that model. Figure 5-4b shows the difference between SPdKS travel times for each ULVZ model and SPdKS travel times for PREM, as well as the mean SPdKS travel time delay relative to PREM. It is clear from a comparison of the mean SPdKS delays in Figure 5-4b that very similar results are produced for the ULVZ_40km_1D_5P_15S, ULVZ_20km_1D_10P_30S, and ULVZ_fullgrad_10P_30S (linear gradient from zero perturbation at the top of the 40 km layer to full perturbation at the bottom of the layer).

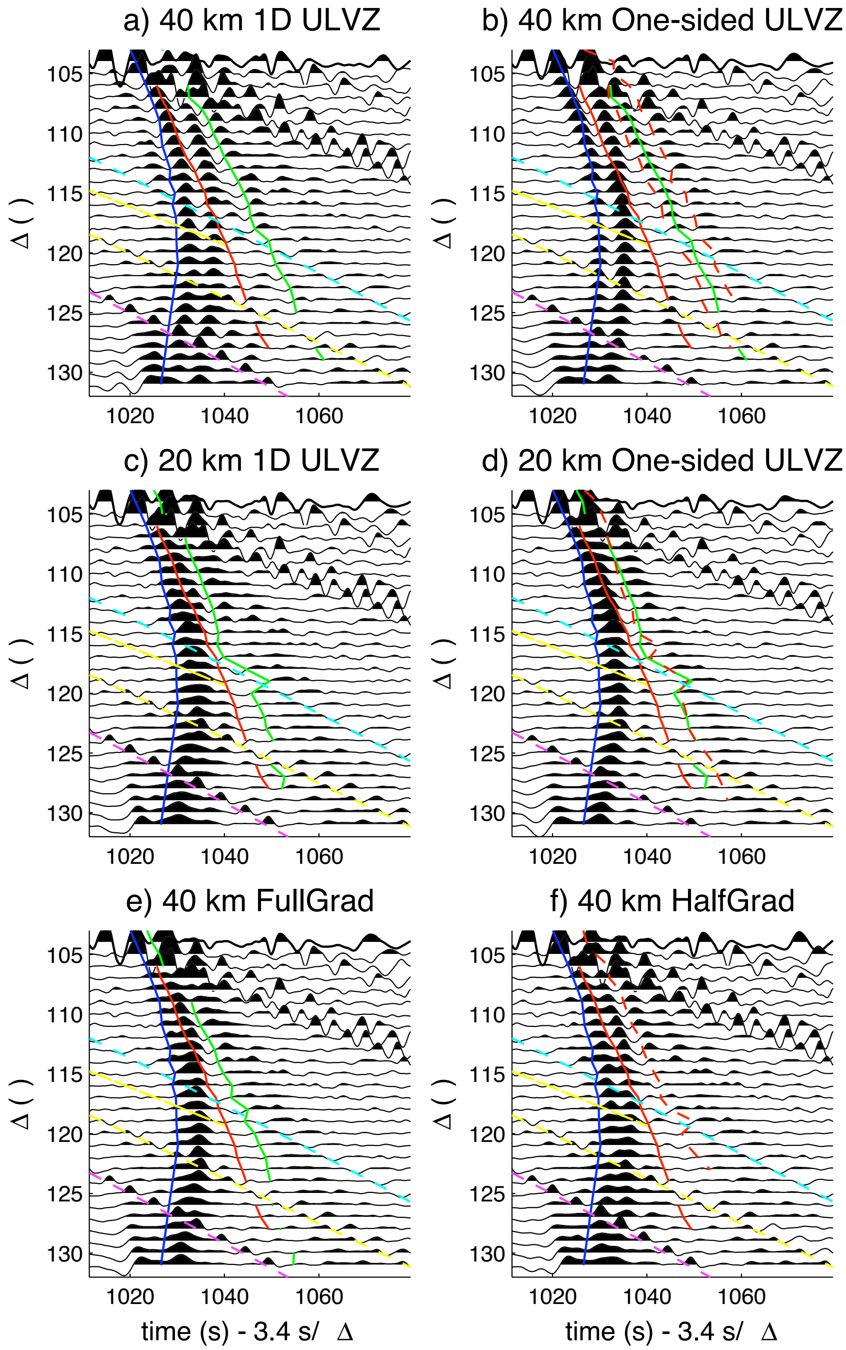

Figure 5-3: Synthetic seismograms produced by running the pseudospectral seismic wave propagation code on the 1-D, 10% P and 30% S-velocity reduction ULVZ velocity models (section 5.4.1 and Figure 5-2a), the source-side ULVZ velocity models (sections 5.4.1 and Figure 5-2b), and PREM [*Dziewonski and Anderson*, 1981]. The solid blue line shows the PREM SKS arrival and the solid red line shows the PREM SPdKS arrival. On 1-D ULVZ plots, the solid green line shows the SPdKS picks for that model. On the one-sided ULVZ plots, dashed red lines show the SPdKS picks for the one-sided model and the solid green line repeats the SPdKS for the equivalent 1-D model. Cyan, yellow, and magenta dashed lines show the predicted travel times of sPPP, PPPP, and pPPP, respectively.

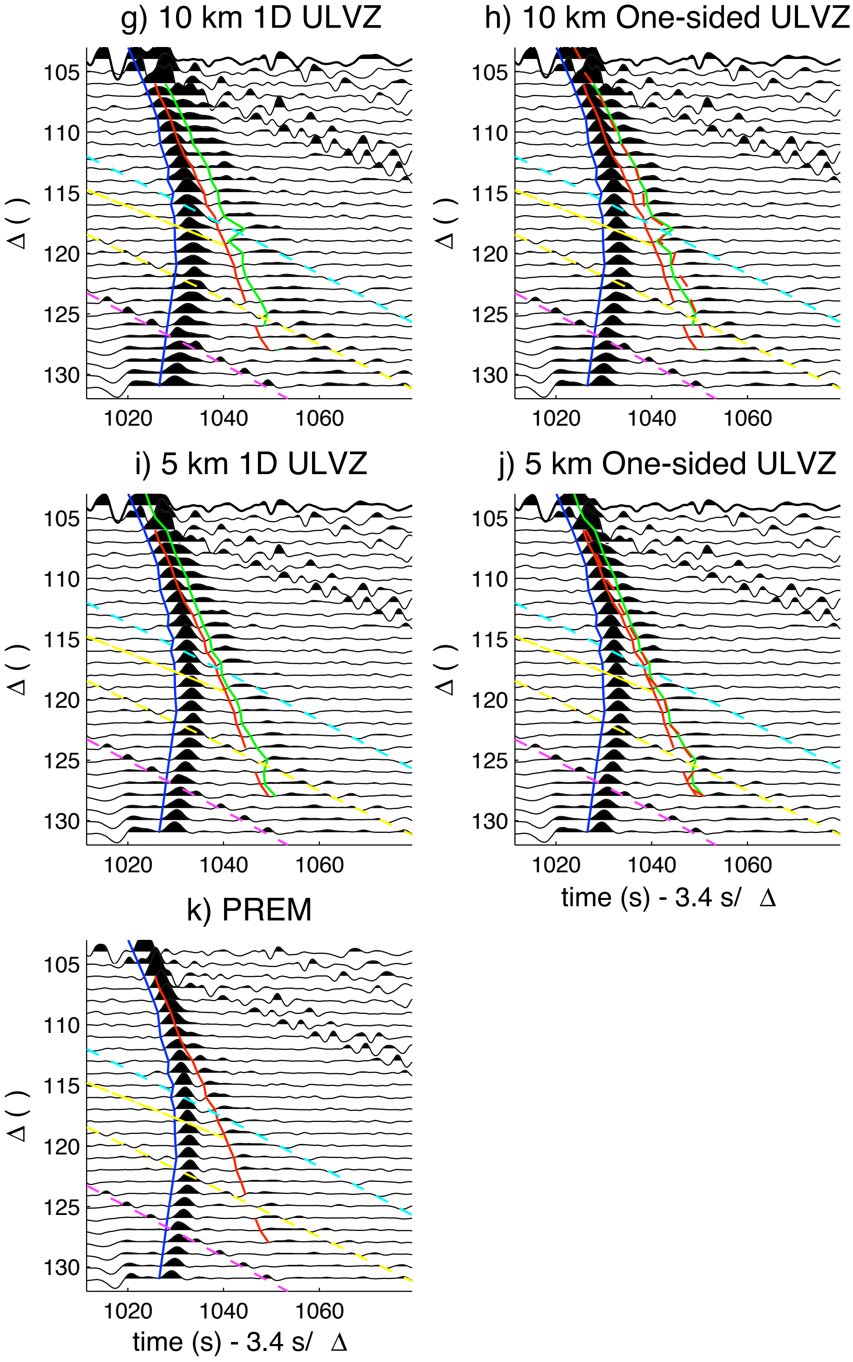

Figure 5-3 (continued)

Likewise, the mean SPdKS delay is almost the same for the ULVZ_20km_1D_5P_15S and ULVZ_10km_1D_10P_30S models.

These similarities in mean SPdKS delays between different models point to two aspects of the non-uniqueness of ULVZ modeling. First, there is a clear tradeoff between ULVZ layer thickness and velocity and density perturbations, which has been documented before [*Helmberger et al.*, 1996; *Garnero and Helmberger*, 1998; *Garnero et al.*, 1998; *Garnero and Jeanloz*, 2000a]; it is reassuring to see that our modeling produces similar results. Second, there is also non-uniqueness with respect to vertical variations in ULVZ properties.

The SPdKS traveltime delay due to a linear gradient in velocity perturbations over thickness h (Figure 5-3e) seems to be equivalent to that of a simple homogenous layer with a sharp upper boundary and the full velocity perturbation over thickness h/2 (Figure 5-3c). At the wavelengths under consideration for SKS and SPdKS here, the travel times are sensitive to the average vertical properties of the ULVZ and are largely insensitive to details of the vertical velocity structure. There are slight differences between the SKS and SPdKS waveforms produced with sharp versus gradational upper boundaries; however, they are not detectable using the SPdKS-SKS travel time delay metric which we use here. For this reason, the rest of the models presented here have simple vertical velocity profiles corresponding to constant velocity perturbations on PREM.

We parameterize the ULVZ "strength" as the product of the ULVZ effective thickness, h (km), and the P-velocity perturbation at the base of the ULVZ, dVp (%). Figure 5-5 shows the linear least-squares fit of the SPdKS delays relative to PREM, dt, and their corresponding ULVZ "strength". This reduction of 9 seismic sections of 35 traces each to 8 mean SPdKS relative delay times and then to 2 polynomial parameters suggests the ability to constrain some combination of ULVZ properties from the SPdKS travel time delays. If our h*dVp parameterization of ULVZ "strength" captured all the relevant ULVZ properties, we would expect the intercept of the dt = f(h*dVp) equation to be zero. As our fit is instead dt = 0.019 h*dVp + 0.81, it suggests that almost a whole second of SPdKS delay is unaccounted for in our current parameterization. This may suggest the need to include the S-velocity and density perturbations in a more complete measure of ULVZ "strength".

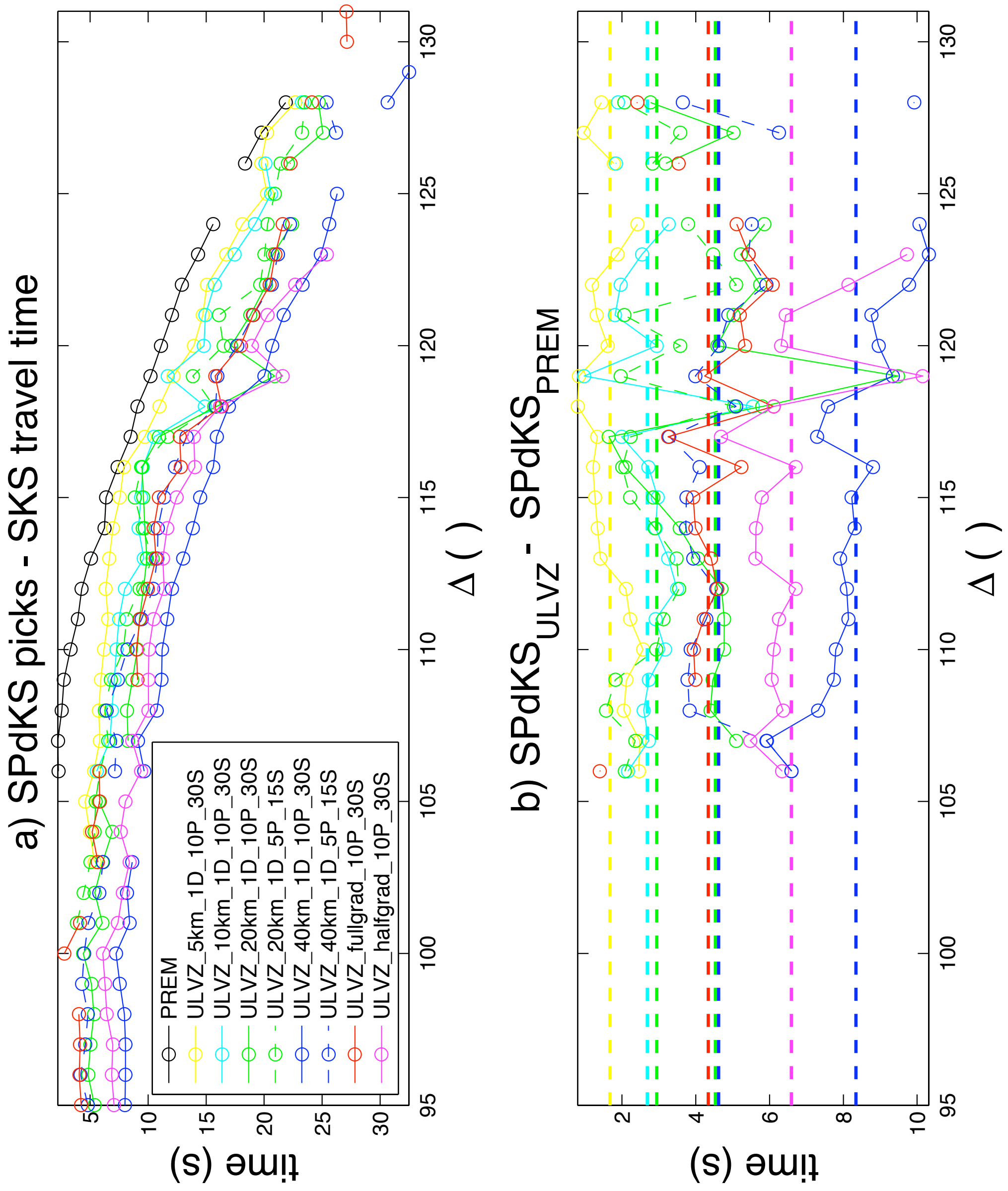

Figure 5-4: SPdKS travel time picks from 1-D models. a) SPdKS travel time picks relative to the SKS travel times for each model. b) SPdKS travel time picks relative to the SPdKS travel time for PREM. Dotted lines show the mean SPdKS travel time delay relative to PREM for each model; this value is plotted in Figure 5-5.

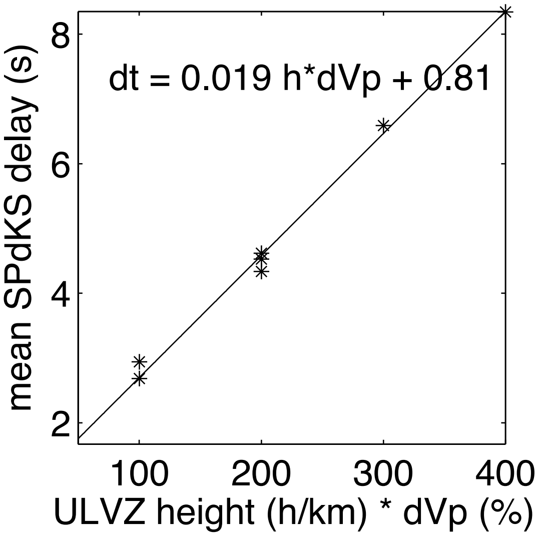

Figure 5-5: Relationship between ULVZ "strength" and the mean SPdKS delay relative to the SPdKS travel time in PREM, dt. The ULVZ "strength" is parameterized as the thickness of the ULVZ, h, times the P-velocity perturbation at the base of the ULVZ, dVp. For the 40 km-thick "fullgrad" model the effective thickness is taken to be 20 km. For the 40 km-thick "halfgrad" model, the effective thickness is taken to be 30 km. Stars show mean SPdKS delays from Figure 5-4b and line shows the linear fit to those points given by the equation for dt.

5.5.2 One-Sided ULVZ Results

We model seismic wave propagation through ULVZ models which perturbed only the source or the receiver side of the CMB (Figure 5-2b and c), and SPdKS picks from both sets of models are presented in Figure 5-6, however we plot only the source-side synthetic seismograms in Figure 5-3 as they are identical to the receiver-side synthetic seismograms. This ambiguity between SPdKS signals due to source and receiver side CMB velocity structure is well discussed by *Garnero and Helmberger* [1995], who point out that the "SPdKS" phase is actually the combination of an infinite set of raypaths which sample both sides of the CMB in various proportions; the SPdKS and SKPdS rays pictured in Figure 4-1 which sample only the source or the receiver side of the CMB are actually just end members of a spectrum of raypaths that contribute to the observed SPdKS signal on a seismic trace.

Comparing the synthetic seismograms in Figure 5-3g to Figure 5-3h and Figure 5-3i to Figure 5-3j, we see that the 1-D and one-sided SPdKS travel times for thin ULVZs are the same within picking errors (∼0.5 s), while still being measurably slower than the PREM SPdKS travel times (∼1–3 s). This is confirmed by directly comparing the SPdKS picks in Figure 5-6b. Examining the SPdKS waveforms in those same figures, it seems that the SPdKS pulse in the one-sided ULVZ synthetics is narrower than that in the 1-D 5 km and 10 km models. This is counter-intuitive, as it might be expected that the two-dimensional model with different velocity structures on the source and receiver side would have more complex SPdKS waveforms.

For the strongest ULVZ we model (40 km thick with 10% P and 30% S-velocity perturbations), we observe two important differences between the 1-D and one-sided ULVZ models (Figure 5-3a and b). First, the one-sided ULVZ model has two distinct arrivals with SPdKS moveout (dashed red lines in Figure 5-3b). The first of these has the same delay relative to the one-sided S_{ULVZ}pKS arrival time as the singular SPdKS arrival in the 1-D synthetics (Figure 5-6a). The second SPdKS-moveout arrives ∼5.6 s later than the first. It is perhaps not a coincidence that this is the same travel time separation predicted for SKS - S_{ULVZ}pKS by the full wave theory. Two SPdKS pulses are expected for a model with two different CMB velocity structures on the SPdKS / SKPdS path with different expected ray parameters for Pdiff inception [*Helmberger et al.*, 1996]. However, since one of those two CMB velocity structures is PREM, it is also expected that one of SPdKS arrivals in the

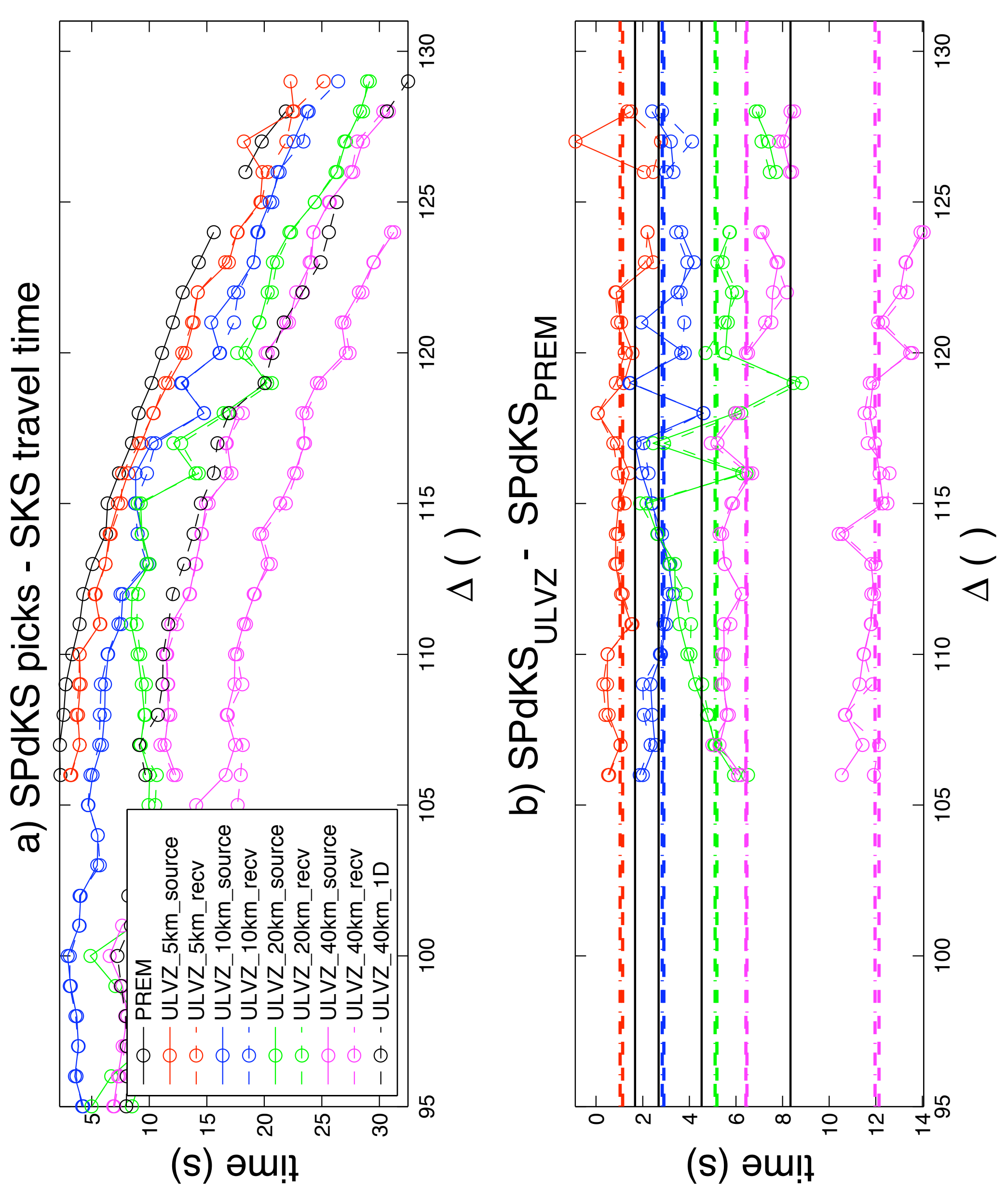

Figure 5-6: SPdKS travel time picks from one-sided ULVZ models. a) SPdKS travel time picks relative to the SKS travel time for each model. Black symbols and lines show PREM and the 40 km-thick 1-D ULVZ for comparison. b) SPdKS travel time picks relative to the SPdKS travel time for PREM. Colored dotted lines show the mean SPdKS delay relative to PREM for the source-side models and colored dash-dot lines show the mean value for the receiver-side models. Black lines show mean SPdKS delay relative to PREM for the 1-D 5km, 10km, 20km, and 40 km 10%P 30§-velocity perturbation models from Figure 5-4.

one-sided synthetics would correspond to that modeled for PREM. Instead, we find that one SPdKS pulse corresponds to that observed for an equivalent 1-D ULVZ model and the other comes in ~12 s after the PREM SPdKS arrival.

The second observation from comparison of the 1-D and one-sided 40 km-thick ULVZ synthetic seismograms has to do with the SKS waveform. While the one-sided model shows a similar splitting of the SKS waveform through the appearance of the S_{ULVZ}pKS precursor as observed in the 1-D synthetics, there are two important differences. First, for the one-sided synthetics, the S_{ULVZ}pKS / SKS amplitude ratio is ~0.6–0.9, similar to that predicted by *Stutzmann et al.* [2000], while for the 1-D synthetics the ratio is ~1.2. Second, the series of S_{ULVZ}pKS, SKS, and SPdKS pulses arrives ~2 s earlier in the one-sided models, which is clear given their position relative to the PREM SKS arrival times in Figures 5-3a and b. This slightly earlier arrival means that the first one-sided SPdKS arrival comes in a few seconds earlier than the 1-D SPdKS arrival relative to the PREM SPdKS (Figure 5-6b) even though they have the same delay relative to the S_{ULVZ}pKS of their own models.

The 20 km-thick one-sided ULVZ models (Figure 5-3d) result in synthetic seismograms with intermediate properties. Their SPdKS arrival times are similar to those observed for the equivalent 20 km-thick 1-D model. They have more complicated SKS waveforms than the 5 and 10 km-thick models, but not as distinctly split as the 40 km-thick model. Whatever processes cause the SKS split in the very strong ULVZ are probably occurring in this half-as-strong ULVZ, but are more compressed in travel time and therefore less distinct.

5.5.3 Pdiff Path Sensitivity

The synthetic seismograms modeled in this section test whether the SPdKS waveforms recorded at the surface are more sensitive to the velocity structure of the CMB at the Pdiff inception point, the Pdiff core entry point, or the middle of the Pdiff path between those two points.

Synthetic seismograms generated by propagating seismic waves through the finite width "inception point" ULVZ models described in section 5.4.1 are shown in Figure 5-7, and SPdKS picks from those seismograms are presented in Figure 5-8. The 20 km-thick models and the 40 km-thick 5% P 15% S-velocity perturbation models all show negligible deviations from PREM SKS and SPdKS travel times. The "strongest" ULVZ model, the 40 km-thick, 10% P and 30% S-velocity perturbation model, shows SPdKS arrivals at the same travel time as the equivalent "one-sided" ULVZ model for epicentral distances between 107° and 110° and then transitions back to the travel times similar to PREM SPdKS between 110° and 115°. These results for ∼240 km wide ULVZs led us to pose the question: How wide does a ULVZ need to be in order to produce significant deviations in SPdKS travel time from PREM? We attempt to answer this question in the next section.

Synthetic seismograms for the "core exit" finite width ULVZ models described in section 5.4.1 are shown in Figure 5-9 and SPdKS picks from these seismograms are presented in Figure 5-10. The SPdKS travel times in these models are identical to PREM, and the waveforms look very similar from model to model. The presence of a ULVZ around the area in which the P diffracted energy enters the core has no measurable effects on the SPdKS arrival in our models.

Synthetic seismograms for the "middle" finite width ULVZ models described in section 5.4.1 (Figure 5-2e) are shown in Figure 5-11 and SPdKS picks from these seismograms are presented in Figure 5-12. The 20 km-thick and 40 km-thick ULVZ models with 5% P-velocity perturbations (Figure 5-11a and c) show SPdKS arrival times fairly similar to PREM, but with somewhat wider pulses. The 20 km-thick and 40 km-thick ULVZ models with 10% P-velocity perturbations (Figure 5-11b and d) show something more interesting – dual SPdKS arrivals. A first, smaller pulse arrives at a travel time only slightly delayed relative to PREM (∼1.5–2 s) and a second, larger pulse is delayed ∼6.5 seconds relative to PREM SPdKS between 105° and 120°. This second apparently converges with the first pulse between 120° and 125°, although this convergence may be a picking artifact. This ∼6.5 s delay of the second pulse at epicentral distances smaller than 120° is approximately the same travel time delay as the first SPdKS pulse observed on the equivalent one-sided ULVZ models.

These "middle" models show the SPdKS phase propagating through them to be more sensitive to the P-velocity perturbation than the thickness of the layer (Figure 5-12). This may reflect that the ray parameter of the Pdiff wave is being reset as it propagates horizontally along the CMB from its inception point in the PREM area outside the ULVZ through the region with reduced velocities. This is similar to the observation by *Wysession et al.* [1999] that apparent slownesses for the Sdiff and Pdiff phases are a function of the mean velocity at the base of the mantle.

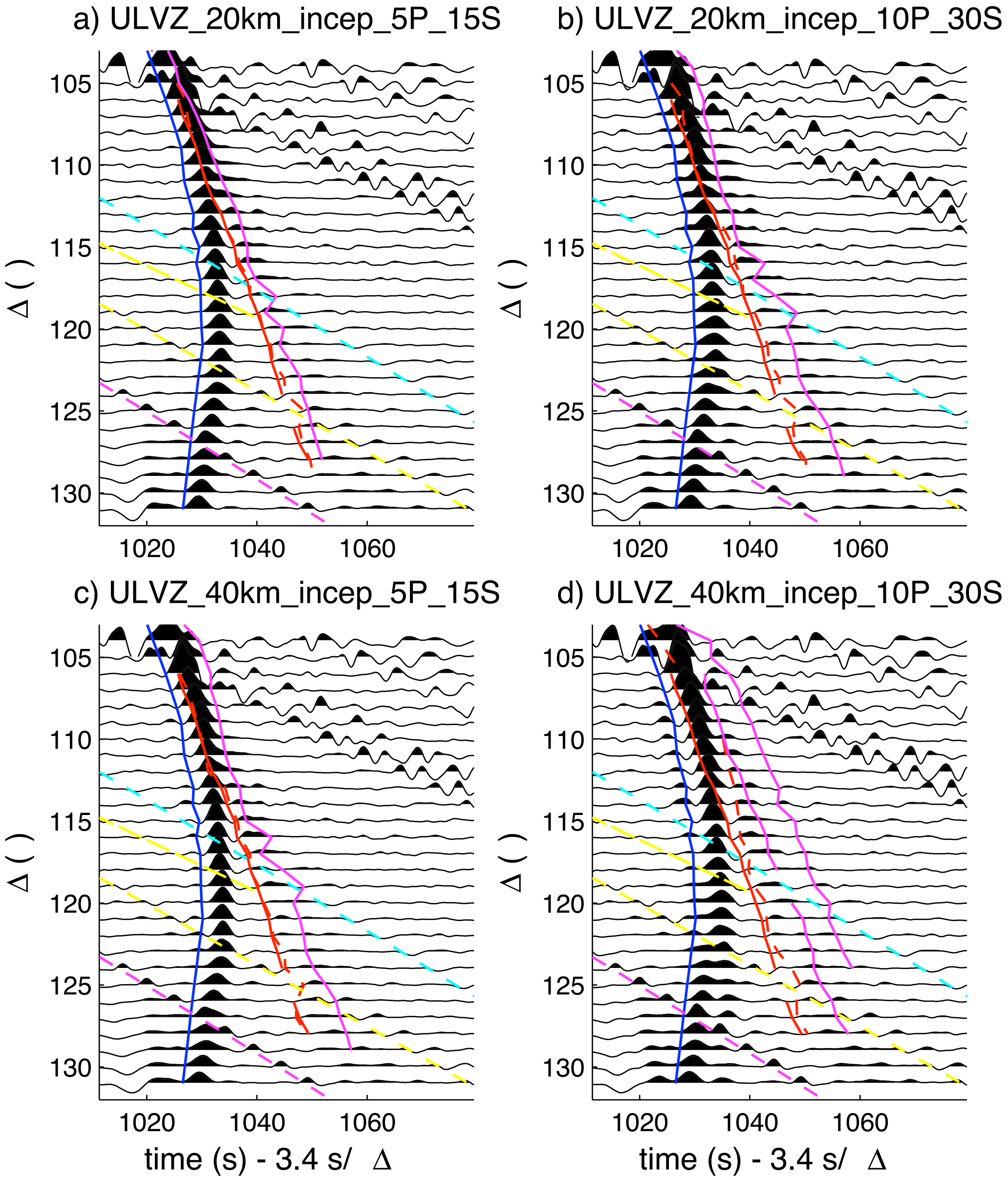

Figure 5-7: Synthetic seismograms for first set of finite width inception models. Blue line shows SKS picks from PREM pseudospectral synthetic seismograms. Solid red line shows PREM SPdKS picks. Dashed red line shows SPdKS picks for this model. Solid magenta lines show SPdKS picks for equivalent (same height and velocity perturbations) one-sided ULVZ model. Dashed cyan, yellow, and magenta lines show travel time predictions for sPPP, PPPP, and pPPP, respectively.

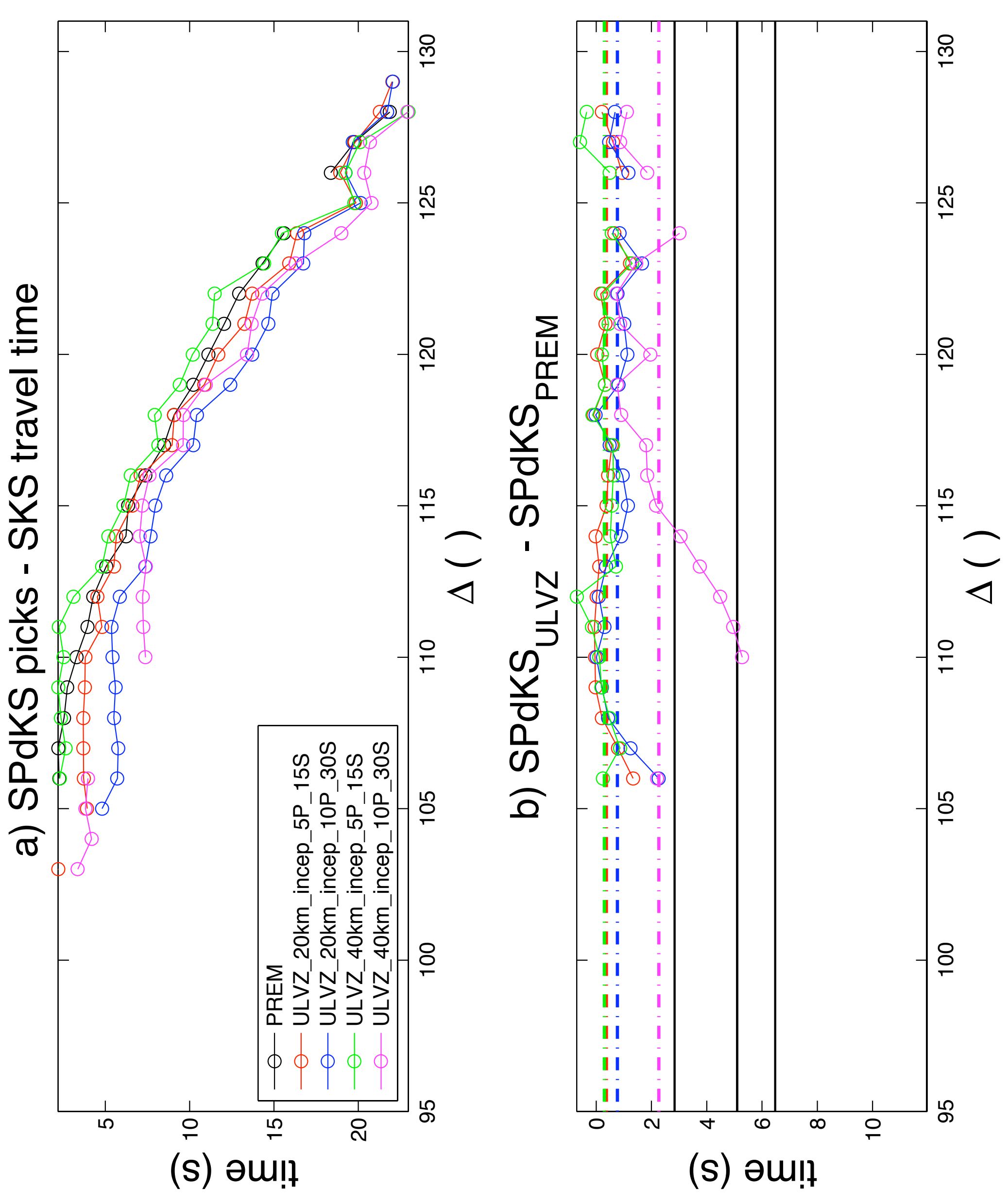

Figure 5-8: SPdKS travel time picks from the first set of finite width inception models (Figure 5-7). a) SPdKS travel time picks relative to the SKS travel time for each model. Black symbols and lines show PREM for comparison. b) SPdKS travel time picks relative to the SPdKS travel time for PREM (solid lines and circles). Colored dotted lines show the mean SPdKS delay relative to PREM for the inception models. Black dashed lines show mean SPdKS delay relative to PREM for the one-sided 10 km, 20 km, and 40 km 10%P and 30§-velocity perturbation models from Figure 5-6.

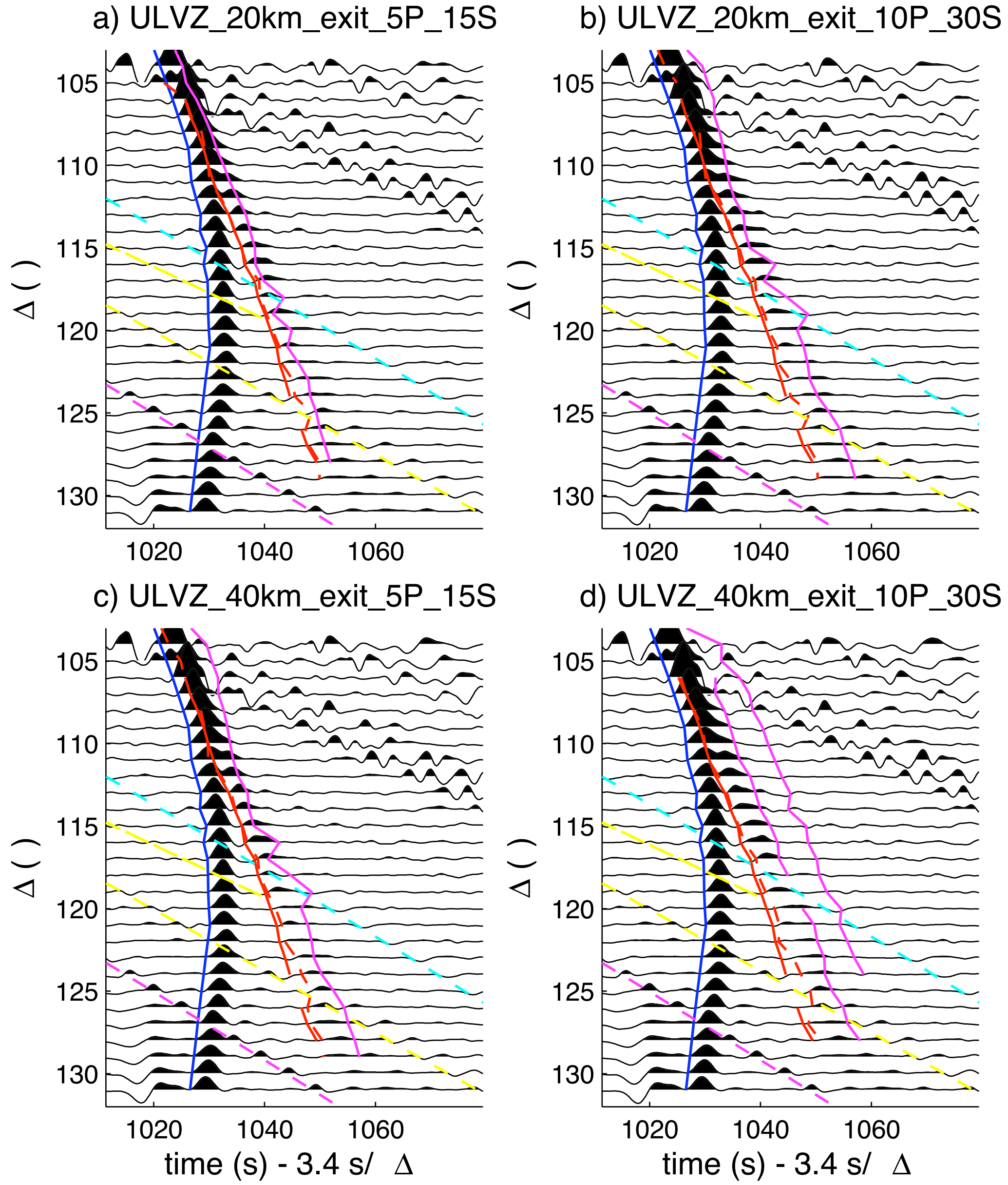

Figure 5-9: Synthetic seismograms for finite width "core exit" models. Blue line shows SKS picks from PREM pseudospectral synthetic seismograms. Solid red line shows PREM SPdKS picks. Dashed red line shows SPdKS picks for this model. Solid magenta lines show SPdKS picks for equivalent one-sided ULVZ model. Dashed cyan, yellow, and magenta lines show travel time predictions for sPPP, PPPP, and pPPP, respectively.

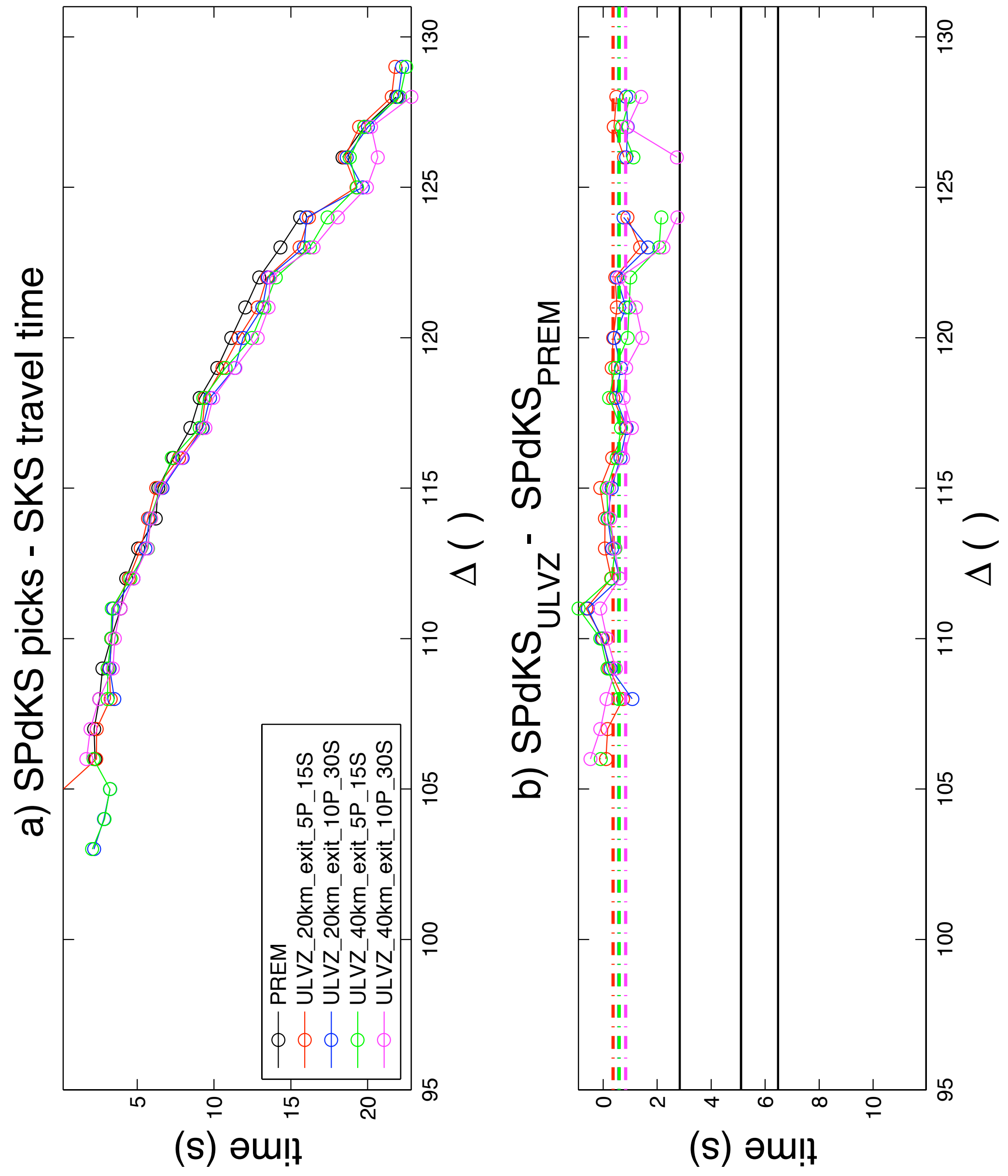

Figure 5-10: SPdKS travel time picks from the finite width "core exit" ULVZ models (Figure 5-9). a) SPdKS travel time picks relative to the SKS travel time for each model. Black symbols and lines show PREM for comparison. b) SPdKS travel time picks relative to the SPdKS travel time for PREM (solid lines and circles). Colored dotted lines show the mean SPdKS delay relative to PREM for the "core exit" ULVZ models. Black lines show mean SPdKS delay relative to PREM for the one-sided 10 km, 20 km, and 40 km 10%P and 30§-velocity perturbation models from Figure 5-6.

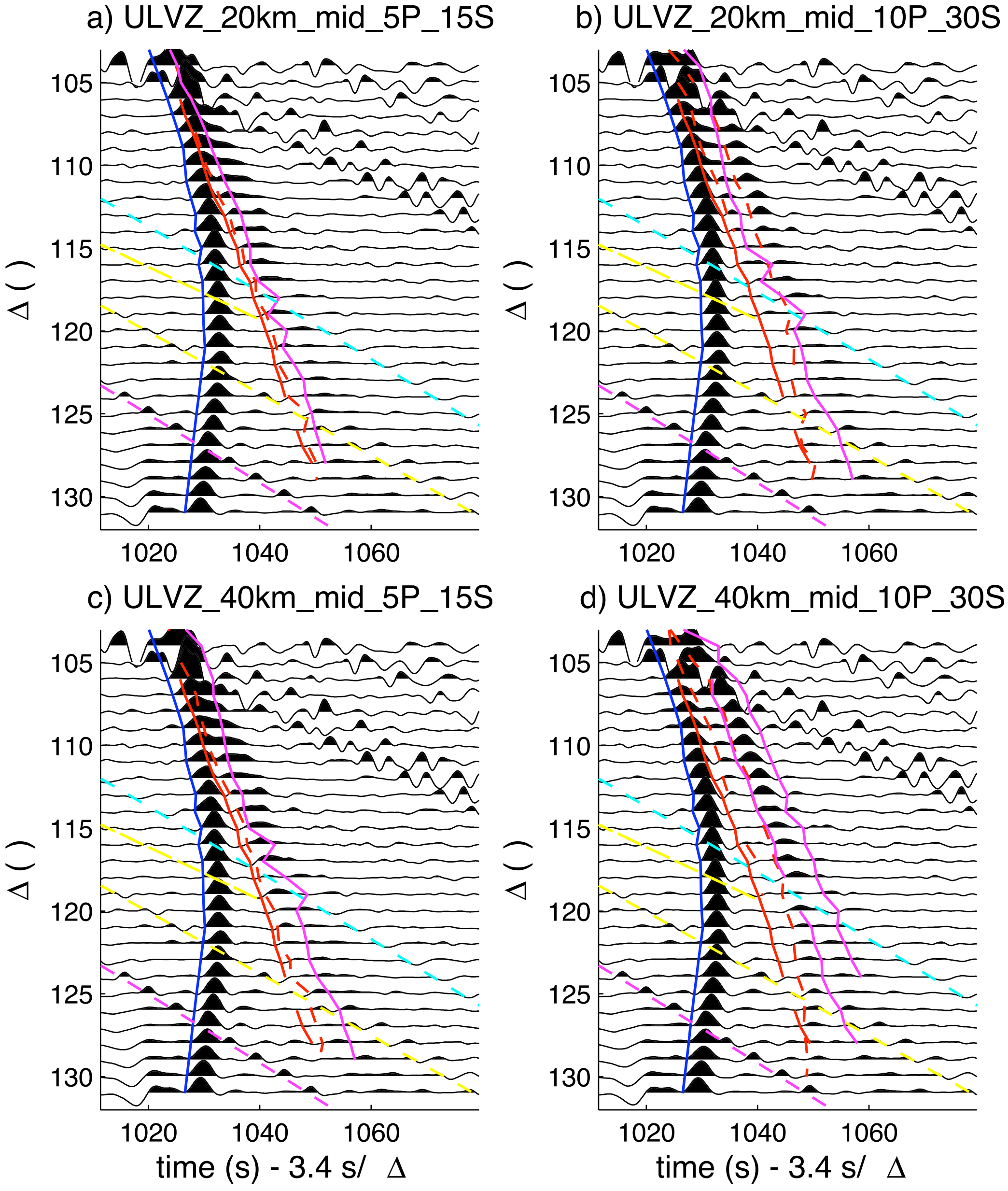

Figure 5-11: Synthetic seismograms for finite width "middle" models (Figure 5-2e). Blue line shows SKS picks from PREM pseudospectral synthetic seismograms. Solid red line shows PREM SPdKS picks. Dashed red line shows SPdKS picks for this model. Solid magenta lines show SPdKS picks for equivalent one-sided ULVZ model. Dashed cyan, yellow, and magenta lines show travel time predictions for sPPP, PPPP, and pPPP, respectively.

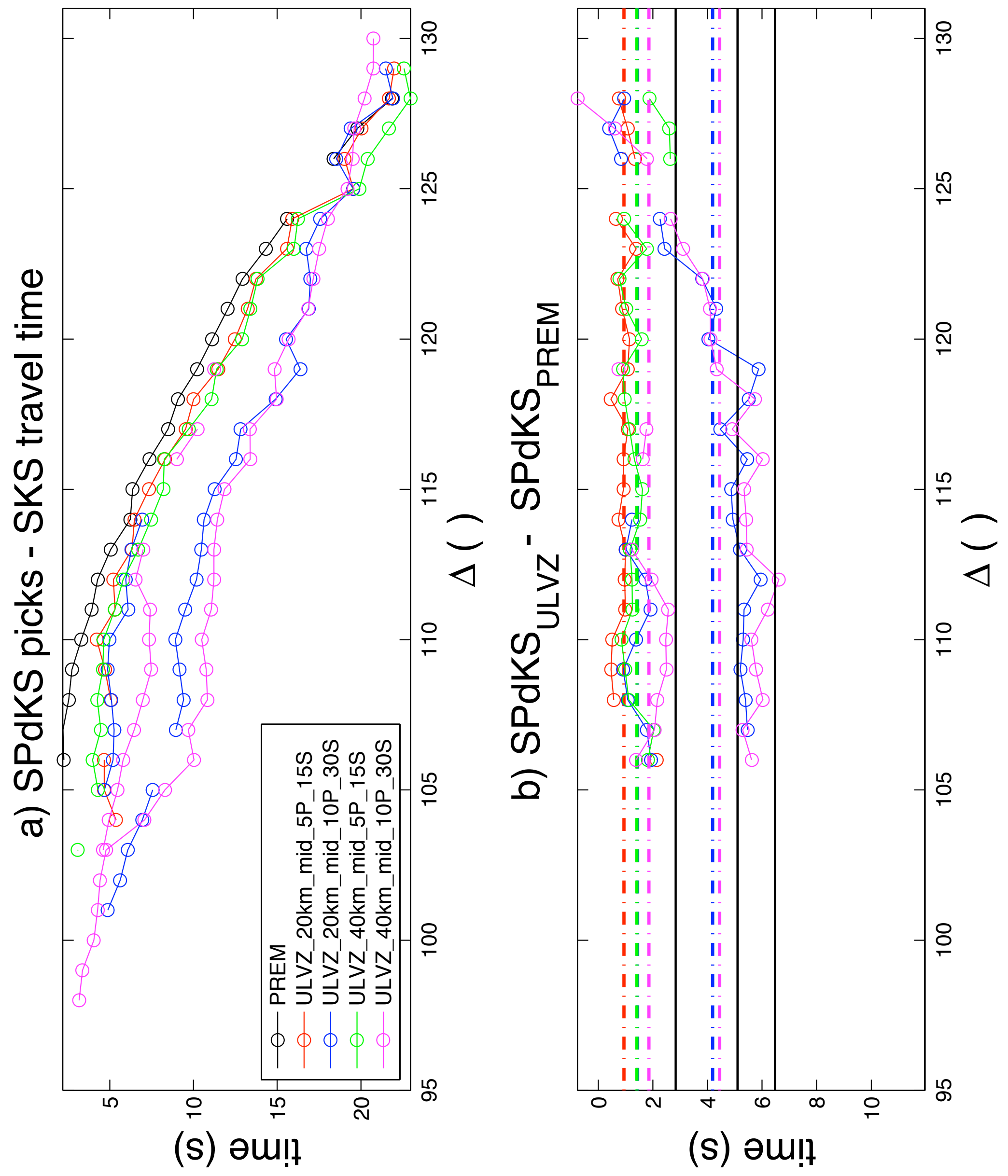

Figure 5-12: SPdKS travel time picks from the finite width "middle" ULVZ models (Figure 5-11). a) SPdKS travel time picks relative to the SKS travel time for each model. Black symbols and lines show PREM for comparison. b) SPdKS travel time picks relative to the SPdKS travel time for PREM (solid lines and circles). Colored dotted lines show the mean SPdKS delay relative to PREM for the "middle" ULVZ models. Black dashed lines show mean SPdKS delay relative to PREM for the one-sided 10 km, 20 km, and 40 km 10%P and 30§-velocity perturbation models from Figure 5-6.

5.5.4 Inception Point Sensitivity

The results for the 240 km-wide "inception point" models presented in section 5.5.3 lead us to explore how the sensitivity of SPdKS to ULVZs might depend on the width of a ULVZ centered on the Pdiff inception point. Synthetic seismograms from the inception ULVZ models described in section 5.4.1 are shown in Figures 5-13 through 5-16. The seismograms for the 10 km, 20 km, and 30 km-wide ULVZs are omitted as they are visually identical to PREM for all ULVZ thicknesses.

We calculate the mean SPdKS delay relative to PREM for all inception point sensitivity models. The results from these thirty-six models are summarized in Figure 5-17. They show that SPdKS travel times have no measurable sensitivity to ULVZs narrower than ∼100 km. The SPdKS traveltimes are slightly delayed for ULVZ widths between 100 and 500 km, with greater delays for stronger (thicker / larger velocity perturbation) ULVZs. And for ULVZ widths on the order of 1000 km or greater, the SPdKS arrivals are the same as the equivalent one-sided models. Figure 5-17 provides constraints on the combination of ULVZ thickness, P-velocity perturbation, and width that could cause a given SPdKS delay relative to PREM.

The set of mean SPdKS delays versus ULVZ strength can be fit with a line for each ULVZ width, and the slope of that line can be used as a proxy for the sensitivity of SPdKS to ULVZs of a given width (Figure 5-18). These slopes capture the limited sensitivity of SPdKS to 100–500 km-wide ULVZs and the full sensitivity to ULVZs with width of 1000 km or greater. It would be useful to compare these values with other estimates of the volume sensitivity or Fresnel zone of SPdKS at the CMB. However, directly calculating the Fresnel zone at the CMB for SPdKS is difficult due to the non-ray theoretical nature of this seismic phase. Published estimates for Fresnel zone dimensions at the CMB for related seismic phases are similar to our requirements for full ULVZ sensitivity: *Tkalcic and Romanowicz* [2002] estimate a 480 km Fresnel zone width for PcP at 1 Hz and an epicentral distance of 70°; *Thomas et al.* [2004] estimate a 220 km by 400 km Fresnel zone for SdS (the reflection from the top of the D" discontinuity) for a dominant period of 6 s; and *Braña and Helffrich* [2004] quote a ∼400 x 400 km Fresnel zone for PcP at the core mantle boundary. All of these are slightly smaller than the 500–1000 km width we require to achieve "full ULVZ sensitivity" in our results, but this difference is probably because these phases are higher

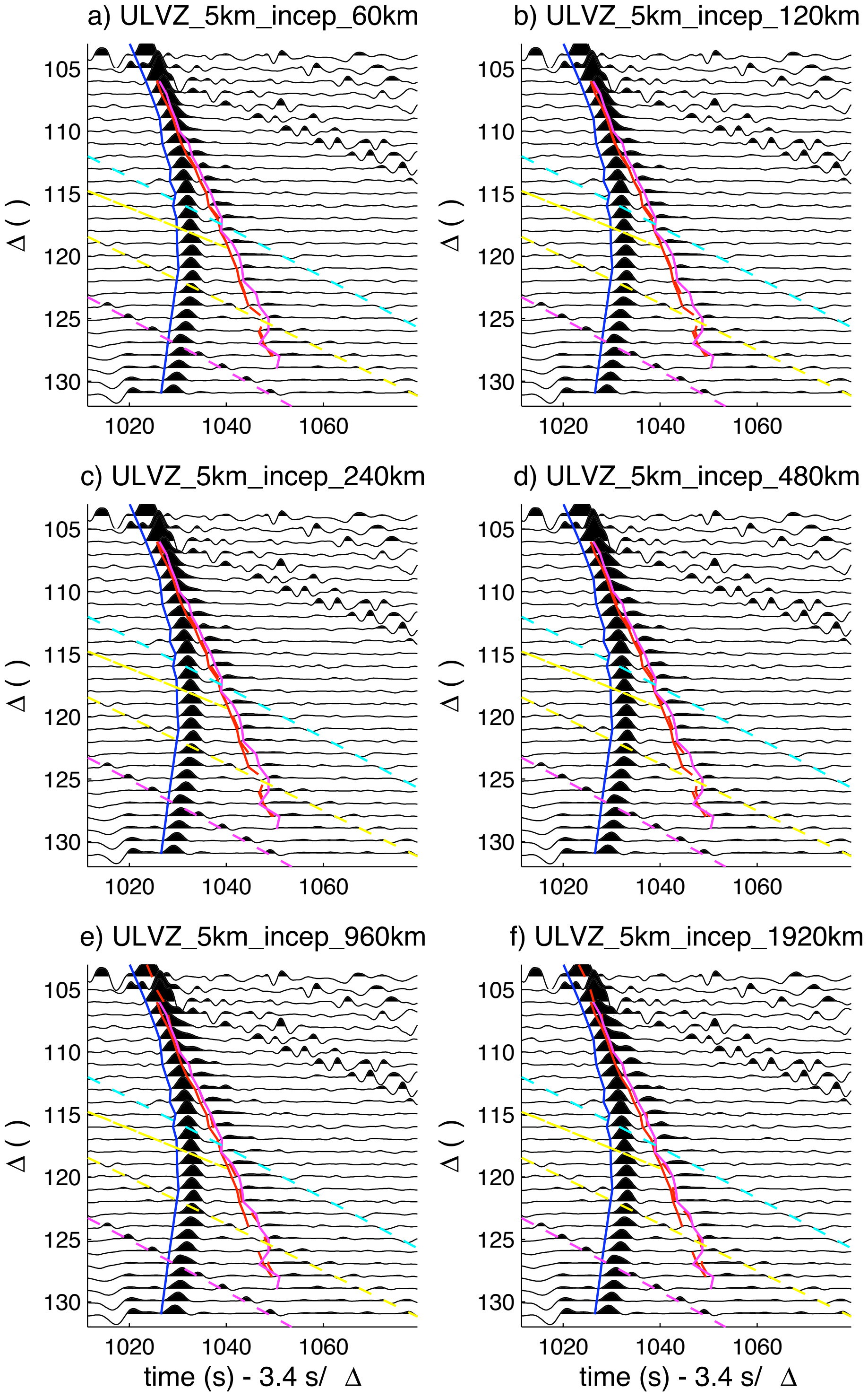

Figure 5-13: Synthetic seismograms for 5 km-thick, varying width ULVZ inception models. Blue line shows SKS picks from PREM pseudospectral synthetic seismograms. Solid red line shows PREM SPdKS picks. Dashed red line shows SPdKS picks for this model. Solid magenta lines show SPdKS picks for equivalent one-sided ULVZ model. Dashed cyan, yellow, and magenta lines show travel time predictions for sPPP, PPPP, and pPPP, respectively.

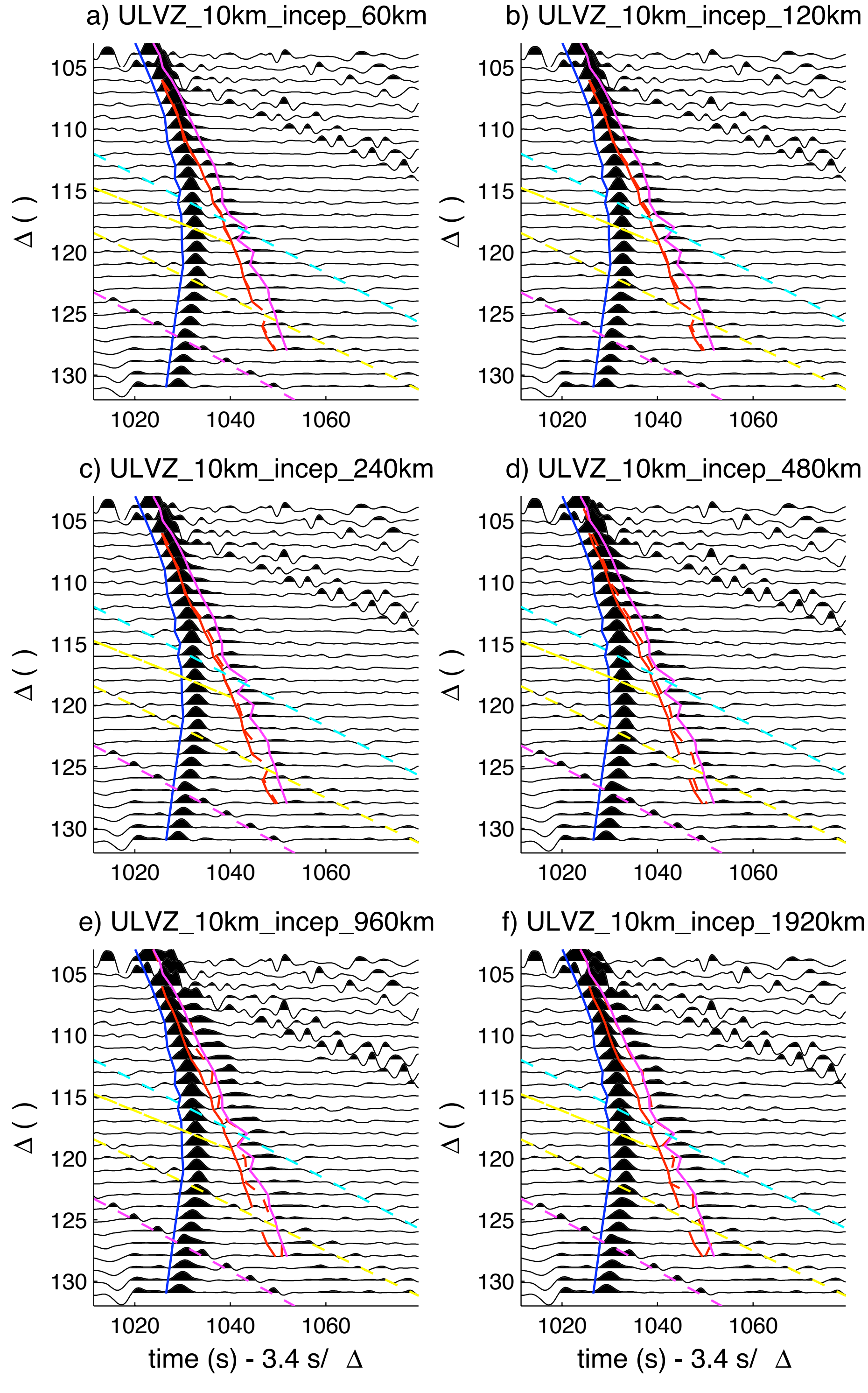

Figure 5-14: Synthetic seismograms for 10 km-thick, varying width ULVZ inception models. Blue line shows SKS picks from PREM pseudospectral synthetic seismograms. Solid red line shows PREM SPdKS picks. Dashed red line shows SPdKS picks for this model. Solid magenta lines show SPdKS picks for equivalent one-sided ULVZ model. Dashed cyan, yellow, and magenta lines show travel time predictions for sPPP, PPPP, and pPPP, respectively.

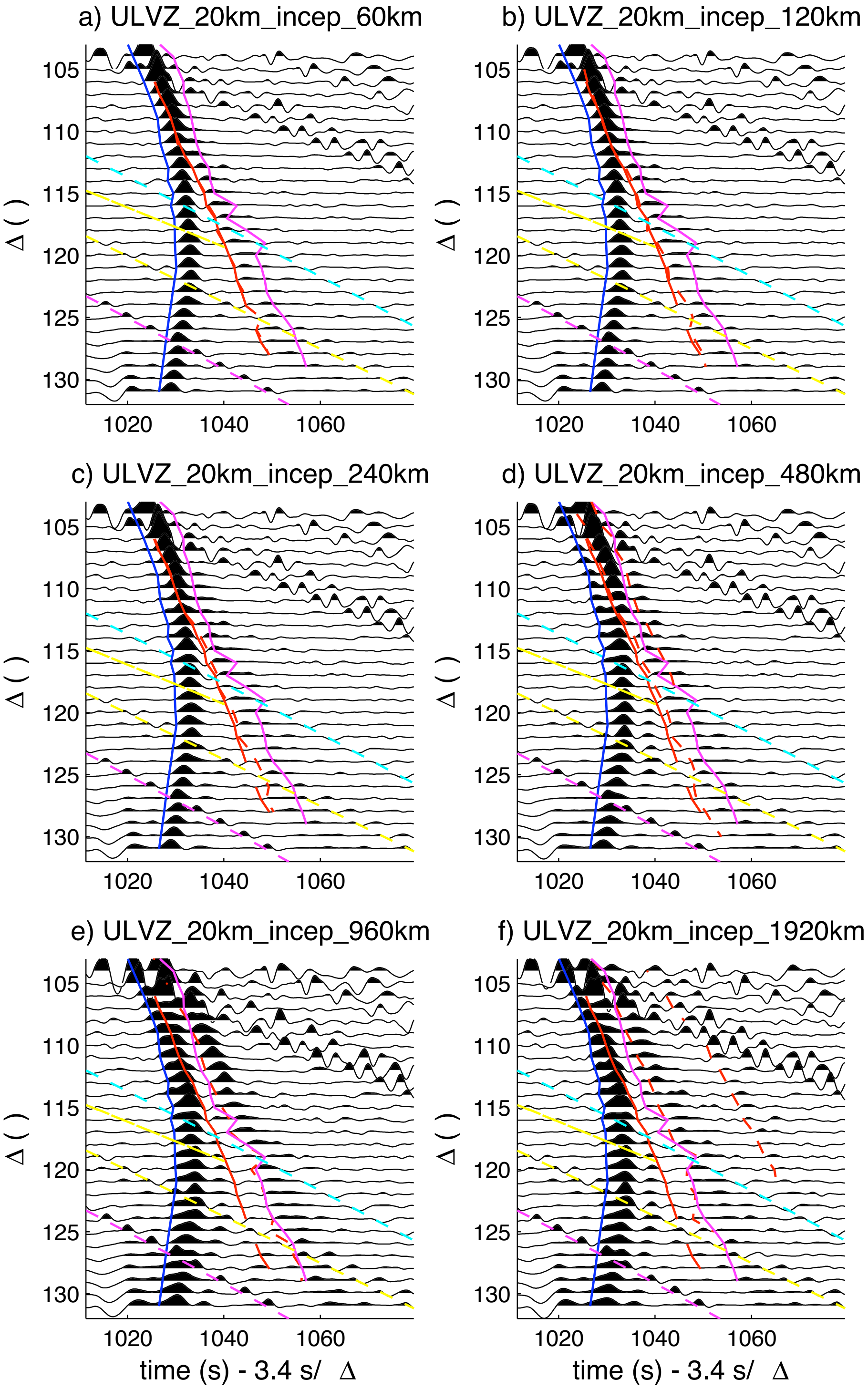

Figure 5-15: Synthetic seismograms for 20 km-thick, varying width ULVZ inception models. Blue line shows SKS picks from PREM pseudospectral synthetic seismograms. Solid red line shows PREM SPdKS picks. Dashed red line shows SPdKS picks for this model. Solid magenta lines show SPdKS picks for equivalent one-sided ULVZ model. Dashed cyan, yellow, and magenta lines show travel time predictions for sPPP, PPPP, and pPPP, respectively.

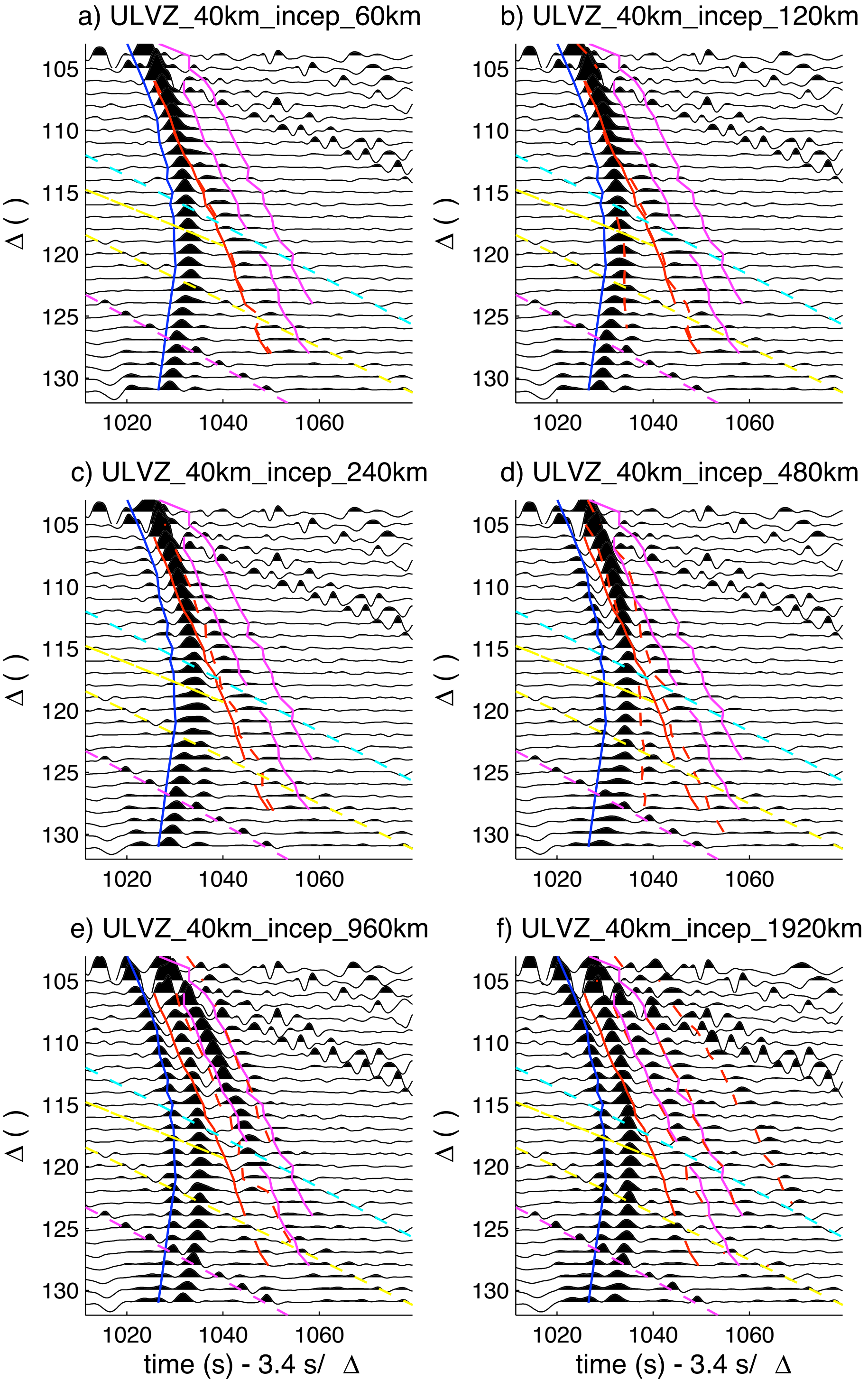

Figure 5-16: Synthetic seismograms for 40 km-thick, varying width ULVZ inception models. Blue line shows SKS picks from PREM pseudospectral synthetic seismograms. Solid red line shows PREM SPdKS picks. Dashed red line shows SPdKS picks for this model. Solid magenta lines show SPdKS picks for equivalent one-sided ULVZ model. Dashed cyan, yellow, and magenta lines show travel time predictions for sPPP, PPPP, and pPPP, respectively.

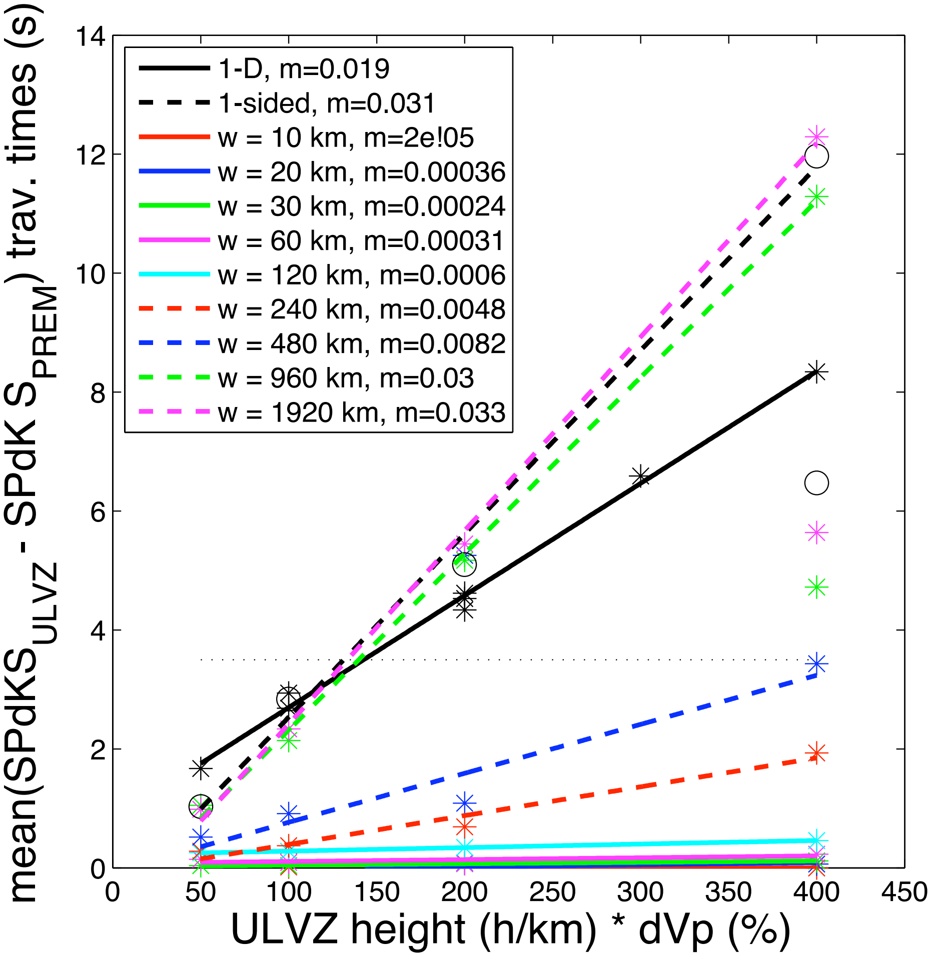

Figure 5-17: SPdKS delay versus ULVZ strength for various ULVZ widths. Solid black line and black stars are for 1-D models as in Figure 5-5. Dashed black line and black circles are for the one-sided models, and colored line are as labeled.

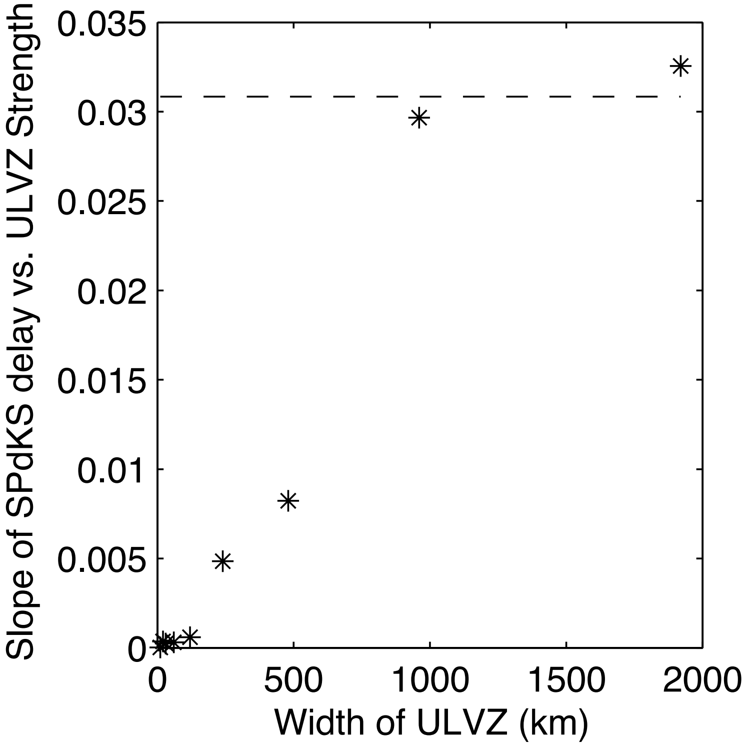

Figure 5-18: Slopes of 1-D fits to inception model results from Figure 5-17 versus ULVZ width. This slope, while having no physical meaning, is a reasonable proxy for SPdKS sensitivity to ULVZs of a given finite width centered on the Pdiff inception point.

frequency and / or have shorter ray path lengths than the SPdKS waves we model here.

The 20 and 40 km-thick synthetic seismograms also show two interesting secondary features. The 1920 km-wide models (Figures 5-15f and 5-16f) show a third SPdKS-moveout event arriving 21 - 22 s after the PREM SPdKS. Figure 5-15d-f and Figure 5-16a-d have an SKS post-cursor developing at epicentral distances greater than ~120°. These phases are currently unexplained, although the SKS postcursor may be related to the development of the "split SKS" arrival due to the S to P conversion at the top of the strong ULVZs.

5.6 Discussion

5.6.1 2-D ULVZ Signatures

Given the above modeling results, the following signatures of 2-D ULVZ structures might be found in real seismograms. The presence of more than one SPdKS-moveout event is diagnostic of SKS exposure to more than one CMB P-velocity structure. The relative amplitude of the different SPdKS arrivals may offer clues to the relative exposure of the Pdiff phase to each velocity structure. One-sided ULVZ models with PREM on the other side of the SPdKS path can produce two SPdKS paths with relatively equal amplitudes. ULVZ models placed so that Pdiff inception occurs just outside them with the Pdiff then propagating through the ULVZ result in a low amplitude PREM-travel time SPdKS arrival and a higher amplitude ULVZ-travel time SPdKS arrival. In addition, if the multiple SPdKS arrivals can be traced back to their inception epicentral distance, that distance may characterize the P-velocities at the base of the mantle.

If the ULVZ is strong enough to produce an S_{ULVZ}pKS converted phase with a measurable separation from the SKS arrival, then the relative amplitudes of those two phases may be diagnostic for 1-D versus one-sided ULVZ structure. However, such SKS precursors have not been commonly observed in previous ULVZ studies. The lack of S_{ULVZ}pKS observations in data might be attributed to a gradational, non-sharp ULVZ upper boundary. However, our 1-D ULVZ results indicate that vertical gradients in ULVZ velocity perturbations produce SKS waveforms and precursors very similar to those produced by ULVZs with sharp upper boundaries and equivalent combinations of height and average velocity perturbations. If a strong SKS precursor were observed in data, it might be the result of S splitting due to general anisotropy rather than an S to P conversion at the top of a ULVZ; it should be possible to distinguish these two models based on whether the SKS precursor travel time and amplitude and the SPdKS travel time and amplitude perturbations point towards similar ULVZ properties. The usual absence of such strong SKS precursors in data indicates that very strong ($\geq$300 km%) ULVZs are not common on the CMB.

We do not find any way of distinguishing strong but narrow (less than 1000 km wide) ULVZs from weaker but wider ULVZs using only the SPdKS travel time delay. The ULVZ width thus becomes another of the parameters in the non-unique ULVZ modeling space which may be traded off against layer thickness, velocity perturbations, and density perturbations. However, the SPdKS travel time delay does impose constraints on the minimum combinations of ULVZ strength and width which are required, and these constraints are more restrictive for larger SPdKS travel time delays. Most minimally, any observable SPdKS delay indicates a ULVZ width of at least 100 km.

5.6.2 Data and the Real Earth

Thorne and Garnero [2004] have made their extensive collection of SPdKS seismograms available online (http://ulvz.asu.edu/). They compiled this data set from publicly available data at the Incorporated Research Institutions for Seismology Data Management Center (IRIS DMC), the Observatories and Research Facilities for European Seismology (ORFEUS) Data Center (ODC), and the Canadian National Seismic Network (CNSN). They chose events with depths greater than 100 km and moment magnitudes greater than 6.0, and then selected seismograms with clearly distinguishable SKS arrivals. The seismograms for each event-station pair were instrument deconvolved to displacement, bandpass filtered with a window of 0.01 to 1.0 Hz, rotated to great circle path radial and transverse components, and resampled at 10 Hz. A 400 s window of the radial component, roughly centered on the SKS arrival, is available for each of the 443 records *Thorne and Garnero* [2004] used in their study.

Because we model the effect of 2-D structural features on synthetic seismograms in linear arrays implicitly aligned with the event–station great circle paths, the series of ten seismograms presented in Figure 5-19 is a good subset of the *Thorne and Garnero* [2004] data for comparison with our results. The earthquake source is an August 14, 1995 event with a moment magnitude of 6.3 and a depth of 126 km, located near Papua New Guinea. The event was recorded at ten stations in the MoMa (Missouri to Massachusetts) linear array [*Wysession et al.*, 1996] with epicentral distances between 115.6° and 125.8°.

Figure 5-20 shows the expected source-side and receiver-side Pdiff portions of the SPdKS paths for the traces in Figure 5-19, overlaid on a lower mantle slice from a 3-D S-velocity model [*Grand*, 2002]. While the MoMa array was not aligned exactly with the great circle path of these event-station pairs, it is close enough that the source-side SPdKS paths are only separated laterally by a ∼3° (∼180 km). The receiver-side SPdKS paths are more dispersed (∼10° lateral spacing).

Previous studies [*Thorne and Garnero*, 2004; *Rondenay and Fischer*, 2003; *Garnero*

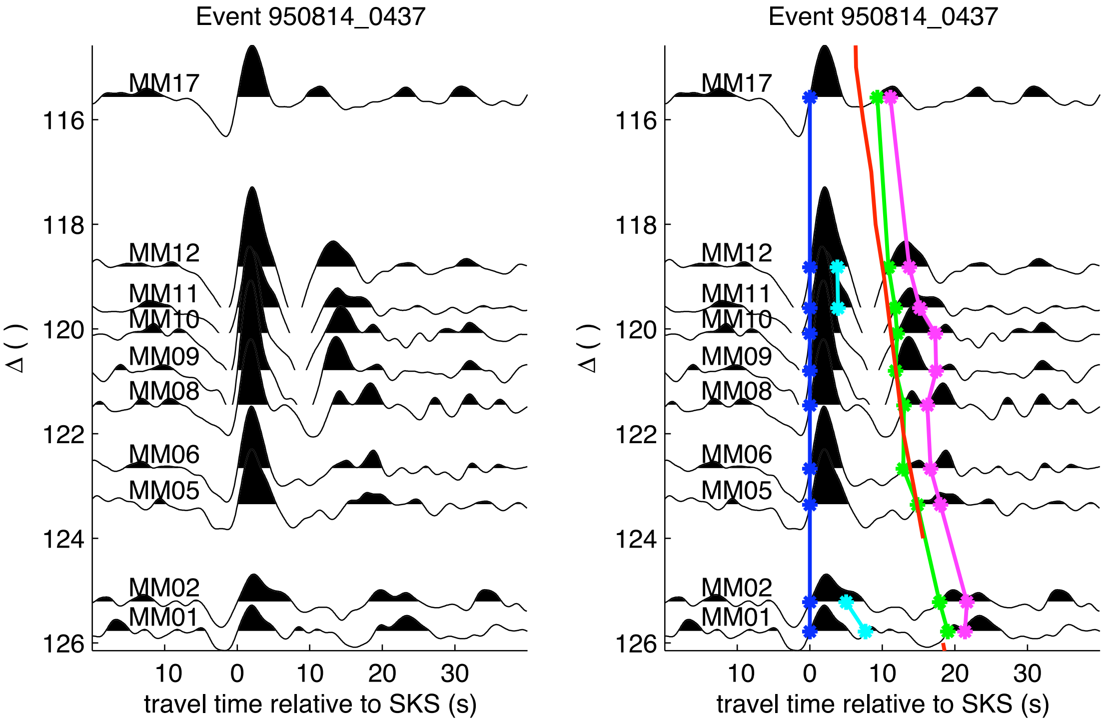

Figure 5-19: Data section for August 14, 1995 earthquake with a moment magnitude of 6.3 and a depth of 126 km, located near Papua New Guinea and recorded at ten stations in the MoMa array [*Thorne and Garnero*, 2004]. Left section shows data aligned on SKS picks. Right section shows same data but with SKS picks (blue), SPdKS picks (green and magenta), and PREM predicted SPdKS relative to observed SKS arrivals (red line).

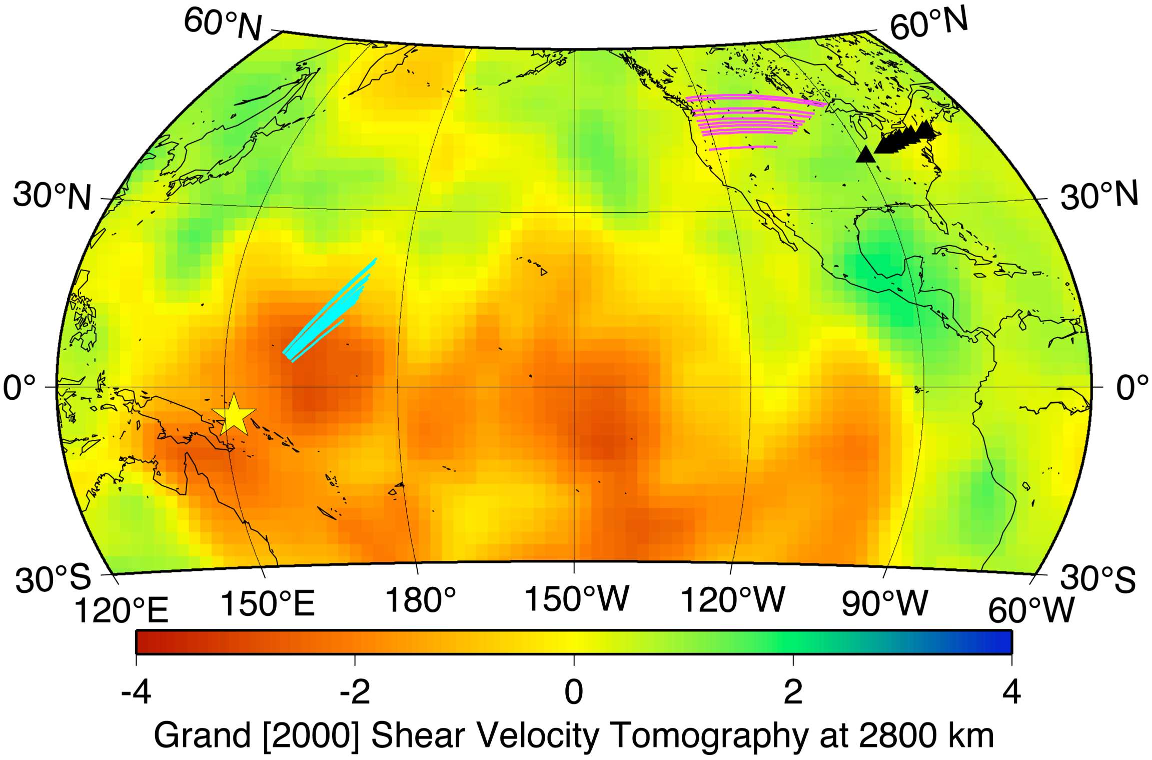

Figure 5-20: Location of the event (yellow star) and receivers (black triangle) for the seismograms shown in Figure 5-19, as well as the expected SPdKS source-side (cyan lines) and receiver-side (magenta lines) sampling regions on the CMB plotted on the 2800-km deep slice of the 3-D mantle shear wave model of *Grand* [2002].

Table 5.2: Best fitting 1-D models [*Thorne and Garnero*, 2004] for each of the individual traces in Figure 5-19. ULVZ = ultra-low velocity zone, CRZ = core-rigidity zone (small finite rigidity at top of outer core), CMTZ = core-mantle transition zone (linear gradient between lower mantle properties and upper outer core properties). PREM-like results indicates that the best fitting models are PREM and thin ($\leq$ 10 km) "ULVZs" with density perturbations but no velocity perturbations.

Station	Δ (°)	**Best-fitting CMB Models**
MM17	115.6	PREM-like
MM12	118.8	PREM
MM11	119.6	CRZ or strong ULVZ
MM10	120.1	CRZ, CMTZ, or strong ULVZ
MM09	120.8	PREM-like
MM08	121.5	thin ULVZ with 1:1 V_P:V_S perturbations
MM06	122.7	PREM-like
MM05	123.4	PREM
MM02	125.2	PREM
MM01	125.8	thin ULVZ with 1:1 V_P:V_S perturbations

et al., 1998] have consistently detected ULVZs in the Pacific region sampled by the source-side paths of these events; results for the CMB under the portion of North America sampled by these receiver-side paths are more ambiguous. Three-dimensional shear velocity models of the lower mantle from global travel time tomography [*Grand et al.*, 1997; *Masters et al.*, 2000; *Mégnin and Romanowicz*, 2000; *Gu et al.*, 2001; *Masters et al.*, 2000; *Ritsema and van Heijst*, 2000; *Grand*, 2002] show higher velocities in the region sampled by the receiver-side paths and low velocities in the region sampled by the source-side paths (http://mahi.ucsd.edu/Gabi/rem.html). These two lines of evidence hint that a one-sided ULVZ model might be appropriate for the data presented here.

Thorne and Garnero [2004] individually compared each of the traces in Figure 5-19 to 1-D reflectivity synthetics [*Fuchs and Müller*, 1971; *Müller*, 1985] for a variety of CMB boundary layer models. Table 5.2 shows the best fitting 1D models for each of these traces. Six of the ten traces are fit best by PREM and PREM-like models (thin "ULVZs" with density perturbations but no velocity perturbations). Two are fit best by thin (h $\leq$ 10 km) ULVZs with 1:1 V_P:V_S perturbation ratios. And two are fit best by models incorporating fairly strong ULVZs, core-rigidity zones (CRZs), or core-mantle transition zones (CMTZs). This is a lot of variety for ten paths which nearly overlap for much of their sampling of the CMB, especially along the source-side Pdiff path where ULVZs are most likely to exist.

If instead we look at the ten traces together and compare them to the various 2-D modeling results presented in section 5.5, we notice that the SPdKS arrival in Figure 5-19 actually seems to have two pulses. The first is very close to that predicted for PREM, while the second is ∼3.5 s delayed relative to PREM SPdKS. The SPdKS energy which arrives at the time predicted for PREM may indicate Pdiff inception outside the ULVZ and then propagation into the ULVZ as in the "middle" models presented in section 5.5.3. If instead the PREM-arrival time SPdKS is due to receiver-side structure, as suggested by Figure 5-20, then looking up this 3.5 s relative delay of the second SPdKS on Figure 5-17 imposes some minimum constraints on the source-side ULVZ: it can have a minimum ULVZ strength (height multiplied by P-velocity perturbation) of ∼130 km% if the ULVZ is very wide (1000 km or greater). Based on SPdKS delay alone, it can also have greater ULVZ strength for narrower ULVZ models, however it requires very strong ULVZs (greater than 400 km%) in order for ULVZs with widths smaller than ∼500 km to produce a large enough SPdKS travel time delay. Following *Stutzmann et al.* [2000], we note that the lack of a strong S_{ULVZ}pKS in Figure 5-19 indicates that the ULVZ is probably not as strong as 400 km% and therefore is probably wider than 500 km.

An attempt to extrapolate the second set of SPdKS picks in Figure 5-19 back to the SKS picks gives an estimated inception epicentral distance of 105.9°, which is very close to the 106.1° we model for PREM (Table 5.1). This may be because the second SPdKS peak seems stronger for larger epicentral distances in this section, which might indicate support for the hypothesis that the Pdiff portion of the SPdKS path has its inception outside the ULVZ and then travels into it.

To further examine our hypotheses about the origin of the dual SPdKS signal, in Figure 5-21 we plot the source-side SPdKS paths on several different S-velocity tomography models of the lower mantle (2800 km depth, compiled at http://mahi.ucsd.edu/Gabi/rem.html) [*Grand et al.*, 1997; *Masters et al.*, 2000; *Mégnin and Romanowicz*, 2000; *Gu et al.*, 2001; *Masters et al.*, 2000; *Ritsema and van Heijst*, 2000; *Grand*, 2002]. While these tomography models are generally consistent for large-scale features (all have slow S-velocities in the southwest Pacific), the details of the models can differ significantly. In general, the Pdiff paths seem to have inception points in higher amplitude portions of the slow S-wave features and to propagate outward into lower-amplitude regions, which may lend more support to constraining the ULVZ parameters by comparing the second SPdKS travel time delay to the models of finite width ULVZs centered on the

Pdiff inception point.

5.6.3 Implications for Data Collection and Analysis

We have seen that multiple SPdKS arrivals may be a powerful tool for identifying 2-D (and, by extension, 3-D) ULVZ velocity structures. However the identification of a wiggle on a seismogram as a second or third SPdKS arrival is virtually impossible using travel times from a single trace; it is the moveout of an event over a range of epicentral distances that is diagnostic of the SPdKS. If 2-D and 3-D modeling of seismic wave propagation through more complex ULVZ structures is to be of use in understanding CMB structure in the real world, the collection and creative exploitation of 2-D and 3-D array data sets with relatively dense station spacing (on the order of 1°) in a useful epicentral distance range (100–130°) from many large, deep events will be required.

The synthetic seismograms in this paper also show that for strong ULVZs the typical first step of SPdKS data analysis, aligning data traces on "the SKS arrival", may be easier said than done. The S to P conversion at the top of strong ULVZs and other complexities of the SKS interaction with the anomalous layer can be seen in various SKS precursors and postcursors in our synthetic sections. For the strongest ULVZ models we study here, the precursors and postcursors can be picked separately from the true SKS arrival, and for the weakest models the separation between these phases is so small that the simple SKS pulse is unaffected. However, for models of intermediate strength there is too little separation to easily isolate the SKS pulse and too much separation for the pick of the first arrival to be accurately used as a measure of SKS travel time.

For this reason, all "SPdKS mean delay" results presented here are inherently calculated with respect to the SKS travel time in PREM rather than the measured SKS travel time for each model. While it might seem more correct to use (SPdKS_{ULVZ} - SKS_{ULVZ}) - (SPdKS_{PREM} - SKS_{PREM}) as the measure of relative SPdKS delay, the difficulty of correctly determining the travel time of SKS_{ULVZ} for some of our models made (SPdKS_{ULVZ} - SKS_{PREM}) - (SPdKS_{PREM} - SKS_{PREM}) = (SPdKS_{ULVZ} - SPdKS_{PREM}) a more robust measure of SPdKS delay.

5.6.4 Comparison with Other 2D Modeling of ULVZs

Helmberger et al. [1996] used generalized ray synthetics to study the effect of one-sided

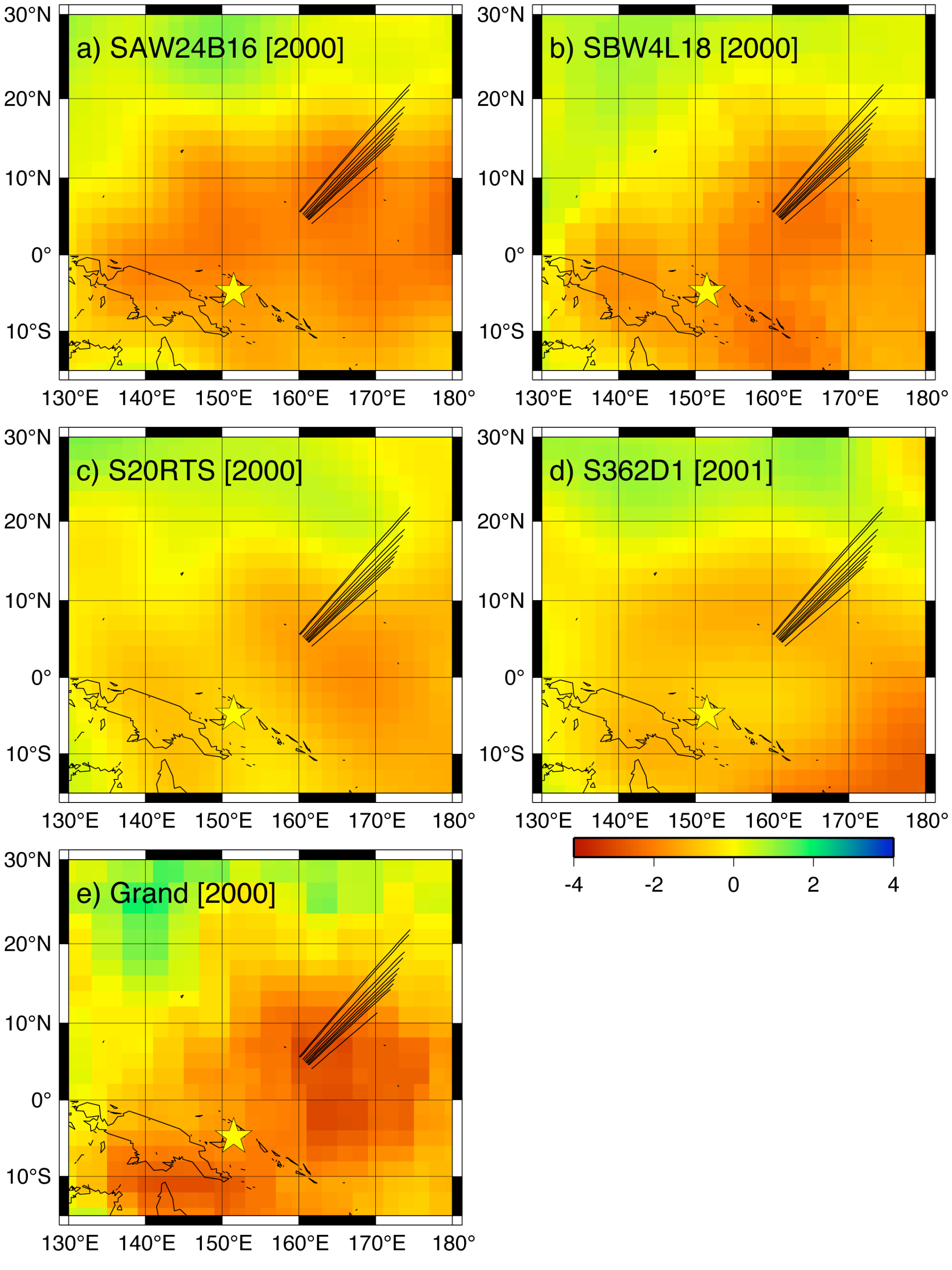

Figure 5-21: Location of the event (yellow star) and the expected SPdKS source-side paths (black lines) for the seismograms shown in Figure 5-19 overlaid on the 2800-km deep slice of the 3-D mantle shear wave models of a) *Mégnin and Romanowicz* [2000], b) *Masters et al.* [2000], c) *Ritsema and van Heijst* [2000], d) *Gu et al.* [2001], e) *Grand* [2002], all compiled at the Reference Earth Model website (http://mahi.ucsd.edu/Gabi/rem.html). Grid line are drawn every 10° ($\sim$ 600 km).

ULVZ models on SPdKS. They established the presence of two SPdKS diffraction events in their synthetic seismograms, each corresponding to the Pdiff inception slowness of one side of the model, with greater separation between the two arrivals for larger P-velocity perturbations at the base of the mantle. They also modeled the P to S conversion at the top of a ULVZ layer and the response of a PP bounce within the layer. Their results seem consistent with the one-sided results presented in section 5.5.2, as expected from other comparisons of generalized ray and pseudospectral synthetics [*Ni et al.*, 2003]. However, the generalized ray synthetics are limited to quasi-1-D models on each side of the CMB and therefore cannot explore the finite width effects we present here.

Wen and Helmberger [1998b] used a hybrid method to model 2-D ULVZ structures: they coupled downgoing generalized ray theory solutions from a seismic source to finite difference modeling of the CMB region of interest, and used the Kirchhoff method to couple the outgoing wavefield from the finite difference region to receivers on the Earth's surface using WKB Green's functions. They studied ULVZ structures with dome and boxcar shapes, and found that their effect on SKS and SPdKS waveforms was very dependent on the ULVZ position on the CMB, which agrees with our results in section 5.5.3. They also observed trade-offs between the ULVZ dimensions and velocity perturbations and found that a minimum lateral dimension of 100 km was required to produce detectable changes in the SKS - SPdKS waveforms, which is similar to the results in section 5.5.4. Finally, they found noticeable differences in the broadband SKS and SPdKS waveforms produced by the dome and box-car shaped ULVZs, although those differences were muted in long period data. We do not have equivalent results, as we dealt with only boxcar type models.

Between them, *Helmberger et al.* [1996] and *Wen and Helmberger* [1998b] capture many of the same fundamental observations about the effect of 2-D ULVZ structures on SKS - SPdKS waveforms that we find in this work. This is reassuring, because the generalized ray, hybrid, and pseudospectral methods used by these three projects to produce the synthetic seismograms were all very different. Our results are distinguished by three unique results. First, the observations of dual SPdKS for the finite-width ULVZ models which begin just beyond the Pdiff inception point offer a glimpse at more complex aspects of the 2-D behavior of SPdKS. Second, the production of Figure 5-17 offers a useful tool for examining the trade-offs between different aspects of the ULVZ parameterization in a quantitative way. Third, our approach provides a new, independent, and robust estimate of the spatial sensitivity of

SPdKS at the CMB, something which can not be found in the literature to date.

5.6.5 Implications for ULVZ Hypotheses

In the introduction, several hypotheses for the origin of ULVZs on the CMB were mentioned: partial melt, chemical heterogeneity (due to subducted slabs or iron enrichment from the core), phase transitions between perovskite and post-perovskite, and outer-core "sediments" collecting on the CMB. Here we consider whether the results from this study help to discriminate between these different theories of the origin of ULVZs.

The use of SPdKS alone can provide two constraints which may be useful in distinguishing the possible causes of ULVZs. First, 2-D modeling provides limits on the horizontal spatial scale over which the ULVZ originating process must be occurring. All processes which create velocity anomalies detectable by SPdKS must occur on a lateral scale greater than 100 km, and if they create strong (greater than ~3.5 s) SPdKS delays they are probably more than 500 km across. (They may also occur on smaller length scales, but if they only occur in zones narrower than 100 km, they will not produce detectable SPdKS anomalies.) This may be a constraint useful in distinguishing between geodynamic models of ULVZ formation. Second, we may be able to provide constraints on P-velocities at the base of the mantle using the inception point for SPdKS events in a data section. For 2-D structures, the difference between the inception epicentral distances for two SPdKS events may help pin down the range of P-velocities to which the SPdKS wave is exposed. This may be useful in distinguishing between different models of composition (iron or calcium or aluminum content in the magnesium silicate) and phase (perovskite versus post-perovskite versus partial melt) at the base of the mantle.

Using SPdKS alone, we can provide direct constraints only on combinations of ULVZ material properties (seismic velocities and density) and dimensions (thickness and lateral dimensions). However, it may be possible to constrain individual material and dimensional properties of ULVZs by incorporating more phases. For example, stacks of short period ScP, ScS, and PcP precursors and postcursors can tease apart ULVZ thickness versus P-velocity, S-velocity, and density perturbations [*Rost and Revenaugh*, 2003; *Avants et al.*, 2006]. It would be an interesting challenge in experiment design to create arrays of seismic receivers which, given the Earth's natural distribution of earthquake sources, would allow the same patch of CMB to be sampled by multiple core-sensitive phases, for example, both SPdKS and ScP.

This leads to the question: what constraints on ULVZ origin would be offered by a perfectly seismically constrained ULVZ with well determined thickness, lateral dimension, shape, seismic velocities, attenuation, and densities? Can partial melting be distinguished from iron-enriched post-perovskite or other chemical heterogeneities with perfect seismic knowledge? A full investigation of this question is beyond the scope of this paper, but *Lay and Garnero* [submitted] suggest that it is hard to seismically distinguish between iron-enriched post-perovskite and partial melting as origins for ULVZs. For any given hypothesis, it seems likely that the uncertainties in chemical composition, equations of state, and thermal state of the CMB will combine to allow a range of viable ULVZ models which would satisfy the seismic parameters. However, it is still useful to attempt to combine seismic constraints with those from mineral physics, geochemistry, and geodynamics modeling to narrow the range of possibilities.

5.6.6 Questions for Future Work

It would be useful to further study a few aspects of the model space explored here. First, as the width of ULVZ models increases between 500 km and 1000 km, does the SPdKS sensitivity increase smoothly or abruptly, and if abruptly, at what width? Second, how far away can a ULVZ be from the inception point while still having an effect on the SPdKS? In section 5.5.3 we see that the "middle" ULVZ models which begin 2.5° (∼150 km) away from the Pdiff inception point produce SPdKS energy which is largely at the ULVZ SPdKS arrival time while the "exit" models which begin 9° (∼540 km) after the Pdiff inception point produce SPdKS energy exclusively at the PREM arrival time. Is the transition between these two results smooth or abrupt, and if abrupt, at what distance does it occur? Third, if the ULVZs centered on the inception points had smooth lateral decreases in the velocity perturbations rather than sharp edges as described in section 5.4.1, would the associated SPdKS phases change in amplitude due to decreased scattering?

The following unexplained features were observed in the synthetic seismograms for our various models: the third SPdKS-moveout arrival in Figures 5-15f and 5-16f at travel times 21–22 s after PREM SPdKS; SKS post-cursors developing for epicentral distances greater than ∼120° in Figure 5-15d-f and Figure 5-16a-d; the arrival of the second SPdKS arrival in Figure 5-3b 5.6 s after the first SPdKS arrival rather than at PREM SPdKS travel times. Future modeling should attempt to understand the appearance of all these phases and whether they might be used in the analysis of data from the real Earth to further understand ULVZs.

The global pseudospectral wave propagation method also offers the opportunity to model the constraints on ULVZ structure that might be provided by the combination of multiple seismic phases. It would be useful to examine the effect of the 2-D ULVZ models presented here on ScP, ScS, ScP, and other CMB-sensitive phases. Are they sensitive to narrower ULVZs than SPdKS? Are they sensitive to finite-width ULVZs offset from the core-reflection point? If so, how far can the ULVZ be offset from the core-reflection point while still resulting in measurable changes in the waveforms of these phases? How tightly can these phases, in combination with SPdKS, constrain the thickness, velocity perturbations, and lateral dimensions of ULVZs? And what configuration of seismometers would enable the collection of data against which the results of these various models might be tested?

Finally, it would be possible to modify the pseudospectral code so that the grid nodes follow curved ULVZ upper boundaries. This would enable the modeling of ULVZ topography and shapes such as the domes modeled by *Wen and Helmberger* [1998b], which might allow for better constraints on ULVZ shape than the simple ULVZ box models presented here.

5.7 Conclusions

Seismic wave propagation through two-dimensional core-mantle boundary (CMB) ultralow velocity zones (ULVZs) is modeled using a global pseudospectral algorithm. Synthetic seismograms are constructed for several types of ULVZ models, focusing on SKS and the related SPdKS / SKPdS phase which results from the intersection of the SKS wave with the CMB at the inception slowness. One-dimensional (1-D) models with sharp and gradational upper boundaries and one-sided two-dimensional (2-D) models with different quasi-1-D CMB structures on the source and receiver sides of the CMB are run to provide a baseline for comparison of other 2-D models. Upper boundaries with linear gradients in velocity perturbations result in waveforms and traveltimes very similar to models with sharp upper boundaries, the full velocity perturbation throughout the layer, and half the height of the linear gradient. P to S conversions at the top of the ULVZ result in the appearance of a high amplitude SKS precursor in the synthetic seismograms, although only if the ULVZ is strong enough to produce an observable time separation between the two phases. The absence of such SKS precursors in data indicates that ULVZs in the Earth are likely weaker than 300 km%, where ULVZ strength is parameterized as the ULVZ thickness multiplied by the average P-velocity perturbation. Different velocity structures on the source and receiver sides of the CMB result in two SPdKS arrivals on the seismograms, one at the appropriate travel time for each side of the model, however these are only observable if the velocity structures are different enough to produce measurable travel time differences in the SPdKS arrival.

Finite width 2-D ULVZ models are used to test the sensitivity of the SPdKS travel time and waveform to different portions of the P-diffracted portion of the wavepath and to explore the minimum width necessary for a ULVZ to produce observable changes in SPdKS. The SPdKS traveltimes and waveforms are completely insensitive to ULVZ structures placed at the exit points of Pdiff to the core for epicentral distances greater than 110°. However, the SPdKS traveltime and waveforms are strongly affected by 6°-wide (∼360 km-wide) ULVZs placed along the Pdiff path but 2° (∼120 km) beyond the Pdiff inception point. Finally, sensitivity to a ULVZ centered on the Pdiff inception point is strongly dependent on the width of the ULVZ. There is no sensitivity to ULVZs narrower than 100 km, a linear increase in small SPdKS travel time delays for widths between 100 and 500 km, and the full SPdKS observed for equivalent one-sided quasi-1-D models is observed for models with widths of 1000 km or greater. The non-uniqueness of small SPdKS travel time delays ($\leq$1 s) for 1-D models incorporating ULVZ thickness, velocity, and density perturbations must therefore be extended to include ULVZ width.

Our results give four tools useful for identifying and characterizing 2-D ULVZ structures, all most useful if array data in something resembling a 2-D geometry is available. First, dual SPdKS pulses on a seismogram indicate exposure to at least two different CMB velocity structures. If the two SPdKS pulses are similar in amplitude, they probably indicate different quasi-1-D velocity structures on the source and receiver-side CMB. If the first pulse is PREM-like and significantly smaller than the second ULVZ-like SPdKS, it may indicate Pdiff inception outside of and propagation into a ULVZ. Second, a strong SKS precursor probably indicates a very strong ULVZ. If the precursor is similar in amplitude to the SKS pulse, it indicates similarly strong ULVZ structure on both source and receiver-side CMB regions, and if the precursor is smaller than the SKS pulse, it may indicate a ULVZ on only the source or receiver side of the CMB. Third, we present a graph of mean SPdKS delays relative to PREM which provides constraints on minimum ULVZ strength and width combinations required to produce a given travel time delay, which is more restrictive the greater the delay. Finally, tracing SPdKS arrivals back to the inception epicentral distance on seismic sections may offer an independent tool for identifying P-velocity perturbations at the base of the mantle. Combining all of this with other CMB-sensitive phases (especially ScS, PcP, and ScP precursors and postcursors) may provide the best constraints on fine-scale CMB structure.

Bibliography

Aki, K., and P. G. Richards (2002), *Quantitative Seismology*, 2nd ed., University Science Books, Sausalito, CA.

Alt, J. C. (1995), Subseafloor processes in mid-ocean ridge hydrothermal systems, in *Seafloor hydrothermal systems; physical, chemical, biological, and geological interactions*, *Geophysical Monograph*, vol. 91, edited by S. E. Humphris, R. A. Zierenberg, L. S. Mullineaux, and R. E. Thomson, pp. 85–114, American Geophysical Union, Washington, DC.

Arnaud-Vanneau, A., and W. V. Sliter (1995), Early Cretaceous shallow-water benthic foraminifers and fecal pellets from Leg 143 compared with coeval faunas from the Pacific Basin, Central America, and the Tethys, in *Proceedings of the Ocean Drilling Program; scientific results, Northwest Pacific atolls and guyots; covering Leg 143 of the cruises of the Drilling Vessel JOIDES Resolution, Honolulu, Hawaii, to Majuro, Republic of Marshall Islands, sites 865-870, 18 March-19 May 1992*, *Proceedings of the Ocean Drilling Program, Scientific Results*, vol. 143, edited by E. L. Winterer, W. W. Sager, J. V. Firth, H. M. Arnaud, P. E. Baker, F. Baudin, T. J. Bralower, P. R. Castillo, P. A. Cooper, P. G. Flood, X. Golovchenko, Y. Iryu, M. K. Ivanov, H. C. Jenkyns, J. A. M. Kenter, I. O. Murdmaa, J. Mutterlose, Y. Nogi, C. K. Paull, E. L. Polgreen, U. Roehl, W. V. Sliter, A. Strasser, N. H. M. Swinburne, J. A. Tarduno, R. J. van Waasbergen, and S. K. Stewart, pp. 537–564, Texas A & M University, Ocean Drilling Program, College Station, TX.

Asimow, P. D., M. M. Hirschmann, and E. M. Stolper (2001), Calculation of peridotite partial melting from thermodynamic models of minerals and melts, iv. Adiabatic decompression and the composition and mean properties of mid-ocean ridge basalts, *J. Petrol.*, *42*(5), 963–998.

Avants, M., T. Lay, and E. J. Garnero (2006), A new probe of ULVZ S-wave velocity structure: Array stacking of ScS waveforms, *Geophys. Res. Lett.*, *33*, L07314, doi: 10.1029/2005GL024989.

Bach, W., and S. E. Humphris (1999), Relationship between the Sr and O isotope compositions of hydrothermal fluids and the spreading and magma-supply rates at oceanic spreading centers, *Geology*, *27*(12), 1067–1070.

Baker, E. T., et al. (2002), Hydrothermal venting along Earth's fastest spreading center: East Pacific Rise, 27.5°–32.3°S, *J. Geophys. Res.*, *107*(7), 2130, doi: 10.1029/2001JB000651.

Baran, J. M., J. R. Cochran, S. M. Carbotte, and M. Nedimovic (2005), Variations in upper crustal structure due to variable mantle temperature along the Southeast Indian Ridge, *Geochem. Geophys. Geosys.*, *6*, Q11002, doi:10.1029/2005GC000943.

Barclay, A. H., and W. S. D. Wilcock (2004), Upper crustal seismic velocity structure and microearthquake depths at the Endeavour Segment, Juan de Fuca Ridge, *Geochem. Geophys. Geosys.*, *5*(1), Q01004, doi:10.1029/2003GC000604.

Bargar, K. E., and E. D. Jackson (1974), Calculated volumes of individual shield volcanoes along the Hawaiian-Emperor chain, *J. Res. U.S.G.S.*, *2*(5), 545–550.

Berryman, J. G. (2000), Seismic velocity decrement ratios for regions of partial melt in the lower mantle, *J. Geophys. Res.*, *27*(3), 421–424, doi:1999GL008402.

Bhat, V., P. R. Shaw, and J. R. Delaney (1997), The Endeavour Ridge as observed by DSL120 sidescan sonar; interplay of volcanic, tectonic, and hydrothermal processes, *Eos Trans. AGU*, *78*(46, suppl.), 805.

Blacic, T. M., G. T. Ito, J. P. Canales, R. S. Detrick, and J. M. Sinton (2004), Constructing the crust along the Galapagos Spreading Center 91.3°–95.5°W: Correlation of seismic layer 2a with axial magma lens and topographic characteristics, *J. Geophys. Res.*, *109*, B10310, doi:10.1029/2004JB003066.

Blackman, D. K., and D. W. Forsyth (1991), Isostatic compensation of tectonic features of the Mid-Atlantic Ridge; 25 degrees - 27 degrees 30'S, *Journal of Geophysical Research*, *96*(7), 11,741–11,758.

Bohnenstiehl, D. R., R. P. Dziak, M. Tolstoy, C. G. Fox, and M. Fowler (2004), Temporal and spatial history of the 1999-2000 Endeavour Segment seismic series, Juan de Fuca Ridge, *Geochem. Geophys. Geosys.*, *5*, Q09003, doi:10.1029/2004GC000735.

Braña, L., and G. Helffrich (2004), A scattering region near the core-mantle boundary under the North Atlantic, *Geophys. J. Int.*, *158*(2), 625–636, doi:10.1111/j.1365-246X.2004.02306.x.

Buck, W. R., S. M. Carbotte, and C. Z. Mutter (1997), Controls on extrusion at mid-ocean ridges, *Geology*, *25*(10), 935–938, doi:10.1130/0091-7613(1997)025<0935:COEAMO>2.3.CO;2.

Buffett, B. A., E. J. Garnero, and R. Jeanloz (2000), Sediments at the top of earth's core, *Science*, *290*(5495), 1338–1342, doi:10.1126/science.290.5495.1338.

Bukowinski, M. S. T., and S. Akber-Knutson (2005), The role of theoretical mineral physics in modeling the Earth's interior, in *Earth's deep mantle; structure, composition, and evolution*, *Geophysical Monograph*, vol. 160, edited by R. D. van der Hilst, J. D. Bass, J. Matas, and J. Trampert, pp. 137–163, American Geophysical Union, Washington, DC.

Butterfield, D. A., and G. J. Mossoth (1994), Geochemistry of north Cleft segment vent fluids: Temporal changes in chlorinity and their possible relation to recent volcanism, *J. Geophys. Res.*, *99*(B3), 4951–4968.

Butterfield, D. A., R. E. McDuff, M. J. Mottl, M. D. Lilley, J. E. Lupton, and G. J. Massoth (1994), Gradients in the composition of hydrothermal fluids from the Endeavour Segment vent field; phase separation and brine loss, *J. Geophys. Res.*, *99*(5), 9561–9583.

Butterfield, D. A., et al. (1997), Seafloor eruptions and evolution of hydrothermal fluid chemistry [and discussion], *Phil. Trans.: Math., Phys. and Eng. Sci.*, *355*(1723), 369–386.

Calmant, S. (1987), The elastic thickness of the lithosphere in the Pacific Ocean, *Earth Planet. Sci. Lett.*, *85*(1-3), 277–288.

Canales, J. P., J. A. Collins, J. Escartn, and R. S. Detrick (2000), Seismic structure across the rift valley of the Mid-Atlantic Ridge at 23°20' (MARK area): Implications for crustal accretion processes at slow spreading ridges, *J. Geophys. Res.*, *105*(B12), 28.411–28.426.

Canales, J. P., R. S. Detrick, S. M. Carbotte, G. M. Kent, J. B. Diebold, A. Harding, J. Babcock, M. Nedimovic, and E. V. Ark (2005), Upper crustal structure and axial topography at intermediate spreading ridges: Seismic constraints from the southern Juan de Fuca Ridge, *J. Geophys. Res.*, *110*, B12104, doi:10.1029/2005JB003630.

Cann, J. R., and M. R. Strens (1989), Modeling periodic megaplume emission by black smoker systems, *J. Geophys. Res.*, *94*(B9), 12,227–12,237.

Carbotte, S., C. Mutter, J. Mutter, and G. Ponce-Correa (1998), Influence of magma supply and spreading rate on crustal magma bodies and emplacement of the extrusive layer: Insights from the East Pacific Rise at lat 16°N, *Geology*, *26*(5), 455–458, doi:10.1130/0091-7613(1998)026<0455:IOMSAS>2.3.CO;2.

Carbotte, S., et al. (2002), A multi-channel seismic investigation of ridge crest and ridge flank structure along the Juan de Fuca Ridge, *Eos Trans. AGU*, *83*(47), Fall Meeting Supplement, Abstract T72C–07.

Carbotte, S. M., A. Solomon, and G. Ponce-Correa (2000), Evaluation of morphological indicators of magma supply and segmentation from a seismic reflection study of the East Pacific Rise 15°30'-17°N, *J. Geophys. Res.*, *105*(2), 2737–2759.

Carbotte, S. M., R. S. Detrick, A. Harding, J. P. Canales, J. Babcock, G. Kent, E. V. Ark, M. Nedimovic, and J. Diebold (2006), Rift topography linked to magmatism at the intermediate spreading Juan de Fuca Ridge, *Geology*, *34*(3), 209–212, doi:10.1130/G21969.1.

Castle, J. C., and R. D. van der Hilst (2000), The core-mantle boundary under the Gulf of Alaska: No ULVZ for shear waves, *Earth Plan. Sci. Lett.*, *176*(3-4), 311–321, doi: 10.1016/S0012-821X(00)00027-3.

Chen, Y. J., and J. Lin (2004), High sensitivity of ocean ridge thermal structure to changes in magma supply: the Galápagos Spreading Center, *Earth Planet. Sci. Lett.*, *221*(1-4), 263–273, doi:10.1016/S0012-821X(04)00099-8.

Choy, G. L. (1977), Theoretical seismograms of core phases calculated by frequency-dependent full wave theory, and their interpretation, *Geophys. J. Royal Astron. Soc.*, *51*(2), 275–312.

Choy, G. L., V. F. Cormier, R. Kind, G. Müller, and P. G. Richards (1980), A comparison of synthetic seismograms of core phases generated by the full wave theory and by the reflectivity method, *Geophys. J. Roy. Astr. Soc.*, *61*(1), 21–39.

Collier, J. S., and S. C. Singh (1997), Detailed structure of the top of the melt body beneath the East Pacific Rise at 9°40'N from waveform inversion of seismic reflection data, *J. Geophys. Res.*, *102*(9), 20,287–20,304.

Collier, J. S., and S. C. Singh (1998), A seismic inversion study of the axial magma chamber reflector beneath the east pacific rise near 10 degrees n, in *Modern ocean floor processes and the geological record*, *Geological Society Special Publications*, vol. 148, edited by R. A. Mills, pp. 17–28, Geological Society of London, London, UK.

Collier, J. S., and M. C. Sinha (1992), Seismic mapping of a magma chamber beneath the Valu Fa Ridge, Lau Basin, *J. Geophys. Res.*, *97*(10), 14,031–14,053.

Cormier, V. F. (2000), D" as a transition in the heterogeneity spectrum of the lowermost mantle, *J. Geophys. Res.*, *105*(7), 16,193–16,205, doi:2000JB900141.

Cormier, V. F. (in press), Forward modeling: Synthetic body wave seismograms, in *Seismology and Structure of the Earth*, *Treatise on Geophysics*, vol. 1, edited by A. M. Dziewonski and B. Romanowicz, Elsevier.

Cormier, V. F., and P. G. Richards (1988), Spectral synthesis of body waves in Earth models specified by vertically varying layers, in *Seismological algorithms; computational methods and computer programs*, edited by D. J. Doornbos, pp. 3–45, Academic Press, San Diego, CA, United States.

Cottrell, R. D., and J. A. Tarduno (2003), A late cretaceous pole for the Pacific plate: Implications for apparent and true polar wander and the drift of hotspots, *Tectonophys.*, *362*(1-4), 321–333, doi:10.1016/S0040-1951(02)00643-1.

Crotwell, H. P., T. J. Owens, and J. Ritsema (1999), The TauP Toolkit: Flexible seismic travel-time and ray-path utilities, *Seis. Res. Lett.*, *70*(2), 154–160.

Crough, S. T. (1978), Thermal origin of mid-plate hot-spot swells, *Geophys. J. Royal Astron. Soc.*, *55*(2), 451–469.

Crough, S. T. (1983), Hotspot swells, *Ann. Rev. Earth Planet. Sci.*, *11*, 165–193.

Cudrak, C. F. (1988), Shallow crustal structure of the Endeavour Ridge Segment, Juan de Fuca Ridge, from a detailed seismic refraction survey, Master's, University of British Columbia.

Cudrak, C. F., and R. M. Clowes (1993), Crustal structure of Endeavour Ridge Segment, Juan de Fuca Ridge, from a detailed seismic refraction survey, *J. Geophys. Res.*, *98*(B4), 6329–6349.

Cudrak, C. F., D. J. White, and R. M. Clowes (1987), A 3-D seismic refraction survey of crustal structure, Endeavour Segment, Juan de Fuca Ridge, *Eos Trans. AGU*, *68*, 1371.

Davies, G. F. (1988), Ocean bathymetry and mantle convection; 1, large-scale flow and hotspots, *J. Geophys. Res.*, *93*(9), 10,467–10,480.

Davies, G. F. (1992), Temporal variation of the hawaiian plume flux, *Earth Planet. Sci. Lett.*, *113*(1-2), 277–286.

Delaney, J. R., R. E. McDuff, V. Robigou, A. Schultz, M. Smith, J. Wells, V. A. Atnipp, and J. McClain (1990), Covariation in microseismicity and hydrothermal output in the Endeavour vent field, *Eos Trans. AGU*, *71*(43), 1609.

Delaney, J. R., V. Robigou, R. E. McDuff, and M. K. Tivey (1992), Geology of a vigorous hydrothermal system on the Endeavour Segment, Juan de Fuca Ridge, *Journal of Geophysical Research, B, Solid Earth and Planets*, *97*(13), 19,663–19,682.

Delaney, J. R., D. S. Kelley, M. D. Lilley, D. A. Butterfield, R. E. McDuff, J. A. Baross, J. W. Deming, H. P. Johnson, and V. Robigou (1997), The Endeavour hydrothermal system I: Cellular circulation above an active cracking front yields large sulfide structures, "fresh" vent water, and hyperthermophilic archaea, *RIDGE Events*, *8*(2), 11–19.

DeMets, C., R. G. Gordon, D. F. Argus, and S. Stein (1994), Effect of recent revisions to the geomagnetic reversal time scale on estimates of current plate motions, *Geophys. Res. Lett.*, *21*(20), 2191–2194.

Den, N., et al. (1969), Seismic-refraction measurements in the northwest Pacific Basin, *J. Geophys. Res.*, *74*(6), 1421–1434.

Detrick, R. S., and S. T. Crough (1978), Island subsidence, hot spots, and lithospheric thinning, *J. Geophys. Res.*, *83*(B3), 1236–1244.

Detrick, R. S., S. Carbotte, E. M. V. Ark, J. P. Canales, G. Kent, A. Harding, J. Diebold, and M. Nedimovic (2002a), New multichannel seismic constraints on the crustal structure of the Endeavour Segment, Juan de Fuca Ridge: Evidence for a crustal magma chamber, *Eos Trans. AGU*, *83*(47), Fall Meeting Supplement, Abstract T12B–1316.

Detrick, R. S., et al. (2002b), Correlated geophysical, geochemical, and volcanological manifestations of plume-ridge interaction along the Galápagos Spreading Center, *Geochem. Geophys. Geosys.*, *3*(10), 8501, doi:10.1029/2002GC000350.

Divins, D. (2001), Total sediment thickness of the world's oceans & marginal seas.

Divins, D. L., and B. Eakins (in preparation), Total sediment thickness map for the southeast pacific ocean, in *International Geological-Geophysical Atlas of the Pacific Ocean*, edited by G. B. Udintsev, Intergovernmental Oceanographic Commission.

Divins, D. L., and P. D. Rabinowitz (1991), Total sediment thickness map for the south atlantic ocean, in *International Geological and Geophysical Atlas of the Atlantic and Pacific Oceans (GAPA)*, edited by G. B. Udintsev, pp. 147–148, Intergovernmental Oceanographic Comission.

Dunn, R. A., D. R. Toomey, R. S. Detrick, and W. S. D. Wilcock (2001), Continuous mantle melt supply beneath an overlapping spreading center on the East Pacific Rise, *Science*, *291*(5510), 1955–1958, doi:10.1126/science.1057683.

Dziewonski, A. M., and D. L. Anderson (1981), Preliminary reference earth model, *Physics of the Earth and Planetary Interiors*, *25*(4), 297–356.

Escartin, J., M. Cannat, G. Pouliquen, A. Rabain, and J. Lin (2001), Crustal thickness of v-shaped ridges south of the azores; interaction of the mid-atlantic ridge (36 degrees -39 degrees n) and the azores hot spot, *J. Geophys. Res.*, *106*(10), 21,719–21,735, doi: 2001JB000224.

Fornari, D. J., and R. W. Embley (1995), Tectonic and volcanic controls on hydrothermal processes at the mid-ocean ridge; an overview based on near-bottom and submersible studies, in *Seafloor hydrothermal systems; physical, chemical, biological, and geological interactions*, *Geophysical Monograph*, vol. 91, edited by S. E. Humphris, R. A. Zierenberg, L. S. Mullineaux, and R. E. Thomson, pp. 1–46, American Geophysical Union, Washington, DC.

Fornberg, B. (1988), The pseudospectral method: Accurate representation of interfaces in elastic wave calculations, *Geophysics*, *53*(5), 625–637.

Fornberg, B. (1996), *A practical guide to pseudospectral methods*, Cambridge Monographs on Applied and Computational Mathematics, Cambridge University Press, New York.

Frey, F. A., S. Huang, J. Blichert-Toft, M. Regelous, and M. Boyet (2005), Origin of depleted components in basalt related to the Hawaiian hot spot: Evidence from isotopic and incompatible element ratios, *Geochem. Geophys. Geosys.*, *6*, Q02L07, doi: 10.1029/2004GC000757.

Fuchs, K. (1968), The reflection of spherical waves from transition zones with arbitrary depth-dependent elastic moduli and density, *J. Phys. Earth*, *16*, 27–41.

Fuchs, K., and G. Müller (1971), Computation of synthetic seismograms with the reflectivity method and comparison with observations, *Geophys. J. Roy. Astr. Soc.*, *23*(4), 417–433.

Furumura, T., and H. Takenaka (1995), A wraparound elimination technique for the pseudospectral wave synthesis using an antiperiodic extension of the wavefield, *Geophysics*, *60*(1), 302–307, doi:10.1190/1.1443760.

Furumura, T., B. L. N. Kennett, and M. Furumura (1998), Seismic wavefield calculation for laterally heterogeneous whole earth models using the pseudospectral method, *Geophys. J. Int.*, *135*(3), 845–860, doi:10.1046/j.1365-246X.1998.00682.x.

Garnero, E. J. (2004), A new paradigm for Earth's core-mantle boundary, *Science*, *304*(5672), 834–836, doi:10.1126/science.1097849.

Garnero, E. J., and D. V. Helmberger (1995), A very slow basal layer underlying large-scale low-velocity anomalies in the lower mantle beneath the pacific: evidence from core phases, *Physics of the Earth and Planetary Interiors*, *91*(1-3), 161–176, doi:10.1016/0031-9201(95)03039-Y.

Garnero, E. J., and D. V. Helmberger (1996), Seismic detection of a thin laterally varying boundary layer at the base of the mantle beneath the Central-Pacific, *Geophys. Res. Lett.*, *23*(9), 977–980.

Garnero, E. J., and D. V. Helmberger (1998), Further structural constraints and uncertainties of a thin laterally varying ultralow-velocity layer at the base of the mantle, *J. Geophys. Res.*, *103*(6), 12,495–12,509.

Garnero, E. J., and R. Jeanloz (2000a), Fuzzy patches on the Earth's core-mantle boundary?, *Geophys. Res. Lett.*, *27*(17), 2777–2780.

Garnero, E. J., and R. Jeanloz (2000b), Earth's enigmatic interface, *Science*, *289*(5476), 70–71, doi:10.1126/science.289.5476.70.

Garnero, E. J., and J. E. Vidale (1999), ScP; a probe of ultralow velocity zones at the base of the mantle, *Geophys. Res. Lett.*, *26*(3), 377–380.

Garnero, E. J., S. P. Grand, and D. V. Helmberger (1993), Low P-wave velocity at the base of the mantle, *Geophys. Res. Lett.*, *20*(17), 1843–1846.

Garnero, E. J., J. Revenaugh, Q. Williams, T. Lay, and L. H. Kellogg (1998), Ultralow velocity zone at the core-mantle boundary, in *The core-mantle boundary region*, *Geodynamics Series*, vol. 28, edited by M. Gurnis, M. E. Wysession, E. Knittle, and B. A. Buffett, pp. 319–334, American Geophysical Union, Washington, DC.

Gettrust, J. F., K. Furukawa, and L. W. Kroenke (1980), Crustal structure of the Shatsky Rise from seismic refraction measurements, *J. Geophys. Res.*, *85*(10), 5411–5415.

Gordon, R. G., and D. M. Jurdy (1986), Cenozoic global plate motions, *J. Geophys. Res.*, *91*(12), 12,389–12,406.

Grand, S. P. (2002), Mantle shear-wave tomography and the fate of subducted slabs, *Phil. Trans. Roy. Soc.*, *360*(1800), 2475–2491.

Grand, S. P., R. D. van der Hilst, and S. Widiyantoro (1997), Global seismic tomography: A snapshot of convection in the earth, *GSA Today*, *7*(4), 1–7.

Gropp, W., E. Lusk, and A. Skjellum (1998), *Using MPI: Portable Parallel Programming with the Message Passing Interface*, 2nd ed., MIT Press, Cambridge, MA.

Gropp, W., E. Lusk, and R. Thakur (1999), *Using MPI-2: Advanced Features of the Message Passing Interface*, 1st ed., MIT Press, Cambridge, MA.

Gu, Y. J., A. M. Dziewonski, W. Su, and G. Ekström (2001), Models of the mantle shear velocity and discontinuities in the pattern of lateral heterogeneities, *J. Geophys. Res.*, *106*(B6), 11,169–11,200, doi:10.1029/2001JB000340.

Hannington, M. D., I. R. Jonasson, P. M. Herzig, and S. Petersen (1995), Physical and chemical processes of seafloor mineralization at mid-ocean ridges, in *Seafloor hydrothermal systems; physical, chemical, biological, and geological interactions*, *Geophysical Monograph*, vol. 91, edited by S. E. Humphris, R. A. Zierenberg, L. S. Mullineaux, and R. E. Thomson, pp. 115–157, American Geophysical Union, Washington, DC.

Harding, A. J., G. M. Kent, and J. A. Orcutt (1993), A multichannel seismic investigation of upper crustal structure at 9°N on the East Pacific Rise: Implications for crustal accretion, *J. Geophys. Res.*, *98*(8), 13,925–13,944.

Havens, E., and J. Revenaugh (2001), A broadband seismic study of the lowermost mantle beneath mexico: Constraints on ultralow velocity zone elasticity and density, *J. Geophys. Res.*, *106*(B12), 30,809–30,820, doi:2000JB000072.

Hayes, D. E., and J. L. LaBrecque (1991), Sediment isopachs: Circum-antarctic to 30s, in *Marine Geological and Geophysical Atlas of the Circum-Antarctic to 30S*, edited by D. E. Hayes, pp. 29–33, American Geophysical Union, Washington, DC.

Haymon, R. M., D. J. Fornari, M. H. Edwards, S. Carbotte, D. Wright, and K. C. Macdonald (1991), Hydrothermal vent distribution along the East Pacific Rise crest (9°09'–54'N) and its relationship to magmatic and tectonic processes on fast-spreading mid-ocean ridges, *Earth Planet. Sci. Lett.*, *104*(2-4), 513–534.

Haymon, R. M., et al. (1993), Volcanic eruption of the mid-ocean ridge along the East Pacific Rise crest at 9°45–52'N: Direct submersible observations of seafloor phenomena associated with an eruption event in April, 1991, *Earth Planet. Sci. Lett.*, *119*(1-2), 85–101.

Helmberger, D., S. Ni, L. Wen, and J. Ritsema (2000), Seismic evidence for ultralow-velocity zones beneath africa and eastern atlantic, *J. Geophys. Res.*, *105*(10), 23,865–23,878.

Helmberger, D. V., E. J. Garnero, and X. Ding (1996), Modeling two-dimensional structure at core-mantle boundary, *J. Geophys. Res.*, *101*(B6), 13,963–13,972.

Helmberger, D. V., L. Wen, and X. Ding (1998), Seismic evidence that the source of the iceland hotspot lies at the coremantle boundary, *Nature*, *396*(6708), 251–255, doi: 10.1038/24357.

Hilde, T. W. C., N. Isezaki, and J. M. Wageman (1976), Mesozoic sea-floor spreading in the north pacific, in *Geophysical Monograph, no.19, The geophysics of the Pacific Ocean basin and its margin*, *Geophysical Monograph*, vol. 19, edited by G. H. Sutton, M. H. Manghnani, and R. Moberly, pp. 205–226, AGU, Washington, DC.

Hoffman, A. W. (1997), Mantle geochemistry: the message from oceanic volcanism, *Nature*, *385*, 219–229.

Holmes, M. L., and H. P. Johnson (1993), Upper crustal densities derived from sea floor gravity measurements; northern Juan de Fuca Ridge, *Geophys. Res. Lett.*, *20*(17), 1871–1874.

Hooft, E. E. E., R. S. Detrick, and G. M. Kent (1997), Seismic structure and indicators of magma budget along the southern East Pacific Rise, *J. Geophys. Res.*, *102*(12), 27,319–27,340.

Ito, G., and A. Taira (2000), Compensation of the Ontong Java Plateau by surface and subsurface loading, *J. Geophys. Res.*, *105*(5), 11,171–11,183.

Ito, G. T. (2001), Reykjanes "V"-shaped ridges originating from a pulsing and dehydrating mantle plume, *Nature*, *411*(6838), 681–684, doi:10.1038/35079561.

Ito, G. T., and J. Lin (1995a), Mantle temperature anomalies along the present and paleoaxes of the Galapagos spreading center as inferred from gravity analyses, *J. Geophys. Res.*, *100*(B3), 3733–3745.

Ito, G. T., and J. Lin (1995b), Oceanic spreading center-hotspot interactions: Constraints from along-isochron bathymetric and gravity anomalies, *Geology*, *23*(7), 657–660.

Ito, G. T., J. Lin, and C. W. Gable (1996), Dynamics of mantle flow and melting at a ridge-centered hotspot; Iceland and the Mid-Atlantic Ridge, *Earth Planet. Sci. Lett.*, *144*(1-2), 53–74.

Jacobs, A. M., A. J. Harding, G. M. Kent, and J. A. Collins (2003), Along-axis crustal structure of the Lau Back-Arc Basin from multichannel seismic observations, *Eos Trans. AGU*, *84*(46), Fall Meet. Suppl., Abstract B12A–0728.

Jeanloz, R., and Q. Williams (1998), The core-mantle boundary region, in *Ultrahigh-pressure mineralogy; physics and chemistry of the Earth's deep interior*, *Reviews in Mineralogy*, vol. 37, edited by R. J. Hemley, pp. 241–259, Mineralogical Society of America, Washington, DC.

Jenkyns, H. C. (1995), Carbon-isotope stratigraphy and paleoceanographic significance of the Lower Cretaceous shallow-water carbonates of Resolution Guyot, Mid-Pacific Mountains, in *Proceedings of the Ocean Drilling Program; scientific results, Northwest Pacific atolls and guyots; covering Leg 143 of the cruises of the Drilling Vessel JOIDES Resolution, Honolulu, Hawaii, to Majuro, Republic of Marshall Islands, sites 865-870, 18 March-19 May 1992*, *Proceedings of the Ocean Drilling Program, Scientific Results*, vol. 143, edited by E. L. Winterer, W. W. Sager, J. V. Firth, H. M. Arnaud, P. E. Baker, F. Baudin, T. J. Bralower, P. R. Castillo, P. A. Cooper, P. G. Flood, X. Golovchenko, Y. Iryu, M. K. Ivanov, H. C. Jenkyns, J. A. M. Kenter, I. O. Murdmaa, J. Mutterlose, Y. Nogi, C. K. Paull, E. L. Polgreen, U. Roehl, W. V. Sliter, A. Strasser, N. H. M. Swinburne, J. A. Tarduno, R. J. van Waasbergen, and S. K. Stewart, pp. 99–104, Texas A & M University, Ocean Drilling Program, College Station, TX.

Jenkyns, H. C., C. K. Paull, D. I. Cummins, and P. D. Fullagar (1995), Strontium-isotope stratigraphy of Lower Cretaceous atoll carbonates in the Mid-Pacific Mountains, in *Proceedings of the Ocean Drilling Program; scientific results, Northwest Pacific atolls and guyots; covering Leg 143 of the cruises of the Drilling Vessel JOIDES Resolution, Honolulu, Hawaii, to Majuro, Republic of Marshall Islands, sites 865-870, 18 March-19 May 1992*, *Proceedings of the Ocean Drilling Program, Scientific Results*, vol. 143, edited by

E. L. Winterer, W. W. Sager, J. V. Firth, H. M. Arnaud, P. E. Baker, F. Baudin, T. J. Bralower, P. R. Castillo, P. A. Cooper, P. G. Flood, X. Golovchenko, Y. Iryu, M. K. Ivanov, H. C. Jenkyns, J. A. M. Kenter, I. O. Murdmaa, J. Mutterlose, Y. Nogi, C. K. Paull, E. L. Polgreen, U. Roehl, W. V. Sliter, A. Strasser, N. H. M. Swinburne, J. A. Tarduno, R. J. van Waasbergen, and S. K. Stewart, pp. 89–97, Texas A & M University, Ocean Drilling Program, College Station, TX.

Johnson, H. P., K. Becker, and R. P. V. Herzen (1993), Near-axis heat flow measurements on the northern Juan de Fuca Ridge; implications for fluid circulation in oceanic crust, *Geophys. Res. Lett.*, *20*(17), 1875–1878.

Johnson, H. P., M. Hutnak, R. P. Dziak, C. G. Fox, I. Urcuyo, J. P. Cowen, J. Nabelek, and C. Fisher (2000), Earthquake-induced changes in a hydrothermal system on the Juan de Fuca mid-ocean ridge, *Nature*, *407*(6801), 174–177.

Jordan, T. H. (1979), Mineralogies, densities and seismic velocities of garnet lherzolites and their geophysical implications, in *The mantle sample; inclusions in kimberlites and other volcanics; Proceedings of the Second international kimberlite conference; Volume 2*, edited by F. R. Boyd and H. O. A. Meyer, pp. 1–14, AGU, Washington, DC.

Kadko, D. C., N. D. Rosenberg, J. E. Lupton, R. W. Collier, and M. D. Lilley (1990), Chemical reaction rates and entrainment within the Endeavour Ridge hydrothermal plume, *Earth Planet. Sci. Lett.*, *99*(4), 315–335.

Kappel, E. S., and W. B. F. Ryan (1986), Volcanic episodicity and a non-steady state rift valley along Northeast Pacific spreading centers; evidence from Sea MARC I, *J. Geophys. Res.*, *91*(14), 13,925–13,940.

Karsten, J. L., S. R. Hammond, E. E. Davis, and R. G. Currie (1986), Detailed geomorphology and neotectonics of the Endeavour Segment, Juan de Fuca Ridge; new results from Seabeam swath mapping, *Geol. Soc. Am. Bull.*, *97*(2), 213–221.

Karsten, J. L., J. R. Delaney, J. M. Rhodes, and R. A. Liias (1990), Spatial and temporal evolution of magmatic systems beneath the Endeavour Segment, Juan de Fuca Ridge; tectonic and petrologic constraints, *J. Geophys. Res.*, *95*(12), 19,235–19,256.

Kelemen, P. B., N. Shimizu, and V. J. M. Salters (1995), Extraction of mid-ocean-ridge basalt from the upwelling mantle by focused flow of melt in dunite channels, *Nature*, *375*(6534), 747–753.

Kelemen, P. B., G. Hirth, N. Shimizu, M. Spiegelman, and H. J. B. Dick (1999), A review of melt migration processes in the adiabatically upwelling mantle beneath oceanic spreading ridges, in *Mid-ocean ridges; dynamics of processes associated with creation of new ocean crust*, edited by J. R. Cann, H. Elderfield, and A. Laughton, pp. 67–102, Cambridge University Press, Cambridge, UK.

Keller, R. A., M. R. Fisk, and W. M. White (2000), Isotopic evidence for Late Cretaceous plume-ridge interaction at the Hawaiian hotspot, *Nature*, *405*(6787), 673–676.

Keller, R. A., D. W. Graham, K. A. Farley, R. A. Duncan, and J. E. Lupton (2004), Cretaceous-to-recent record of elevated ^{3}he/^{4}he along the Hawaiian-Emperor volcanic chain, *Geochem. Geophys. Geosys.*, *5*, Q12L05, doi:10.1029/2004GC000739.

Kelley, D. S., J. R. Delaney, and D. R. Yoerger (2001), Geology and venting characteristics of the Mothra hydrothermal field, Endeavour Segment, Juan de Fuca Ridge, *Geology*, *29*(10), 959–962, doi:10.1130/0091-7613(2001)029<0959:GAVCOT>2.0.CO;2.

Kelley, D. S., J. A. Baross, and J. R. Delaney (2002), Volcanoes, fluids, and life at mid-ocean ridge spreading centers, *Ann. Rev. Earth Planet. Sci.*, *30*, 385–491, doi: 10.1146/annurev.earth.30.091201.141331.

Kelley, D. S., J. R. Delaney, M. D. Lilley, D. A. Butterfield, and J. D. Baross (2003), Geological, biological, and chemical linkages within the Endeavour hydrothermal system, in *Geological Society of America, 2003 annual meeting*, *Abstracts with Programs - Geological Society of America*, vol. 35, p. 220, Geological Society of America (GSA), Seattle, WA.

Kent, G. M., A. J. Harding, and J. A. Orcutt (1993a), Distribution of magma beneath the East Pacific Rise near the 9 degrees 03'N overlapping spreading center from forward modeling of common depth point data, *J. Geophys. Res.*, *98*(8), 13,971–13,995.

Kent, G. M., A. J. Harding, and J. A. Orcutt (1993b), Distribution of magma beneath the East Pacific Rise between the Clipperton Transform and the 9 degrees 17'N Deval from forward modeling of common depth point data, *J. Geophys. Res.*, *98*(9), 13,945–13,969.

Kent, G. M., A. J. Harding, J. A. Orcutt, R. S. Detrick, J. C. Mutter, and P. Buhl (1994), Uniform accretion of oceanic crust south of the Garrett Transform at 14 degrees 15'S on the East Pacific Rise, *J. Geophys. Res.*, *99*(5), 9097–9116.

Kent, G. M., I. I. Kim, A. J. Harding, R. S. Detrick, and J. A. Orcutt (1996), Suppression of sea-floor-scattered energy using a dip-moveout approach: Application to the mid-ocean ridge environment, *Geophys.*, *61*(3), 821–834.

King, S. D., J. P. Lowman, and C. W. Gable (2002), Episodic tectonic plate reorganizations driven by mantle convection, *Earth Planet. Sci. Lett.*, *203*(1), 83–91, doi: doi:10.1016/S0012-821X(02)00852-X.

Kinzler, R. J., and T. L. Grove (1992a), Primary magmas of mid-ocean ridge basalts 1. Experiments and methods, *J. Geophys. Res.*, *97*(B5), 6885–6906.

Kinzler, R. J., and T. L. Grove (1992b), Primary magmas of mid-ocean ridge basalts 2. Applications, *J. Geophys. Res.*, *97*(B5), 6907–6926.

Kinzler, R. J., and T. L. Grove (1993), Corrections and further discussion of the primary magmas of mid-ocean ridge basalts, 1 and 2, *J. Geophys. Res.*, *98*(B12), 22,339–22,348.

Klaus, A., and W. W. Sager (2002), High-resolution site survey seismic reflection data for odp leg 198 drilling on Shatsky Rise, *Proc. Ocean Drill. Prog. Init. Rep.*, *198*, 21.

Knittle, E. (1998), The solid/liquid partitioning of major and radiogenic elements at lower mantle pressures; implications for the core-mantle boundary region, in *The core-mantle boundary region*, edited by M. Gurnis, M. E. Wysession, E. Knittle, and B. A. Buffett, Geodynamics Series, pp. 119–130, American Geophysical Union, Washington, DC.

Kogan, L. I., L. P. Zonenshayn, and O. A. Schmidt (1982), Structure of the Hess Rise, Pacific Ocean (from data of deep reflection seismic profiles), *Geotectonics*, *16*(3), 179–189.

Kohler, M. D., J. E. Vidale, and P. M. Davis (1997), Complex scattering with D" observed on the very dense Los Angelos Region Seismic Experiment passive array, *Geophys. Res. Lett.*, *24*(15), 1855–1858, doi:97GL01823.

Komatitsch, D., and J. Tromp (2002a), Spectral-element simulations of global seismic wave propagation – I. Validation, *Geophys. J. Int.*, *149*(2), 390–412, doi:10.1046/j.1365-246X.2002.01653.x.

Komatitsch, D., and J. Tromp (2002b), Spectral-element simulations of global seismic wave propagation – II. Three-dimensional models, oceans, rotation and self-gravitation, *Geophys. J. Int.*, *150*(1), 303–318, doi:10.1046/j.1365-246X.2002.01716.x.

Komatitsch, D., J. Ritsema, and J. Tromp (2002), The spectral-element method, Beowulf computing, and global seismology, *Nature*, *298*(5599), 1737–1742, doi: 10.1126/science.1076024.

Kosloff, D., and D. Kessler (1990), Seismic numerical modeling, in *Tomographie ocenographique et geophysique–Oceanographic and geophysical tomography*, edited by Y. Desaubies, A. Tarantola, and J. Zinn-Justin, pp. 249–312, Elsevier Science Pub. Co., New York.

Kroenke, L. W., and K. Nemoto (1982), Marine geology of the Hess Rise; 2, basement morphology, sediment thickness, and structural geology, *J. Geophys. Res.*, *87*(11), 9259–9278.

Kunze, A. W. G. (1980), On the flexural rigidity and effective viscosity of the lithosphere in the Hawaiian area, *Tectonophys.*, *69*(3-4), T1–T8.

Kuo, B. Y., and D. W. Forsyth (1988), Gravity anomalies of the ridge-transform system in the South Atlantic between 31 and 34.4 S: Upwelling centers and variations in crustal thickness, *Marine Geophys. Res.*, *10*, 205–232.

Larson, R. L., and C. G. Chase (1972), Late Mesozoic of the Western Pacific Ocean, *Geol. Soc. Am. Bull.*, *83*(12), 3627–3643.

Lay, T., and E. J. Garnero (submitted), Reconciling the post-perovskite phase with seismological observations of lowermost mantle structure, in *Special Monograph on Post-Perovskite*, edited by K. Hirose, D. Yuen, T. Lay, and J. Brodholst, American Geophysical Union, Washington, DC.

Li, X., R. Kind, X. Yuan, I. Wolbern, and W. Hanka (2004), Rejuvenation of the lithosphere by the Hawaiian plume, *Nature*, *427*, 827–829, doi:10.1038/nature02349.

Lilley, M. D., M. C. Landsteiner, E. A. McLaughlin, C. B. Parker, A. S. M. Cherkaoui, G. Lebon, S. R. Viers, and J. R. Delaney (1995), Real-time mapping of hydrothermal plumes on the Endeavor Segment of the Juan de Fuca, *Eos Trans. AGU*, *76*(46 suppl.), 420.

Lilley, M. D., D. A. Butterfield, J. E. Lupton, and E. J. Olson (2003), Magmatic events can produce rapid changes in hydrothermal vent chemistry, *Nature*, *422*(6934), 878–881, doi:10.1038/nature01569.

Lister, C. R. B. (1974), On the penetration of water into hot rock, *Geophys. J. Royal Astron. Soc.*, *39*(3), 465–509.

Lister, C. R. B. (1980a), Heat flow and hydrothermal circulation, *Ann. Rev. Earth Planet. Sci.*, *8*, 95–117.

Lister, C. R. B. (1980b), Rock and water histories during sub-oceanic hydrothermal events, in *Geologie des oceans, colloque C4; 26eme Congres geologique international*, *Publications du 26eme congres geologique international*, vol. Oceanologica Acta , 4, supplement, edited by X. Le Pichon, J. Debyser, and F. Vine, pp. 41–46, Gauthier-Villars, Paris, France.

Lister, C. R. B. (1982), "Active" and "passive" hydrothermal systems in the oceanic crust; predicted physical conditions, in *The Dynamic Environment of the Ocean Floor*, edited by K. A. Fanning and F. T. Manheim, pp. 441–470, D. C. Heath and Co., Lexington, MA.

Lowenthal, D., L. Lu, R. Roberson, and J. Sherwood (1976), The wave equation applied to migration, *Geophys. Prospect.*, *24*, 380–399.

Lowman, J. P., S. D. King, and C. W. Gable (2003), The role of the heating mode of the mantle in intermittent reorganization of the plate velocity field, *Geophys. J. Int.*, *152*(2), 455–467, doi:10.1046/j.1365-246X.2003.01862.x.

Mammerickx, J., and G. F. Sharman (1988), Tectonic evolution of the North Pacific during the Cretaceous quiet period, *J. Geophys. Res.*, *93*(B4), 3009–3024.

Manga, M., and R. Jeanloz (1996), Implications of a metal-bearing chemical boundary layer in D" for mantle dynamics, *Geophys. Res. Lett.*, *23*(22), 3901–3904, doi:96GL03021.

Mao, W. L., H. k. Mao, W. Sturhahn, J. Zhao, V. B. Prakapenka, Y. Meng, J. Shu, Y. Fei, and R. J. Hemley (2006), Iron-rich post-perovskite and the origin of ultralow-velocity zones, *Science*, *312*(5773), 564–565, doi:10.1126/science.1123442.

Masters, G., G. Laske, H. Bolton, and A. Dziewonski (2000), The relative behavior of shear velocity, bulk sound speed, and compressional velocity in the mantle; implications for chemical and thermal structure, in *Earth's deep interior; mineral physics and tomography from the atomic to the global scale*, *Geophysical Monograph*, vol. 117, edited by S.-i. Karato, A. M. Forte, R. C. Liebermann, G. Masters, and L. Stixrude, pp. 64–86, American Geophysical Union, Washington, DC.

McClain, J. S., M. L. Begnaud, M. A. Wright, J. Fondrk, and G. K. V. Damm (1993), Seismicity and tremor in a submarine hydrothermal field; the northern Juan de Fuca Ridge, *Geophys. Res. Lett.*, *20*(17), 1883–1886.

McNutt, M., and L. Shure (1986), Estimating the compensation depth of the Hawaiian Swell with linear filters, *J. Geophys. Res.*, *91*(14), 13,915–13,923.

McNutt, M. K., and A. V. Judge (1990), The superswell and mantle dynamics beneath the South Pacific, *Science*, *248*(4958), 969–975.

Mégnin, C., and B. Romanowicz (2000), The threedimensional shear velocity structure of the mantle from the inversion of body, surface and highermode waveforms, *Geophys. J. Int.*, *143*(3), 709–728, doi:10.1046/j.1365-246X.2000.00298.x.

Montelli, R., G. Nolet, F. A. Dahlen, G. Masters, R. Engdahl, and S.-H. Hung (2004), Finite-frequency tomography reveals a variety of plumes in the mantle, *Science*, *303*(5656), 338–343, doi:10.1126/science.1092485.

Morgan, W. J. (1971), Convection plumes in the lower mantle, *Nature*, *230*(5288), 42–43.

Mori, J., and D. V. Helmberger (1995), Localized boundary layer below the mid-Pacific velocity anomaly identified from a PcP precursor, *J. Geophys. Res.*, *100*(10), 20,359–20,365.

Müller, G. (1985), The reflectivity method; a tutorial, *J. Geophysics*, *58*(1-3), 153–174.

Muller, R. D., W. R. Roest, J.-Y. Royer, L. M. Gahagan, and J. G. Sclater (1997), Digital isochrons of the world's ocean floor, *J. Geophys. Res.*, *102*(B2), 3211–3214.

Murakami, M., K. Hirose, K. Kawamura, N. Sata, and Y. Ohishi (2004), Post-perovskite phase transition in MgSiO3, *Science*, *304*(5672), 855–858, doi:10.1126/science.1095932.

Mutter, J. C., S. M. Carbotte, W. Su, L. Xu, P. Buhl, R. S. Detrick, G. M. Kent, J. A. Orcutt, and A. J. Harding (1995), Seismic images of active magma systems beneath the East Pacific Rise between 17°05' and 17°35'S, *Science*, *268*(5209), 391–395.

Nakanishi, M., K. Tamaki, and K. Kobayashi (1989), Mesozoic magnetic anomaly lineations and seafloor spreading history of the northwestern Pacific, *J. Geophys. Res.*, *94*(11), 15,437–15,462.

Nedimovic, M. R., S. Mazzotti, and R. D. Hyndman (2003), Three-dimensional structure from feathered two-dimensional marine seismic reflection data: The eastern Nankai Trough, *J. Geophys. Res.*, *108*(B10), 2456, doi:10.1029/2002JB001959.

Nedimovic, M. R., S. M. Carbotte, A. J. Harding, R. S. Detrick, J. P. Canales, J. B. Diebold, G. M. Kent, M. Tischer, and J. M. Babcock (2005), Frozen magma lenses below the oceanic crust, *Nature*, *436*(7054), 1149–1152, doi:10.1038/nature03944.

Neumann, G. A., D. W. Forsyth, and D. T. Sandwell (1993), Comparison of marine gravity from shipboard and high-density satellite altimetry along the Mid-Atlantic Ridge, 30.5 degrees -35.5 degrees S, *Geophys. Res. Lett.*, *20*(15), 1639–1642.

Ni, S., and D. V. Helmberger (2001), Probing an ultra-low velocity zone at the core mantle boundary with P and S waves, *Geophys. Res. Lett.*, *28*(12), 2345–2348, doi:2000GL012766.

Ni, S., and D. V. Helmberger (2003), Ridge-like lower mantle structure beneath South Africa, *J. Geophys. Res.*, *108*(B2), 2094, doi:10.1029/2001JB001545.

Ni, S., V. F. Cormier, and D. V. Helmberger (2003), A comparison of synthetic seismograms for 2D structures: Semianalytical versus numerical, *Bull. Seis. Soc. Am.*, *93*(6), 2752–2757, doi:10.1785/0120030011.

Nielsen, P., F. If, P. Berg, and O. Skovgaard (1994), Using the pseudospectral technique on curved grids for 2D acoustic forward modelling, *Geophys. Prospecting*, *42*(4), 321–341.

Niu, F., and L. Wen (2001), Strong seismic scatterers near the core-mantle boundary west of Mexico, *Geophys. Res. Lett.*, *28*(18), 3557–3560, doi:2001GL013270.

Olson, P., and U. Christensen (1986), Solitary wave propagation in a fluid conduit within a viscous matrix, *J. Geophys. Res.*, *91*, 6367–6374.

Parker, R. L. (1972), The rapid calculation of potential anomalies, *Geophys. J. Royal Astron. Soc.*, *31*, 447–455.

Parsons, B., and J. G. Sclater (1977), An analysis of the variation of ocean floor bathymetry and heat flow with age, *J. Geophys. Res.*, *82*(5), 803–827.

Party, S. S. (2002a), Leg 197 summary: motion of the Hawaiian hotspot, a paleomagnetic test, in *Proceedings of the Ocean Drilling Program, Initial Reports*, vol. 197, edited by J. A. Tarduno, R. A. Duncan, and D. W. Scholl, pp. 1–92, Ocean Drilling Program, College Station, TX.

Party, S. S. (2002b), Leg 198 summary: Extreme warmth in the Cretaceous and Paleogene: a depth transect on Shatsky Rise, Central Pacific, in *Proceedings of the Ocean Drilling Program, Initial Reports*, vol. 198, edited by T. J. Bralower, I. P. Silva, and M. J. Malone, pp. 1–148, Ocean Drilling Program, College Station, TX.

Persh, S. E., J. E. Vidale, and P. S. Earle (2001), Absence of short-period ULVZ precursors to PcP and ScP from two regions of the CMB, *Geophys. Res. Lett.*, *28*(2), 387–390, doi: 2000GL011607.

Phipps Morgan, J., and Y. J. Chen (1993), The genesis of oceanic crust; magma injection, hydrothermal circulation, and crustal flow, *J. Geophys. Res.*, *98*(4), 6283–6297.

Phipps Morgan, J., W. J. Morgan, and E. Price (1995), Hotspot melting generates both hotspot volcanism and a hotspot swell?, *J. Geophys. Res.*, *100*(B5), 8045–8062.

Pringle, M. S., and G. B. Dalrymple (1993), Geochronological constraints on a possible hot spot origin for Hess Rise and the Wentworth seamount chain, in *The Mesozoic Pacific; geology, tectonics, and volcanism*, *Geophysical Monograph*, vol. 77, edited by M. S. Pringle, W. W. Sager, W. V. Sliter, and S. Stein, pp. 263–277, American Geophysical Union, Washington, DC.

Pringle, M. S., and R. A. Duncan (1995), Radiometric ages of basaltic lavas recovered at sites 865, 866, and 869, in *Proceedings of the Ocean Drilling Program; scientific results, Northwest Pacific atolls and guyots; covering Leg 143 of the cruises of the Drilling Vessel JOIDES Resolution, Honolulu, Hawaii, to Majuro, Republic of Marshall Islands, sites 865-870, 18 March-19 May 1992*, *Proceedings of the Ocean Drilling Program, Scientific Results*, vol. 143, edited by E. L. Winterer, W. W. Sager, J. V. Firth, H. M. Arnaud, P. E. Baker, F. Baudin, T. J. Bralower, P. R. Castillo, P. A. Cooper, P. G. Flood, X. Golovchenko, Y. Iryu, M. K. Ivanov, H. C. Jenkyns, J. A. M. Kenter, I. O. Murdmaa, J. Mutterlose, Y. Nogi, C. K. Paull, E. L. Polgreen, U. Roehl, W. V. Sliter, A. Strasser, N. H. M. Swinburne, J. A. Tarduno, R. J. van Waasbergen, and S. K. Stewart, pp. 277–283, Texas A & M University, Ocean Drilling Program, College Station, TX.

Purdy, G. M., L. S. L. Kong, G. L. Christeson, and S. C. Solomon (1992), Relationship between spreading rate and the seismic structure of mid-ocean ridges, *Nature*, *355*(6363), 815–817, doi:10.1038/355815a0.

Reasoner, C., and J. Revenaugh (2000), ScP constraints on ultralow-velocity zone density and gradient thickness beneath the Pacific, *J. Geophys. Res.*, *105*(B12), 28,173–28.182, doi:2000JB900331.

Regelous, M., A. W. Hofmann, W. Abouchami, and S. J. G. Galer (2003), Geochemistry of lavas from the Emperor Seamounts, and the geochemical evolution of Hawaiian magmatism from 85 to 42 ma, *J. Petrol.*, *44*(1), 113–140.

Revenaugh, J., and R. Meyer (1997), Seismic evidence of partial melt within a possibly ubiquitous low-velocity layer at the base of the mantle, *Science*, *277*(5326), 670–673.

Ribe, N. M., and U. R. Christensen (1994), Three-dimensional modeling of plume-lithosphere interaction, *J. Geophys. Res.*, *99*(B1), 669–682.

Ribe, N. M., and U. R. Christensen (1999), The dynamical origin of Hawaiian volcanism, *Earth Planet. Sci. Lett.*, *171*(4), 517–531.

Ritsema, J., and H. J. van Heijst (2000), Seismic imaging of structural heterogeneity in Earth's mantle: Evidence for large-scale mantle flow, *Science Progress*, *83*, 243–259.

Robertsson, J. O. A., J. O. Blanch, and W. W. Symes (1994), Viscoelastic finite-difference modeling, *Geophysics*, *59*(9), 1444–1456, doi:10.1190/1.1443701.

Robigou, V., J. R. Delaney, and D. S. Stakes (1993), Large massive sulphide deposits in a newly discovered active hydrothermal system, the High-Rise Field, Endeavour Segment, Juan de Fuca Ridge, *Geophys. Res. Lett.*, *20*(17), 1887–1890.

Robinson, E. M. (1988), The topographic and gravitational expression of density anomalies due to melt extraction in the uppermost oceanic mantle, *Earth Planet. Sci. Lett.*, *90*(2), 221–228.

Rohr, K. M. M., B. Milkereit, and C. J. Yorath (1988), Asymmetric deep crustal structure across the Juan de Fuca Ridge, *Geology*, *16*, 533–537.

Rondenay, S., and K. M. Fischer (2003), Constraints on localized core-mantle boundary structure from multichannel, broadband SKS coda analysis, *J. Geophys. Res.*, *108*(B11), 2537, doi:10.1029/2003JB002518.

Ross, A. R., H. Thybo, and L. N. Solidilov (2004), Reflection seismic profiles of the core-mantle boundary, *J. Geophys. Res.*, *109*, B08303, doi:10.1029/2003JB002515.

Rost, S., and J. Revenaugh (2001), Seismic detection of rigid zones at the top of the core, *Science*, *294*(5548), 1911–1914, doi:10.1126/science.1065617.

Rost, S., and J. Revenaugh (2003), Small-scale ultralow-velocity zone structure imaged by ScP, *J. Geophys. Res.*, *108*(1), 2056, doi:10.1029/2001JB001627.

Sager, W. W., and H.-C. Han (1993), Rapid formation of the Shatsky Rise oceanic plateau inferred from its magnetic anomaly, *Nature*, *364*(6438), 610–613.

Sager, W. W., D. W. Handschumacher, T. W. C. Hilde, and D. R. Bracey (1988), Tectonic evolution of the northern Pacific Plate and Pacific-Farallon-Izanagi triple junction in the Late Jurassic and Early Cretaceous (m21-m10), *Tectonophys.*, *155*(1-4), 345–364.

Sandwell, D. T. (1982), Thermal isostasy; response of a moving lithosphere to a distributed heat source, *J. Geophys. Res.*, *87*(2), 1001–1014.

Sandwell, D. T., and W. H. F. Smith (1995), Marine gravity from satellite altimetry.

Sandwell, D. T., and W. H. F. Smith (1997), Marine gravity anomaly from Geosat and ERS 1 satellite altimetry, *J. Geophys. Res.*, *102*(B5), 10,039–10,054.

Sarrazin, J., V. Robigou, S. K. Juniper, and J. R. Delaney (1997), Biological and geological dynamics over four years on a high-temperature sulfide structure at the Juan de Fuca Ridge hydrothermal observatory, *Marine Ecology Progress Series*, *153*, 5–24.

Schilling, J.-G. (1991), Fluxes and excess temperatures of mantle plumes inferred from their interaction with migrating mid-ocean ridges, *Nature*, *352*, 397–403.

Scott, D. R., D. J. Stevenson, and J. A. Whitehead (1986), Observations of solitary waves in a viscously deformable pipe, *Nature*, *319*, 759–761.

Sharp, W. D., and D. A. Clague (2002), An older, slower Hawaii-Emperor bend, *Eos Trans. AGU*, *Fall Meeting Supplement*, Abstract T61C–04.

Shim, S.-H. (2005), Stability of mgsio$_3$ perovskite in the lower mantle, in *Earth's deep mantle; structure, composition, and evolution*, *Geophysical Monograph*, vol. 160, edited by R. D. van der Hilst, J. D. Bass, J. Matas, and J. Trampert, pp. 261–282, American Geophysical Union, Washington, DC.

Simmons, N. A., and S. P. Grand (2002), Partial melting in the deepest mantle, *Geophys. Res. Lett.*, *29*(11), 1552, doi:10.1029/2001GL013716.

Sleep, N. H. (1990), Hotspots and mantle plumes: Some phenomenology, *J. Geophys. Res.*, *95*(B5), 6715–6736.

Sleep, N. H. (1992), Time dependence of mantle plumes; some simple theory, *J. Geophys. Res.*, *97*(13), 20,007–20,019.

Smith, W. H. F., and D. T. Sandwell (1994), Bathymetric prediction from dense altimetry and sparse shipboard bathymetry, *J. Geophys. Res.*, *99*(B11), 21,803–21,824.

Smith, W. H. F., and D. T. Sandwell (1997), Global sea floor topography from satellite altimetry and ship depth soundings, *Science*, *277*, 1956–1962.

Sohn, R. A., D. J. Fornari, K. L. V. Damm, J. A. Hildebrand, and S. C. Webb (1998), Seismic and hydrothermal evidence for a cracking event on the East Pacific Rise crest at 9°50'N, *Nature*, *396*(6707), 159–161.

Sohn, R. A., J. A. Hildebrand, and S. C. Webb (1999), A microearthquake survey of the high-temperature vent fields on the volcanically active East Pacific Rise, *J. Geophys. Res.*, *104*(11), 25,367–25,377.

Sours-Page, R., K. T. M. Johnson, R. L. Nielsen, and J. L. Karsten (1999), Local and regional variation of MORB parent magmas; evidence from melt inclusions from the Endeavour Segment of the Juan de Fuca Ridge, *Contrib. Min. Pet.*, *134*(4), 342–363.

Stacey, F. D. (1992), *Physics of the Earth*, third ed., Brookfield Press, Kenmore, Queensland, Australia.

Stein, C. A., and S. Stein (1992), A model for the global variation in oceanic depth and heat flow with lithospheric age, *Nature*, *359*(6391), 123–129.

Steinberger, B. (2000), Plumes in a convecting mantle; models and observations for individual hotspots, *J. Geophys. Res.*, *105*(5), 11,127–11,152.

Steinberger, B., and R. J. O'Connell (1998), Advection of plumes in mantle flow; implications for hot spot motion, mantle viscosity and plume distribution, *Geophys. J. Int.*, *132*(2), 412–434.

Stutzmann, E., L. Vinnik, A. Ferreira, and S. Singh (2000), Constraint on the S-wave velocity at the base of the mantle, *Geophys. Res. Lett.*, *27*(11), 1571–1574, doi:1999GL010984.

Tackley, P. J. (1998), Three-dimensional simulations of mantle convection with a thermochemical basal boundary layer; D"?, in *The core-mantle boundary region*, *Geodynamics Series*, vol. 28, edited by M. Gurnis, M. E. Wysession, E. Knittle, and B. A. Buffett, pp. 231–253, American Geophysical Union, Washington, DC.

Tackley, P. J., S. Xie, T. Nakagawa, and J. W. Hernlund (2005), Numerical and laboratory studies of mantle convection; philosophy, accomplishments, and thermochemical structure and evolution, in *Earth's deep mantle; structure, composition, and evolution*, *Geophysical Monograph*, vol. 160, edited by R. D. van der Hilst, J. D. Bass, J. Matas, and J. Trampert, pp. 83–99, American Geophysical Union, Washington, DC.

Tarduno, J. A., and R. D. Cottrell (1997), Paleomagnetic evidence for motion of the Hawaiian hotspot during formation of the Emperor seamounts, *Earth Planet. Sci. Lett.*, *153*(3-4), 171–180.

Tarduno, J. A., and W. W. Sager (1995), Polar standstill of the Mid-Cretaceous Pacific Plate and its geodynamic implications, *Science*, *269*(5226), 956–959.

Tarduno, J. A., et al. (2003), The Emperor Seamounts: Southward motion of the Hawaiian hotspot plume in earth's mantle, *Science*, *301*(5636), 1064–1069, doi: 10.1126/science.1086442.

Ten Brink, U. S., and T. M. Brocher (1987), Multichannel seismic evidence for a subcrustal intrusive complex under Oahu and a model for Hawaiian volcanism, *J. Geophys. Res.*, *92*(B13), 13,687–13,707.

Ten Brink, U. S., and T. M. Brocher (1988), Multichannel seismic evidence for variations in crustal thickness across the Molokai fracture zone in the Mid-Pacific, *J. Geophys. Res.*, *93*(2), 1119–1130.

Tessmer, E., D. Kosloff, and A. Behle (1992), Elastic wave propagation simulation in the presence of surface topography, *Geophys. J. Int.*, *108*(2), 621–632.

Thomas, C., M. Weber, C. W. Wicks, and F. Scherbaum (1999), Small scatterers in the lower mantle observed at German broadband arrays, *J. Geophys. Res.*, *104*(B7), 15,073–15,088, doi:1999JB900128.

Thomas, C., J.-M. Kendall, and J. Lowman (2004), Lower-mantle seismic discontinuities and the thermal morphology of subducted slabs, *Earth Plan. Sci. Lett.*, *225*(1-2), 105–113, doi:10.1016/j.epsl.2004.05.038.

Thomson, R. E., J. R. Delaney, R. E. McDuff, D. R. Janecky, and J. S. McClain (1992), Physical characteristics of the Endeavour Ridge hydrothermal plume during July 1988, *Earth Planet. Sci. Lett.*, *111*(1), 141–154.

Thorne, M. S., and E. J. Garnero (2004), Inferences on ultralow-velocity zone structure from a global analysis of SPdKS waves, *J. Geophys. Res.*, *109*, B08301, doi: 10.1029/2004JB003010.

Tivey, M. A., and H. P. Johnson (1987), The Central Anomaly Magnetic High; implications for ocean crust construction and evolution, *J. Geophys. Res.*, *92*(12), 12,685–12,694.

Tivey, M. A., and H. P. Johnson (2002), Crustal magnetization reveals subsurface structure of Juan de Fuca Ridge hydrothermal vent fields, *Geology*, *30*(11), 979–982, doi: 10.1130/0091-7613(2002)030<0979:CMRSSO>2.0.CO;2.

Tivey, M. K., and J. R. Delaney (1986), Growth of large sulfide structures on the Endeavour Segment of the Juan de Fuca Ridge, *Earth Planet. Sci. Lett.*, *77*(3-4), 303–317.

Tivey, M. K., D. S. Stakes, T. L. Cook, M. D. Hannington, and S. Petersen (1999), A model for growth of steep-sided vent structures on the Endeavour Segment on the Juan de Fuca Ridge; results of a petrologic and geochemical study, *J. Geophys. Res.*, *104*(10), 22,859–22,883.

Tkalcic, H., and B. Romanowicz (2002), Short scale heterogeneity in the lowermost mantle: insights from PcP-P and ScS-S data, *Earth Plan. Sci. Lett.*, *201*(1), 57–68, doi: 10.1016/S0012-821X(02)00657-X.

Trampert, J., and R. D. van der Hilst (2005), Towards a quantitative interpretation of global seismic tomography, in *Earth's deep mantle; structure, composition, and evolution*, *Geophysical Monograph*, vol. 160, edited by R. D. van der Hilst, J. D. Bass, J. Matas, and J. Trampert, pp. 47–62, American Geophysical Union, Washington, DC.

Turcotte, D. L., and G. Schubert (2002), *Geodynamics*, 2nd ed., Cambridge University Press, Cambridge, UK.

Vallier, T. L., D. K. Rea, W. E. Dean, J. Thiede, and C. G. Adelseck (1981), The geology of Hess Rise, central north Pacific Ocean, in *Initial Reports of the Deep Sea Drilling Project*, vol. 62, edited by J. Thiede, T. L. Vallier, C. G. Adelseck, A. Boersma, P. Cepek, W. E. Dean, N. Fujii, V. I. Koporulin, D. K. Rea, C. A. Sancetta, W. O. Sayre, K. E. Seifert, A. Schaaf, R. R. Schmidt, K. E. Windom, and E. Vincent, pp. 1031–1072, Ocean Drilling Program, College Station, TX.

Vallier, T. L., W. E. Dean, D. K. Rea, and J. Thiede (1983), Geologic evolution of Hess Rise, central North Pacific Ocean, *Geol. Soc. Am. Bull.*, *94*(11), 1289–1307.

van der Hilst, R. D., S. Widiyantoro, and E. R. Engdahl (1997), Evidence for deep mantle circulation from global tomography, *Nature*, *386*(6625), 578–584, doi:10.1038/386578a0.

van der Hilst, R. D., S. Widiyantoro, K. C. Creager, and T. J. McSweeney (1998), Deep subduction and aspherical variations in P-wavespeed at the base of Earth's mantle, in *The core-mantle boundary region*, *Geodynamics Series*, vol. 28, edited by M. Gurnis, M. E. Wysession, E. Knittle, and B. A. Buffett, pp. 5–20, American Geophysical Union, Washington, DC.

van Thienen, P., J. van Summeren, R. D. van der Hilst, A. P. van den Berg, and N. J. Vlaar (2005), Numerical study of the origin and stability of chemically distinct reservoirs deep in Earth's mantle, in *Earth's deep mantle; structure, composition, and evolution*, *Geophysical Monograph*, vol. 160, edited by R. D. van der Hilst, J. D. Bass, J. Matas, and J. Trampert, pp. 117–136, American Geophysical Union, Washington, DC.

Veirs, S. R., R. E. McDuff, M. D. Lilley, and J. R. Delaney (1999), Locating hydrothermal vents by detecting buoyant, advected plumes, *J. Geophys. Res.*, *104*(B12), 29,239–29,247.

Vidal, V., and A. Bonneville (2004), Variations of the Hawaiian hot spot activity revealed by variations in the magma production rate, *J. Geophys. Res.*, *109*(B03104), B03104, doi:10.1029/2003JB002559.

Vidale, J. E., and H. M. Benz (1992), A sharp and flat section of the core-mantle boundary, *Nature*, *359*(6396), 627–629, doi:10.1038/359627a0.

Vidale, J. E., and M. A. H. Hedlin (1998), Evidence for partial melt at the core-mantle boundary north of Tonga from the strong scattering of seismic waves, *Nature*, *391*(6668), 682–685.

Virieux, J. (1984), Sh-wave propagation in heterogeneous media: Velocity-stress finite-difference method, *Geophysics*, *49*(11), 1933–1942.

Virieux, J. (1986), P-SV wave propagation in heterogeneous media: Velocity-stress finite-difference method, *Geophysics*, *51*(4), 889–901, doi:10.1190/1.1442147.

Von Damm, K. L. (2000), Chemistry of hydrothermal vent fluids from 9°–10°N, East Pacific Rise: "time zero," the immediate posteruptive period, *J. Geophys. Res.*, *105*(B5), 11,203–11,222.

Walcott, R. I. (1970), Flexure of the lithosphere at Hawaii, *Tectonophys.*, *9*(5), 435–446.

Ward, S. N. (1978), Long-period reflected and converted upper-mantle phases, *Bull. Seis. Soc. Am.*, *68*(1), 133–153.

Watts, A. B. (1976), Gravity and bathymetry in the central Pacific Ocean, *J. Geophys. Res.*, *81*(8), 1533–1553.

Watts, A. B. (1978), An analysis of isostasy in the world's oceans; 1, Hawaiian-Emperor seamount chain, *J. Geophys. Res.*, *83*(B12), 5989–6004.

Watts, A. B. (2001), *Isostasy and Flexure of the Lithosphere*, 1st ed., Cambridge University Press, Cambridge, UK.

Watts, A. B., and J. R. Cochran (1974), Gravity anomalies and flexure of the lithosphere along the Hawaiian-Emperor seamount chain, *Geophys. J. Royal Astron. Soc.*, *38*(1), 119–141.

Watts, A. B., and S. Zhong (2000), Observations of flexure and the rheology of oceanic lithosphere, *Geophys. J. Int.*, *142*(3), 855–875.

Watts, A. B., U. S. T. Brink, P. Buhl, and T. M. Brocher (1985), A multichannel seismic study of lithospheric flexure across the Hawaiian-Emperor seamount chain, *Nature*, *315*, 105–111.

Weekly, R. T., M. Tolstoy, F. Waldhauser, D. R. Bohnenstiehl, and W. Kim (2005), Increasing seismic activity at 9°50'N on the East Pacific Rise RIDGE 2000 Integrated Studies Site from October 2003 through April 2004, *Eos Trans. AGU*, *86*(52), Fall Meeting Suppl., Abstract T31A–0495.

Wen, L. (2000), Intense seismic scattering near the Earth's core-mantle boundary beneath the Comoros Hotspot, *Geophys. Res. Lett.*, *27*(22), 3627–3630.

Wen, L. (2001), Seismic evidence for a rapidly varying compositional anomaly at the base of the Earth's mantle beneath the Indian Ocean, *Earth Planet. Sci. Lett.*, *194*(1-2), 83–95, doi:10.1016/S0012-821X(01)00550-7.

Wen, L., and D. V. Helmberger (1998a), Ultra-low velocity zones near the core-mantle boundary from broadband PKP precursors, *Science*, *279*(5357), 1701–1703.

Wen, L., and D. V. Helmberger (1998b), A two-dimensional P-SV hybrid method and its application to modeling localized structures near the core-mantle boundary, *J. Geophys. Res.*, *103*(8), 17,901–17,918.

Wentzcovitch, R. M., N. L. Ross, and G. D. Price (1995), Ab initio study of mgsio3 and casio3 perovskites at lower-mantle pressures, *Phys. Earth Plan. Int.*, *90*(1-2), 101–112, doi:10.1016/0031-9201(94)03001-Y.

White, D. J., and R. M. Clowes (1990), Shallow crustal structure beneath the Juan de Fuca Ridge from 2-D seismic refraction tomography, *Geophys. J. Int.*, *100*(3), 349–367.

White, R. S. (1993), Melt production rates in mantle plumes, *Phil. Trans. Phys. Sci. Eng.*, *342*(1663), 137–153.

White, S. N., S. E. Humphris, and M. C. Kleinrock (1998), New observations on the distribution of past and present hydrothermal activity in the TAG area of the Mid-Atlantic Ridge, *Marine Geophys. Res.*, *20*(1), 41–56, doi:10.1023/A:1004376229719.

Whitehead, J. A. (1987), A laboratory deomonstration of solitons using a vertical watery conduit in syrup, *Am. J. Phys.*, *55*(11), 998–1003.

Wilcock, W. S., et al. (2004), Local earthquakes on the Endeavour Segment of the Juan de Fuca Ridge: first seismic results from the Keck seismic/hydrothermal observatory, *Eos Trans. AGU*, *85*(47), Fall Meeting Suppl., Abstract B13A–0180.

Wilcock, W. S. D., and J. R. Delaney (1996), Mid-ocean ridge sulfide deposits: Evidence for heat extraction from magma chambers or cracking fronts?, *Earth Planet. Sci. Lett.*, *145*, 49–64.

Wilcock, W. S. D., S. D. Archer, and G. M. Purdy (2002), Microearthquakes on the Endeavour Segment of the Juan de Fuca Ridge, *J. Geophys. Res.*, *107*(B12), 2336, doi: 10.1029/2001JB000505.

Williams, Q., and E. J. Garnero (1996), Seismic evidence for partial melt at the base of Earth's mantle, *Science*, *273*(5281), 1528–1530.

Williams, Q., J. Revenaugh, and E. Garnero (1998), A correlation between ultra-low basal velocities in the mantle and hot spots, *Science*, *281*(5376), 546–549, doi: 10.1126/science.281.5376.546.

Wilson, D. S. (1993), Confidence intervals for motion and deformation of the Juan de Fuca Plate, *J. Geophys. Res.*, *98*(9), 16,053–16,071.

Wilson, J. T. (1963), A possible origin of the Hawaiian Islands, *Can. J. Phys.*, *41*(6), 863–870.

Witte, D. C. (1989), The pseudospectral method for simulating wave propagation, Ph.D. thesis, Columbia University.

Witte, D. C., and P. G. Richards (1990), The pseudospectral method for simulating wave propagation, in *Computational Acoustics*, vol. 3, edited by D. Lee, A. Cakmak, and R. Vichnevetsky, pp. 1–18, Elsevier Scence Pulishers, B.V., Princeton, NJ.

Wysession, M. E., K. M. Fischer, T. J. Clarke, G. I. Al-Eqabi, M. J. Fouch, P. J. Shore, R. W. Valenzuela, A. Li, and J. M. Zaslow (1996), Slicing into the Earth, *Eos Trans. AGU*, *77*(48), 477, 480–482, doi:10.1029/96EO00316.

Wysession, M. E., A. Langenhorst, M. J. Fouch, K. M. Fischer, G. I. Al-Eqabi, P. J. Shore, and T. J. Clarke (1999), Lateral variations in compressional/shear velocities at the base of the mantle, *Science*, *284*(5411), 120–125, doi:10.1126/science.284.5411.120.

Yoerger, D. R., D. S. Kelley, and J. R. Delaney (2000), Fine-scale three-dimensional mapping of a deep-sea hydrothermal vent site using the Jason ROV system, *Int. J. Robotics Res.*, *19*(11), 1000–1014.

Zelt, C. A., and R. B. Smith (1992), Seismic traveltime inversion for 2-D crustal velocity structure, *Geophys. J. Int.*, *108*(1), 16–34.

Zerr, A., A. Diegeler, and R. Boehler (1998), Solidus of Earth's deep mantle, *Science*, *281*(5374), 243–246.